SURFACE MODIFIED TRANSITION METAL OXIDE BASED MAGNETIC NANOSTRUCTURES FOR INTRINSIC FLUORESCENCE, CATALYTIC PROPERTIES AND DRUG DELIVERY

Thesis submitted for the award of the degree of

Doctor of Philosophy

in

Chemistry (Physical)

by

Souvanik Talukdar

Department of Chemistry

University of Calcutta

January, 2019

Dedicated to

my beloved parents…

Acknowledgement

First of all I would like to convey my gratitude to my supervisor Prof. Kalyan Mandal for his help, valuable discussions and humble guidance. Without his wisdom, patience, and support, any of my research work would not get success. Thank you Sir for providing me opportunity to work in your laboratory and making my Ph.D. life very much enjoyable.

I am grateful to S. N. Bose National Centre for Basic Sciences (SNBNCBS), Kolkata, and Department of Science and Technology (DST), India, for providing a beautiful campus, advanced instrumental facilities, wonderful research environment, and financial supports. I also wish to express my sincere gratitude to Prof. Frank A. Müller of Otto Schott Institute for Materials Research (OSIM) of the Friedrich Schiller University Jena, Germany for his collaboration.

I thank all those faculty members of our centre, especially Prof. Amitabha Lahiri whose encouragement me to carry forward my research work. I thank all the staff members, the security men, the cleaner, the cook, and the gardener for their sincere cooperation which makes my centre beautiful. I would also like to thank all the technical staff members: Urmi Chakraborty, Dipankar Roy, Amit Chanda, Samik Roy Moulik, Surajit Mukherjee, Joy Bandopadhyay, Shakti Nath Das and Dipayan Banerjee for their help in sample characterization.

I must acknowledge my seniors and labmates: Dr. Madhuri Mandal, Dr. Rupali Rakshit, Dr. Monalisa Pal, Dr. Arup Ghosh, Dr. Srabantika Ghose, Indranil Chakraborty, Priyanka Saha, Mahebub Alam, Keshab Karmakar, Esma Khatun, Anupam Gorai, Rupam Saha, Deblina Majumdar, Dipanjan Maity, Dipika Mandal, Subrata Ghosh, Swarnali Hait, Kaushik Baishya and Suchandra Mukherjee for providing me a homely and cheerful environment in lab. I thank them for their patience and helping attitude. I must thank especially to Rupali, Monalisa, Indranil and Priyanka, whitout them I could not have achieved this.

I am grateful to: Subrata, Subhadip, Aslam and Kartik for being my best friends and for bearing up with me. I am also thankful to all my friends: Debashish, Ananda, Sudipta, Rakesh, Nirnay, Sumanta, Shirsendu, Sarowar, Victor, Sutapa, Sankar, Dhimadri, Samrat, Supriyo, Subham, Ejaj, Rahul, Vinod, Imadul, Sourav, Suman Da, Ashutosh Da, Bipul Da, Anuradha Di, Tamisra Di, Dhiraj, Rituparna, Anirban, Shauri, Pratik Da, Poonam, Aritra and Tanumoy Da for providing joyous company in several instances.

I am, especially, thankful to Sayani Di, Chaoba Di, Subhasish Da, Arghya Da, Biplab Da, Sriraj Da, Animesh Da, Arindam Da, Abhishek Da and Arnab Da. They help me to figure out my confusions, and shared various glorious as well as miserable moments.

I am grateful to all of my school, college, and university teachers especially to Ajay Kumar Satpati and Kushal Bandhapadhyay of Tufanganj N. N. M. High School (H.S.); Menoka Di, Narsima Di and Rupali Di of Maharani School, Darjeeling; Ambarish Roy and Dr. Parthapratim Parui of A. B. N. Seal College, Coochbehar, who motivated me.

I must name some of my oldest friends: Abirbarna, Tamalika, Biswajit, Shuvendu, Nirmalya, Subhabrata, Kaushik and Sankar for their colourful company. Those friends who must be named are: Susobhan, Kawsar and Jayanta.

Finally, I express my intense gratitude to my Mother Mrs. Papi Talukdar and Father Mr. Bimal Kanti Talukdar, for their sacrifice, moral support, inspiration, affection, love, guidance and everything they have done for me. They are my best teachers. I thank my maternal Uncle Mr. Ranjan Kar and elder brother Mr. Amit Talukdar for their constant motivation in my life.

Souvanik Talukdar

List of Publications

[1] "Facile Surface Modification of Nickel Ferrite Nanoparticles for Inherent Multiple Fluorescence and Catalytic Activities" **Souvanik Talukdar**, Rupali Rakshit and Kalyan Mandal, **RSC Advances**, 2018, 8, 38.

[2] "Surface modification of Cobalt ferrite nano-hollowspheres for inherent multiple photoluminescence and enhanced photocatalytic activities." **Souvanik Talukdar**, Dipika Mandal and Kalyan Mandal, **Chemical Physics Letters**, 2017, 672, 57.

[3] Three dimensional nanoarchitechture of bismuth ferrite anchored cobalt ferrite nano-hollowspheres for multiferroic" Mahebub Alam, Souvanik Talukdar and Kalyan Mandal, **Materials Letters**, 2018, 210, 80.

[4] "Influence of functional group of dye on the adsorption behaviour of $CoFe_2O_4$ nano–hollow spheres." Rupali Rakshit, Esma Khatun, Monalisa Pal, Souvanik Talukdar, Dipika Mandal, Priyanka Saha and Kalyan Mandal, **New Journal of Chemistry**, 2017, 41, 9095.

[5] "Surface engineered magneto fluorescent $MnFe_2O_4$ nanoparticles in the realm of biomedical applications." Indranil Chakraborty, Deblina Majumder, **Souvanik Talukdar**, Somenath Roy and Kalyan Mandal, **Surfaces and Interfaces**, 2017, 9, 154.

[6] "Design and development of bioactive α-hydroxy carboxylate group modified $MnFe_2O_4$ nanoparticle: Comparative fluorescence study, magnetism and DNA nuclease activity" Indranil Chakraborty, Urmila Saha, Rupali Rakshit, **Souvanik Talukdar**, Gopinatha Suresh Kumar and Kalyan Mandal, **Materials Today Chemistry**, 2107, 5, 92.

[7] “Developing Multifunctional Magneto-fluorescent $CoFe_2O_4$ Nano-Hollowspheres through Simple Surface Functionalization.” **Souvanik Talukdar**, Rupam Saha, Priyanka Saha, Kalyan Mandal [Manuscript to be submitted]

[8] “Folate functionalized zinc ferrite nano-hollowspheres for drug delivery and intrinsic fluorescence.” **Souvanik Talukdar**, Priyanka Saha, Anupam Gorai and Kalyan Mandal [Manuscript to be submitted]

Contents

Chapter 1

Introduction

This introductory chapter contains literature review of various works that enthused me to work in this specific area, a brief sketch of the entire work done by me and theoretical aspects required to explain the findings.

1. Introduction

1.1 Nanomaterials

The advancement of science and technology has contributed significantly to the evolution of human civilization. The humanity has passed through the industrial and space revolution which is still continuing with the nano revolution since last few decades. The impression of nanotechnology was first introduced by Richard Feynman in his talk "There's Plenty of Room at the Bottom" in 1959, where he described the potential to grow a system by manipulating individual atoms and molecules. The researchers gained the capability to realize Feynman's prediction after 20 years later and started the new era of nanoscience and nanotechnology with the invention of the scanning tunneling microscope (STM) and high resolution transmission microscope (HRTEM). The understanding that 'size reduction of materials affects the physiochemical properties significantly' has opened the doors to an exciting field of nanomaterials. The field of nanotechnology incorporates the synthesis, study and manipulation of particles which are between 1 to 100 nanometres; where a nanometre is well-defined as one billionth (or 10^{-9}) of a metre.

1.2 Advantages of Nanomaterials

Simply the miniaturization of particles is not that what makes nanomaterials (NMs) such an interesting area of research. At the nanoscale, some material properties are affected by the laws of atomic physics, and so behave in an unalike way or exhibit properties dissimilar those of the traditional bulk material. Due to large surface area to volume ratio and quantum confinement, NMs interact with each other, surrounding substances, light, electric, and magnetic field in different way. Chemical reactivity, optical property, electronic excitation, conductivity etc. of metal or semiconductors nanoparticles (NPs) are found to be influenced significantly by their size. Due to the increased surface

area to volume ratio of NMs, compared to bulk or even micron-scale particles, nano-catalysts have demonstrated higher efficiencies or rates of conversion with a smaller mass of material. These NMs are suitable for biological applications due to their similar size comparable to that of most primitive biological components such as proteins [1-4], while their unique optical, electrical and physical properties arise from quantum mechanical effects. The properties of NMs can likewise be customized by controlling self-arranging systems of their nanoscale building block. The NMs having building blocks with same composition but different morphology like sphere, cube, disc, rod, wire, tube, film, etc exhibit different properties [5-6]. Fabricating nano-hollowspheres (NHSs) are being the area of interest for researchers because of its hollow interior which enhances its effective surface area. These hollow structures have numerous applications such as in catalysis, controlled delivery, light fillers, artificial cells, low dielectric constant materials, high density magnetic storage, radar absorbing materials etc. The hollow core of NHSs can be used to encapsulate drugs, proteins and DNA and also for their controlled release [7-10]. Moreover, due to hollow interior and large effective surface area they have low density, which prevents sedimentation in the colloidal form. As a consequence of these superior properties, NMs have been utilized in a plethora of applications [11-30].

1.3 Transition Metal Oxide Magnetic Nanomaterials

So far, 60 bio-minerals have been recognized as being essential for the correct function of organisms, and among these more than 60% are reported to be coordinated to either hydroxyl moieties or water molecules. Specifically, Metal oxides are the fundamental stepping - stone for the development of functional nanomaterials. The atmosphere of the Earth is an oxidative environment and oxides are the lowest free energy states for most metals in the periodic table and

demonstrate applications ranging from industries to bio-medicine. Magnetic nanoparticles belong to the group of nanotechnology-based materials with an impact in fields of analytical chemistry [31-35], biosensing [36-40], and nanomedicine [40-44]. Among the different types of ferrites, spinel ferrite nanoparticles have been a subject of interest in recent years due to their promising technological applications, especially in biomedicine applications. Iron oxide particles such as magnetite (Fe_3O_4) or its oxidized form maghemite (γ -Fe_2O_3) are by far the most commonly employed for biomedical applications. Cobalt ferrite ($CoFe_2O_4$) has specific properties which make it a suitable candidate for different applications and recently in medical science. The main reason for using the $CoFe_2O_4$ for bio-medical applications is its high magneto-crystalline anisotropy which originates from the spin–orbit (L–S) coupling in crystal lattices. Manganese ferrites ($MnFe_2O_4$) serve as potential MRI contrast agents with higher saturation magnetization among other ferrites. The low cost of synthesis, high chemical stability and excellent magnetic, optical and electrical properties of the spinel ferrites drew the attention.

1.4 Crystal Structure

3d transition metal oxide based magnetic NMs, spinel ferrites are a class of compounds of general formula MFe_2O_4 (M= Mn, Co, Fe etc). The word spinel is derived from Italian spinella, diminutive of spine, thorn (from its sharply pointed crystals). Spinel crystallizes in the cubic system, forming octahedral crystals. In the MFe_2O_4 formula, M is usually a divalent cation such as manganese (Mn^{+2}), nickel (Ni^{+2}), cobalt (Co^{+2}), zinc (Zn^{+2}), copper (Cu^{+2}), or magnesium (Mg^{+2}). M can also represent the monovalent lithium cation (Li^{+}) or even vacancies, as long as these absences of positive charge are compensated for by additional trivalent iron cations (Fe^{+3}). The general formula for spinel ferrites is $M_{\delta}^{+2}Fe_{1-\delta}^{+3}\left[M_{1-\delta}^{+2}Fe_{1+\delta}^{+3}\right]O_4^{-2}$, octahedral sites are represented by

square brackets and the cations prior to square brackets are that of tetrahedral sites. $\boldsymbol{\delta}$ is degree of inversion which determines the classification of ferrites. Depending on the cation distribution over different crystallographic sites, the spinel compounds can be generally classified into three categories.

(1) Normal spinel structure: δ = 1

In normal spinel ferrites all M^{+2} ions occupy tetrahedral sites i.e. 8 bivalent cations occupy 8 tetrahedral sites and 16 trivalent cations occupy 16 octahedral sites. Structural formula of such ferrites is $M^{+2}[Fe_2^{+3}]O_4^{-2}$. Zinc ferrite $Zn^{+2}[Fe_2^{+3}]O_4^{-2}$ belongs to this class.

(2) Inverse spinel structure: δ = 0

All M^{+2} are in octahedral sites and Fe^{+3} ions are equally distributed between tetrahedral and octahedral sites in inverse spinel ferrites. The structural formula of these ferrites is $Fe^{+3}[M^{+2}Fe^{+3}]O_4^{-2}$. Fe_3O_4, $NiFe_2O_4$ and $CoFe_2O_4$ have inversed spinel structure.

(3) Mixed spinel structure: 0< δ <1

If the bivalent cations (M^{+2}) are present in both tetrahedral and octahedral sites, the spinel is mixed spinel structure. Structural formula of such ferrites is $M_{1-\delta}^{+2}Fe_{\delta}^{+3}\left[M_{\delta}^{+2}Fe_{2-\delta}^{+3}\right]O_4^{-2}$ $MnFe_2O_4$ is an important candidate for this type of structure and has an inversion degree of δ = 0.2 and therefore it has structural formula $M_{0.8}^{+2}Fe_{0.2}^{+3}[M_{0.2}^{+2}Fe_{1.8}^{+3}]O_4^{-2}$.

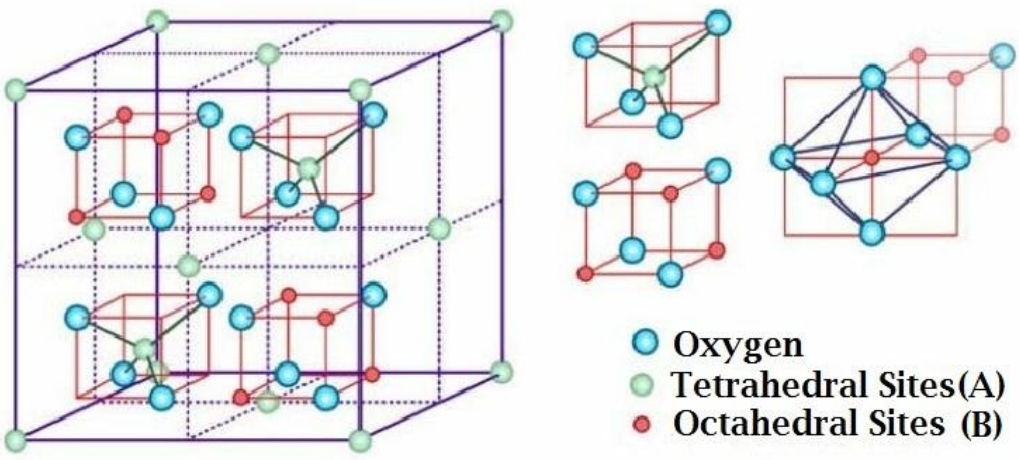

Figure1.1: Face centered cubic spinel structure (© Ristanovic. et al., SCI SINTER, **2015**, 47, 3-14)

Spinel ferrites crystallize in the cubic system, in the space group *Fd3m*. There are 8 units per cubic unit cell that contains 32 O^{-2} anions in a face-centered cubic packing (fcc). Inside the anion lattice, cations have 32 octahedral (B) and 64 tetrahedral (A) interstices available however only 24 of the total 96 interstices are occupied in a spinel lattice. A-site tetrahedra in spinel are isolated from each other and share corners with neighbouring B-site octahedra. B-site octahedra share six of twelve O-O edges with nearest neighbour B-site octahedral, as shown in Figure 1.1.

1.5 Cation Distribution in Spinel Ferrite

Chemical and Physical properties of spinel ferrites are determined by the type and concentration of various cations incorporated at tetrahedral and octahedral sites. The ferrite unit cell consists of 56 atoms, among them 32 oxygen anions are distributed in close-packed cubic structure and 24 cations occupy 8 of the 64 tetrahedral sites and 16 of 32 octahedral sites available [45]. The oxygen atoms in ferrites are non-magnetic but play a very crucial role in regulating electrical and magnetic properties. A wide variety of cations can occupy the interstitial

sites. So the knowledge of cation distribution is an important criteria for understanding of the expressed electrical and magnetic properties. The distribution of cations is influenced by a number of factors namely synthesis method, ionic radii, ionic charge, lattice energy, octahedral site preference energy, crystal field stabilization energy [46].

The ideal tetrahedral site can fit in a cation with maximum radius of 0.30 Å and octahedral site can house a cation with maximum radius 0.55 Å. Then again as the transition metal ions such as Mg, Ni, Zn, Fe, Mn etc. are larger than the ideal volume accessible at these sites, tetrahedral and octahedral sites undergo expansion in order to accommodate larger ions. Octahedral sites always experience lesser expansion compared to tetrahedral sites. Then oxygen ions are forced to move outwards leading to increase in oxygen position parameter or anion positional parameter, *u* [47].

The radii of ions on tetrahedral and octahedral sites, r_A and r_B respectively are,

$$r_A = \left(u - \frac{1}{4}\right) a\sqrt{3} - r_{O^{-2}} \qquad (1.1)$$

$$r_B = \left(\frac{5}{8} - u\right) a - r_{O^{-2}} \qquad (1.2)$$

Where, $r_{O^{-2}}$ is radius of oxygen ion and *a* is lattice parameter.

1.5 Surface Modification and Functionalization

A wide range of surface modification procedures is involved in nanofabrication that is significant in many different areas of nanotechnology. To attain the

desired physical, thermal, electrical, and mechanical properties of NMs, surface functionalization techniques with various chemical approaches are required. Surface modification and functionalization can also be applied to a variety of different NMs for their target properties by designing appropriate chemical reactions. Surface functionalization can be widely applied to tailor the optical, magnetic and catalytic properties metal oxides NMs. The modification can be done by different methods with a view to altering a wide range of characteristics of the surface, such as: roughness, hydrophilicity, surface charge, surface energy, biocompatibility and reactivity. Surface modification of NMs can be done in different ways, such as (1) vapor deposition, (2) chemical functionalization, (3) plasma sprayed coating.

Among the aforementioned processes, chemical functionalization primarily aims to gain hydrophilic, hydrophobic, biocompatible, catalytic, conductive and anti-corrosive properties. The results from experiments in earlier days have suggested that functionalization of nanoparticles with some definite chemical moieties results in multifunctional nanoparticles with enhanced efficacy, while simultaneously reducing side effects, due to properties such as targeted localization in tumors and active cellular uptake. The prerequisite for evolving this area of research is the advancement of chemical methods to conjugate chemical moieties onto NMs in a consistent method. Recently, a number of chemical methods have been established to synthesize functionalized NMs specifically for drug delivery, cancer therapy, diagnostics, tissue engineering and molecular biology. Indeed, functionalization has been used to conjugate drug molecules, polymers and organic groups to NMs. Furthermore, functionalization has also been shown to prevent NMs against agglomeration [48], stabilize the nuclei and control the growth of NMs in terms of rate, final size or geometric shape.

The biomedical applications of metal oxide NMs have increased in the last decades due to their easy synthesis and optical properties. The targeted organs can highly intake if proper ligand functionalization is used [49]. Metal oxide NMs are excellent tool for tracing and therapeutic agents and can be easily functionalized. The desired properties of NMs can be manipulated in an anticipated way for the precise applications [50-51]. The processes used to engender, control and set up functionalized nanoparticles (FNPs) provides new prospects for the advancement of multifunctional tools to be used in biomedical applications. Moreover, magnetic NPs have gained substantial attention in diagnostic applications due to their magnetic properties, high surface area and the possibilities of surface functionalization, which show a great versatility in specialized fields such as medical diagnosis (MRI – magnetic resonance imaging), therapy and targeted drug delivery [52-60].

There are two conventional approaches for functionalizing the NMs. The first of these methods includes direct functionalization, where the whole functional ligand is a bi-functional organic compound. In organic chemistry, when a single organic molecule has two different functional groups, it is called a bifunctional molecule . A bifunctional molecule has the properties of two different types of functional groups, such as an alcohol (-OH), amide (-$CONH_2$), aldehyde (-CHO), nitrile (-CN) or carboxylic acid (-COOH). In this approach, one of the functionally reactive groups is used to attach to the NMs surface (complexing agent) and the second group contains the required active functionality. Direct functionalization is preferred because it only requires a single conjugation step. The second approach consists of planting chelating agent on the surfaces of NMs and further the functional group moieties are attached with the chelating agent. The second process is called the post-functionalization. Other functionalization processes have also been used, including the encapsulation with a polymer that possesses both the chelating

and the functional group.

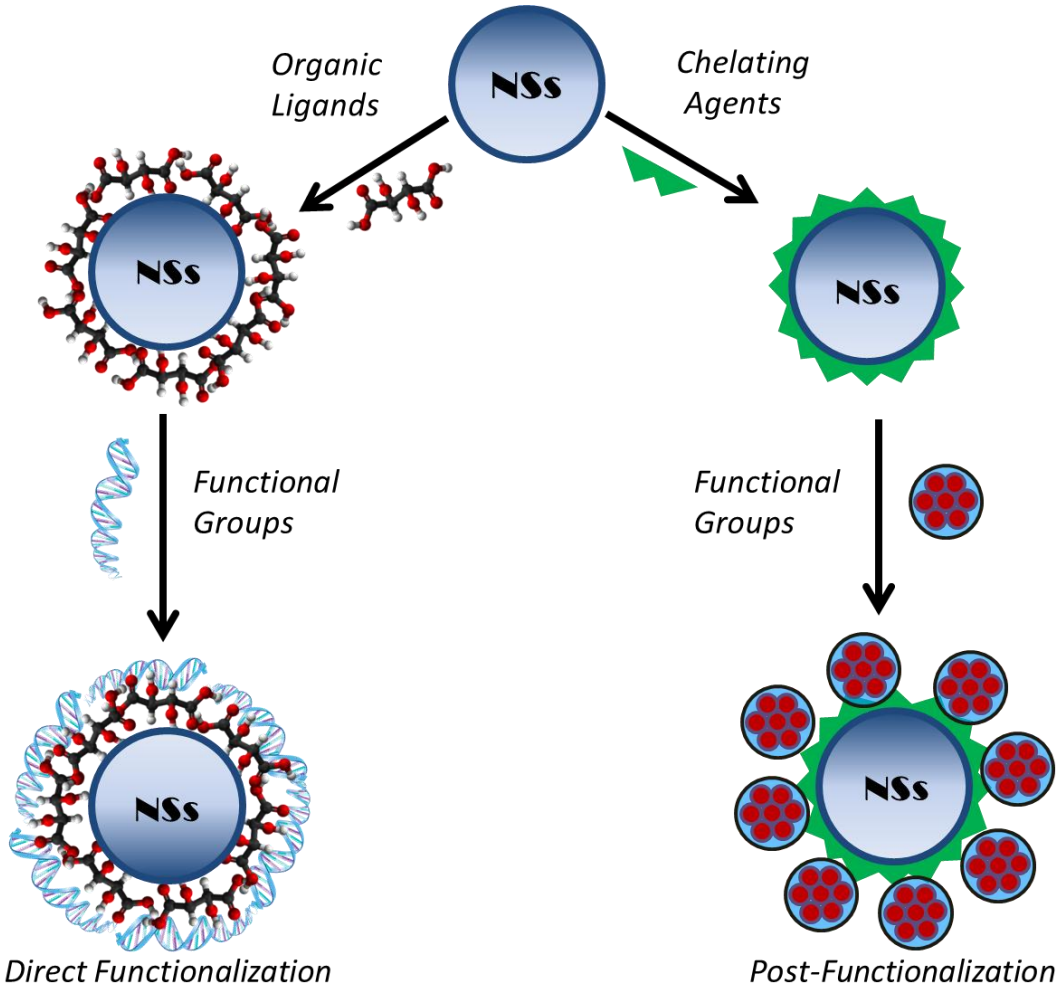

Figure 1.2: Schematic diagram of surface functionalization.

1.6 Consequences of Surface Modification on Metal Ion

The surface of the NMs contains numerous uncompensated coordination spheres due to broken bonds. Metal ions residing within those uncompensated coordination spheres form complexes with the ligands upon functionalization, resulting completely new optical, magnetic, catalytic properties. Orientation of the d orbitals is shown in Figure 1.3. The $d_{x^2-y^2}$ and d_{z^2} axis are aligned along the axis and the rests, d_{xy}, d_{yz}, d_{xz} are aligned in between the axis. According to Ligand field theory, the interaction between a transition metal

and ligands arises from the attraction between the positively charged metal cation and negative charge on the non-bonding electrons of the ligand. The theory is developed by considering energy changes of the five degenerate *d*-orbitals upon being surrounded by an array of point charges consisting of the ligands. As a ligand approaches the metal ion, the electrons from the ligand will be closer to some of the *d*-orbitals and farther away from others, causing a loss of degeneracy. The electrons in the *d*-orbitals and those in the ligand repel each other as alike charges repel. Thus the d-electrons closer to the ligands will have a higher energy than those further away which results in the *d*-orbitals splitting in energy.

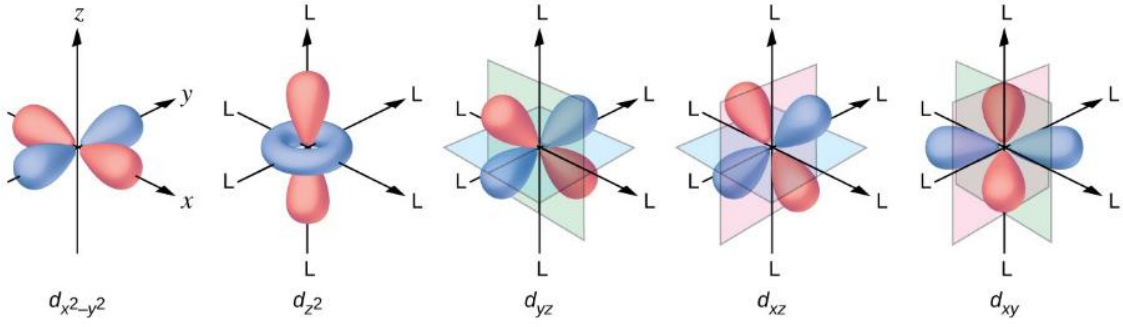

Figure 1.3: The directional characteristics of the five d orbitals are shown here. The shaded portions indicate the phase of the orbitals. The ligands (L) coordinate along the axes in case of octahedral complexes.

By merging the principles laid out in molecular orbital theory and crystal field theory, ligand field theory was resulted, which describes the loss of degeneracy of metal d orbitals in transition metal complexes. In ligand field theory, the various d orbitals are affected differently when surrounded by a field of neighboring ligands and are raised or lowered in energy based on the strength of their interaction with the ligands.

There are two ways in which the effect of ligands on the d electrons on a metal can be described. On the basis of simple electron-electron repulsion, donation of a lone pair might raise an occupied d orbital in energy. Alternatively, bonding

interactions between ligand orbitals and d orbitals can be taken into account. Anyway, there are interactions between ligand electrons and d electrons that generally results in raising the energy of d electrons. The effect depends on the coordination geometry of the ligands. Ligands in a tetrahedral coordination sphere will have a different effect than ligands in an octahedral coordination sphere, because they will interact with the different d orbitals in different ways.

In octahedral co-ordination sphere, ligands approach from the direction of axes resulting in destabilization of the orbitals along the axes ($d_{x^2-y^2}$ and d_{z^2}) and stabilization of the orbitals lying in between the axes (d_{xy}, d_{yz}, d_{xz}). But in case of tetrahedral co-ordination sphere, d_{xy}, d_{yz}, d_{xz} orbitals are closer to the direction of approaching ligands than the $d_{x^2-y^2}$ and d_{z^2} orbitals, so the reverse situation is observed. Metal *d* orbitals split in the following manner as shown in Figure 1.4.

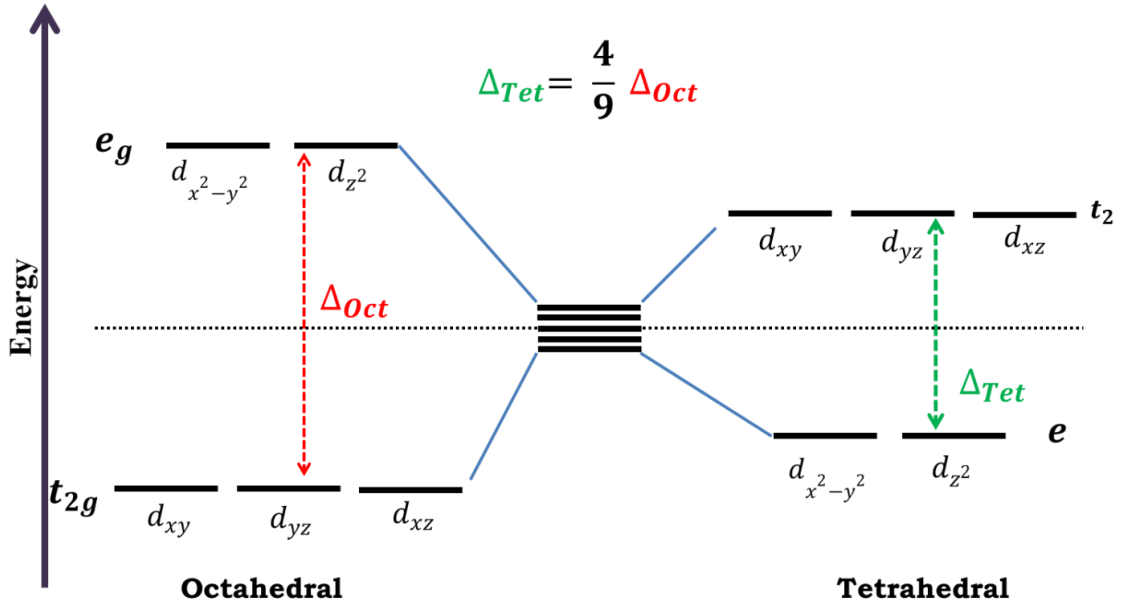

Figure 1.4: Energy levels of d orbitals in common stereochemistry.

1.7 Strength of the Ligands

The difference in energy (Δ) between the sets of *d* orbitals (t_{2g} and e_g) depends on several factors, including the ligands and geometry of the complex. Ligands that interact weakly will produce little change in the d orbital energy levels, whereas ligands that interact strongly produce a larger alteration in d orbital energy levels. The spectrochemical series is a list of ligands arranged in order of their field strength.

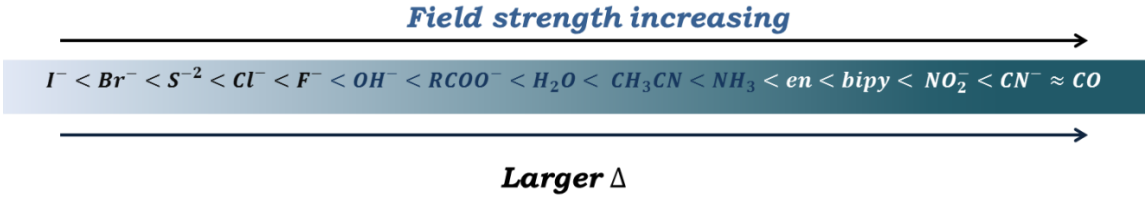

Figure 1.5: Spectrochemical series of ligands in the increasing order of field strength.

The nature of ligands coordinated to the center metal is an important feature of a complex compound along with other properties such as oxidation state of the metal. Being more specific, the capability of the ligand to donate electrons to the center atom or accept from the same, will determine the molecular orbitals. The spectrochemical series shows the trend of compounds as weak field to strong field ligands. Furthermore, ligands can be characterized by their π-bonding interactions. This interaction reveals the amount of splitting between t_{2g} and e_g energy levels of the molecular orbitals that ultimately dictate the strength of field of the ligands. π donor ligands having occupied *p* orbitals tend to donate π electrons to the metal ions along with the σ bonding electrons, exhibiting stronger metal-ligand interactions and an effective decrease of CFSE. π acceptor ligands having vacant π* with comparable energy to metal *d* orbitals, can undergo π back bonding, resulting in increase of CFSE. The metal ions can

also be arranged in order of increasing CFSE, as $Mn^{+2} < Ni^{+2} < Co^{+2} < Fe^{+2} < V^{+2} < Fe^{+3} < Cr^{+3} < V^{+3} < Co^{+3}$.

1.7 Tanabe-Sugano Diagrams

Tanabe-Sugano diagrams are used in coordination chemistry to predict electromagnetic absorptions of metal coordination compounds of tetrahedral and octahedral complexes. In Tanabe-Sugano diagram, the x-axis is expressed in terms of the crystal field splitting parameter, 10Dq, or Δ_{oct}, scaled by the *B* Racah Parameter. The y-axis is in terms of energy of an electronic transition, E, scaled by *B*. Racah parameter, *B* denotes the interelectronic repulsion. Three Racah parameters exist, *A, B, and C*, which define various aspects of interelectronic repulsion. *A* is an average total interelectron repulsion. *B* and *C* correspond to individual d-electron repulsions. As *A* is constant among d-electron configuration, it is not necessary for calculating relative energies. Hence it is absent from Tanabe and Sugano's studies of complex ions. *C* is necessary only in certain cases. *B* is the most important of Racah's parameters in this case. Each line in the Tanabe-Sugano diagram corresponds to each electronic state. The bending of certain lines is due to the mixing of terms with the same symmetry. The relative order of energies is determined using Hund's rules. Tanabe–Sugano diagrams (d^4, d^5, d^6, and d^7) also have a vertical line drawn at a specific Dq/*B* value, which corresponds to a discontinuity in the slopes of the excited states' energy levels. This pucker in the lines occurs when the spin pairing energy, P, is equal to the ligand field splitting energy, Dq. Complexes to the left of this line (lower Dq/*B* values) are high-spin, while complexes to the right (higher Dq/*B* values) are low-spin. There is no low-spin or high-spin designation for d^2, d^3, or d^8. For instance, Tanabe-Sugano diagram of d^8 system is demonstrated in Figure 1.6.

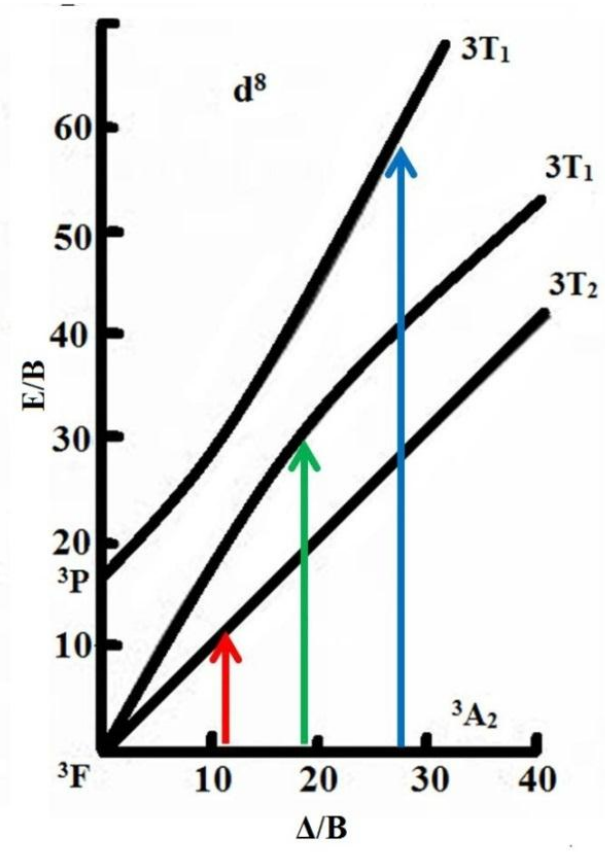

Figure 1.6: Tanabe-Sugano diagram of d^8 system.

1.8 Selection Rules

There are two spectroscopic selection or transition rules that govern the electronic transitions within the *d* orbitals. First, the Laporte rule is a selection rule formally stated as follows: In a centrosymmetric environment (i.e. octahedral co-ordination sphere), transitions between like atomic orbitals such as *s-s*, *p-p*, *d-d*, or *f-f*, transitions are forbidden. The allowed transition involves change in parity. The orbitals possess either symmetry or antisymmetry with respect to inversion centre – i.e., *g* (geared = even) or *u* (ungerade = odd). As per the laporte selection rule, transitions involving *g* to *g* and *u* to *u* are forbidden but *g* to *u* and *u* to *g* transitions are allowed.

The second one is spin selection rule, which states that transitions involving a

change in spin multiplicity are forbidden. It follows that transitions in which the spin "direction" changes are forbidden. In formal terms, only states with the same total spin quantum number are "spin-allowed".

1.9 Charge Transfer Bands

In transition metal complexes a change in electron distribution between the metal and a ligand gives rise to charge transfer (CT) bands when performing Ultraviolet-visible spectroscopy experiments. Depending on the direction of charge transfer they are classified as either ligand-to-metal (LMCT) or metal-to-ligand (MLCT) charge transfer, shown in Figure 1.7.

1.9.1 Ligand to Metal Charge Transfer Bands

Ligand-to-metal charge transfer (LMCT) complexes arise from transfer of electrons from molecular orbitals of ligand to molecular orbitals of metal. This type of transfer is predominant if complexes have ligands with relatively high-energy lone pairs (example S or Se) or if the metal has low-lying empty orbitals. Many such complexes have metals in high oxidation states (even d^0). These conditions imply that the acceptor level is available and low in energy. If the ligand molecular orbitals are full, charge transfer may occur from the ligand molecular orbitals to the empty or partially filled metal d-orbitals. Ligand to metal charge transfer results in the reduction of the metal.

1.9.2 Metal to Ligand Charge Transfer Bands

Metal-to-ligand charge transfer (MLCT) complexes arise from transfer of electrons from molecular orbitals of metal to molecular orbital of ligand. This is most commonly observed in complexes with ligands having low-lying π^* orbitals, especially aromatic ligands. The transition will occur at low energy if the metal ion has a low oxidation number, for its d orbitals will be relatively high in energy. Upon the absorption of light, electrons in the metal orbitals are

excited to the ligand π* orbitals.

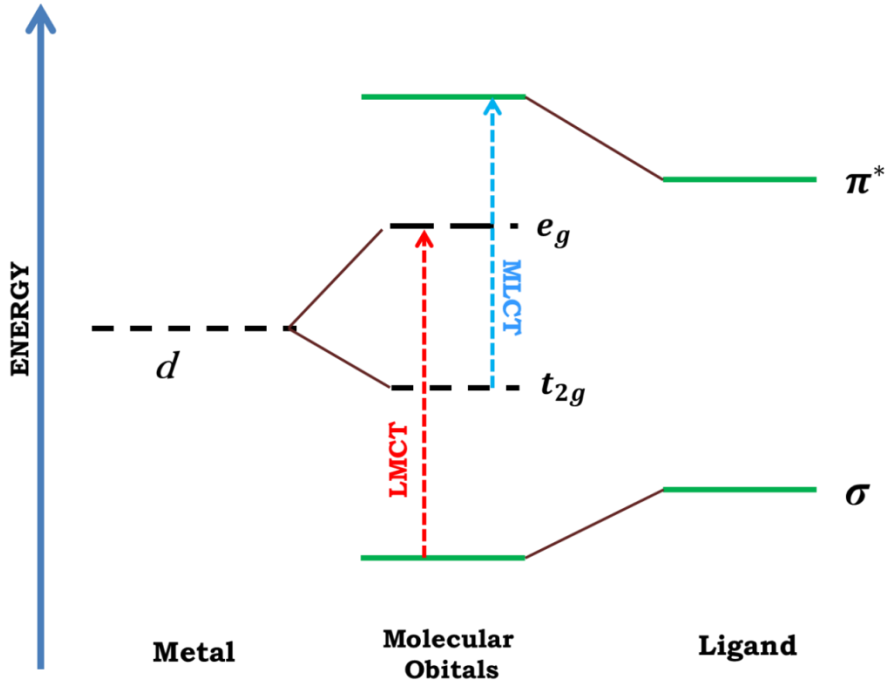

Figure 1.7: Electronic transitions responsible for charge transfer spectra in metal complexes.

1.10 Nanocatalysis

Nanocatalysis is a rapidly growing field which involves the use of NMs as catalysts for a variety of homogeneous and heterogeneous catalysis applications. Since NMs have large surface to volume ratio compared to bulk materials, they are attractive candidates for use as catalysts. Heterogeneous catalysis represents one of the oldest practices of nanoscience; nanoparticles of metals, metal oxides, semiconductors and other compounds have been widely used for important chemical reactions. NM catalysts have a very large surface area, which has a positive effect on reaction rate. Yet, there are structure- and shape-based properties at the nanoscale, which can also affect the catalytic activity of a material.

Homogeneous catalysts are used in the same medium as the reactants - for nanoparticles this typically means a solution or suspension of nanoparticles in a solvent. The most important issue to consider when designing a nanocatalyst for

use in a solution is to prevent aggregation. Nanoparticles are naturally attracted towards one another in these conditions, and will clump together to form larger particles. If the agglomeration is not prevented, their large surface to volume ratio and other benefits will be wasted. The most effective way to stabilize nanoparticles in solution is to attach long chain molecules to the surface. These make it impossible for the nanoparticles to get so close that they stick together. However, they can also reduce the access to the nanoparticle surface for the reacting molecules, decreasing overall catalytic activity. The other main concern with homogeneous nanocatalysts is recovery. Nanoparticles are especially difficult to remove from a solution, and the extra steps needed to do so could completely negate the process simplification due to using the catalyst in the first place. In homogeneous catalysis, nanoscaled structures in colloidal solutions are used as catalysts. In this type of catalysis, the colloidal nanostructures are finely dispersed in an organic or aqueous solution, or a solvent mixture. Metal colloids are very efficient catalysts because a large number of atoms are present on the surface of the nanoparticles. Heterogeneous catalysis (catalyst which is in a different phase to the reactants) is always considered as more environmentally friendly catalysis due to its high recoverability. The heterogeneous catalyst may be usually a solid or immobilized on a solid inert matrix. In heterogeneous catalysis, NSs are supported on various substrates like carbon, silica, alumina, titania and polymers by chemical methods like grafting. Heterogeneous metal nanocatalysts are prepared by adsorption of nanoparticles on to supports, which involves functionalization of supports to adsorb nanoparticles on to them and, fabrication of nanostructures on the supports by lithographic techniques.

Since nanocatalysts are made of nanoparticles or/and nanomaterials, as a metal or metal oxide active phase or as a support or a combination of both, nanoparticles and nanomaterials have been the object of an ever increasing interest during recent decades [61-65]. The common goal is the development of

well-defined nanoparticles/ nanomaterials displaying well-controlled properties to get efficient and selective nanocatalysts for numerous relevant catalytic reactions. The main objectives of research on nanocatalysis are to increase activity and specificity, minimize the energy consumption and enhancing the lifetime of catalysts. Advances in nanocatalysis in past few years with present day's developments open a new vision for nanocatalysis and its future aspects such as inspired design, synthesis and formulation of industrially and biologically important catalytic materials.

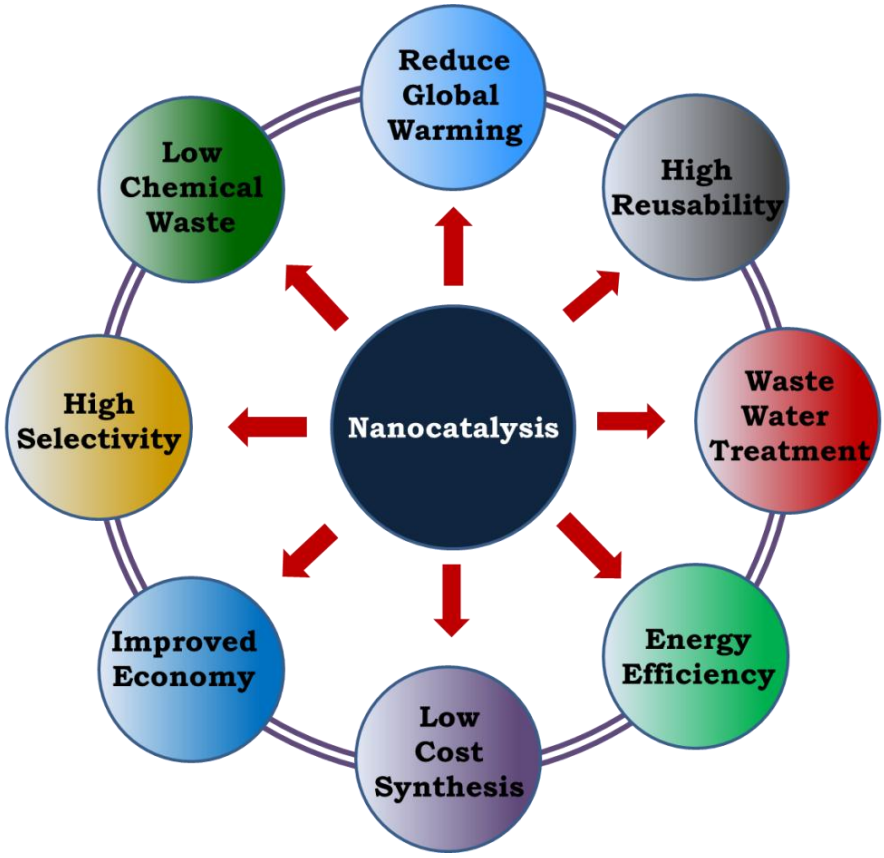

Figure 1.8: Advantages of nanocatalysis.

1.11 Adsorption on the surface

Adsorption is the adhesion of atoms, ions or molecules from a gas, liquid or dissolved solid to a surface. This process creates a film of the *adsorbate* on the

surface of the *adsorbent*. Adsorption is present in many natural, physical, biological and chemical systems and is widely used in industrial applications such as heterogeneous catalysts. The molecules of gases or liquids or the solutes in solutions adhere to the surface of the solids. In adsorption process, two substances are involved. One is the solid or the liquid on which adsorption occurs and it is called adsorbent. The second is the adsorbate, which is the gas or liquid or the solute from a solution which gets adsorbed on the surface.

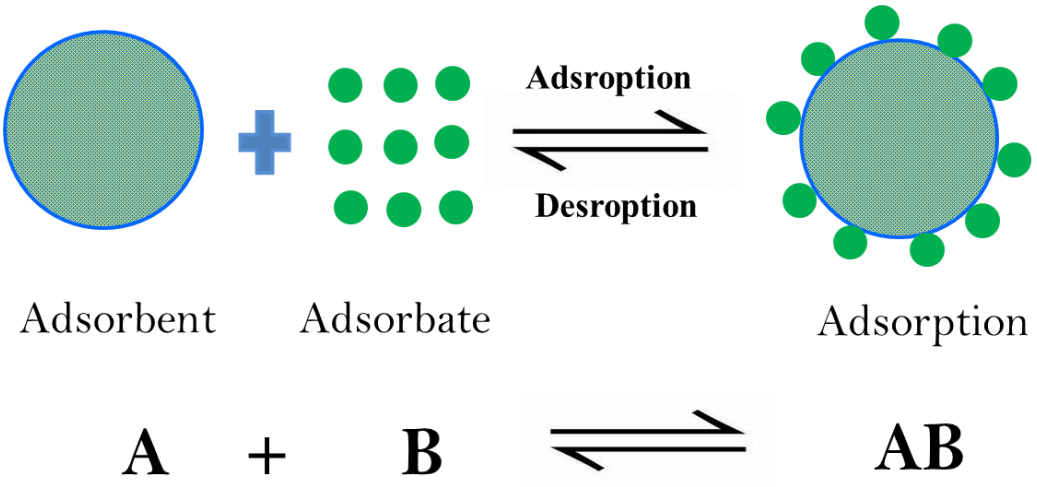

Figure 1.9: Schemaic representation of Adsorption process.

Depending upon the nature of forces existing between adsorbate molecules and adsorbent, the adsorption can be classified into two types:

(1) **Physical adsorption (physisorption):** If the force of attraction existing between adsorbate and adsorbent are Vander Waal's forces, the adsorption is called physical adsorption. It is also known as Vander Waal's adsorption. In physical adsorption the force of attraction between the adsorbate and adsorbent are very weak, therefore this type of adsorption can be easily reversed by heating or by decreasing the pressure.

(2) **Chemical adsorption (chemisorption):** If the force of attraction existing between adsorbate and adsorbent are almost same strength as chemical bonds, the adsorption is called chemical adsorption, also known as Langmuir adsorption. In chemisorption the force of attraction is very strong, therefore adsorption cannot be easily reversed.

According to Le-Chatelier principle, the direction of equilibrium would shift in that direction where the stress can be relieved. In case of application of excess pressure to the equilibrium system, the equilibrium will shift in the direction where the number of molecules decreases. Since number of molecules decreases in forward direction, with the increases in pressure, forward direction of equilibrium will be favored.

Freundlich Adsorption Isotherm

In 1909, Freundlich gave an empirical expression representing the isothermal variation of adsorption of a quantity of gas adsorbed by unit mass of solid adsorbent with pressure. This equation is known as Freundlich Adsorption Isotherm or Freundlich Adsorption equation or simply Freundlich Isotherm.

$$\frac{x}{m} = kP^{\frac{1}{n}} \qquad (1.3)$$

where, x is the mass of the gas adsorbed on mass m of the adsorbent at pressure P and k, n are constants whose values depend upon adsorbent and gas at particular temperature. Though Freundlich Isotherm correctly established the relationship of adsorption with pressure at lower values, it failed to predict value of adsorption at higher pressure.

Langmuir Adsorption Isotherm

In 1916 Langmuir proposed another Adsorption Isotherm known as Langmuir Adsorption Isotherm. This isotherm was based on different assumptions one of

which is that dynamic equilibrium exists between adsorbed gaseous molecules and the free gaseous molecules.

$$A(g) + B(S) \underset{\text{desorption}}{\overset{\text{Adsorption}}{\rightleftharpoons}} AB$$

where, *A(g)* is unadsorbed gaseous molecule, *B(s)* is unoccupied metal surface and *AB* is Adsorbed gaseous molecule.

Based on his theory, he derived Langmuir Equation which depicted a relationship between the number of active sites of the surface undergoing adsorption and pressure.

$$\theta = \frac{KP}{1+KP} \qquad (1.4)$$

where, θ is the number of sites of the surface which are covered with gaseous molecule, *P* represents pressure and *K* is the equilibrium constant for distribution of adsorbate between the surface and the gas phase .The basic limitation of Langmuir adsorption equation is that it is valid at low pressure only.

At lower pressure, *KP* is so small, that factor (1+*KP*) in denominator can almost be ignored. So Langmuir equation reduces to

$$\theta = KP \qquad (1.5)$$

At high pressure *KP* is so large, that factor (1+*KP*) in denominator is nearly equal to *KP*. So Langmuir equation reduces to

$$\theta = \frac{KP}{KP} = 1 \qquad (1.6)$$

BET adsorption Isotherm

BET Theory, put forward by Brunauer, Emmett and Teller explained that multilayer formation is the true picture of physical Adsorption.

One of the basic assumptions of Langmuir Adsorption Isotherm was that adsorption is monolayer in nature. Langmuir adsorption equation is applicable under the conditions of low pressure. Under these conditions, gaseous molecules would possess high thermal energy and high escape velocity. As a result of this less number of gaseous molecules would be available near the surface of adsorbent.

Under the condition of high pressure and low temperature, thermal energy of gaseous molecules decreases and more and more gaseous molecules would be available per unit surface area. Due to this multilayer adsorption would occur. The multilayer formation was explained by BET Theory. The BET equation is given as

$$V_{total} = \frac{V_{mono} C (\frac{P}{P_0})}{(1-\frac{P}{P_0})(1+C(\frac{P}{P_0})-(\frac{P}{P_0})} \qquad (1.7)$$

where, V_{mono} be the adsorbed volume of gas at high pressure conditions so as to cover the surface with a unilayer of gaseous molecules,

$$\frac{K_1}{K_l}$$

the ratio is designated C. K_1 is the equilibrium constant when single molecule adsorbed per vacant site and K_l is the equilibrium constant to the saturated vapor liquid equilibrium.

1.14 Kinetics of Adsorption

In order to examine the controlling mechanism of adsorption such as mass transfer, physisorption, and chemisorption; different kinetic models such as intraparticle diffusion (mass transfer) model, pseudo 1st order (physisorption), and pseudo 2nd order (chemisorption) models are applied to test the obtained experimental data for different absorbent concentration. The amount of dye on adsorbent is calculated from the following equation:

$$q_e = \frac{(C_0 - C_e)V}{m} \qquad (1.8)$$

where, q_e (mg/g) is the amount of dye adsorbed at equilibrium, C_0 and C_e (mg/L) are the liquid phase concentrations of dye at initial and equilibrium points respectively. *V* is the volume of the solution and *m* is the mass of dry adsorbent used.

Intraparticle diffusion model based on the theory proposed by Weber and Morris [66] is tested to identify the diffusion mechanism. Adsorption is a multistep process involving the transport of solute molecules from the aqueous phase to the surface of solid particulates followed by diffusion into the interior of pores. According to this theory, the rate expression for Intraparticle diffusion model is,

$$q_t = k_i t_{1/2} + C \qquad (1.9)$$

where, k_i (mg/g $h^{1/2}$), the intraparticle diffusion rate constant, is obtained from the slope of the straight line of q_t vs. $t_{1/2}$.

The pseudo 1st order rate expression of Lagergren [67] is:

$$\log(q_{e_1} - q_t) = log q_{e_1} - \frac{k_1}{2.303} t \qquad (1.10)$$

where, q_e and q_t (mg/g) are the amounts of dye adsorbed at equilibrium and at time *t*(h), respectively and k_1 (h^{-1}) is the adsorption rate constant. A straight line of $\log(q_{e_1} - q_t)$ would suggest the applicability of this kinetic model.

The pseudo 2nd order [68] equation based on equilibrium adsorption data is expressed as:

$$\frac{t}{q_t} = \frac{1}{k_2 q_{e_2}^2} + \frac{1}{q_{e_2}} t \qquad (1.11)$$

where, k_2 (g/mg h) is the rate constant for the pseudo second order adsorption kinetics.

1.14.1 Equilibrium Modelling

The analysis of equilibrium sorption data by fitting them into different isotherm models is an important step for the description of how adsorbate will interact with an adsorbent [69]. The Langmuir equation is valid for monolayer adsorption on a surface with a finite number of identical sites and is expressed as [70]:

$$\frac{C_e}{q_e} = \frac{1}{k_L q_m} + \frac{C_e}{q_m} \qquad (1.12)$$

where, C_e (mg/L) is the initial concentration of adsorbate and q_e (mg/g) is the amount of adsorbate adsorbed per unit mass of adsorbent at equillibrium. q_m is the maximum amount of the dye per unit mass of adsorbent to form a complete monolayer on the surface at high C_e (mg/L) and k_L (L/mg) is a constant related to the affinity of the binding sites.

The empirical Freundlich isotherm [71] based on adsorption on a heterogeneous surface is given by the following equation:

$$logq_e = logk_F + \frac{1}{n} logC_e \qquad (1.13)$$

where, k_F (mg/g (L/mg)$^{1/n}$) and n are Freundlich constants with n providing an indication of how favorable is the adsorption process. k_F is the adsorption capacity of the adsorbent which can be defined as the adsorption or distribution coefficient. It represents the quantity of dye adsorbed onto adsorbent for a unit equilibrium concentration. The slope of 1/n ranging between 0 and 1 is a measure of adsorption intensity or surface heterogeneity, becoming more heterogeneous as its value gets closer to zero [72]. Value for 1/n below one indicates a normal Langmuir isotherm while 1/n above one is an indicator for cooperative adsorption [73].

1.15 Magnetic Properties of Nanomaterials

In cubic spinel structure ions are arranged in octahedral sites and tetrahedral sites. Ions on octahedral sites interact directly with each other with parallel spin orientation, and they also interact with those on tetrahedral sites mediated by the oxygen ions and the spins align antiparallel through super exchange interaction. In inverse spinel ferrites, MFe_2O_4 (where M^{+2} = divalent ions of Fe, Co, Ni), the Fe^{+3} ions on tetrahedral sites are aligned antiparallel to those on octahedral sites, so that there is no net magnetization from these ions. M^{+2} ions having unpaired electrons, tend to align their spins parallel with those of Fe^{+3} ions on adjacent octahedral sites, and hence with those of other M^{+3} ions. This produces a resultant ferromagnetic interaction for those ferrites where M^{+2} ions have unpaired electrons. In normal spinel, MFe_2O_4 (where M^{+2} = divalent ions of Zn), the M^{+2} ions enter the tetrahedral sites and magnetism arises due to the alteration

of super exchange interaction.

Two main issues that govern the magnetic properties of NMs are finite size and surface effects which give rise to various special features. Magnetic domains have dimensions within the range of 10-1000 nm which is comparable to the size of nanocrystals. So if the crystal size approaches to the single domain dimension upon scaling down the particle size of ferromagnetic material, all the spins get aligned to each other, so the demagnetization becomes difficult. Generally, the surface anisotropy in NMs is found to be one order of magnitude higher than the bulk value which is due to larger fraction of superficial ions in smaller particles [74]. These surface spins are disordered because they reside within an uncompensated coordination sphere due to broken bonds, vacancies, and also due to bond formation with capping organic molecule [75]. Thus, the surface anisotropy makes the surface layer magnetically harder than the core region of NMs.

1.15.1 Saturation Magnetization

M_s is the maximum possible magnetization of a magnetic material under a large external field. Assuming each atom has the same magnetic moment; M_s is dependent on the magnitude of atomic moment and also density of atoms. M_s of NMs is found to be affected significantly by the size and their synthesis procedure, as there is a large fraction of superficial ions in NMs. As particle size moved from bulk to nanoscale, M_s decreases which may be due to different reasons. According to Gangopadhay et al. [76], the M_s reduction is due to formation of a disordered nonmagnetic shell layer over the magnetically aligned core in NMs. According to other models this reduction in M_s is owed to surface spin canting due to quantum size effects.

1.15.2 Hysteresis

Magnetic hysteresis loop is a plot of variation of magnetization under applied magnetic field, which is the best possible way to represent the magnetic property of a material. Hysteresis means the inability to trace back the same magnetization curve and it is connected to the presence of magnetic domains within the material. When the domains are magnetized in one direction, it needs some energy to rotate the aligned spins and the area under the hysteresis curve represents this energy. The most useful information obtained the hysteresis loop is maximum amount of work (maximum energy product) performed by a magnetic material, which is the product of maximum field (H_{max}) and maximum magnetization (M_{max}). Coercivity (H_c) is the field that is required to reduce remanence (M_r) to zero. It is a measure of how strongly a magnetic material can oppose an external magnetic field. M_r is the remaining magnetization of a magnetic material when the external field is reduced to zero after its complete magnetization.

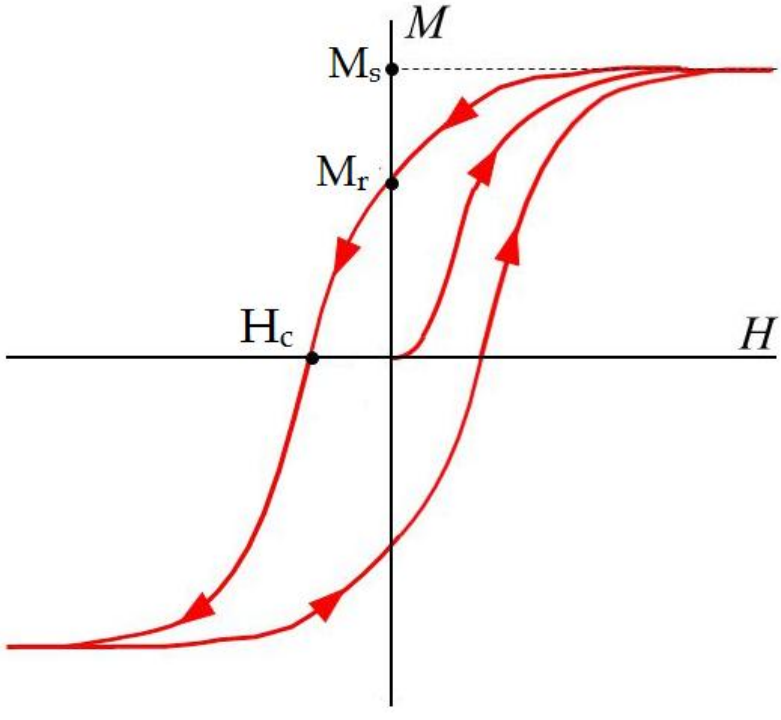

Figure 1.10: Graphical representation of ferromagnetic hysteresis loop.

1.16. Motivation and Objective of Thesis

As a vital branch in the burgeoning field of nanoscience, NMs possess a whole range of new physicochemical properties and a wealth of potential applications. Novel designs of nanostructures are emerging in intricate ways, while flexible preparation techniques for nanomaterials are consistently being developed. Particular emphasis is given to the investigation of the origin of the magnetic, electromagnetic, optical, thermal, mechanical, chemical, acoustic, and biological properties of the nanostructures. In addition, the low-cost mass production and industrial applications of nanomaterials are strongly deliberated as well.

The field of nanotechnology has led to the development of many innovative strategies for effective detection and treatment of cancer, overcoming limitations associated with conventional cancer diagnosis and therapy. Multifunctional nanoparticle systems can integrate imaging, targeting and treatment moieties on the surface and in the core, resulting in targeted delivery of the imaging or treatment modalities, specifically to the tumor. Multifunctional nanoparticles also enable simultaneous delivery of multiple treatment agents, resulting in effective combinatorial therapeutic regimens against cancer.

The main reason for the NMs to gain significance is their surface to volume ratio which is much higher than that of the other materials, their efficiency to adsorb and carry other materials. Magnetic nanostructures with intrinsic fluorescence are in high demand. To be used in biomedical field, they should possess criteria such as biocompatibility, monodispersity, dispersibility in water, and non-toxicity. The commonly used procedure for synthesizing magneto-fluorescent nanomaterials involves processes like making nanocomposites with quantum dots (QDs) or coatings with fluorescent dyes. In

order to make the nanomaterials biocompatible, surface modifications were carried out with biomolecules like proteins, DNA, RNA, small organic ligands, and polymers, but none of them were able to generate intrinsic fluorescence. In addition, their applications towards the biomedical field are narrowed due to chemical instability, photo bleaching of fluorescent dyes, and inherent toxicity of QDs (due to the presence of heavy metals like Cd^{+2}, Pb^{+2}). Therefore, to open up a wide applicability of the nanomaterials in biomedical field, a facile and proper process for surface modification is highly required. The main purpose of our present work is to design water dispersible 3d transition metal oxide based magnetic nanostructures with intrinsic fluorescence for their applications in cell imaging as well as nano-carriers for targeted drug delivery.

The key features of the thesis are,

- We have synthesized transition metal oxide ($NiFe_2O_4$, $CoFe_2O_4$ and $ZnFe_2O_4$) base magnetic nanostructures.
- We have functionalized the nanostructures with organic ligands to make them biocompatible.
- We have studied their optical properties and found multiple inherent fluorescence.
- We have dissected the origin of multiple fluorescence of functionalized nanostructures through various spectroscopic tools.
- Catalytic efficiency of functionalized nanostructures has been studied on both environmentally and biologically harmful pigments.
- We have studied the loading and unloading of anti-cancer drug on the functionalized nanostructures in different conditions.
- We have used the functionalized nanostructure as a cell imaging agent.
- We have studied the adsorption of malicious dyes in detail, by the

nanostructures.

- By surface modification, we have developed multifunctional nanostructures which are capable of various applications.

1.17. Organization of the Thesis

The entire thesis has been divided into 7 different chapters. A brief draft of the chapters is given below.

Chapter 1 gives a brief introduction about transition metal based different magnetic NSs, their crystal structure, magnetic and adsorption properties. Here we have also discussed the necessity of surface functionalization of NMs along with types, procedures, and consequences of surface modification on different properties of NMs, particularly the enhancement of optical properties through LFT. Moreover, the motivation of thesis work and the outline of work done are also included.

Chapter 2 provides various facile synthesis procedures of different NSs, and several characterization techniques including instrumental details and experimental methods.

Chapter 3 describes the synthesis of functionalized $NiFe_2O_4$ NPs through reflux method in order to study their optical, magnetic and catalytic properties. The multiple fluorescence of surface functionalized $NiFe_2O_4$ NPs was the result of d-d transition of Ni^{+2} and the ligand to metal charge transfer band. Moreover, they show a good catalytic and photocatalytic activity towards biologically and environmentally harmful dyes.

Chapter 4 demonstrates the generation of multiple photoluminescence of $CoFe_2O_4$ NHSs by facile surface modification. Using the UV/Visible spectroscopy and steady state photoluminescence spectroscopy, we found that LMCT from the ligand to Co^{+2} and d-d transitions in Co^{+2} plays the key role for

inherent fluorescence of functionalized $CoFe_2O_4$ NHSs. Functionalized $CoFe_2O_4$ NHSs showed enhanced photocatalytic activity towards the malicious dyes.

Chapter 5 exhibits synthesis of $CoFe_2O_4$ NHSs and the surface modification with Sodium folate and Sodium tartrate. The anti-cancer drug was loaded on the folate functionalized $CoFe_2O_4$ NHSs and release efficiency was studied in different conditions. The functionalized NHSs showed excellent catalytic activity towards a certain organic transformation.

Chapter 6 exhibits origin of excellent dye adsorption behavior of $CoFe_2O_4$ NHSs which are synthesized by a facile template free solvothermal technique and we investigate the influence of different anionic functional groups of the dyes on their adsorption rate. The adsorption kinetics and isotherms of the adsorbents are found to follow pseudo 1st order kinetics and the Freundlich isotherm, respectively, implying heterogeneous physisorption of the dyes over the NHS surface. $CoFe_2O_4$ NHSs can be regenerated through desorption of dyes at higher pH and still exhibit high adsorption capacity even for 5 cycles of desorption–adsorption.

Chapter 7 demonstrates the improvement of multiple fluorescence and drug binding ability of folate functionalized $ZnFe_2O_4$ NHSs. The UV/Vis absorption spectroscopy and steady state photoluminescence spectroscopy revealed that the LMCT from folate to unoccupied molecular orbitals of Fe^{+3} and d-d transitions involving d orbitals of Fe^{+3} are instrumental behind the multicolor fluorescence. The surface modified NHSs showed excellent drug loading and releasing efficiency in different conditions.

Chapter 8 concludes the thesis with an idea about the scope for future work in this direction.

Bibliography

1. J. Sund, H. Alenius, M. Vippola, K. Savolainen, A. Puustinen, *Proteomic Characterization of Engineered Nanomaterial Protein Interactions in Relation to Surface Reactivity*, **ACS Nano**, 2011, 5, 4300-4309
2. R.S. Kane, A.D. Stroock, *Nanobiotechnology: Protein-Nanomaterial Interactions*, **Biotechnol. Prog.**, 2007, 23, 316-319.
3. S. R. Saptarshi, A. Duschl, A.L. Lopata, *Interaction of nanoparticles with proteins: relation to bio-reactivity of the nanoparticle*, **J Nanobiotechnology.**, 2013, 11, 26-38.
4. J. Sutkovic, A, Jasarevic, *A review on Nanoparticle and Protein interaction in biomedical applications*, **PEN**, 2016, 4, 34-40.
5. E. Rabani, D.R. Reichman, P.L. Geissler, L.E. Brus, *Drying-mediated self-assembly of nanoparticles*, **Nature (London),** 2003, 426, 271-274.
6. S. Sun, *Recent Advances in Chemical Synthesis, Self-Assembly, and Applications of FePt Nanoparticles*, **Advance Materials**, 2006, 18, 393-403.
7. G. Tian, Z. Gu, X. Liu, L. Zhou, W. Yin, L. Yan, S. Jin, W. Ren, G. Xing, S. Li, Y. Zhao, *Facile Fabrication of Rare-Earth-Doped Gd2O3 Hollow Spheres with Upconversion Luminescence, Magnetic Resonance, and Drug Delivery Properties*, **J. Phys. Chem. C**, 2011, 115, 23790–23796.
8. B. Palazzo, M. Iafisco, M. Laforgia, N. Margiotta, G. Natile, C.L. Bianchi, D. Walsh, S. Mann, N. Roveri, *Biomimetic Hydroxyapatite–Drug Nanocrystals as Potential Bone Substitutes with Antitumor Drug Delivery Properties*, **Adv. Funct. Mater.**, 2007, 17, 2180–2188.
9. Y. Si, M. Chen, L. Wu, *Syntheses and biomedical applications of hollow micro-/nano-spheres with large-through-holes*, **Chem. Soc. Rev.**, 2016, 45, 690-714.
10. R. Lv, S. Gai, Y. Dai, N. Niu, F. He, P. Yang, *Highly Uniform Hollow GdF_3 Spheres: Controllable Synthesis, Tuned Luminescence, and Drug-Release Properties*, **ACS Appl. Mater. Interfaces**, 2013, 5, 10806-10818.

11. P.V. Kamat, *Meeting the Clean Energy Demand: Nanostructure Architectures for Solar Energy Conversion*, **J. Phys. Chem. C**, 2007, 111, 2834-2860.

12. Z.S. Wang, H. Kawauchi, T. Kashima, H. Arakawa, *Significant influence of TiO2 photoelectrode morphology on the energy conversion efficiency of N719 dye-sensitized solar cell*, **Coord. Chem. Rev.**, 2004, 248, 1381-1389.

13. M.G. Hosseini, R. Mahmoodi, *Improvement of energy conversion efficiency and power generation in direct borohydride-hydrogen peroxide fuel cell: The effect of Ni-M core-shell nanoparticles (M = Pt, Pd, Ru)/Multiwalled Carbon Nanotubes on the cell performance*, **J. Power Sources**, 2017, 370, 87-97.

14. L. Dai, *Functionalization of Graphene for Efficient Energy Conversion and Storage*, **Acc. Chem. Res.**, 2013, 46, 31-42.

15. Y.-G. Guo, J.-S. Hu, L.-J. Wan, *Nanostructured Materials for Electrochemical Energy Conversion and Storage Devices*, **Adv. Mater.**, 2008, 20, 2878–2887.

16. X. Sun, Y. Zhang, G. Chen, Z. Gai, *Application of Nanoparticles in Enhanced Oil Recovery: A Critical Review of Recent Progress*, **Energies**, 2017, 10, 345-378.

17. D. Boraschi, P. Italiani, *From Antigen Delivery System to Adjuvanticy: The Board Application of Nanoparticles in Vaccinology*, **Vaccines**, 2015, 3, 930-939.

18. A. Dingler, R. P. Blum, H. Niehus, R. H. Muller, S. Gohla, *Solid lipid nanoparticles (SLNTM/LipopearlsTM) a pharmaceutical and cosmetic carrier for the application of vitamin E in dermal products*, **J. Microencapsul.**, 1999, 16, 751-767.

19. J. Pardeike, A.Hommoss, R.H.Müller, *Lipid nanoparticles (SLN, NLC) in cosmetic and pharmaceutical dermal products*, **Int. J. Pharm.**, 2009, 366, 170-184.

20. L. Mu, R.L. Sprando, *Application of Nanotechnology in Cosmetics*, **Pharm Res**, 2010, 27, 1746–1749.

21. S. Prabhu, E.K. Poulose, *Silver nanoparticles: mechanism of antimicrobial action, synthesis, medical applications, and toxicity effects*, **Int. Nano Lett.**, 2012, 2, 32-42.

22. Y. Lee, J.-R. Choi, K.J. Lee, N.E. Stott, D. Kim, *Large-scale synthesis of copper nanoparticles by chemically controlled reduction for applications of inkjet-printed electronics*, **Nanotechnology**, 2008, 19, 415604-415610.

23. J. Jang, J. Ha, J. Cho, *Fabrication of Water-Dispersible Polyaniline-Poly (4-styrenesulfonate) Nanoparticles For Inkjet-Printed Chemical-Sensor Applications*, **Adv. Mater.**, 2007, 19, 1772–1775.

24. W.J. Stark, P.R. Stoessel, W. Wohlleben, A. Hafner, *Industrial applications of nanoparticles*, **Chem. Soc. Rev.**, 2015, 44, 5793-5805.

25. E.K. Athanassiou, R.N. Grass, W. J. Stark, *Large-scale production of carbon-coated copper nanoparticles for sensor applications*, **Nanotechnology**, 2006, 17, 1668–1673.

26. X. Luo, A. Morrin, A.J. Killard, M.R. Smyth, *Application of Nanoparticles in Electrochemical Sensors and Biosensors*, **Electroanalysis**, 2006, 18, 319–326.

27. Y. Li, Y. Wu, B.S. Ong, *Facile Synthesis of Silver Nanoparticles Useful for Fabrication of High-Conductivity Elements for Printed Electronics*, **J. Am. Chem. Soc.**, 2005, 127, 3266-3267.

28. H.-C. Kim, S.-M. Park, W.D. Hinsberg, *Block Copolymer Based Nanostructures: Materials, Processes, and Applications to Electronics*, **Chem. Rev.**, 2010, 110, 146-177.

29. Y. Diebold, M. Calonge, *Applications of nanoparticles in ophthalmology*, **Prog Retin Eye Res.**, 2010, 29, 596-609.

30. F.-K. Liu, *Analysis and applications of nanoparticles in the separation sciences: A case of gold nanoparticles*, **J. Chromatogr. A**, 2009, 1216, 9034-9047.

31. J.S. Beveridge, J.R. Stephens, M. E. Williams, *The Use of Magnetic Nanoparticles in Analytical Chemistry*, **Annu. Rev. Anal. Chem.**, 2011, 4, 251-273.

32. K. Scida, P.W.Stege, G. Haby, G.A. Messina, C.D. García, *Recent applications of carbon-based nanomaterials in analytical chemistry: Critical review*, **Anal. Chim. Acta**, 2011, 691, 6-17.

33. H. Wei, E. Wang, *Fe_3O_4 Magnetic Nanoparticles as Peroxidase Mimetics and Their Applications in H_2O_2 and Glucose Detection*, **Anal. Chem.**, 2008, 80, 2250-2254.

34. J.-fu Liu, Z.-shan Zhao, G.-bin Jiang, *Coating Fe_3O_4 Magnetic Nanoparticles with Humic Acid for High Efficient Removal of Heavy Metals in Water*, **Environ. Sci. Technol.**, 2008, 42, 6949-6954.

35. Y.-C. Chang, D.-H. Chen, *Preparation and adsorption properties of monodisperse chitosan-bound Fe_3O_4 magnetic nanoparticles for removal of Cu(II) ions*, **J. Colloid Interface Sci.**, 2005, 283, 446-451.

36. M.Il Kim, J. Shim, T. Li, J. Lee, H.G. Park, *Fabrication of Nanoporous Nanocomposites Entrapping Fe_3O_4 Magnetic Nanoparticles and Oxidases for Colorimetric Biosensing*, **Chem. Eur. J.**, 2011, 17, 10700 – 10707.

37. M. Hasanzadehk, N. Shadjou, M. la Guardia, *Iron and iron-oxide magnetic nanoparticles as signal-amplification elements in electrochemical biosensing*, **Trends Anal. Chem.**, 2015, 72, 1-9.

38. S.H. Chunga, A. Hoffmann, S.D. Bader, C. Liu, B. Kay, L. Makowski, L. Chen, *Biological sensors based on Brownian relaxation of magnetic nanoparticles*, **Appl. Phys. Lett.**, 2004, 85, 2971-2973.

39. H. Teymourian, A. Salimi, S. Khezrian, *Fe_3O_4 magnetic nanoparticles/reduced graphene oxide nanosheets as a novel electrochemical and bioeletrochemical sensing platform*, **Biosens. Bioelectron.**, 2013, 49, 1-8.

40. G.K. Kouassi, J. Irudayaraj, *Magnetic and Gold-Coated Magnetic Nanoparticles as a DNA Sensor*, **Anal. Chem.**, 2006, 78, 3234-3241.

41. C. Boyer, M.R. Whittaker, V. Bulmus, J. Liu, T.P. Davis, *The design and utility of polymer-stabilized iron-oxide nanoparticles for nanomedicine applications*, **NPG Asia Mater.**, 2010, 2, 23–30.

42. Y.H. Xu, Ji.Bai J.-P.Wang, *High-magnetic-moment multifunctional nanoparticles for nanomedicine applications*, **J. Magn. Magn. Mater.**, 2007, 311, 131-134.

43. C.C. Berry, *Progress in functionalization of magnetic nanoparticles for applications in biomedicine*, **J. Phys. D: Appl. Phys.**, 2009, 42, 224003-224011.

44. B. Issa, I.M. Obaidat, B.A. Albiss, Y. Haik, *Magnetic Nanoparticles: Surface Effects and Properties Related to Biomedicine Applications*, **Int. J. Mol. Sci.**, 2013, 14, 21266-21305.

45. D. Carta, M.F. Casula, G. Mountjoy, A. Corrias, *Synthesis and microstructure of manganese ferrite colloidal nanocrystals*, **Phys. Chem. Chem. Phys.**, 2008, 10, 3108-3117.

46. E.V. Gopalan, I.A. Al-Omari, K.A. Malini, P.A. Joy, D.S. Kumar, Y.Yoshida, M.R. Anantharaman, *Impact of zinc substitution on the structural and magnetic properties of chemically derived nanosized manganese zinc mixed ferrites*, **J. Magn. Magn. Mater.**, 2009, 321, 1092-1099.

47. J. Smit, *Magnetic properties of materials*, **McGraw-Hill**, **New York**, 1971. 22-23.

48. S.G. Grancharov, H. Zeng, S. Sun, S.X. Wang, S. O'Brien, C.B Murray, J.R. Kirtley, G.A. Held, *Bio-functionalization of monodisperse magnetic nanoparticles and their use as biomolecular labels in a magnetic tunnel junction based sensor*, **J. Phys. Chem. B.**, 2005, 109, 13030-13035.

49. R. Arshady, *Microspheres for biomedical applications: preparation of reactive and labelled microspheres*, **Biomaterials**, 1993, 14, 5-15.

50. M.-A. Neouze, U. Schubert, *Surface modification and functionalization of metal and metal oxide nanoparticles by organic ligands*, **Monatsh. Chem.**, 2008, 139, 183-195.

51. C.C Berry, A.S.G. Curtis, *Functionalisation of magnetic nanoparticles for applications in biomedicine*, **J. Phys. D: Appl. Phys.**, 2003, 36, R198–R206.

52. O. Veiseh, J.W. Gunn, M. Zhang, *Design and fabrication of magnetic nanoparticles for targeted drug delivery and imaging*, **Adv. Drug Deliv. Rev**, 2010, 62, 284-304.

53. C. Sun, J.S.H. Lee, M. Zhang, *Magnetic nanoparticles in MR imaging and drug delivery*, **Adv. Drug Deliv. Rev,** 2008, 60, 1252-1265.

54. J.R. McCarthy, R. Weissleder, Multifunctional magnetic nanoparticles for targeted imaging and therapy, **Adv. Drug Deliv. Rev,** 2008, 60, 1241-1251.

55. S.C. McBain, H.H.P. Yiu, J. Dobson, *Magnetic nanoparticles for gene and drug delivery*, **Int J. Nanomedicine**, 2008, 3, 169–180.

56. A.K. Gupta, A.S.G. Curtis, *Surface modified superparamagnetic nanoparticles for drug delivery: Interaction studies with human fibroblasts in culture***, J. Mater. Sci. Mater. Med.**, 2004, 15, 493-496.

57. M. Arruebo, R.Fernández-Pacheco, M.R. Ibarra, J. Santamaría, *Magnetic nanoparticles for drug delivery*, **Nano Today**, 2007, 2, 22-32.

58. X. Mou, Z. Ali, S. Li, H. Nongyue, *Applications of Magnetic Nanoparticles in Targeted Drug Delivery System*, **J. Nanosci. Nanotechnol.**, 2015, 15, 54-62.

59. M. Liong, J. Lu, M. Kovochich, T. Xia, S.G. Ruehm, A.E. Nel, F. Tamanoi, J.I. Zink, *Multifunctional Inorganic Nanoparticles for Imaging, Targeting, and Drug Delivery*, **ACS Nano**, 2008, 2, 889-896.

60. S. Kayal, R.V. Ramanujan, *Doxorubicin loaded PVA coated iron oxide nanoparticles for targeted drug delivery*, **Mater. Sci. Eng. C.**, 2010, 30, 484-490.

61. N. Zheng, G.D. Stucky, *A General Synthetic Strategy for Oxide-Supported Metal Nanoparticle Catalysts*, **J. Am. Chem. Soc.**, 2006, 128, 14278-14280.

62. C. Wang, H. Yin, S. Dai, S. Sun, *A General Approach to Noble Metal−Metal Oxide Dumbbell Nanoparticles and Their Catalytic Application for CO Oxidation*, **Chem. Mater.**, 2010, 22, 3277-3282.

63. C.L. Carnes, K.J. Klabunde, *The catalytic methanol synthesis over nanoparticle metal oxide catalysts*, **J. Mol. Catal. A: Chem.**, 2003, 194, 227-236.

64. D. Astruc, F. Lu, J.R. Aranzaes, *Nanoparticles as Recyclable Catalysts: The Frontier between Homogeneous and Heterogeneous Catalysis*, **Angew. Chem. Int. Ed.**, 2005, 44, 7852 – 7872.

65. G. Li, Z. Tang, *Noble metal nanoparticle@metal oxide core/yolk–shell nanostructures as catalysts: recent progress and perspective*, **Nanoscale**, 2014, **6**, 3995-4011.

66. W.J. Weber, J.C. Morris, *Kinetics of adsorption on carbon from solution.*, **J. Sanit. Eng. Div.**, 1963, 89, 31-60.

67. S. Lagergren, *About the theory of so-called adsorption of soluble substances*, **K. vet. akad. handl**, 1898, 24, 1-39.

68. Y.S. Ho, G. McKay, *Sorption of dye from aqueous solution by peat*, **Chem. Eng. J.**, 1998, 70, 115-124.

69. M.S. El-Geundi, *Homogeneous Surface Diffusion Model for the Adsorption of Basic Dyestuffs onto Natural Clay in Batch Adsorbers*, **ADSORPT SCI TECHNOL**, 1991, 8, 217- 225.

70. I. Langmuir, *Adsorption of gases on plain surfaces of glass mica platinum*, **J. Am. Chem. Soc.**, 1918, 40, 1361-1403.

71. H.M.F. Freundlich, *Uber die Adsorption in Losungen*., **Zeitschrift für Physikalische Chemie**, 1906, 57, 385-470.

72. F. Haghseresht, G. Lu, *Adsorption characteristics of phenolic compounds onto coal- reject-derived adsorbents*, **Energy Fuels**, 1998, 12, 1100-1107.

73. K. Fytianos, E. Voudrias, E. Kokkalis, *Sorption–desorption behavior of 2,4- dichloriphenol by marine sediments*, **Chemosphere**, 2000, 40, 3-6.

74. H. Shao, Y. Huang, H. Lee, Y.J. Suh, C.O. Kim, *Effect of PVP on the morphology of cobalt nanoparticles prepared by thermal decomposition of cobalt acetate,* **Curr. Appl. Phys.**, 2006, 6, e195-e197.

75. H. Wen-yao, X. Guo.-cai, *Characterization of nano-Ag/PVP composites synthesized via ultra-violet irradiation*, **J. Coal Sci. Eng.**, 2010, 16, 188-192.

76. S. Gangopadhyay, G.C. Hadjipanayis, B. Dale, C.M. Sorensen, V. Klabunde, K.J. Papaefthymiou, A. Kostikas, *Magnetic properties of ultrafine iron particles*, **Phys. Rev. B**, 1992, 45, 9778-9787.

Chapter 2

Experimental Details

In this chapter we have discussed different synthesis techniques of nanomaterials and also various methods of characterization.

2. Material Synthesis and Characterization Techniques

2.1 Preamble

In this chapter, different experimental procedures such as wet chemical method and solvothermal methods used to synthesize various 3d transition metal oxide based magnetic nanostructures (NSs) are described. In addition, the functionalization technique which was employed for the surface modification of the NSs is discussed here in detail. Moreover, the characterization procedures, which are employed to study their physical, optical and magnetic properties, are also presented here.

The phase and morphology of as-prepared NSs were studied using X-ray Diffraction (XRD), Field Emission Scanning Electron Microscope (FESEM), Transmission Electron Microscope (TEM), High Resolution Transmission Electron Microscope (HRTEM), Energy Dispersive X-ray (EDX) Analysis and Selected Area Electron Diffraction (SAED). The phase transition of the sample was studied by the Differential Thermal Analysis (DTA). Spectroscopic analyses are carried out through UV-Visible (UV-Vis) and Fourier Transformed Infrared (FTIR) Spectrometer, steady state fluorometer and Fluorescence microscope. In order to confirm the degradation of dyes, Liquid Chromatography-Mass spectrometry (LC-MS) was carried out. The magnetic Characterizations were carried out employing Vibrating Sample Magnetometer (VSM).

2.2 Synthesis of Nanostructures

Nanostructures can be made in numerous ways. A broad classification divides methods into either those which build from the bottom up, atom by atom, or those which construct from the top down, using processes that involve the

removal or reformation of atoms to create the desired structure. The various synthesizing routes for the fabrication of different nanostructures can be segregated into two simple groups, (1) top-down (i.e. bulk to nano) and (2) bottom-up (i.e. atom to nano) approaches.

2.2.1 Top-Down Approach

The top-down approach is a process of miniaturizing or breaking down bulk materials (macro-crystalline) structures while retaining the original integrity. The top-down approaches are inherently simpler and rely either on the removal or division of bulk material, or on the miniaturization of bulk fabrication processes to produce the desired structure with the appropriate properties. Attrition or Milling is a usual top-down method in making nanostructures. The biggest problem with top-down approach is the imperfection of surface structure and significant crystallographic damage to the processed patterns. These imperfections in turn lead to extra challenges in the device design and fabrication. But this approach leads to the bulk production of nano material. Regardless of the defects produced by top-down approach, they will continue to play an important role in the synthesis of nanostructures.

2.2.2 Bottom-Up Approach

In the bottom-up approach, atoms, molecules and even nanoparticles themselves can be used as the building blocks for the creation of complex nanostructures; the useful size of the building blocks depends on the properties to be engineered. In this route smaller components of atomic or molecular dimensions self-assemble together, according to a natural physical principle or an externally applied driving force, to give rise to larger and more organized systems [1]. Methods to produce nanoparticles from atoms are chemical processes based on transformations in solution e.g. sol-gel processing, chemical vapor deposition (CVD), plasma or flame spraying synthesis, laser pyrolysis, atomic or molecular

condensation. These chemical processes rely on the availability of appropriate "metal-organic" molecules as precursors. A bottom up synthesis method implies that the nanostructures are synthesized onto the substrate by stacking atoms onto each other, which gives rise to crystal planes, crystal planes further stack onto each other, resulting in the synthesis of the nanostructures. A bottom-up approach can thus be viewed as a synthesis approach where the building blocks are added onto the substrate to form the nanostructures.

Both the Top-down and Bottom-up approach are shown schematically in Figure 2.1.

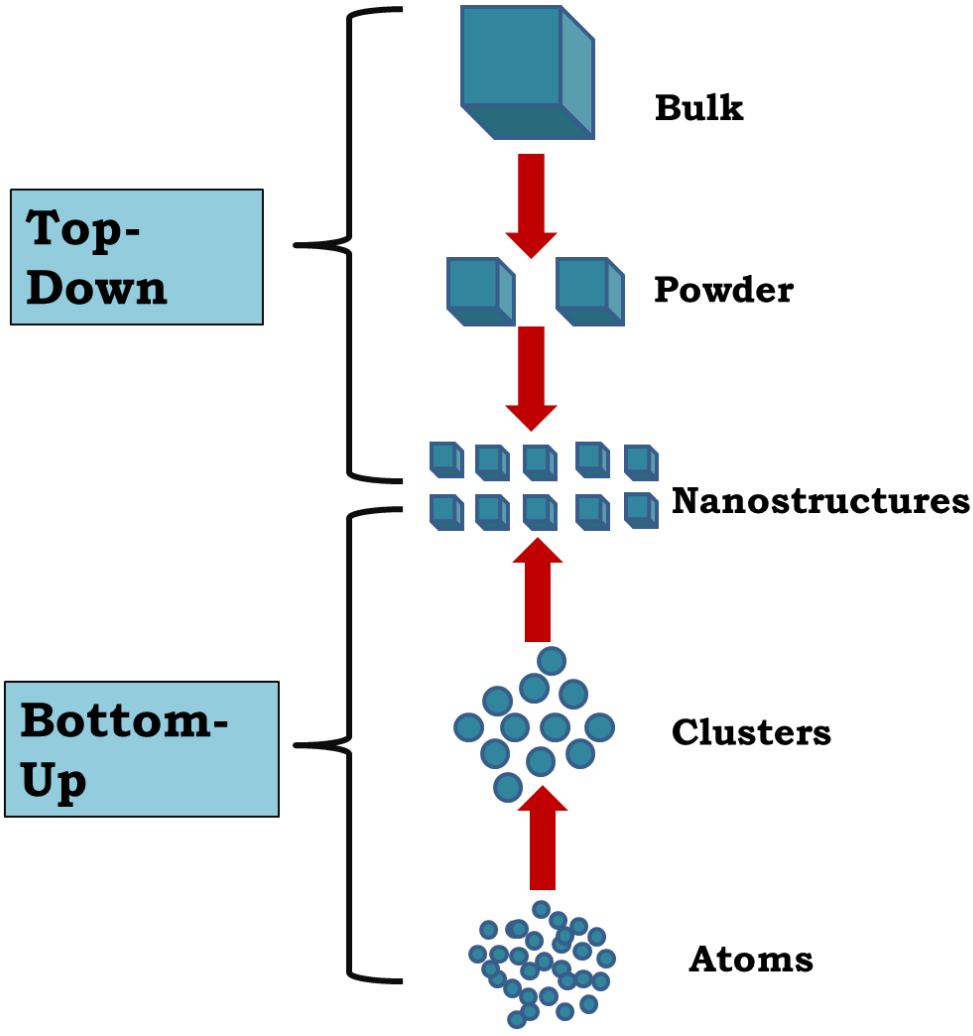

Figure 2.1: Schematic representation of Top-down and Bottom-up approach.

2.3. Formation of Nanoparticles in Wet Chemical Method

In wet chemical synthesis, homogeneous nucleation occurs when nuclei form uniformly throughout the parent phase, called supersaturation. This condition can be attained by rationally controlling the reaction conditions such as solvent, capping agents, temperature etc. The process of homogeneous nuclei formation can be considered thermodynamically by looking at the total free energy (ΔG) of a NP defined as the sum of the surface free energy and the bulk free energy. The overall free energy change (ΔG), related with the homogeneous nucleation process, is the total change in free energy between a small solid particle of a solute and the solute in solution. The excess surface free energy, ΔG_S, is the excess surface energy between the NPs and the corresponding bulk material. ΔG_V, is the excess free energy between a very large particle and the solute in the solution. Dependence of ΔG_S and ΔG_V on particle size with radius (r) can be observed from Equation 2.1 and also depicted in the Figure 2.2 [2],

$$\Delta G = \Delta G_S + \Delta G_V = 4\pi r^2\gamma + \frac{4}{3}\pi r^3 \Delta G_v \qquad (2.1)$$

where, ΔG_v is the free energy change per unit volume and γ is the interfacial tension between the growing NP surface and the supersaturated solution.

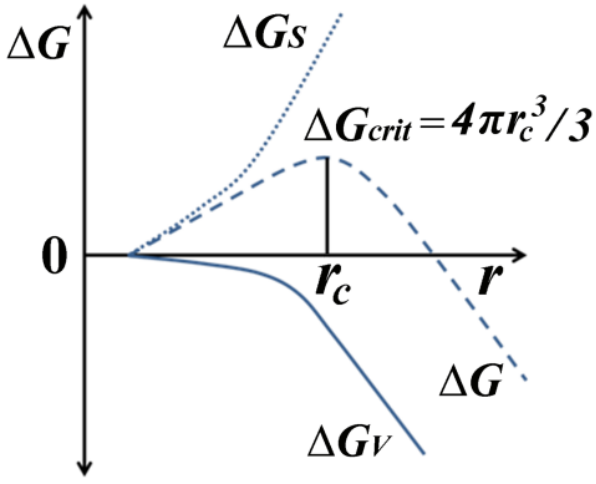

Figure 2.2: Free energy diagram for nucleation process explaining the existence of a "critical nucleus". (© S. Kumar and T. Nann, Small, 2006, 2, 316)

As ΔG_S is always positive and ΔG_V is always negative, it is possible to find a ΔG for a stable nucleus having an optimum size (critical radius, r_c) by differentiating ΔG with respect to r and setting it to zero, which gives a critical free energy as shown in Equation 2.2. The critical radius is defined in Equation 2.3. It is evident from Figure 2.2, that the total excess free energy, ΔG, passes through a maximum, ΔG_{Crit}, corresponding to the critical nucleus size, r_c,

$$\left.\frac{d(\Delta G)}{dr}\right|_{r=r_c} = 8\pi r_c\gamma + 4\pi r_c^2 \Delta G_v = 0 \qquad (2.2)$$

$$\Rightarrow r_c = -\frac{2\gamma}{\Delta G_v} \qquad (2.3)$$

From Equations 2.1 and 2.3, we can obtain the critical value of ΔG as $r = r_c$

$$\Delta G\Big|_{r=r_c} = \Delta G_{Crit} = \frac{16\,\pi\,\gamma^3}{3(\Delta G_v)^2} = \frac{4\pi\gamma r_c^2}{3} \qquad (2.4)$$

i.e. the minimum energy barrier that a nucleation process must overcome is ΔG_{Crit}, which corresponds to the minimum size of a stable spherical nucleus (r_c). This critical radius corresponds to the minimum size at which a particle can survive in solution without being redissolved.

The system and the reaction parameters are responsible for the crystal structure, size, and morphology of the growing particles. The growth of NPs is dependent on two mechanisms: the surface reaction and the monomer's diffusion to the surface. Different theories have been proposed to explain the nucleation and growth mechanism of various reactions [3]. Such as, in the LaMer mechanism, the process of nucleation and growth are divided into three portions. Firstly, a rapid increase in the concentration of free monomers in solution, secondly, the

monomer undergoes “burst nucleation” which significantly reduces the concentration of free monomers in solution. The rate of nucleation is described as “effectively infinite” and after this point, nucleation almost stops due to low concentration of monomers and in third stage, the growth occurs under the control of diffusion of monomers through solution. Ostwald and digestive ripening mechanism say that, growth is caused by the change in solubility of NPs which is dependent on their size. According to Ostwald ripening, due to high solubility and surface energy of smaller particles within solution, they redissolve and in turn allow the larger particles to grow even more. Digestive ripening, described by Lee et al., is effectively the inverse of Ostwald ripening, where smaller particles grow at expense of the larger ones by surface energy controlled process [4]. The Finke-Watzky two step mechanism is a process of nucleation and growth where both steps happen simultaneously [5]. The first is a slow continuous nucleation as shown in Equation 2.5 and the second is the autocatalytic surface growth which is not diffusion controlled, as shown in Equation 2.6.

$$A \rightarrow B \tag{2.5}$$

$$A + B \rightarrow 2B \tag{2.6}$$

Shape of the crystallites occurs either in order to minimize the surface energy of the particles or because of the kinetics of growth. If kinetics dominates, the shape is then determined by the rate at which different crystal faces grow. In thermal equilibrium, the crystal shape is determined by minimization of surface energy.

2.4. Fabrication Methods of Different Nanostructures

2.4.1 Wet Chemical Method

Wet chemical method refers to a particular group of methods where generally

nano- or ultra- dispersed inorganic materials have been produced in aqueous or non- aqueous solutions. It is different from conventional solid state procedure in respect to that it can only be done in liquid phase and more importantly it can produce much smaller, monodispersed grains or crystallites usually at lower temperature and have shorter duration of phase formation. It is mainly a "bottom-up" method to synthesize NPs basically by chemical reduction of metal salts, electrochemical trails or through controlled decomposition of different metastable organometallic compounds.

2.4.1.1 Reflux Condensation Method

The reflux condensation method is carried out by dissolving the organometallic compounds with component elements at appropriate ratio in aqueous or non-aqueous solvents in a round bottom flask in the presence of suitable capping agents, with condenser placed on the top of the flask, followed by a heating at boiling point of the solvent. After the completion of reaction, the reaction medium is cooled to room temperature. Then the product is precipitated by changing the polarity of the medium, and washed several times to remove impurities followed by drying. The condenser, which prevents the solvent vapors from escaping the system, has an outer jacket through which a coolant (usually chilled water) is circulated. The circulating water takes the temperature off the solvent vapors and in turn the vapors condense and fall back into the flask.

Through this method one can control the size, morphology and crystallinity of the materials by varying parameters such as the reaction time, concentration of precursors and the type of solvent employed. This method is employed extensively in material science to synthesize nanoparticles [6], nanowires [7], nanorods [8], nanourchins [9], core–shell nanostructures [10] and hierarchical nanostructures [11] with high crystallinity, compositional homogeneity and

better stoichiometry. The refluxing set up used for our experiment for fabricating $NiFe_2O_4$ is shown in Figure 2.3. The $NiFe_2O_4$ nanoparticles were synthesized by following a previously reported template free wet chemical method, with slight modification [12]. We have used Nickel acetate, Iron Acetylacetonate (organometallic moieties) as the precursors for the synthesis. Di-phenyl Ether was chosen as the solvent. Oleic acid and Oleyl Amine were taken as the capping agents. We had used Cetyl alcohol instead of 1,2-hexadecanediol used by Sun et. al [12]. Then the precursors and the capping agents along with Cetyl alcohol were dissolved in the solvent using ultrasonicator. Further the three neck flask was placed on a heating mantle, equipped with a condenser on the top of it. The mixture was then heated at 270°C for 1 hour. The reaction mixture was then poured into a beaker containing alcohol. Due to the change in polarity precipitation occurs. Then the precipitates were collected after washing them with alcohol for several times.

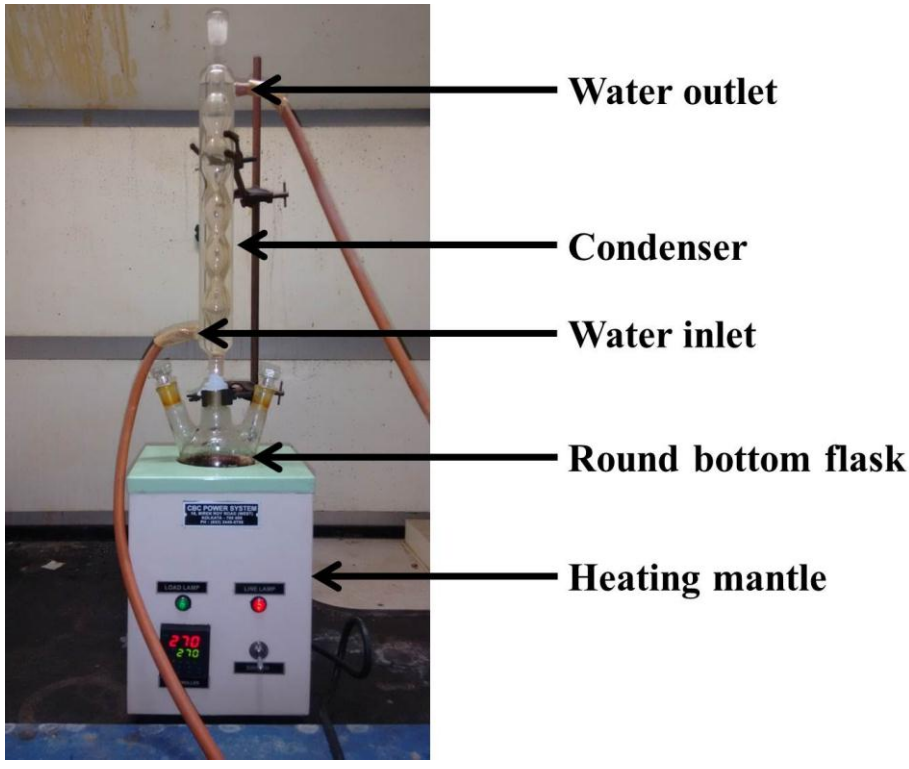

Figure 2.3: Reflux condensation set-up.

2.4.1.2 Solvothermal Method

Solvothermal method is one of the most common and effective synthetic routes to fabricate the nanomaterial with a variety of morphologies by controlling temperature, pressure, capping agent, chemical composition, and duration of reaction. If the reaction medium is non-aqueous, then it is termed as solvothermal method; whereas, if water is used as the reaction medium, it is known as hydrothermal process. Different polar solvents (like, water, ethanol etc) or non-polar solvents (like Benzene, Ethylene Glycol, Ethylene di-amine etc) are used under high pressure and temperature (generally above the boiling point of solvent) to facilitate the interaction of different precursor molecules during the synthesis procedure. The reactants are placed into an autoclave filled with water or non-aqueous solvent to carry out the reaction under high temperature and pressure conditions.

A sealed reaction container and a temperature which is above the boiling point of the solvent are the key elements of solvothermal process. It helps to develop an autogenous pressure [13]. Generally, Teflon-lined autoclaves are capable of working at high temperature and pressure. In addition, it sustains alkaline media and exhibits a strong resistance to hydrofluoric acid when compared to glass and quartz autoclaves. Therefore, Teflon-lined autoclave is chosen as an ideal container to perform the reaction under desired conditions. Precise control in hydrothermal process is the key factor that enables the synthesis of various nanostructured inorganic materials. The pressure within the sealed reaction container is not only found to increase dramatically with temperature, but also depend on other experimental factors, such as the percentage fill of the vessel, any dissolved salts, and capping agents. The reaction mechanism of the solvothermal method is dependent on the physico-chemical properties of the solvent. A number of fundamental properties of solvents are greatly affected by pressure and temperature. For example, the viscosity of water decreases with

increasing temperature, such as at 500°C and 10 bar, the viscosity of water is only 10% of its magnitude under ambient conditions [14]. Thus, it is evident that the mobility of dissolved ions and molecules is higher under solvothermal conditions than at ambient pressure and temperature. Similarly, the dielectric constants of solvents are considerably reduced above the critical pressure and temperature; this can have major implications on the solubility of solid reagents under reaction conditions. In this technique, precursors are dissolved in the solvent by magnetic stirring or sonication, the homogeneous mixture is transferred into Teflon lined stainless steel autoclave chamber, as shown in Figure 2.4.

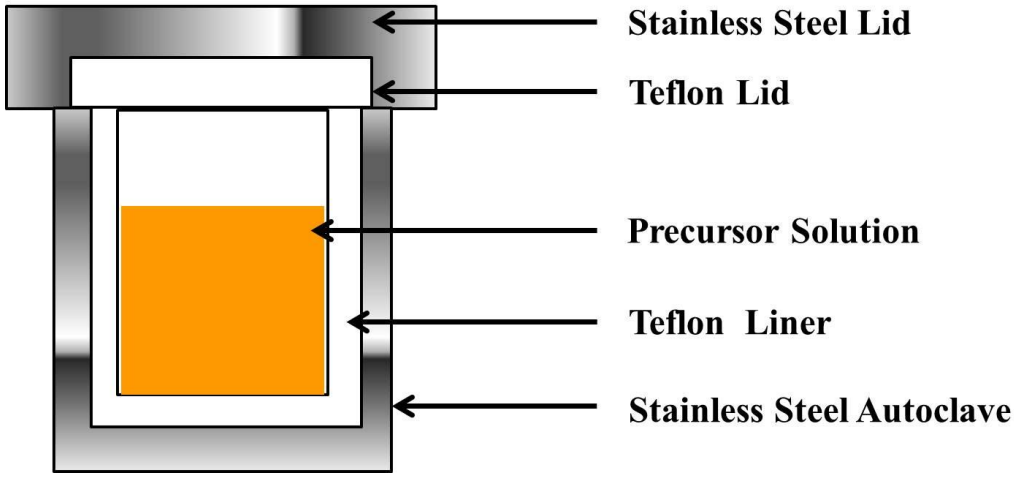

Figure 2.4: Schematic diagram of an autoclave and a Teflon chamber used in solvothermal synthesis.

The precursor solution is poured in the Teflon liner and the Teflon liner in placed in the autoclave. The autoclave is then sealed and heated to a certain temperature in an oven. This method can be used to prepare different types of NSs such as particles, wires, rods, hollow spheres etc. The advantageous feature of the solvothermal synthesis route is products of intermediate state, metastable state and specific phase are easily synthesized.

This template free solvothermal route synthesis of MFe_2O_4 (M = Co and Zn)

requires the temperature of 200°C. Iron (III) chloride [$FeCl_3$, $6H_2O$] is common in both of the synthesis, whereas Cobalt (II) chloride [$CoCl_2$, $6H_2O$] and Zinc (II) chloride [$ZnCl_2$] were used for synthesizing $CoFe_2O_4$ and $ZnFe_2O_4$ NHSs respectively. The metal salts were dissolved in a polar solvent, ethanol and non-polar solvent, ethylene glycol, and heated for 20 h in case of $CoFe_2O_4$ and 18 h in case of $ZnFe_2O_4$ NHSs, in presence of urea [$CO(NH_2)_2$], oleylamine [$CH_3(CH_2)_7CH=CH(CH_2)_7NH_2$] in a Teflon lined stainless steel autoclave.

2.4.2 Functionalization Procedure

The dried as prepared nanostructures were poured in a glass vial along with 0.5 M solution of Sodium tartrate or Sodium folate. Then the glass vial was place on the top of a vibrator-rotor followed by rigorous vibration and rotation of the glass vial for 12h at room temperature. The tartrate or folate solution was made by taking 0.5 M solution of respective acids and then neutralizing them by drop wise adding of NaOH. Figure 2.5 and 2.6 depict the structures of Tartaric Acid and Folic Acid respectively. The non-solubilized larger nanoparticles were filtered out using a syringe filter of 0.22μm diameter. The colorless filtrate was obtained and named as T-$NiFe_2O_4$. For nano-hollowspheres, we collected the supernatant liquid without filtering and named as T-$CoFe_2O_4$, F-$CoFe_2O_4$ and F-$ZnFe_2O_4$. In order to intensify their optical properties, the functionalized nanostructures were heated at 70-80°C under continuous stirring and maintaining the pH at 12 by the drop wise addition of NaOH. After the pH and heat treatment, the functionalized nanostructures showed intense fluorescence under the irradiation of UV light. The powder form of functionalized nanostructured solution was prepared by dialysis (to remove extra ligands) and lyophilization to study the magnetic and FTIR spectroscopic properties.

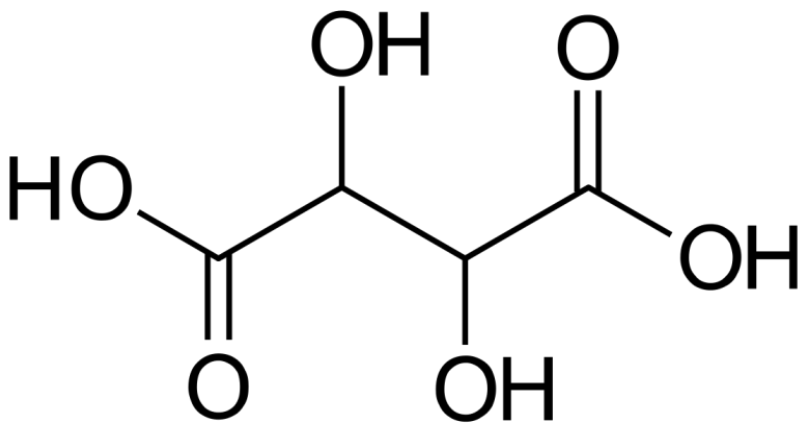

Figure 2.5: Chemical structure of Tartaric acid molecule.

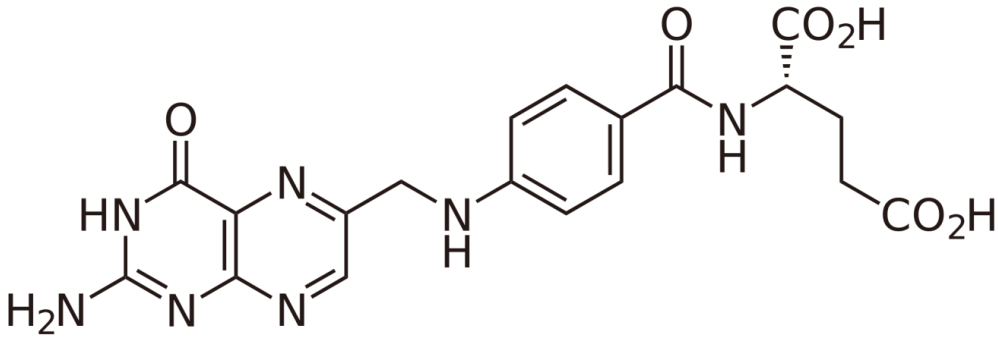

Figure 2.6: Chemical structure of Folic acid molecule.

2.5. Phase and Morphology Characterization Methods

2.5.1. X-Ray Diffractometer (XRD)

X-Ray Diffractometer (XRD) is used to analyze the crystal structure of micro and NSs, thin films, and bulk samples in a non-destructive way. In this method of determining molecular and atomic structure of a crystalline material, atomic planes of the material diffract incident X-rays in different specific directions depending on their orientations. By measuring the angle and intensity of the diffracted beams, a three dimensional idea of the density of electrons within the specified crystal can be obtained. From this density of electrons, mean position of the atoms in the crystal can be determined as shown in Figure 2.7.

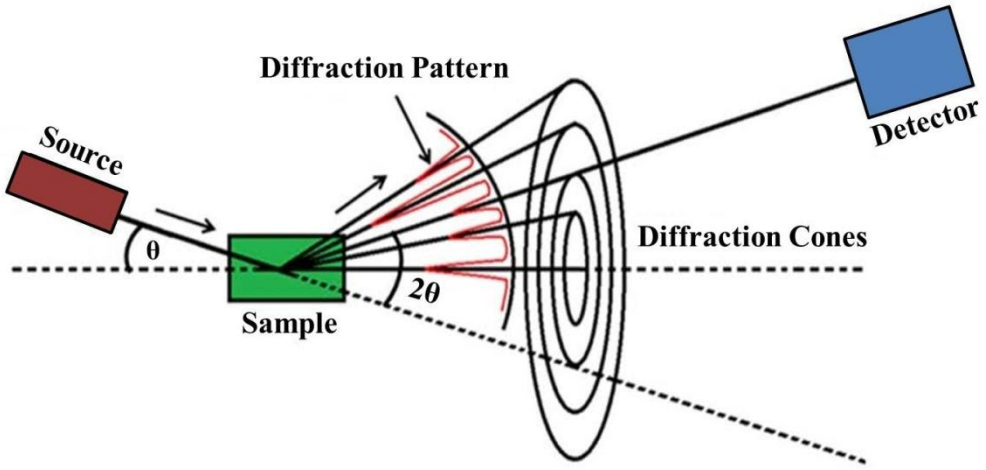

Figure 2.7: Schematic diagram of XRD.

In XRD instrument, a monochromatic beam of X-rays falls on a crystalline sample as shown in Figure 2.8. Those X-rays are scattered elastically by the electrons within the crystal planes. Then the scattered waves interfere constructively in few specific directions that can be determined by Bragg's law given as Equation 2.7

$$2d\sin\theta = n\lambda \qquad (2.7)$$

where, d is the crystal plane spacing, θ is the diffraction angle, n is an integer, and λ is the wavelength of incident light. The angle and the intensity of the diffracted beams are processed and recorded electronically using a detector, resulting in intensity vs. 2θ plot for a specific sample.

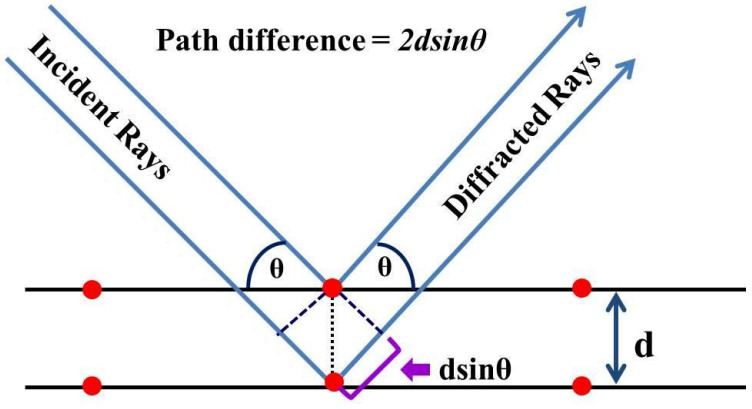

Figure 2.8: Schematic diagram of diffraction of X-rays by a crystal.

The grain size (d) of the sample can be calculated by observing the width of the diffraction peaks and using the relation as given by Debye-Scherrer Equation 2.8:

$$d = (0.9\,\lambda)/\beta\,cos\,\theta \qquad (2.8)$$

where, β is the full width at the half maximum of the diffraction peak at a diffraction angle of 2θ. XRD patterns of our samples were obtained by applying a scanning rate of 0.02° s^{-1} in the 2θ range from 20° to 80° by Rigaku miniflex II diffractometer equipped with Cu Kα (λ~1.54 Å) radiation (at 40 mA and 40 kV).

2.5.2. Energy Dispersive Spectroscopy (EDS)

Energy Dispersive Spectroscopy (EDS) is an analytical technique used for elemental analysis or chemical characterization of a sample. It is based on the investigation of a sample through interactions between electromagnetic radiation and matter, analyzing X−rays emitted by the matter in response to being hit with the electromagnetic radiation. Its characterization capabilities are due in large part to the fundamental principle that each element has a unique atomic structure allowing X−rays that are characteristic of an element's atomic structure to be identified uniquely from each other. This technique is also known as Energy Dispersive Analysis of X−rays (EDAX).

To stimulate the emission of characteristic X−rays from a specimen, a high energy beam of charged particles such as electrons or a beam of X−rays, is focused with the sample being studied. At rest, an atom within the sample contains ground state (or unexcited) electrons in discrete energy levels or electron shells bound to the nucleus. The incident beam may excite an electron in an inner shell, ejecting it from the shell while creating an electron hole where the electron was. A position vacated by an ejected inner shell electron is eventually occupied by a higher energy electron from an outer shell and the

difference in energy between the higher energy shell and the lower energy shell may be released in the form of X−ray as shown in Figure 2.9. The amount of energy released by the transferring electron depends on which shell it is transferring from, as well as which shell it is transferring to. The number and energy of the X−rays emitted from a specimen can be measured by an energy dispersive spectrometer. As the energy of the X−ray is characteristic of the difference in energy between the two shells, and of the atomic structure of the element from which they were emitted, this allows the elemental composition of the specimen to be measured.

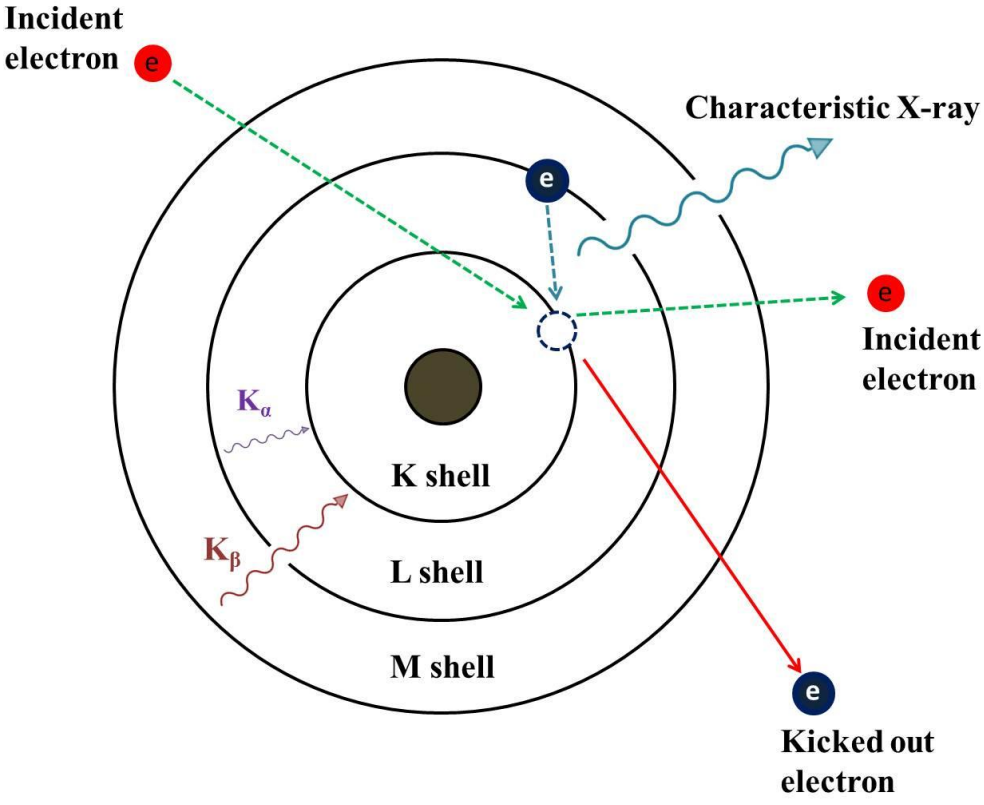

Figure 2.9: Schematic diagram of EDS principle.

The positions of the peaks with appropriate energies give information about the qualitative composition of the sample. The number of the X−ray quanta is the

measure for the concentration of the elements (peak height). There is no linear connection between quantum numbers and concentration portions of the elements. The concentration calculation needs the net count rates.

2.5.3. Electron Microscopes

An electron microscope is a type of microscope with high magnification and resolution, employing highly energetic electron beams in place of light and using electron lenses it produces magnified image of the illuminated specimen. We have used two types of electron microscopes to analyze as-synthesized samples as described below.

2.5.3.1 Scanning Electron Microscope (SEM)

In a typical SEM either thermionically created or field emission electron beam is focused onto the sample. The electrons interact with atoms of the sample, producing various signals containing information about the sample's surface topography and composition, which are recorded and thereby an image is formed pixel by pixel.

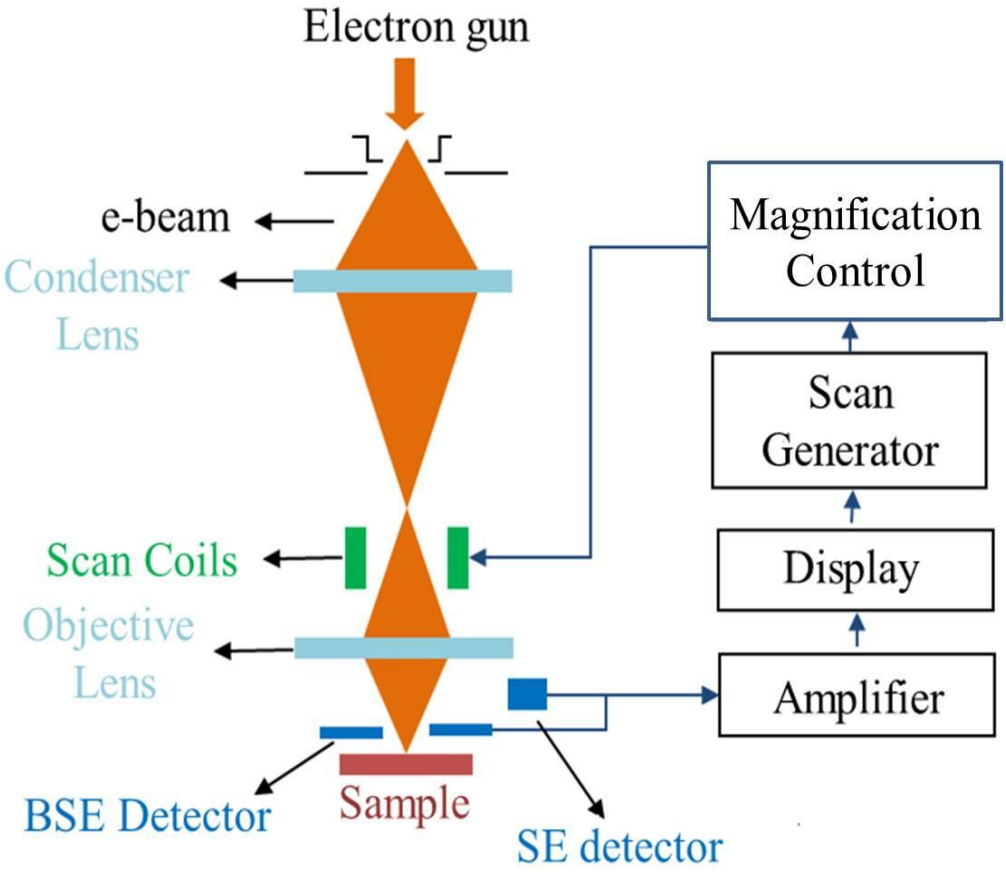

Figure 2.10: Schematic diagram of SEM

SEM typically works within the voltage range of 2 to 50 kV. The interactions which are responsible for an assembly of signal types are back scattered electrons (BSEs), secondary electrons (SEs), X-rays, Auger electrons, and cathodoluminescence. When an incident beam of electrons interact with the electric field of sample's electrons SEs are ejected from the k-shell of the specimen atoms as a result of inelastic scattering. The energy of SEs is less than 50 eV. If the vacancy due to formation of SE is filled from a higher level orbital, the characteristic X-ray of that energy transition is produced. Backscattered electrons (BSEs) are the reflected back electrons of the incident electron beam, which change its direction without altering energy of the electron significantly (<1eV), originating because of Elastic scattering between the beam electron with the electric field of the nucleus of a specimen atom. BSEs have energy in between 50 eV to the energy of incident beam. Basically,

SEM image is formed by mapping of varying intensity of the signal produced by SEs into image corresponding to the exact position of the beam on the specimen. On the other hand the characteristic X-rays are used for elemental analysis and this method is known as EDX (Energy Dispersive X-Ray) Spectroscopy. Morphology of our samples was analyzed by FESEM (FEI QUANTA FEG-250) operating at 5-10 keV. The schematic diagram of SEM is shown in Figure 2.10.

2.5.3.2 Transmission Electron Microscope (TEM)

In TEM mainly two different types of interactions between the electron beam and specimen is used for image formation; such as unscattered electrons (transmitted beam) and elastically scattered electrons (diffracted beam). Schematic diagram of a TEM is shown in Figure 2.11.

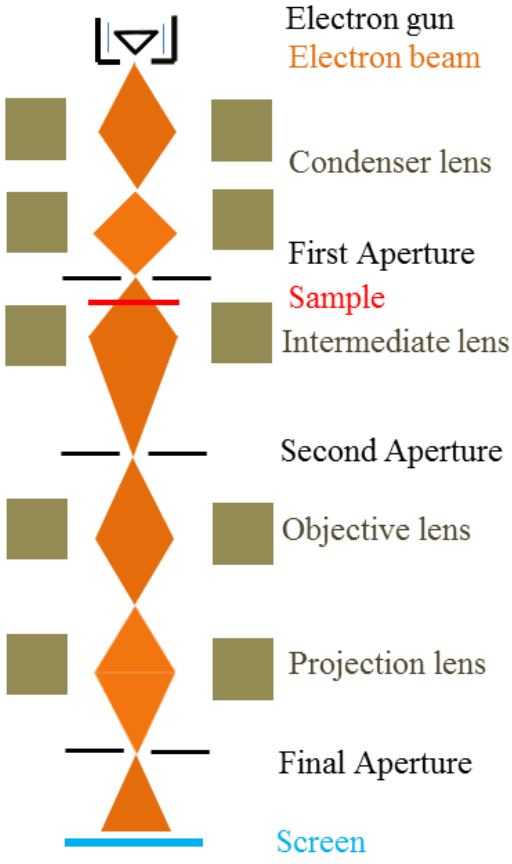

Figure 2.11: Schematic diagram of TEM

TEM image is formed by bright field imaging mode via creating dark and bright contrast in image. In this process, incident electrons are transmitted through the thin specimen without causing any interaction within the specimen. The transmission of unscattered electrons varies inversely with the specimen thickness. Areas of the specimen that are thicker will have less transmitted unscattered electrons and so will appear darker; conversely the thinner areas will have more transmitted and thus will appear brighter.

Electron diffraction is another important mode of TEM imaging. In case of crystalline sample, the electron beam undergoes Bragg scattering according to the Bragg's law as given by Equation 2.7. All incident electrons having the same energy (hence wavelength) enter the specimen perpendicularly to its surface. Now, the electrons that are scattered by the same set of parallel planes can be assembled using magnetic lenses to form a pattern of spots; each spot corresponding to a specific atomic spacing (or crystalline plane). This pattern can then produce information about the alignment, atomic arrangements and phases present in the area being observed.

In case of HRTEM (High Resolution Transmission Electron Microscope) mode we can attain a resolution around 0.2 nm, which is very efficient in observing the lattice fringes and crystal structure of the specimen. As the electron beam is transmitted through the thin section, different types of beam specimen interactions take place that produce transmitted electrons, elastically and inelastically scattered (energy loss) electrons, SEs, BSEs, Auger electrons and X-ray photons. X-ray photons are used in TEM based elemental analysis techniques in EDX and inelastically scattered electrons in electron energy loss spectroscopy (EELS), and energy filtered TEM (EFTEM).

For TEM study, we prepared samples by drop casting the NSs in ethanol or water on 300-mesh carbon coated copper grid and dried overnight in air.

Particle size and morphology were studied from TEM micrographs and elemental analysis was carried out from EDX spectrum recorded by a FEI Tecnai TF-20 field-emission high resolution TEM operating at 200 keV.

2.6. Thermo-Analytical Characterization Methods

2.6.1. Differential Thermal Device

Differential thermal device measures the difference in temperature between a sample and a thermally inert reference as the temperature is raised. The plot of differential thermal analysis (DTA) provides the information on exothermic and endothermic reactions taking place in the sample. The technique is routinely applied in a wide range of studies such as identification, quantitative composition analysis, phase diagrams, hydration-dehydration, thermal stability, phase transitions and melting points. A DTA consists of a sample holder comprising thermocouples, sample containers and a ceramic or metallic block, a furnace, a temperature programmer, and a recording system as shown in Figure 2.12. The key feature is the existence of two thermocouples connected to a voltmeter. One thermocouple is placed in an inert material such as Al_2O_3, while the other is placed in a sample under study. As the temperature is increased, there will be a brief deflection of the voltmeter if the sample is undergoing a phase transition. This occurs because the input of heat will raise the temperature of the inert substance, but be incorporated as latent heat in the material changing phase. To estimate the loading of the tartrate functionalization, we performed Thermogravime try (TG) on the T- $NiFe_2O_4$ and bare $NiFe_2O_4$ NPs using PerkinElmer Diamond TG/DTA with the heating rate of 10°C/min.

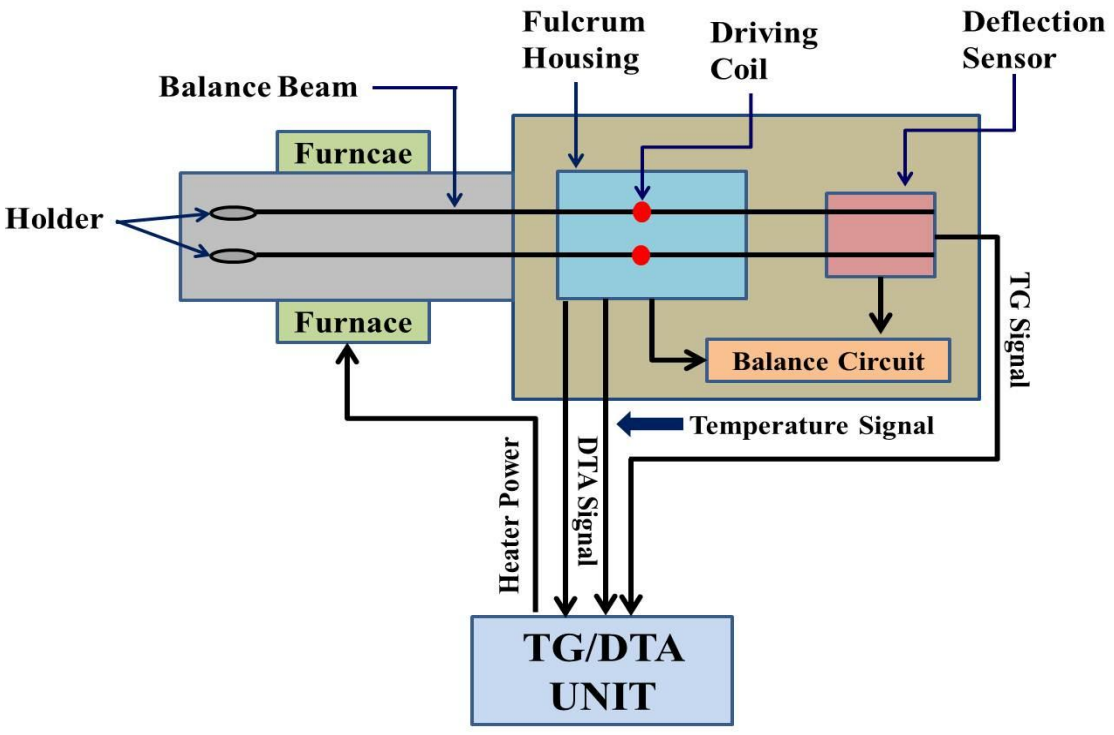

Figure 2.12: Schematic diagram of differential thermal device.

2.7. Optical Characterization Methods

2.7.1. UV-Visible (UV-Vis) Absorption Spectroscopy

UV-Vis spectroscopy is type of absorption spectroscopy in which light of ultra-violet or visible region is absorbed by the molecule. The instrument operates by passing a beam of light through a sample and measuring wavelength of light reaching a detector. The wavelength gives valuable information about the chemical structure and the intensity is related to the number of molecules, means quantity or concentration. This tool is mostly used for the quantitative determination of different organic and inorganic compounds in solution.

Absorption of the visible and adjacent (near-UV) regions of electromagnetic (EM) spectrum result in the excitation of the electrons from the ground state to higher energy state. Light is quantized into tiny packets called photons, the energy of which can be transferred to an electron upon collision. However, transfer occurs only when the energy level of the photon equals the energy

required for the electron to get promoted onto the next energy state, for example from the ground state to the first excitation state. This process is the basis for absorption spectroscopy. Generally, light of a definite wavelength and energy is irradiated on the sample, which absorbs a certain amount of energy from the incident light. The energy of the light transmitted from the sample afterwards is measured using a photo detector, which registers the absorbance of the sample. UV-visible spectroscopy follows the Lambert-Beer Law. This law states that whenever a beam of monochromatic light is passed through a solution with an absorbing substance, the decreasing rate of the radiation intensity along with the thickness of the absorbing solution is actually proportional to the concentration of the solution and the incident radiation (shown schematically in Figure 2.13). This law is expressed through this equation:

$$A = \log_{10}(I_0/I) = \varepsilon \cdot C \cdot l \qquad (2.9)$$

A stands for the absorbance, I_0 refers to the intensity of light upon a sample cell, *I* refers to the intensity of light departing the sample cell, C stands for the concentration of the absorbing species, *l* stands for the length of the sample cell and ε refers to the molar absorptivity or molar extinction coefficient. The molar extinction coefficient is a measurement of how strongly a chemical species attenuates light of a given wavelength.

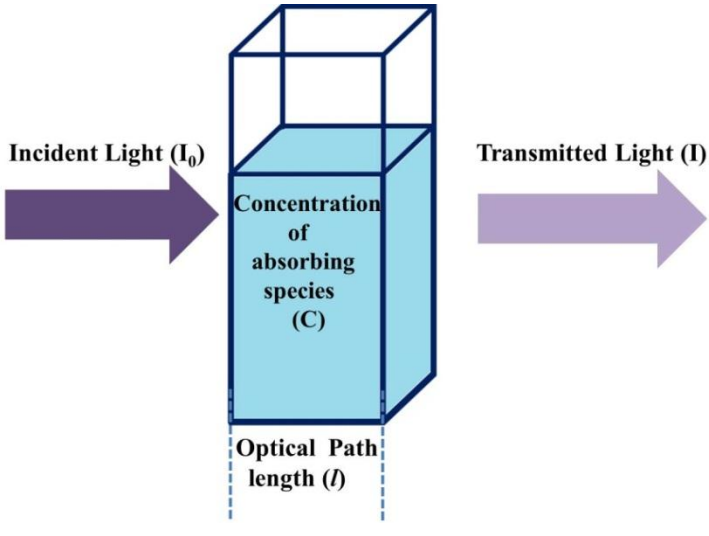

Figure 2.13: Schematic representation of Lambert-Beer Law.

UV-Vis absorbance spectra of our samples were obtained from a Shimadzu Model UV-2600 spectrophotometer using a quartz cuvette of 1 cm path length. The catalytic and photocatalytic study were also carried out by the above mentioned UV-Vis spectrophotometer. Schematic diagram of UV-Vis Spectrophotometer is shown in Figure 2.14.

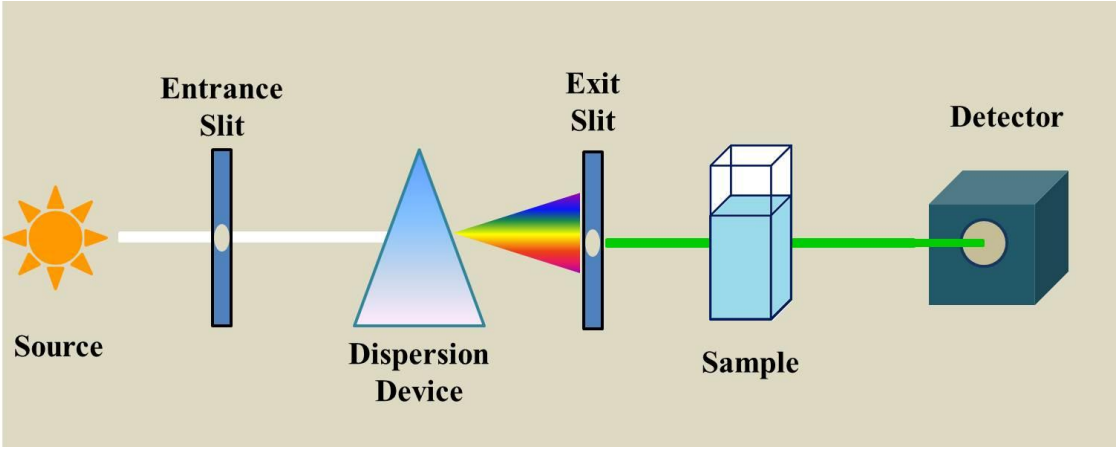

Figure 2.14: Schematic diagram of UV-Vis Spectrophotometer.

2.7.2. Catalysis and Photocatalysis

Biologically harmful pigment, Bilirubin (BR) was chosen for studying catalysis. BR is an yellow-orange breakdown product of normal heme catabolism in mammalian system. Molecular formula of BR is $C_{33}H_{36}N_4O_6$ and the chemical structure is demonstrated in Figure 2.15. Both antioxidant and toxic properties have been attributed to BR, which is normally conjugated with glucoronic acid and then excreted in the bile. However, when it's conjugation with glucoronic acid is inhibited, as neonatal jaundice and in hereditary forms of congenital jaundice, excess BR bind and deposit to various tissues, giving rise to severe hyperbilirubinemia and neurotoxicity. Aqueous solutions of functionalized nanoparticles were added to BR solution (pH 7), in a quartz cuvette placed in dark with continuous stirring. The absorbance of BR was recorded periodically using the UV-Vis spectrophotometer.

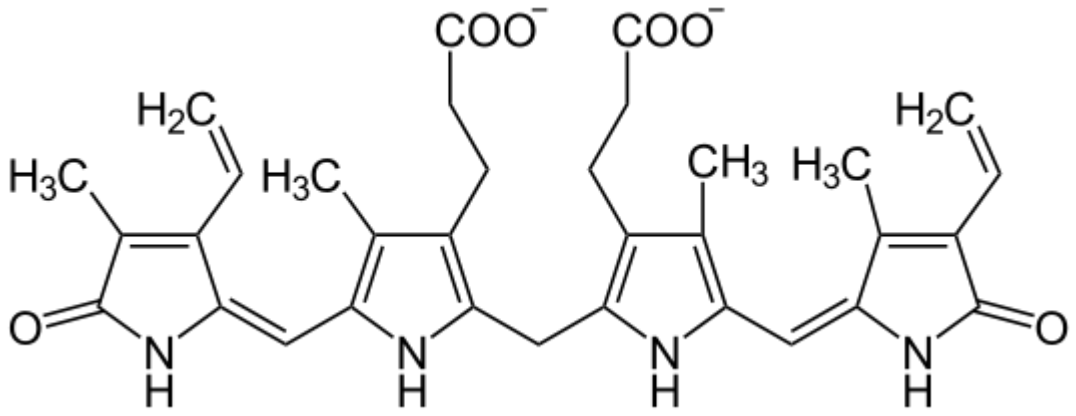

Figure 2.15: Chemical structure of BR.

For the photocatalysis purpose, methylene blue (MB), Rhodamine B (Rh B) and Para-nitrophenol (4-NP) were chosen. The first two of the aforementioned chemicals contain heterocyclic aromatic ring. MB and Rh B have the molecular formula $C_{16}H_{18}ClN_3S$ and $C_{28}H_{31}ClN_2O_3$ respectively and the chemical structure is shown in Figure 2.16. Both the dyes are widely used in textile industry and are the common water contaminant. In order to study the photocatalytic effects of the nanostructures, UV lamp of two different wavelengths (253 nm and 360 nm) from Philips were used. To the dye solutions, the functionalized nanostructures were added and homogeneously mixed by continuous stirring in dark. Absorbance of the dyes was recorded using the UV-Vis Spectrophotometer.

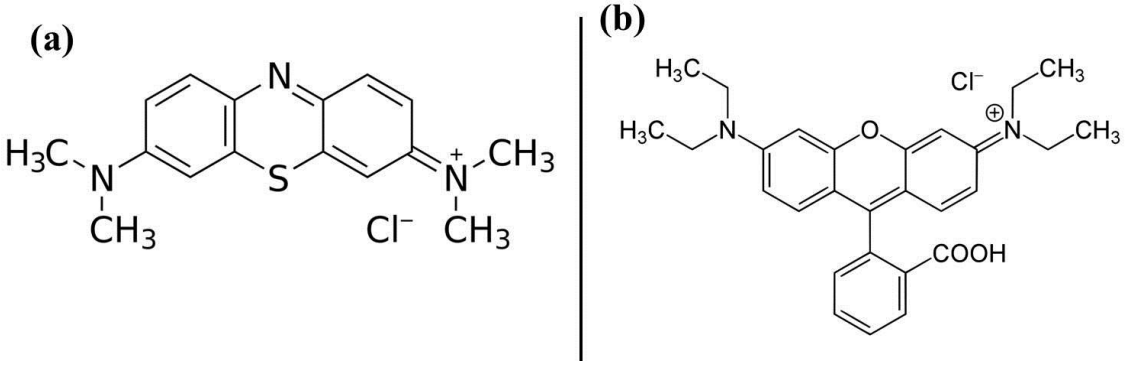

Figure 2.16: Chemical structure of (a) MB and (b) Rh B.

4-NP is the common hazardous product found in pharmaceutical waste. 4-Nitrophenol and derivatives are employed in the production of fungicides, herbicides, pesticides, in the synthesis of dyes and synthetic rubbers. However, the toxicity reached by 4-NP is high even at trace levels in plants and especially in some aquatic organism because it exhibit high solubility and stability in the ecosystem. 4-NP has the molecular formula $C_6H_5NO_3$ and the structure is shown in Figure 2.17.

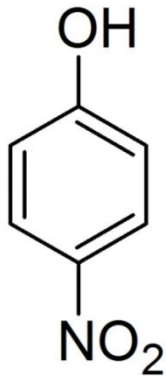

Figure 2.17: Chemical structure 4-NP.

2.7.3. Photoluminescence (PL) Spectroscopy

Photoluminescence (PL) spectroscopy is a contactless, multipurpose, nondestructive and powerful optical method of probing the electronic structure of materials. Light is focused onto a sample, where it is absorbed and imparts excess energy into the material in a process called photo-excitation. This excess energy can be dissipated by the sample through the emission of light or luminescence. In the case of photo-excitation, this luminescence is called photoluminescence. Therefore photoluminescence is the spontaneous emission of light from a material under optical excitation. This light can be collected and analyzed spectrally, spatially and also temporally. The intensity and spectral content of this photoluminescence is a direct measure of various important material properties.

Photo-excitation occurs due to the movement of electrons within the material to allowed excited states. When these electrons return to ground state, the excess energy is released and may include the emission of light (radiative process or photoluminescence) or may not (a non-radiative process) as shown in Figure 2.18. The energy of the emitted light (photoluminescence) is equal to the difference in energy levels between the excited state and the ground state, which are involved in the transition. PL spectroscopy gives information only on the low lying energy levels of the investigated system. The analysis of the PL spectrum leads to the identification of specific defects or impurities and the magnitude of the PL signal allows determining their concentration. PL spectrum is quite different from absorption spectrum in the sense that absorption spectrum measures transitions from the ground state to excited state, while photoluminescence deals with transitions from the excited state to the ground state. The period between absorption and emission is typically extremely short. An excitation spectrum is a graph of emission intensity versus excitation wavelength which looks very much like an absorption spectrum. The value of wavelength at which the molecules absorbs energy can be used as the excitation wavelength which provide a more intense emission at a red shifted wavelength, with a value usually twice of the excitation wavelength.

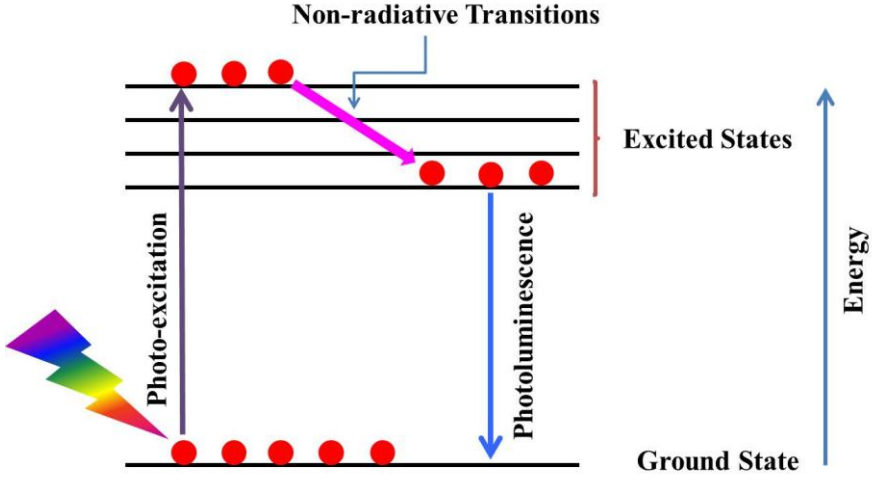

Figure 2.18: Principle of Photoluminescence.

A spectrofluorometer is an analytical instrument used to measure and record the fluorescence of a sample. Figure 2.19 represents the schematic of a fluorescence spectrophotometer.

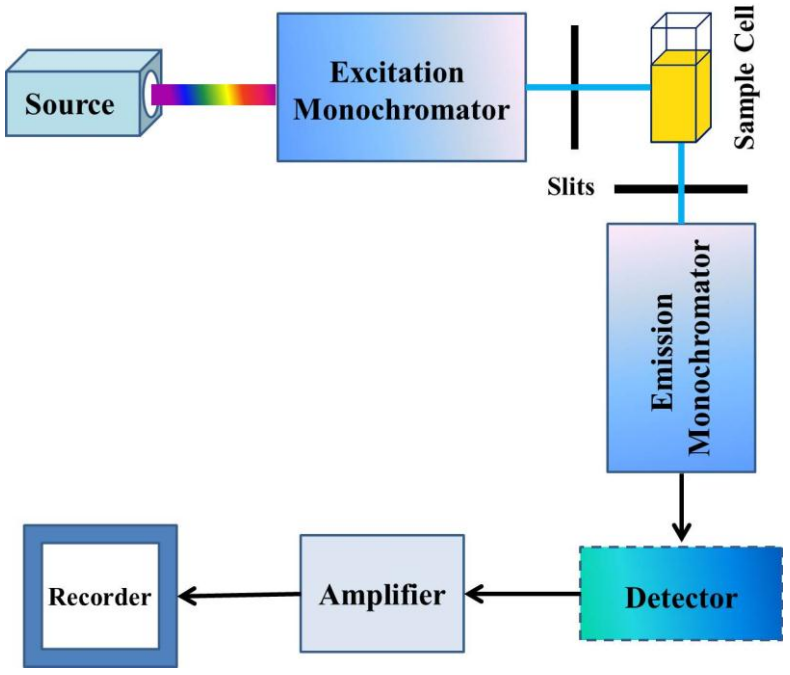

Figure 2.19: Schematic diagram of fluorescence spectrometer.

The fluorescence quantum yield (QY) is calculated by following the relative method, taking Rhodamine B (Rh B) as the standard fluorescent compound. The quantum yield of fluorescence-modified T-$NiFe_2O_4$ NPs was measured according to A Guide to Recording Fluorescence Quantum Yields [15-16], using to the following equation:

$$\Phi_X = \Phi_{ST}\left(\frac{Grad_X}{Grad_{ST}}\right)\left(\frac{\eta_X^2}{\eta_{ST}^2}\right) \qquad (2.10)$$

where, $\boldsymbol{\Phi_X}$ is the fluorescence quantum yield of the test sample we are measuring and $\boldsymbol{\Phi_{ST}}$ is the quantum yield of the standard sample. ***Grad*** refers to the gradient from the plot of fluorescence intensity against the absorbance. $\boldsymbol{\eta}$ is the refractive index of the solvent, and the subscripts ***ST*** and ***X*** mean the standard and test sample respectively.

2.7.3. Fluorescence Microscopy

Fluorescence illumination and observation is the most speedily growing microscopy technique employed today. A fluorescence microscope is an optical microscope that uses fluorescence instead of, or in addition to, reflection and absorption to study properties of organic or inorganic substances. The "fluorescence microscope" refers to any microscope that uses fluorescence to generate an image. The technique of fluorescence microscopy has become an essential tool in biology and the biomedical sciences, as well as in materials science due to attributes that are not readily available in other contrast modes with traditional optical microscopy. The basic function of a fluorescence microscope is to irradiate the specimen with a desired and specific band of wavelengths, and then to separate the much weaker emitted fluorescence from the excitation light. In a properly configured microscope only the emission light should reach the eye or detector, so that the resulting fluorescent structures are superimposed with high contrast against a very dark (or black) background. The limits of detection are generally governed by the darkness of the background and the excitation light is typically several hundred thousand to a million times brighter than the emitted fluorescence. The effective separation and detection of excitation and emission wavelengths are achieved in fluorescence microscopy through the proper selection of filters to block or pass specific wavelength bands in the ultraviolet, visible, and near-infrared spectral regions. In order to generate sufficient excitation light intensity to produce detectable emission, powerful compact light sources, such as high-energy short arc-discharge lamps are necessary. The most common lamps are mercury burners, ranging in wattage from 50 to 200 Watts and the xenon burners that range from 75 to 150 Watts. The microscope arc-discharge lamp external power supply is usually equipped with a timer to track the number of hours the burner has been in operation. Arc

lamps lose efficiency and are more likely to shatter if used beyond their rated lifetime (200-300 hours). A dichroic beam splitter or mirror is used to reflect the excitation light to the sample and simultaneously transmit only the emitted light from the sample back to the detector. The filter that narrows the wavelengths of the incoming light to only those used to excite the sample is called the excitation filter. A filter for emitted light that transmits only the wavelengths of the emitted light from the sample and blocks all the light passed through the excitation filter, called the emission filter. All the components are schematically shown in the Figure 2.20. Olympus BX-53 and Leica DM 1000 were used to capture the fluorescence microscopy images.

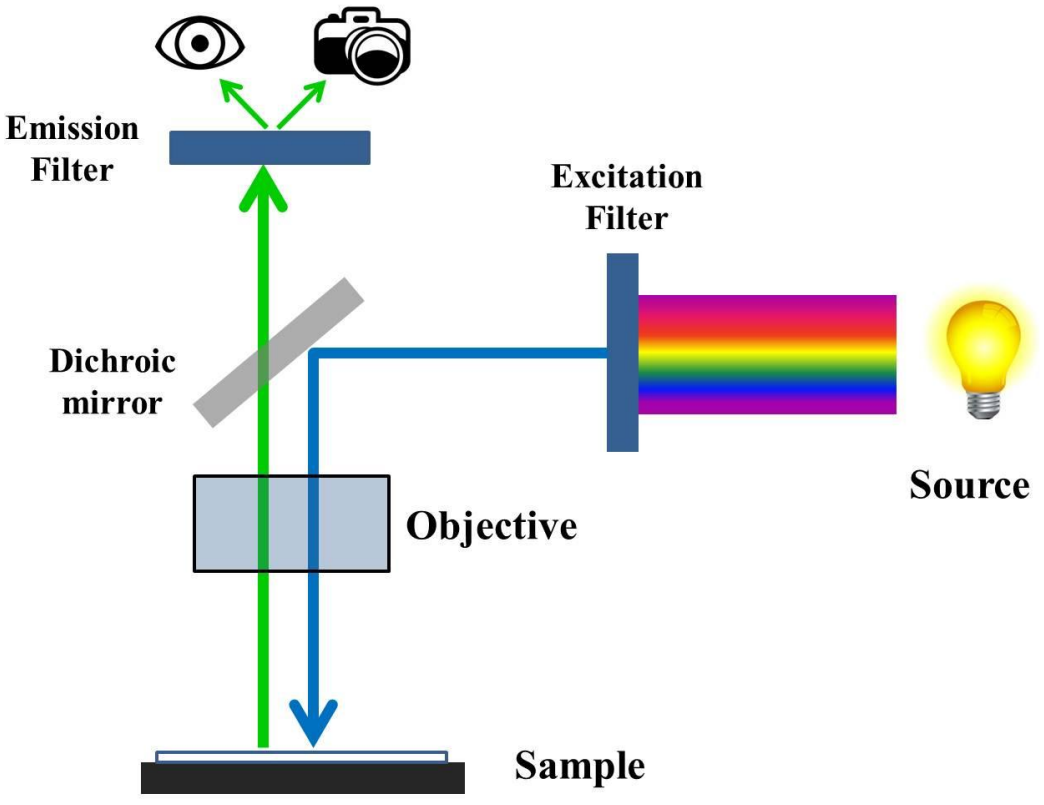

Figure 2.20: Schematic diagram of fluorescence spectrometer.

2.7.4. Fourier Transformed Infrared Spectroscopy (FTIR)

Infrared spectroscopy is an important technique in chemistry. It is an easy way to identify the presence of certain functional groups in a molecule. Also one can use the unique collection of absorption bands to confirm the identity of a pure compound or to detect the presence of specific impurities. Analysis by infrared spectroscopy is based on the fact that molecules have specific frequencies of internal vibrations. These frequencies occur in the infrared region of the electromagnetic spectrum: ~ 4000 cm^{-1} to ~ 200 cm^{-1}.

When a sample is placed in a beam of infrared radiation, the sample will absorb radiation at frequencies corresponding to molecular vibrational frequencies, but will transmit all other frequencies. The frequencies of radiation absorbed are measured by an infrared spectrometer and the resulting plot of absorbed energy vs. frequency is called infrared spectrum of the material. Identification of a substance is possible because different materials have different vibrations and yield different infrared spectra. Furthermore, from the frequencies of the absorption it is possible to determine whether various chemical groups are present or absent in a chemical structure. In addition to the characteristic nature of the absorption, the magnitude of the absorption due to a given species is related to the concentration of that species.

Fourier Transform Infrared (FTIR) spectrometry was developed in order to overcome the limitations encountered with dispersive instruments. The main difficulty was the slow scanning process. A method for measuring all of the infrared frequencies simultaneously, rather than individually, was needed. A solution was developed which employed a very simple optical device called an interferometer. The interferometer produces a unique type of signal which has all of the infrared frequencies "encoded" into it. The signal can be measured

very quickly, usually on the order of one second or so. Thus, the time element per sample is reduced to a matter of a few seconds rather than several minutes. Most interferometers employ a beam splitter which takes the incoming infrared beam and divides it into two optical beams. One beam reflects off a flat mirror which is fixed in place. The other beam reflects off a flat mirror which is on a mechanism which allows this mirror to move a very short distance (typically a few millimeters) away from the beam splitter. The two beams reflect off their respective mirrors and are recombined when they meet back at the beam splitter. Because of the path, that one beam travels is a fixed length and the other is constantly changing as its mirror moves, the signal which exits the interferometer is the result of these two beams "interfering" with each other. The resulting signal is called an interferogram which has the unique property that every data point (a function of the moving mirror position) which makes up the signal has information about every infrared frequency coming from the source. This means that as the interferogram is measured; all frequencies are being measured simultaneously. Thus, the use of the interferometer results in extremely fast measurements. Because the analyst requires a frequency spectrum (a plot of the intensity at each individual frequency) in order to make identification, the measured interferogram signal cannot be interpreted directly.

The basic components of an FTIR are shown schematically in Figure 2.21. The infrared source emits a broad band of different wavelength of infrared radiation. For the mid-IR region (5000–400 cm^{-1}), the most common source is a silicon carbide element heated to about 1200 K. The IR radiation goes through an interferometer that modulates the infrared radiation. For the mid-IR region, the beam splitter is usually made of KBr with a germanium-based coating that makes it semi-reflective. KBr absorbs strongly at wavelengths beyond 25 μm (400 cm^{-1}), so CsI is sometimes used to extend the range to about 50 μm (200 cm^{-1}).The interferometer performs an optical inverse Fourier transform on

entering IR radiation. The modulated IR beam passes through the sample where it is absorbed to various extents at different wavelengths by the various molecules present. Finally, the intensity of the IR beam is detected by a detector. Liquid nitrogen cooled mercury cadmium telluride (MCT) detectors are the most widely used in the mid-IR. With these detectors an interferogram can be measured in as little time as 10 milliseconds. The detected signal is digitized and Fourier transformed by the computer to get the IR spectrum of the sample. A JASCO FTIR-6300 spectrometer was used to carry out the FTIR studies. For the FTIR measurements, powdered samples were mixed with KBr powder and pelletized. The background correction was made using a reference pure KBr pellet before every measurement.

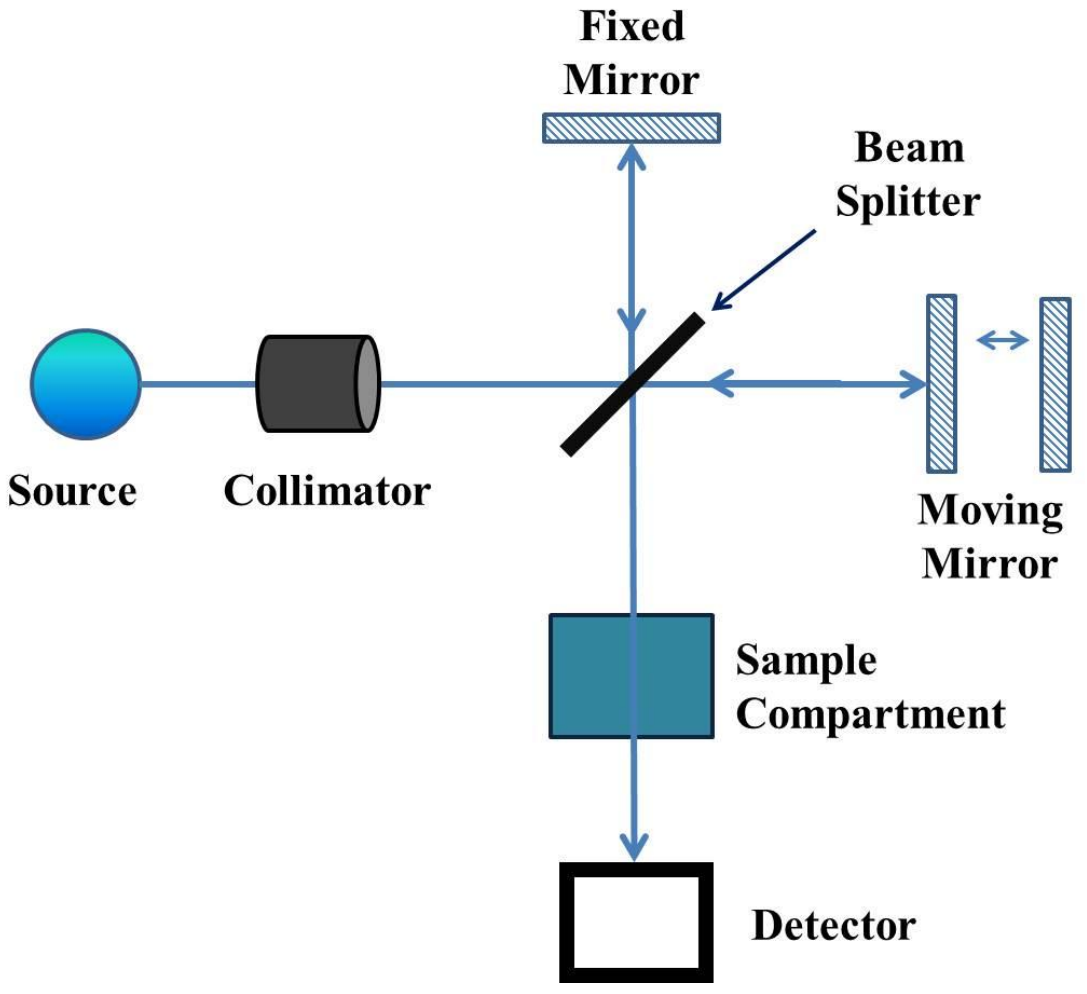

Figure 2.21: Schematic diagram of FTIR spectrometer.

2.8. Analytical Characterization Methods

2.8.1. Liquid Chromatography-Mass Spectrometry (LC-MS)

The Liquid Chromatography-Mass Spectrometry (LC-MS) technology involves use of a High-performance liquid chromatography (HPLC), wherein the individual components in a mixture are first separated followed by ionization and separation of the ions on the basis of their mass/charge ratio. The separated ions are then directed to a photo or electron multiplier tube detector, which identifies and quantifies each ion. The ion source is an important component in any MS analysis, as this basically aids in efficient generation of ions for analysis. To ionize intact molecules, the ion source could be Atmospheric Pressure Chemical Ionization (APCI), Electronspray Ionization (ESI), etc. to name a few popular ones. The choice of ion source also depends on the chemical nature of the analyte of interest i.e. polar or non-polar.

The major advantages of this technology include sensitivity, specificity and precision as analysis is done at molecular level. Also, structural details of the analyte can be deciphered. To confirm the degradation of MB and BR, Liquid chromatography-Mass spectrometry (LC-MS) study of only MB solution and the final reaction mixtures (MB+T-$NiFe_2O_4$ and BR+T-$NiFe_2O_4$) were carried out using Agilent 1260 Infinity Quaternary LC coupled to a 6000 series single quadruple mass analyzer in electrospray ionization mode. The quadrupole analyser consists of a set of four parallel metal rods. A combination of constant and varying (radio frequency) voltages allows the transmission of a narrow band of m/z values along the axis of the rods. Schematic diagram of LC-MS is shown in Figure 2.22.

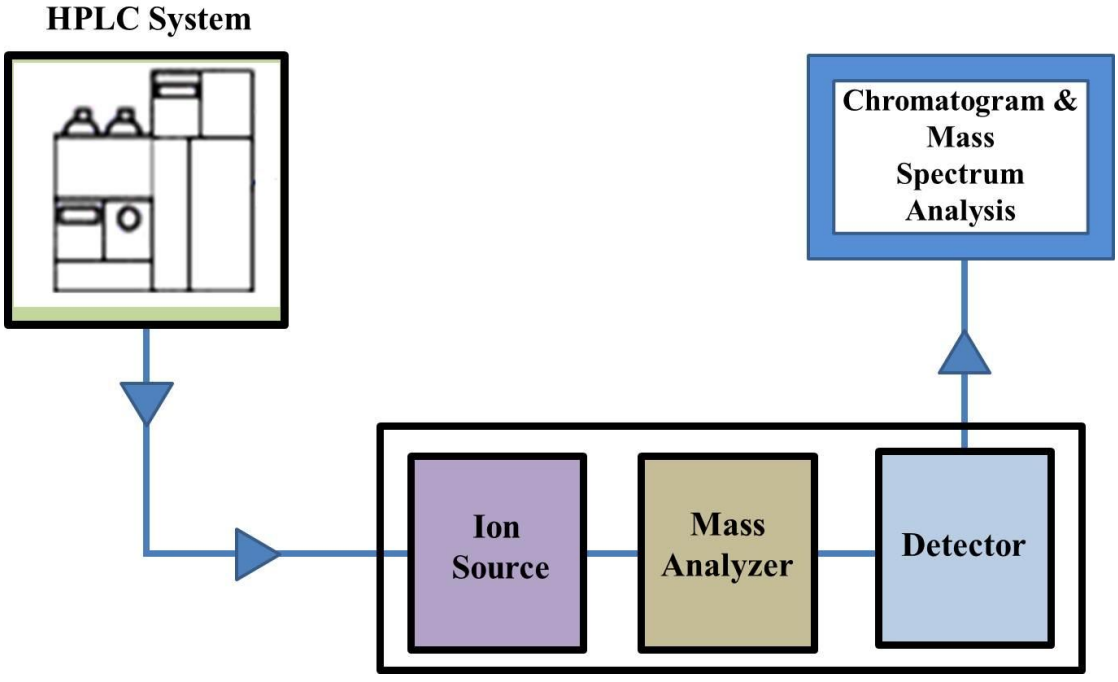

Figure 2.22: Schematic diagram of LC-MS spectrometer.

2.9 Magnetic Measurement Technique

2.9.1 Vibrating Sample Magnetometry (VSM)

A vibrating-sample magnetometer (VSM) is a scientific instrument that measures magnetic properties. In VSM, a sample is vibrated (usually in a direction perpendicular to the coils) sinusoidally by placing it in a direct current (DC) magnetic field (H) and as a result a voltage is induced in the pickup coil due to variation of magnetic flux B. According to Faraday's law of electromagnetic (EM) induction, induced voltage V in a pickup coil with cross sectional area **A** and **N** number of turns is

$$V = -NA\frac{dB}{dt} \qquad (2.11)$$

where, $B = \mu_0 H$ (here μ_0 is permeability of vacuum)

Now, if test specimen placed in the pickup coil is of magnetization M, the total

magnetic induction B can be written as

$$B = \mu_0 (H+M) \qquad (2.12)$$

Therefore, the change in flux due to sample insertion is $\Delta B = \mu_0 M$. Hence, the Equation 2.11, can be rewritten as,

$$V dt = -\mu_0 NAM \qquad (2.13)$$

Intensity of the signal is proportional to the magnetic moment of the sample and the frequency is the same as that of the sinusoidal vibration. A schematic diagram of the sample holder and detection mechanism of a VSM is shown in Figure 2.23. Magnetic measurement of our sample was performed in a Lake Shore VSM equipped with an electromagnet, capable of generating field of up to 1.6 T at 300 K.

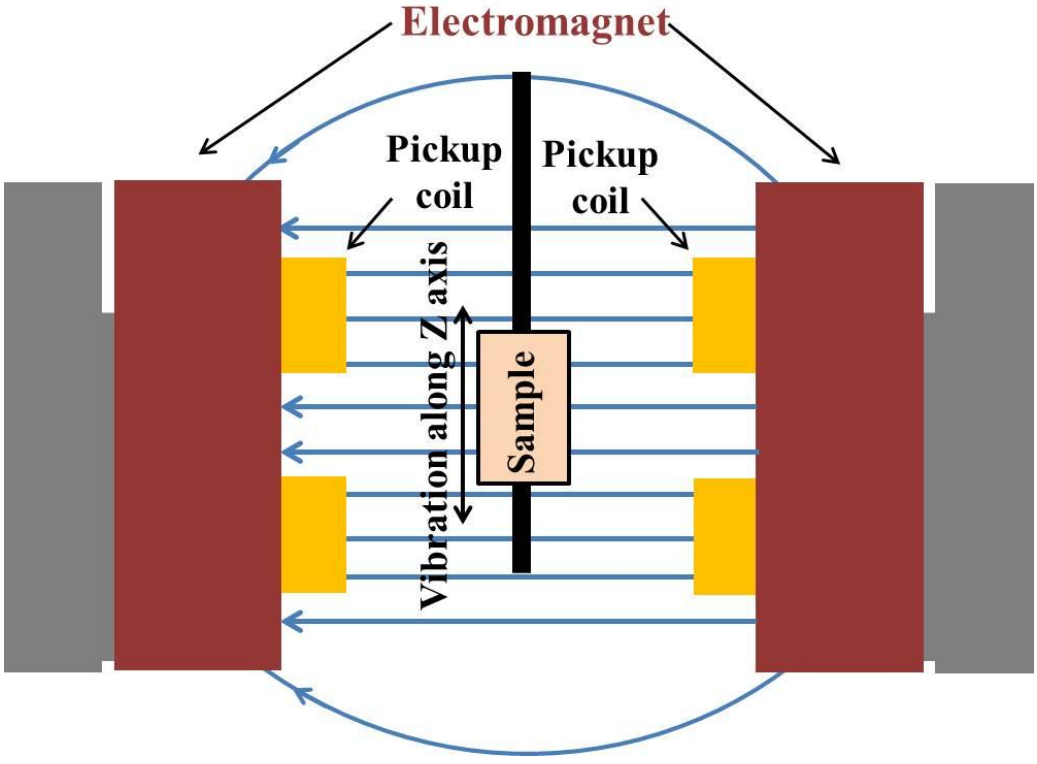

Figure 2.23: Schematic diagram of VSM.

2.10 Porosity Measurement Technique

2.10.1 Surface and Pore Volume Analyzer

Physical adsorption (physisorption) is used to measure surface area and pore size. As more gas molecules are introduced into the system, the adsorbate molecules tend to form a thin layer that covers the entire adsorbent surface. Based on the well-known Brunauer, Emmett and Teller (B.E.T.) theory one can estimate the number of molecules required to cover the adsorbent surface with a monolayer of adsorbed molecules, N_m. Multiplying N_m by the cross-sectional area of an adsorbate molecule yields the sample's surface area. Continued addition of gas molecules beyond monolayer formation leads to the gradual stacking of multiple layers (or multilayers) on top of each other. The formation of multilayers occurs in parallel to capillary condensation. The latter process is described by the proportionality between residual (or equilibrium) gas pressure and the size of capillaries capable of condensing gas within them. Computational methods such as, the classical one by Barrett, Joyner and Halenda (BJH), or preferably state-of-the-art calculations like Density Function Theory (DFT) allows the determination of pore sizes from equilibrium gas pressures. One can therefore generate experimental curves (or isotherms) linking adsorbed gas volumes with relative saturation pressures at equilibrium and convert them to cumulative or differential pore size distributions.

The adsorption/desorption isotherms and pore volumes of the adsorbents were determined by nitrogen adsorption–desorption isotherms, measured at 77 K using Quanta chrome Autosorb 1C system (shown in Figure 2.24). The samples were degassed at 200°C under vacuum before starting N_2 adsorption. Surface area and pore volumes (or pore size distribution) were determined using the Brunauer–Emmet–Teller (BET) equation, Barret–Joyner–Halenda (BJH) and DFT methods respectively.

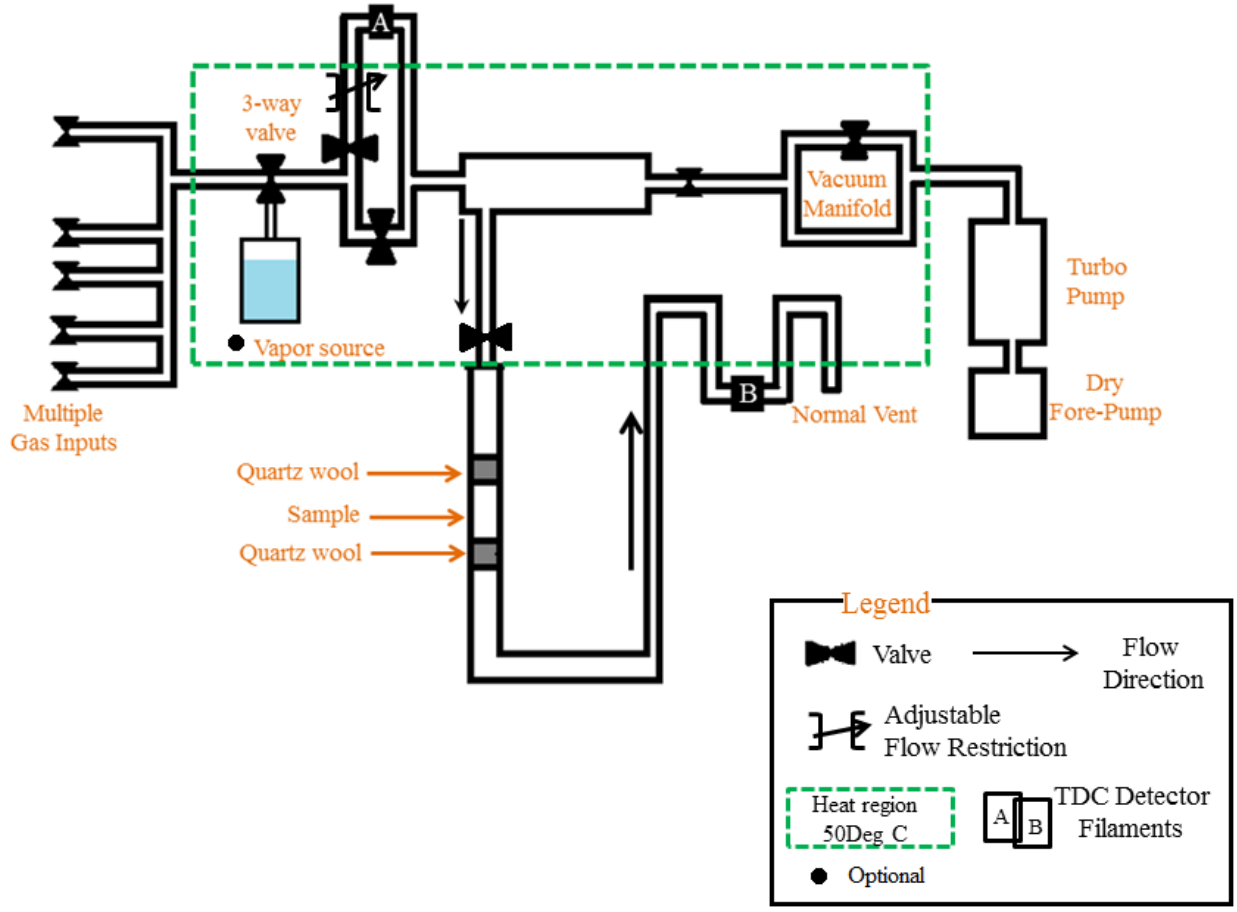

Figure 2.24: Schematic diagram of Surface and Pore Volume Analyzer.

Bibliography

1. K. Ariga, J. P. Hilla, Q. Jia, *Layer-by-layer assembly as a versatile bottom-up nanofabrication technique for exploratory research and realistic application*, **Phys. Chem. Chem. Phys.**, 2007, 9, 2319-2340.

2. S. Kumar, T. Nann, *Shape control of II-VI semiconductor nanomaterials*, **Small**, 2006, 2, 316-329.

3. N.T.K. Thanh, N. Maclean, S. Mahiddine, Mechanisms of Nucleation and Growth of Nanoparticles in Solution, **Chem. Rev**., 2014, 114 , 7610–7630.

4. W.R. Lee, M. G. Kim, J.R. Choi, J.I. Park, S. J. Ko, S. J. Oh, J. Cheon, *Redox−Transmetalation Process as a Generalized Synthetic Strategy for Core−Shell Magnetic Nanoparticles*, **J. Am. Chem. Soc**., 2005, 127, 16090–16097.

5. M.A. Watzky, *R.G. Finke, Nanocluster size-control and "magic number" investigations. Experimental tests of the "living-metal polymer" concept and of mechanism- based size-control predictions leading to the syntheses of iridium(0) nanoclusters centering about four sequential magic numbers*, **Chem. Mater**., 1997, 9, 3083-3095.

6. S. Gupta, S. Neeleshwar, V. Kumar, Y.Y. Chen, *Synthesis of bismuth telluride nanostructures by refluxing method*, **Adv. Mater. Lett.**, 2012, 3, 50–54.

7. Y. Sun, B. Gates, B. Mayers, Y. Xia, *Crystalline silver nanowires by soft solution processing*, **Nano Lett.**, 2002, 2, 165–168.

8. P.D. Cozzoli, A. Kornowski, H. Weller, *Low-temperature synthesis of soluble and processable organic-capped anatase TiO_2 nanorods*, **J. Am. Chem. Soc.,** 2003, 125, 14539–14548.

9. L. Xu, S. Sithambaram, Y. Zhang, C.H. Chen, L. Jin, R. Joesten, S.L. Suib, *Novel urchin-like CuO synthesized by a facile reflux method with efficient olefin epoxidation catalytic performance*, Chem. Mater., 2009, 21, 1253–1259.

10. X. Sun, Y. Li, *Colloidal carbon spheres and their core/shell structures with noble-metal nanoparticles*, **Angew. Chem. Int. Ed**., 2004, 43, 597–601.

11. L.-Q. Mai, F. Yang, Y.-L. Zhao, X. Xu, L. Xu, Y.-Z. Luo, *Hierarchical MnMoO(4)/CoMoO(4) heterostructured nanowires with enhanced supercapacitor performance*, **Nat. Commun.**, 2011, 2, 381.

12. S. Sun, H. Zeng, D.B. Robinson, S. Raoux, P.M. Rice, S.X. Wang, G. Li, *Monodisperse MFe_2O_4 (M = Fe, Co, Mn) Nanoparticles*, **J. Am. Chem. Soc**., 2004, 126, 273-279.

13. R. I. Walton, *Subcritical solvothermal synthesis of condensed inorganic materials*, **Chem. Soc. Rev.**, 2002, 31, 230.

14. A. Rabenau, The role of hydrothermal synthesis in preparative chemistry, **Angew. Chem**., 1985, 24, 1026-1040.

15. A.T.R. Williams, S.A. Winfield, *Relative Fluorescence Quantum Yields Using a Computer-controlled Luminescence Spectrometer*, **Analyst**, 1983, 108, 1067-1071.

16. H.J. Yvon, *A guide to recording fluorescence quantum yields*, **HORIBA Scientific**, 2012.

Chapter 3

Surface Modification of $NiFe_2O_4$ Nanoparticles

In this chapter we have demonstrated facile functionalization strategy of $NiFe_2O_4$ nanoparticles with hydrophilic organic ligand to induce intrinsic photoluminescence and excellent catalytic & photocatalytic property.

3. Facile surface modification of nickel ferrite nanoparticles for inherent multiple fluorescence and catalytic activities

3.1 Preamble

In this era, nanotechnology has widened the limit for innovators, producers and consumers in almost all sectors, by facilitating the engineering of functional systems at the molecular level. The horizon of nanotechnology is still experiencing rapid expansion. An important trend is the development of multifunctional nanoparticles—nanoparticles that are capable of accomplishing multiple objectives such as imaging and therapy or performing advanced tasks through incorporation or attachment of single or multiple functional groups. The attachment of different functional groups on the surface of the Nanoparticles (NPs) is of immense interest for various scientific disciplines requiring multifunctionality at the nanoscale. The controlled manipulation of the external surface of NPs is of paramount importance as it defines the interface between the NP and its surroundings and strongly determines the overall performance of the NP especially in biological environments [1-4].

With increasing applications, particularly in biomedical fields [5-9], the multifunctional magnetic nanoparticles (MNPs) have attracted tremendous attention due to their potential to be used in the ultrasound [10], optical and fluorescence imaging combined with targeted drug delivery [11-14], separation and purification of cells [15], tissue repairing [16], hyperthermia for cancer treatment [17], as they result from biocompatibility, chemical stability and controlled transport property. The MNPs are also useful in the field of catalysis since they are efficient for specific chemical transformations. In addition they are propitious economically and environmentally due to their elevated activity, sufficient stability, controlled separation by an external magnetic field, low price, and facile synthesis [18-24].

MNPs with intrinsic fluorescence are in high demand. To be used in biomedical field, they should possess criteria such as biocompatibility, monodispersity, dispersibility in water, and non-toxicity. The commonly used procedure for synthesizing magneto-fluorescent NPs involves processes like making nanocomposites with quantum dots (QDs) or coatings with fluorescent dyes. In order to make the NPs biocompatible, surface modifications were carried out with biomolecules like proteins, DNA, RNA, small organic ligands, and polymers, but none of them were able to generate intrinsic fluorescence. But, their applications towards the biomedical field are tapered due to disadvantages such as chemical instability, photobleaching of fluorescent dyes, and inherent toxicity of QDs (due to the presence of heavy metals like Cd^{+2}, Pb^{+2}) [25]. Therefore, to stimulate the wide applicability of the nanoparticles (NPs) in biomedical field, a facile and apt process for surface modification is highly required. The main purpose of our present work is to design water dispersible 3d transition metal oxide based MNPs with intrinsic fluorescence for their applications in cell imaging.

In this chapter, we have discussed the synthesis $NiFe_2O_4$ NPs by wet chemical method and development of $NiFe_2O_4$ NPs as multifunctional nano-probes bearing inherent multicolor photoluminescence by the simplistic way of surface modification. Furthermore, we have utilized efficiently the developed MNPs in photocatalysis and catalysis. Using ligand field theory (LFT), we have pointed out the electronic transitions responsible for multicolored photoluminescence of the functionalized $NiFe_2O_4$ NPs. We tried the functionalized NPs as cell imaging agent and found them worthy to be used in imaging applications.

3.2. Experiment

3.2.1 Materials Used

Iron acetylacetonate [$Fe(acac)_3$], Oleyl amine and methylene blue (MB) were obtained from from Sigma-Aldrich. Nickel Acetate [$Ni(CH_3CO_2)_2$], Diphenyl Ether, Oleic Acid, Cetyl alcohol and bilirubin (BR) were purchased from Loba Chemie. Tartaric acid and Sodium Hydroxide (NaOH) were bought from Merck.

3.2.2 Synthesis and Experimental Procedure

We have synthesized $NiFe_2O_4$ NPs with slight modification, by following a template free wet chemical method previously reported by Sun et. al [26]. The solution mixture of Iron (III) acetylacetonate [$Fe(acac)_3$], Nickel(II) acetate [$Ni(CH_3CO_2)_2$], Diphenyl ether, Oleylamine, and Oleic acid was heated to 270°C for 1 h in presence of Cetyl alcohol instead of 1,2-hexadecanediol used by Sun et. al [26]. The as-synthesized $NiFe_2O_4$ NPs were then washed by ethanol and collected after centrifugation. The removal of the mother solution was carried out by heating the NPs on a hotplate at a temperature of 80°C for 30 min.

The functionalization process of Nickel ferrite by tartrate ligand was carried out using a vibrator-rotor. At first in a glass vial of Borosil, we took the solution of Na-tartrate and solid as-prepared Nickel ferrite nanoparticles. Then the glass vial was placed on the top of the vibrator-rotor and the mixture went under vigorous vibration and rotation for 12 hrs. This process is called “cyclomixing”. The non-solubilised $NiFe_2O_4$ NPs were filtered by passing the functionalized NP-solution mixture through a syringe filter of diameter 0.22 μm. We obtained a clear solution of tartrate-functionalized $NiFe_2O_4$ NPs, called T-$NiFe_2O_4$ NPs. The T- $NiFe_2O_4$ NPs were then further surface modified by heating the clear

solution at 70°C for 42 h, while keeping the pH of the solution at 12 by adding NaOH drop wise.

The X-ray powder diffraction (XRD) of as-prepared $NiFe_2O_4$ NPs was carried out using Rikagu miniflex II diffractometer equipped with Cu K_α radiation (at 40 mA and 40 kV) at the scanning rate of 3° per minute in the 2θ range of 20°-70°. A FEI Technai G2 TF-20 field-emission high-resolution transmission electron microscope (TEM), operated at 200 kV was used to study the size distribution, shape, morphology and to record the Energy-dispersive X-ray analysis (EDX) spectrum of the as-prepared and functionalized $NiFe_2O_4$ NPs. The Ultraviolet-visible (UV/Vis) absorbance spectra of T-$NiFe_2O_4$ NPs were obtained on a Shimadzu UV-2600 spectrophotometer, using a quartz cuvette of 1 cm path length. A Horiba Jovin Yvon Model Fluorolog fluorimeter was used to carry out the steady-state fluorescence emission and excitation study of T-$NiFe_2O_4$ NPs. Fluorescence micrographs of T- $NiFe_2O_4$ NPs were captured using a Leica DM1000 LED fluorescence microscope.

To be sure of the attachment of tartrate molecules to the NPs' surface, Fourier transform infrared spectroscopy (FTIR) measurements were performed using a JASCO FTIR-6300 spectrometer. For FTIR study, pellets were made after homogeneous mixing of lyophilized T- $NiFe_2O_4$ powder samples with KBr. The background was corrected using a reference KBr pellet. To estimate the loading of the tartrate functionalization, we performed Thermogravimetry (TG) on the T- $NiFe_2O_4$ and bare $NiFe_2O_4$ NPs using PerkinElmer Diamond TG/DTA with the heating rate of 10°C/min. The magnetic measurements were performed using a Lake Shore Vibrating Sample Magnetometer (VSM) under a magnetic field of 14 kOe.

For cell culture tests, cells of the human osteosarcoma cell line Cal-72 were ordered from the DSMZ (Leibnitz Institute DSMZ – German Collection of Microorganisms and Cell Culture, DSMZ no.: ACC 439). The cells were

cultivated in Dulbecco's Modified Eagle Medium with a concentration of 10% foetal bovine serum. After three days the medium was removed and replaced by mixtures of culture medium and functionalized NPs at concentrations of 6, 2, and 0.5 mg/ml. After one day those mixtures were removed and the cells were fixed using 3% paraformaldehyde in Phosphate Buffered Saline (PBS). Cytotoxicity was performed by watching the phenotype and condition of the cells for several hours using a high resolution optical microscope. Images of the cells along with NPs were taken using a Laser scanning Microscope (LSM).

3.2.3 Photocatalytic Study

In the photocatalytic study, an 8 W UV lamp with a wavelength of 253.7 nm (UV-C) was used. The aqueous solution of T-$NiFe_2O_4$ NPs (50 μL, containing 0.06 mg NPs) and 5 μM aqueous solution of Methylene Blue (MB) (pH~3) were uniformly mixed in a quartz cuvette for 1h in the dark. Then, the cuvette was kept 2 cm away from the light source and the absorbance spectra of MB in presence of T-$NiFe_2O_4$ NPs solution was measured periodically by Shimadzu UV-2600 UV/VIS spectrophotometer. The very first recorded set of data of absorbance was marked as 0 minute. After 60 minutes of irradiation (first cycle), we further added 5 μL methylene blue solution to the reaction mixture but the catalyst solution was not added for the second cycle. Similar procedure was maintained up to 5 cycles.

To confirm the degradation of MB, Liquid chromatography-Mass spectrometry (LC-MS) study of only MB solution and the final reaction mixture (MB+T-$NiFe_2O_4$) was carried out using Agilent 1260 Infinity Quaternary LC coupled to a 6000 series single quadruple mass analyzer in electrospray ionization mode.

In order to find the reaction pathway for the photocatalysis, we carried out the degradation study of MB in the previously mentioned process with radical scavenger (Ethyl alcohol/EtOH) and radical initiator (H_2O_2).

3.2.4 Catalytic Study

In order to determine the catalytic activity of functionalized NPs, the aqueous solution of T-$NiFe_2O_4$ NPs (50 mL, containing 0.06 mg NPs) were added to 15 μL of aqueous solution of bilirubin (BR) (pH~7) kept in a quartz cuvette under continuous stirring in the dark. Then the absorbance spectra of BR in presence of T-$NiFe_2O_4$ NPs solution were recorded at times by using UV/Vis spectrophotometer. The reusability study was carried out by the similar procedure as we did for photocatalysis up to 3 cycles.

To get the confirmation of decomposition of BR, we carried out LC-MS study of BR and the final reaction mixture (BR+T-$NiFe_2O_4$) by the same instrument used for determining the degradation in the photocatalytic study.

3.3. Results and Discussion

The XRD pattern as shown in Figure 3.1.(a) is consistent with the standard inverse spinel face centered cubic structure of $NiFe_2O_4$ (JCPDS Card No. 10-0325).The EDX spectrum of $NiFe_2O_4$ NPs in the inset of Figure 3.1.(a) affirms the presence of nickel, iron and oxygen. To obtain the morphology and particle size of as-synthesized $NiFe_2O_4$ NPs, we carried out TEM analysis, as shown in Figure 3.1.(b). From Figure 3.1.(c), it is apparent that the NPs have a size distribution with an average diameter of 6.8 nm. The high-resolution transmission electron microscope (HRTEM) image, as shown in Figure 3.1.(d) depicts the highly crystalline nature of the as-prepared $NiFe_2O_4$ NPs. The measured interplanar distance between lattice fringes is around 0.253 nm, which corresponds to the distance between the (311) planes of the $NiFe_2O_4$ crystal lattice.

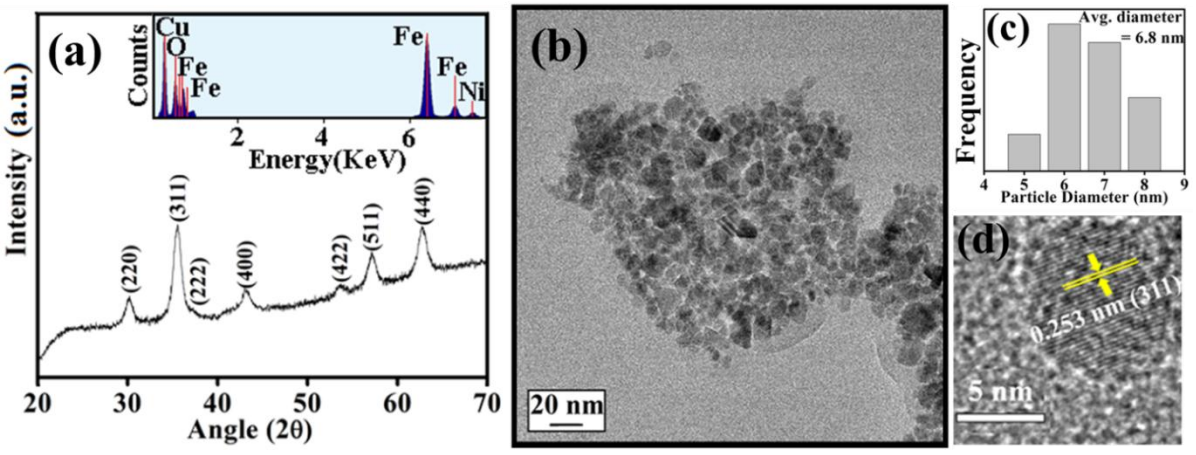

Figure 3.1: (a) XRD of the as-prepared bare $NiFe_2O_4$ NPs. Inset of (a) EDX spectrum of the NPs, indicating the presence of only Ni, Fe, and O.(b) TEM,(c) Size distribution graph, (d) HRTEM of as-prepared $NiFe_2O_4$ NPs. HRTEM image shows the crystallinity of the as-prepared $NiFe_2O_4$ NPs.

To make the $NiFe_2O_4$ NPs biocompatible and water-dispersible, we have functionalized the as-prepared NPs with the aqueous solution of a small organic ligand, Na-Tartrate. After surface functionalization, the size of the NPs was found to remain almost unchanged with an average diameter of 6.6 nm, as evident from Figure 3.2.(a) and the size distribution graph shown in Figure 3.2.(b). The HRTEM image (shown in Figure 3.2.(c)) of the functionalized NPs (T-$NiFe_2O_4$) shows its crystalline nature.

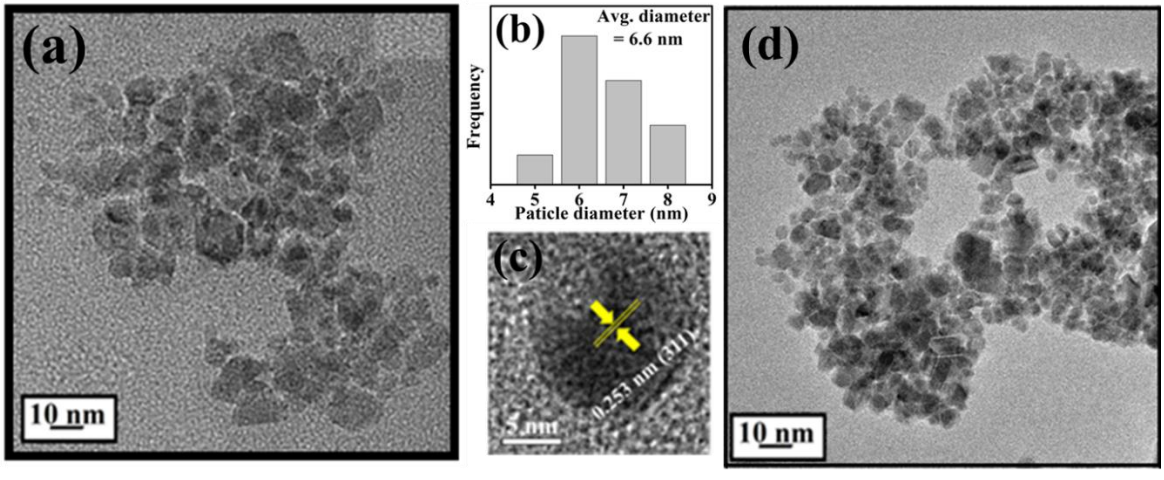

Figure 3.2: (a) TEM, (b) Size distribution graph, (c) HRTEM of water dispersible T- $NiFe_2O_4$ NPs, (d) TEM of fluorescence modified T-$NiFe_2O_4$ NPs. Size distribution graph depicts that the average particle diameter remains almost unchanged after surface modification.

Figure 3.3 shows the UV/VIS absorption spectra of Na-tartrate, T-$NiFe_2O_4$ NPs (pH ~ 7) fluorescence modified (fl. mod.) T-$NiFe_2O_4$ NPs (pH ~ 12). The UV/VIS absorption spectra clearly shows a broad spectrum around 302 nm for T-$NiFe_2O_4$ NPs where such feature was found to be absent for Na-tartrate. This clearly indicates the change in surface of the NPs'.

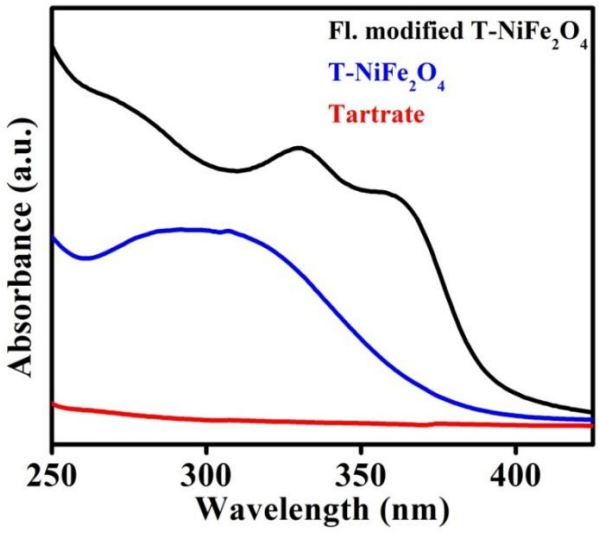

Figure 3.3: UV/VIS absorption spectra of Tartrate, T-$NiFe_2O_4$, and fluorescence modified T-$NiFe_2O_4$ NPs.

After obtaining knowledge from the UV/VIS spectra of functionalized $NiFe_2O_4$ NPs, we have performed a photoluminescence study and have observed photoluminescence at 412 nm (low intensity) on exciting the sample at wavelength of 325 nm. To intensify the photoluminescence, we carried out further surface modification by heating the functionalized $NiFe_2O_4$ NPs solution for 42 h at 70°C and pH~12 which we call fluorescence modified (fl. mod.) T-$NiFe_2O_4$ NPs. They were found to exhibit another absorption band at 365 nm in addition to the band at 325 nm as shown in Figure 3.3. The surface modification is found to result in three photoluminescence peaks with many fold increase in overall intensity, upon excitation at proper wavelengths as shown in Figure 3.4.(a), the normalized steady state photoluminescence emission spectra of fl. mod. T- $NiFe_2O_4$ NPs. This is due to an increase in the strength of the coordination between the functional groups of the ligand ($–COO^-$ and –OH

moieties) and the metal ion (Ni^{+2}) which leads to three more photoluminescence peaks as well as a huge increase in photoluminescence intensity of T-$NiFe_2O_4$ NPs. Upon exciting with wavelengths of 325, 375, 450, and 503 nm, the NPs solution gave rise to significant photoluminescence peaks at 412, 467, 530, and 603 nm, respectively. These bands are clearly distinguishable also in the excitation study as shown in Figure 3.4.(b). The fluorescence micrographs of fl. mod. T-$NiFe_2O_4$ NPs show the photoluminescent colors like blue (Figure 3.4.(c)), green (Figure 3.4.(d)) and red (Figure 3.4.(e)) on excitation of at 375, 450, and 515 nm, respectively, by using proper filters for the excitation wavelengths.

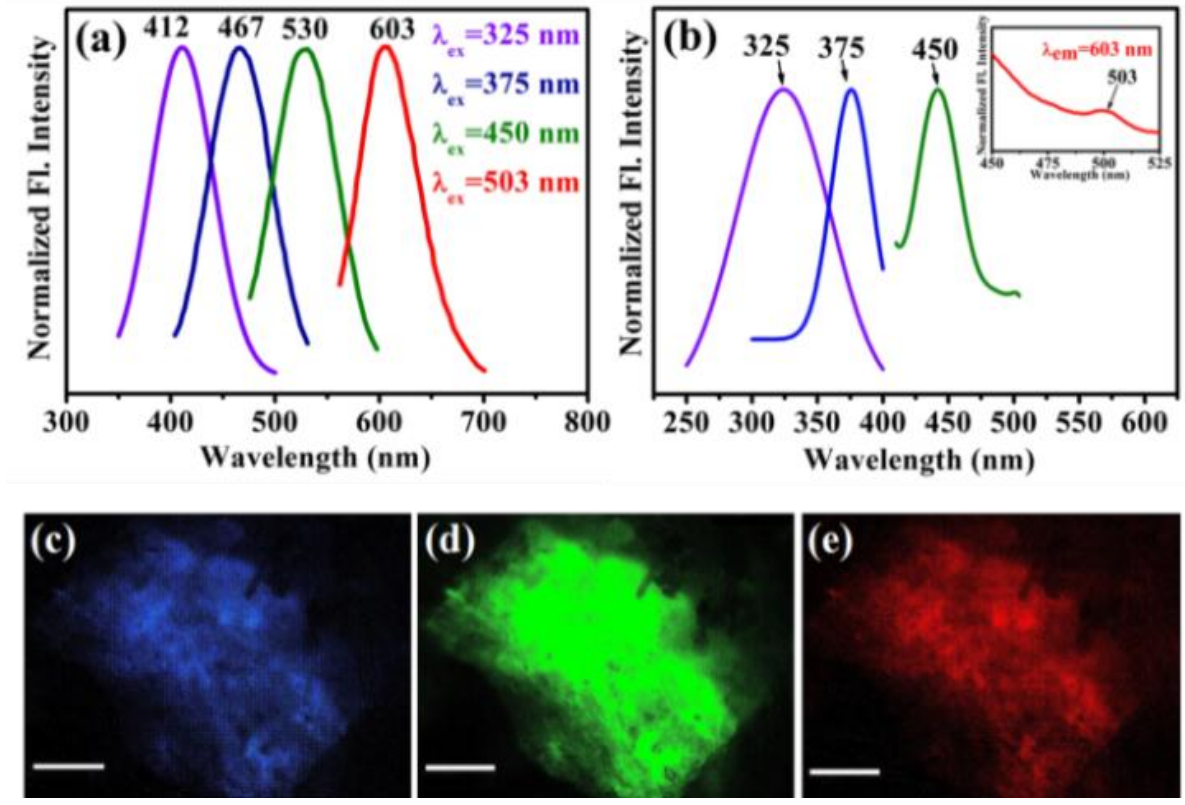

Figure 3.4: (a) Normalized steady-state fluorescence emission spectra obtained from fluorescence-modified T- $NiFe_2O_4$ NPs after excitation at four different wavelengths, λ_{ex} =325, 375, 450, and 503 nm.(b)Fluorescence excitation spectra of fluorescence-modified T-$NiFe_2O_4$ NPs at different emission maxima, that is, λ_{em}= 412, 467, 530, and 603 nm. Fluorescence images of fluorescence-modified T- $NiFe_2O_4$ NPs powder under (c) UV (375 nm), (d) blue (450 nm), and (e) green (515 nm) light irradiation. The scale bars in all images are 500 μm.

The generation of multicolor photoluminescence can be proficiently explained with the aid of The Ligand Field Theory (LFT). Based on the LFT a ligand co-ordination with the NPs' surface plays the key role, which yields the crystal field splitting energy (CFSE) (Δ) generated from d orbital splitting with a magnitude determined by the ligands and a given coordination symmetry. The strength of the metal-ligand σ bond increases as a function of increasing basicity of the solution. As the basicity of the solution increases, the 2-carboxyl and 2-hydroxyl groups become deprotonated resulting in larger interactions with the metal ions and as an outcome, CFSE (Δ) associated with the ligand increases which finally lead to an increased splitting between the previous degenerate d orbitals. The emission peaks at 467, 530 and 603 nm can be attributed to $3A_{2g}$ (F) → $3T_{1g}$ (P), $3A_{2g}$ (F) → $3T_{1g}$ (F) and $3A_{2g}$ (F) → $3T_{2g}$ (F) transitions involving d-d orbitals of Ni^{+2} ions respectively, where these energy levels were obtained from the Tanabe Sugano diagram of Ni^{+2}, shown in the Figure 3.5. These d-d transitions are formally spin allowed transitions. Note that d–d transitions involving only Fe^{+3} are not efficient for the development of such intense fluorescence [27]. On the other hand, due to strong ligand to metal charge transfer (LMCT) from HOMO (Highest Occupied Molecular Orbital, centered on the ligand) to LUMO (Lowest Unoccupied Molecular Orbital, centered on the metal ions), bonding interactions between the metal and the ligand increases considerably. Therefore, the photoluminescence peak arising at 412 nm can be attributed to LMCT involving HOMO of tartrate ligand and LUMO cantered over metal ion Ni^{+2} [28].

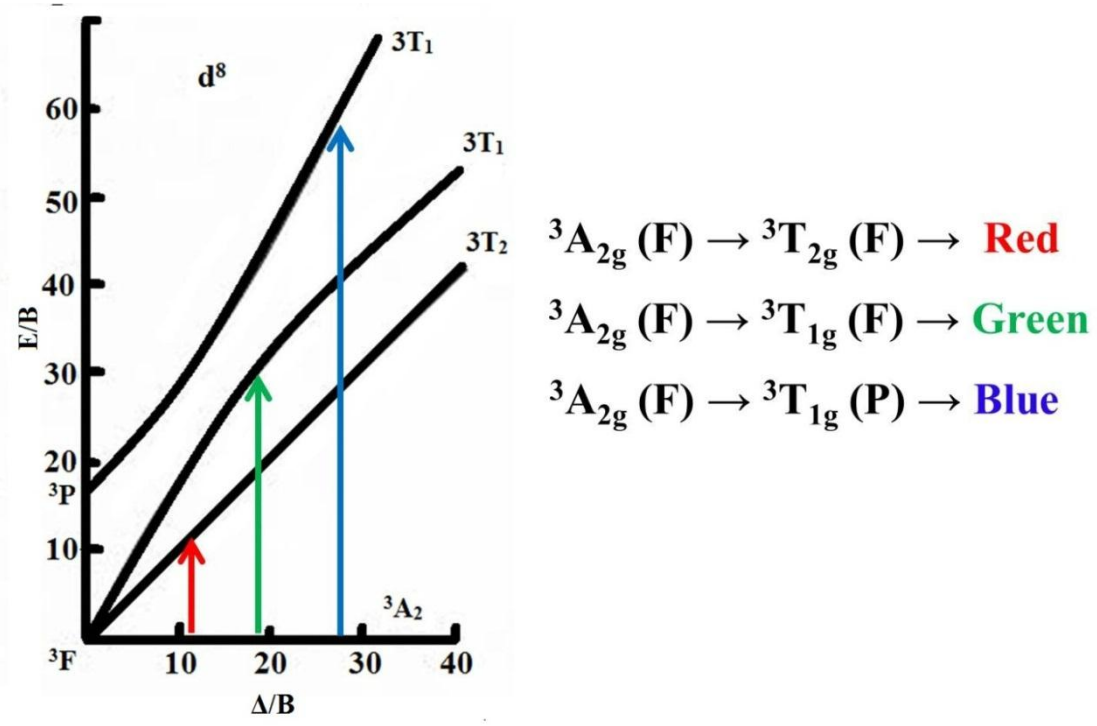

Figure 3.5: The spin-allowed transitions of d^8 system (using Tanabe-Sugano diagram) that results in fluorescence.

The fluorescence quantum yield (QY) is calculated by following the relative method, taking Rhodamine B (Rh B) as the standard fluorescent compound. As shown in the Figure 3.6, the obtained QYs are 15.13% for the 412 nm band, 1.6% for the 467 nm band and the 0.15% for 530 nm band of fl. mod. T-$NiFe_2O_4$ NPs. The quantum yield of fluorescence-modified T-$NiFe_2O_4$ NPs was measured according to A Guide to Recording Fluorescence Quantum Yields [29-30], using to the following equation:

$$\Phi_X = \Phi_{ST}\left(\frac{Grad_X}{Grad_{ST}}\right)\left(\frac{\eta_X^2}{\eta_{ST}^2}\right)$$

where, $\boldsymbol{\Phi_X}$ is the fluorescence quantum yield of the test sample we are measuring and $\boldsymbol{\Phi_{ST}}$ is the quantum yield of the standard sample. ***Grad*** refers to the gradient from the plot of fluorescence intensity against the absorbance. The **η** is the refractive index of the solvent, and the subscripts ST and X mean the standard and test sample respectively.

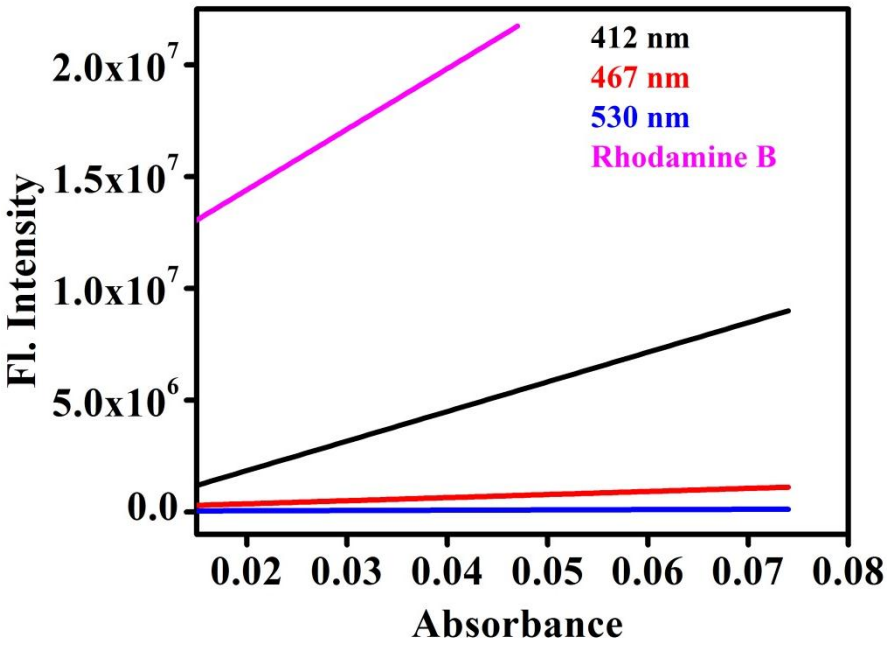

Figure 3.6: Fitting used to calculate the quantum yield (QY) of fluorescence-modified T-$NiFe_2O_4$ NPs dispersed in water. The Rhodamine B dye (Rh B) was used as a reference.

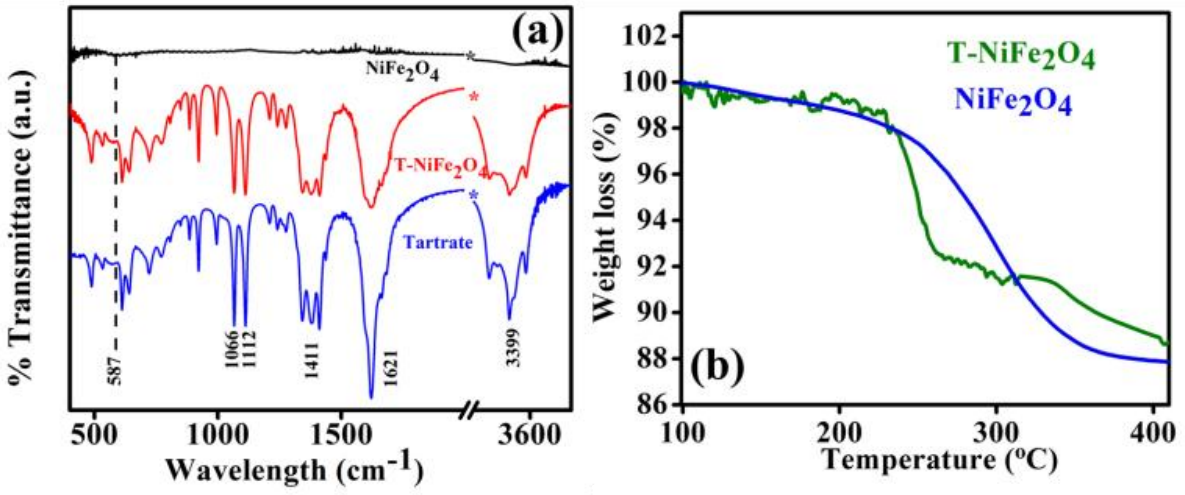

Figure 3.7: (a) FTIR spectra of as-prepared $NiFe_2O_4$ and T-$NiFe_2O_4$ NPs together with Na-tartrate alone, (b) TGA curve of as-prepared $NiFe_2O_4$ and T-$NiFe_2O_4$ NPs.

In order to verify the attachment of the tartrate molecules to the surface of $NiFe_2O_4$ NPs, we performed the FTIR study of bare $NiFe_2O_4$ NPs, T- $NiFe_2O_4$ NPs and pure tartrate ligand. For studying FTIR, we made FTIR pellets by well mixing the KBr salt and the respective NPs followed by placing the mixture in

the pelletizer. As depicted in Figure 3.7.(a), the peak arising at 587 cm^{-1} is due to stretching vibration of metal-oxygen bonds in $NiFe_2O_4$. The peak at 587 cm^{-1} is absent in T-$NiFe_2O_4$ NPs. Two sharp peaks arising at 1066 and 1112 cm^{-1} in the case of tartrate ligand are due to C–OH stretching modes [31] and two other peaks at 1411 and 1621 cm^{-1} are due to the symmetric and asymmetric stretching of the COO^- [32]. In the case of T-$NiFe_2O_4$ NPs, due to the interactions between NPs surface and the functional group moieties of the ligand, all the bands are distinctly perturbed along with the band at 3399 cm^{-1} which arises because of the stretching vibrational modes of the O–H group [31]. This clearly indicates the involvement of $–COO^-$ and –OH group in the functionalization. Thermogravimetric analysis (TGA) data of the as-prepared and tartrate functionalized Nickel ferrite measured under nitrogen atmosphere from 100 to 400°C and shown in Figure 3.7.(b). The amount of tartrate ligand bound to the nanoparticle surface was calculated from the TGA data and found to be ~ 1.88 wt% of the T- $NiFe_2O_4$ NPs.

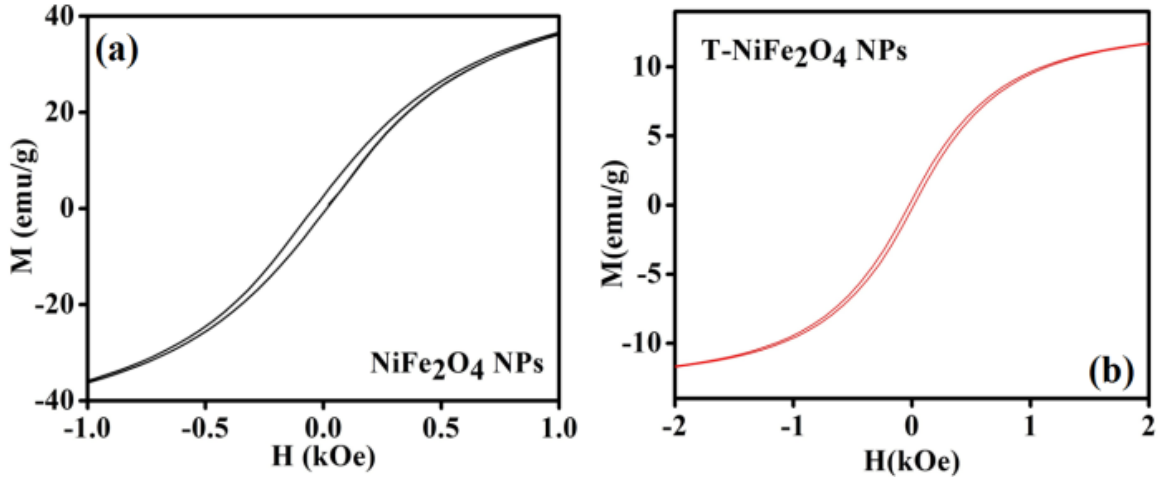

Figure 3.8: (a) Plot of magnetization versus applied magnetic field (M-H) of as-prepared $NiFe_2O_4$ NPs at 300 K, (b) M-H plot for T- $NiFe_2O_4$ NPs at 300 K.

The room temperature magnetic behavior of the as-prepared and T-$NiFe_2O_4$ NPs were studied using VSM. Figure 3.8 depicts the field dependent magnetization (M-H loops) of both as-prepared and functionalized $NiFe_2O_4$ NPs

due to the application of 14 kOe field. From Figure 3.8.(a) and 3.8.(b) it is found that the saturation magnetization and coercivity are reduced from 37.1 emu/g to 11.7 emu/g and from 0.04 kOe to 0.02 kOe, respectively, in case of T-$NiFe_2O_4$ NPs in comparison with as-prepared $NiFe_2O_4$ NPs. The tartrate ligand contains both σ donor (–OH) and π donor($–COO^-$) groups which results in immense LMCT and spin pairing of Ni^{+2} ions in T-$NiFe_2O_4$ NPs, which reduces the saturation magnetization [33].

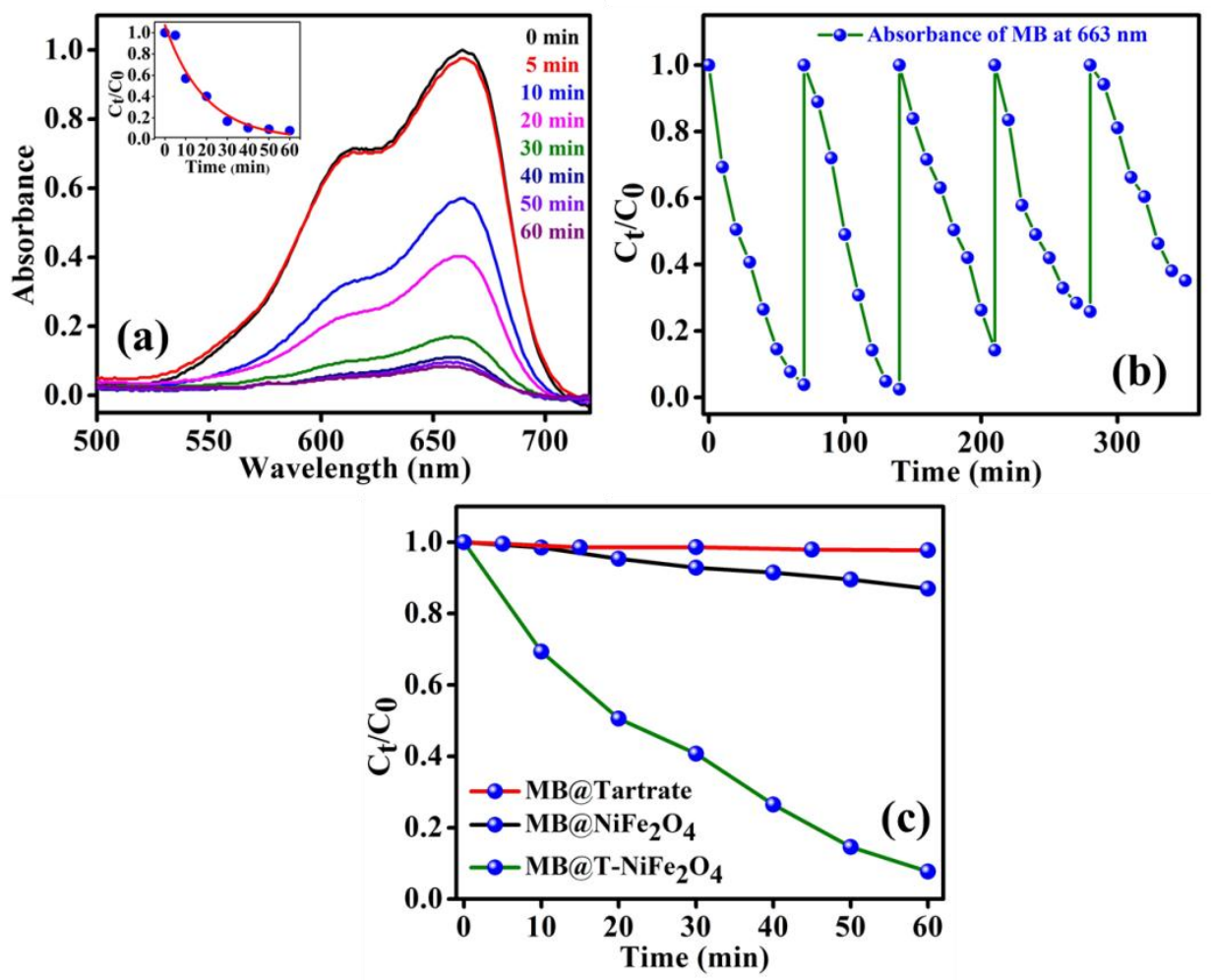

Figure 3.9: (a)The UV/Vis spectral changes of an aqueous solution of MB in the presence of T-$NiFe_2O_4$ NPs with time, under UV irradiation, (inset of (a) fitted first order reaction rate), (b) Plots of relative concentration of MB monitored at 660 nm versus time for five consecutive cycles, showing reusability of T-$NiFe_2O_4$ NPs in MB degradation under UV light, (c) The rate of photocatalytic degradation of MB (monitored at 663 nm) in presence of Na-tartrate, $NiFe_2O_4$ and T- $NiFe_2O_4$ NPs.

After efficiently incorporating the intrinsic fluorescence in $NiFe_2O_4$ NPs, we inspected the optical excitation of the functionalized $NiFe_2O_4$ NPs in photocatalysis for waste water treatment. The T-$NiFe_2O_4$ NPs were found to own efficient photocatalytic properties (as shown in Figure 3.9.(a)). In case of the degradation of MB, a frequently used dye in textile industries and a model water-contaminant, a catalytic effect occur after UV light irradiation. We found that the photodegradation of MB in presence of functionalized $NiFe_2O_4$ NPs at pH~3 takes place exponentially with time following a first-order rate equation (by fitting with equation $A=A_0e^{-kt}$) with a kinetic rate constant k = 2.82 x 10^{-2} min^{-1}. We also carried out a reusability test of the catalyst with 60 min of time interval as shown in Figure 3.9.(b). We kept adding MB up to 5 cycles by keeping the concentration of the catalyst same (by not adding more catalyst after the 1st cycle). We measured the decomposition rate of the MB by monitoring the absorbance at 663 nm by UV/Vis spectroscopy that had led to conclude the reusability of T-$NiFe_2O_4$ NPs as a catalyst. Only Na-tartrate was not found effectual to degrade MB which can be seen in Figure 3.9.(c)., where the comparative rate of degradation of MB by Na-Tartrate, bare $NiFe_2O_4$ NPs and T-$NiFe_2O_4$ NPs is shown.

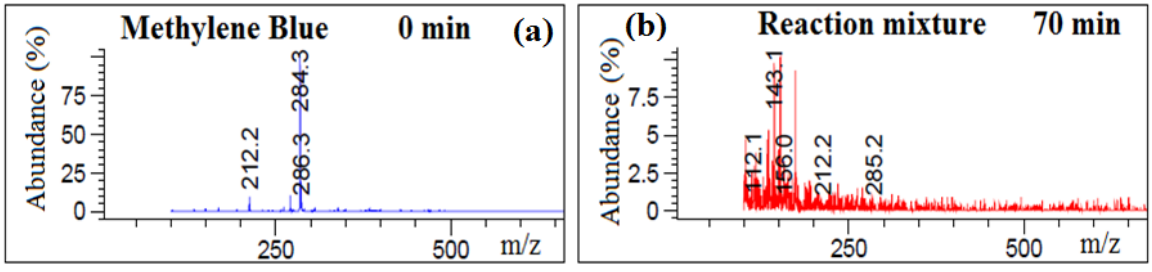

Figure3.10: LC-MS scan of MB (a) before and (b) after photocatalysis.

In order to confirm the decomposition of MB, we carried out LC-MS experiment of the MB and the reaction mixture. The peak at m/z = 284 in the Figure 3.10.(a) confirms to the presence of MB. The peaks in the Figure

3.10.(b) show the results of LC-MS study on MB (after photocatalysis) and correspond to the degraded products of MB after photocatalysis [34].

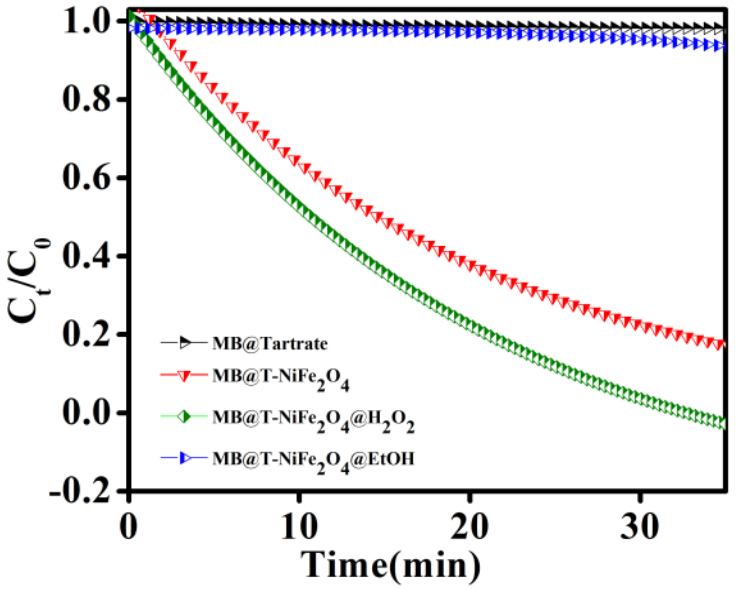

Figure 3.11: Comparative study of degradation of MB (monitored at 663nm) in presence of tartrate, T-$NiFe_2O_4$, T-$NiFe_2O_4$@H_2O_2, and T-$NiFe_2O_4$@EtOH.

To be assuring of the pathway of photocatalysis, we performed the MB degradation study in presence of radical scavenger (EtOH) and radical initiator (H_2O_2). The rate of photocatalytic degradation is expected to be slow down in the presence of EtOH if the photocatalysis follows radical pathway, then, which is a well-known radical scavenger. On the other hand, the rate of photocatalytic degradation should increase in presence of H_2O_2, a known radical initiator. From the Figure 3.11, it is clearly evident that the radical initiator has facilitated the decomposition of MB while the radical scavenger slowed down the reaction rate. We found that in presence of H_2O_2 the reaction rate is increased to 9.8 x 10^{-2} min^{-1} and in presence of ethanol the reaction rate is dropped to 4.7 x 10^{-3} min^{-1}, which confirmed that the photocatalytic degradation of MB by T-$NiFe_2O_4$ NPs follows the Reactive oxygen species (ROS) pathway [35]. The mechanism (shown in Figure 3.12) undergoes the following steps:

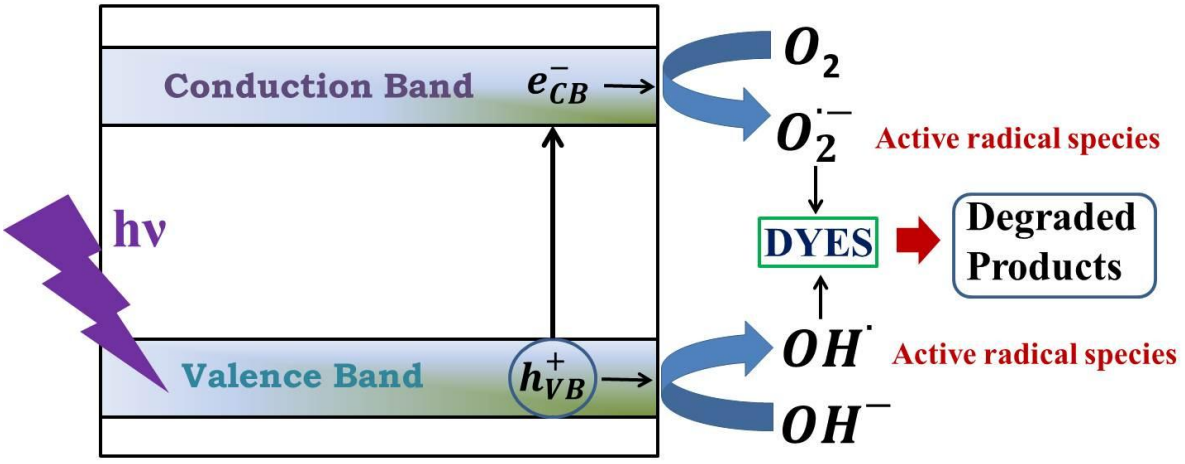

Figure 3.12: Schematic diagram of degradation pathway of MB by T-$NiFe_2O_4$.

1. Absorption of photon by metal oxide

$$\boldsymbol{Metal\ Oxide} + h\upsilon \rightarrow \boldsymbol{e^-_{CB}} + \boldsymbol{h^+_{VB}}$$

2. Oxygen Ionosorption

$$\boldsymbol{O_2} + \boldsymbol{e^-_{CB}} \rightarrow \boldsymbol{O_2^{\cdot -}}$$

3. Neutralization of OH^- groups by photoholes which produces $\boldsymbol{OH^{\cdot}}$ radicals

$$(\boldsymbol{H_2O} \rightarrow \boldsymbol{H^+ + OH^-})\ \boldsymbol{H^+ + OH^- + h^+_{VB} \rightarrow H^+ + OH^{\cdot}}$$

4. Neutralization of $O_2^{\cdot -}$ by protons

$$\boldsymbol{O_2^{\cdot -} + H^+ \rightarrow HO_2^{\cdot}}$$

5. Transient hydrogen peroxide formation and dismutation of oxygen

$$\boldsymbol{2HO_2^{\cdot} \rightarrow H_2O_2 + O_2}$$

6. Decomposition of $\boldsymbol{H_2O_2}$ and second reduction of oxygen

$$\boldsymbol{H_2O_2 + e^- \rightarrow OH^{\cdot} + OH^-}$$

7. Oxidation of the dye via successive attacks by $\boldsymbol{OH^{\cdot}}$ radicals

$$\boldsymbol{R + OH^{\cdot}} \rightarrow \textbf{degradation products}$$

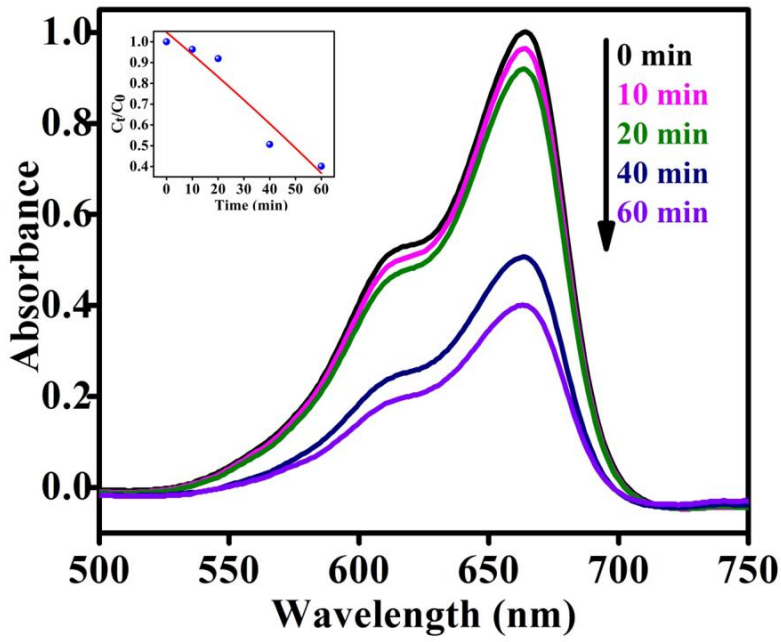

Figure 3.13: The UV/Vis spectral changes of an aqueous solution of MB in the presence of T-$NiFe_2O_4$ NPs with time, under UV irradiation at pH 7, (in the inset the fitted first order reaction rate),

The degradation of Methylene blue (MB), which is a cationic dye, occurs through the adsorption of the dye to the surface of the catalyst. The cationic dye is easily attracted and attached to the surface of the catalyst as the NP's are functionalized by negatively charged tartrate ions. This attachment helps to degrade the dye faster. As the catalytic property of the tartrate functionalized nickel ferrite does not change significantly up to several cycles, we can infer that no significant amount of tartrate leaching is occurred. From the Figure 3.13., it is evident that at pH 7 the rate of degradation is decreased significantly. The rate of degradation was found (k) to be 2.59 x 10^{-3} min^{-1}, which is 11 times slower than the rate in pH 3. At higher pH, the availability of OH^- ions increases, which in results competes with the electron reach dye to get attached on the NP's surface. Also the attachment of OH^- ions to the surface of NP's makes the surface negatively charged which obstructs the electron rich dye to approach and results in the fall of the rate degradation happens.

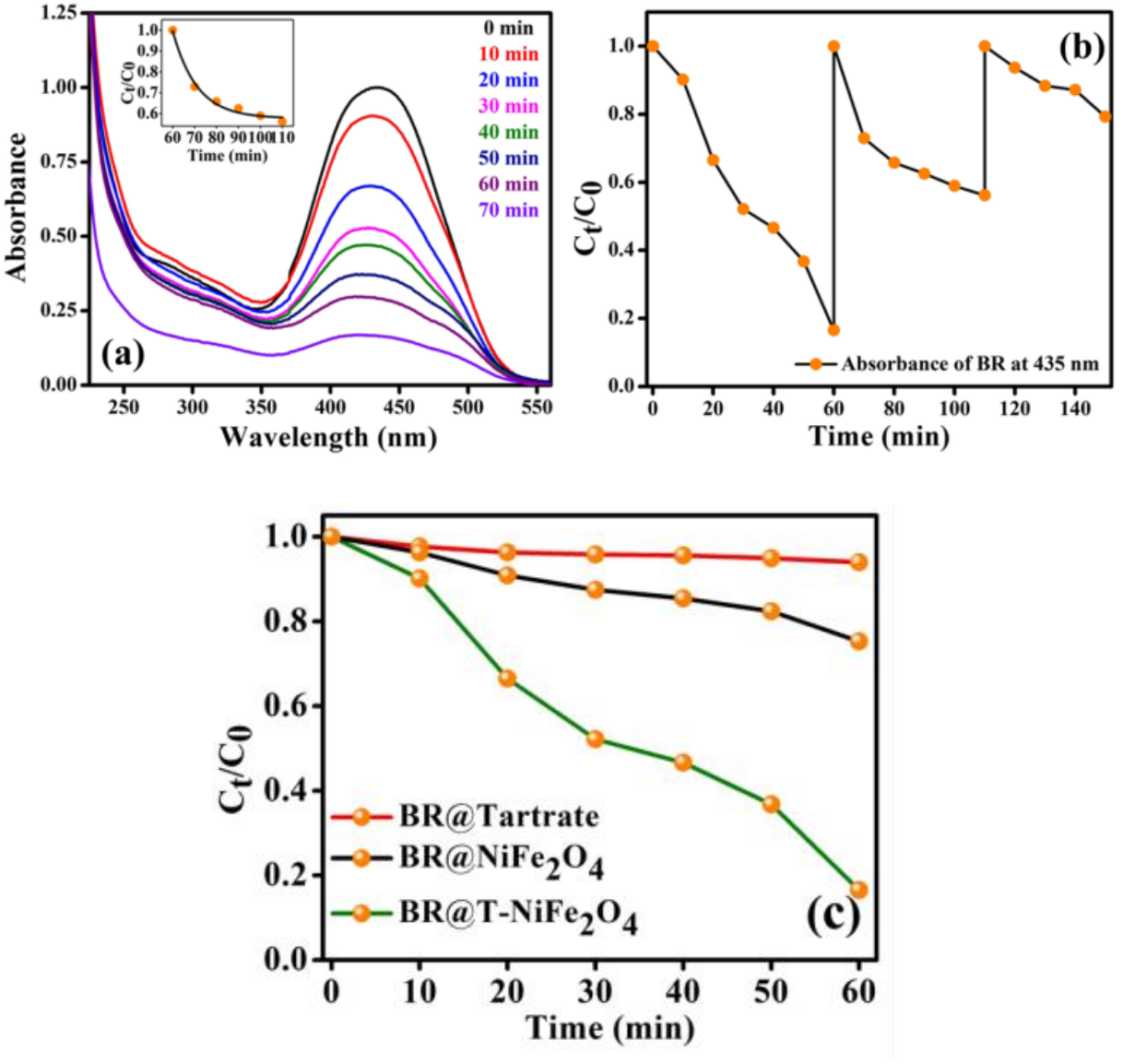

Figure 3.14: (a) The UV/Vis spectral changes of an aqueous solution of BR in the presence of T- $NiFe_2O_4$ NPs with time, (inset of (a) fitted first order reaction rate) (b) Plots of the relative concentration of BR monitored at 435 nm versus time for five consecutive cycles, showing reusability of T- $NiFe_2O_4$ NPs in the degradation of BR, (c) The rate of catalytic degradation of BR (monitored at 435 nm) in presence of Na-tartrate, $NiFe_2O_4$ and T- $NiFe_2O_4$ NPs.

Stimulated by the photocatalytic property of the functionalized $NiFe_2O_4$ NPs on MB, we have performed similar experiment on a biologically toxic pigment, BR which is responsible for the occurrence of yellow coloration of skin in jaundice. T-$NiFe_2O_4$ NPs shows a good catalytic activity in the degradation of BR without any photoexcitation at pH ~ 7 at room temperature as shown in Figure

3.14.(a). The reaction follows first order kinetics with the reaction rate constant $k = 6.5 \times 10^{-3}$ min^{-1}. We investigated the recyclability of the catalytic efficiency of T-$NiFe_2O_4$ for degradation of BR by adding the same amount of BR to the reaction mixture in every 60 min up to 3 cycles, keeping the concentration of the catalyst unchanged. We measured the fall in absorbance of the BR at 435 nm at regular intervals by UV/Vis spectroscopy. The plot of relative BR concentration as a function of time for up to three consecutive cycles, as demonstrated in Figure 3.14.(b), confirms the reusability of the $NiFe_2O_4$ NPs catalyst. Figure 3.14.(c) depicts the comparative rate of degradation of BR by Na-Tartrate, bare $NiFe_2O_4$ NPs and T-$NiFe_2O_4$ NPs which indicates the incapability of pure Na-tartrate to degrade BR.

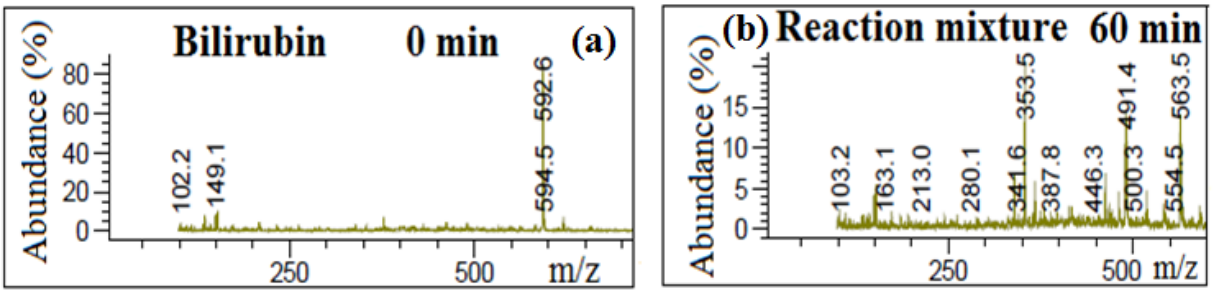

Figure 3.15: LC-MS scan of BR (a) before and (b) after catalysis.

To be assured of the degradation of RB, LC-MS experiment of the BR and the reaction mixture was carried out. The peak at m/z = 594 in the Figure 3.14.(a) corresponds to the presence of Bilirubin only. The peaks in the Figure 3.15.(b) show the results of LC-MS study on BR (after catalysis) and correspond to the degraded products of BR after catalysis [37]. The degradation pathway proceeds through oxidation of BR via reactive oxygen species (ROS) [38-39].

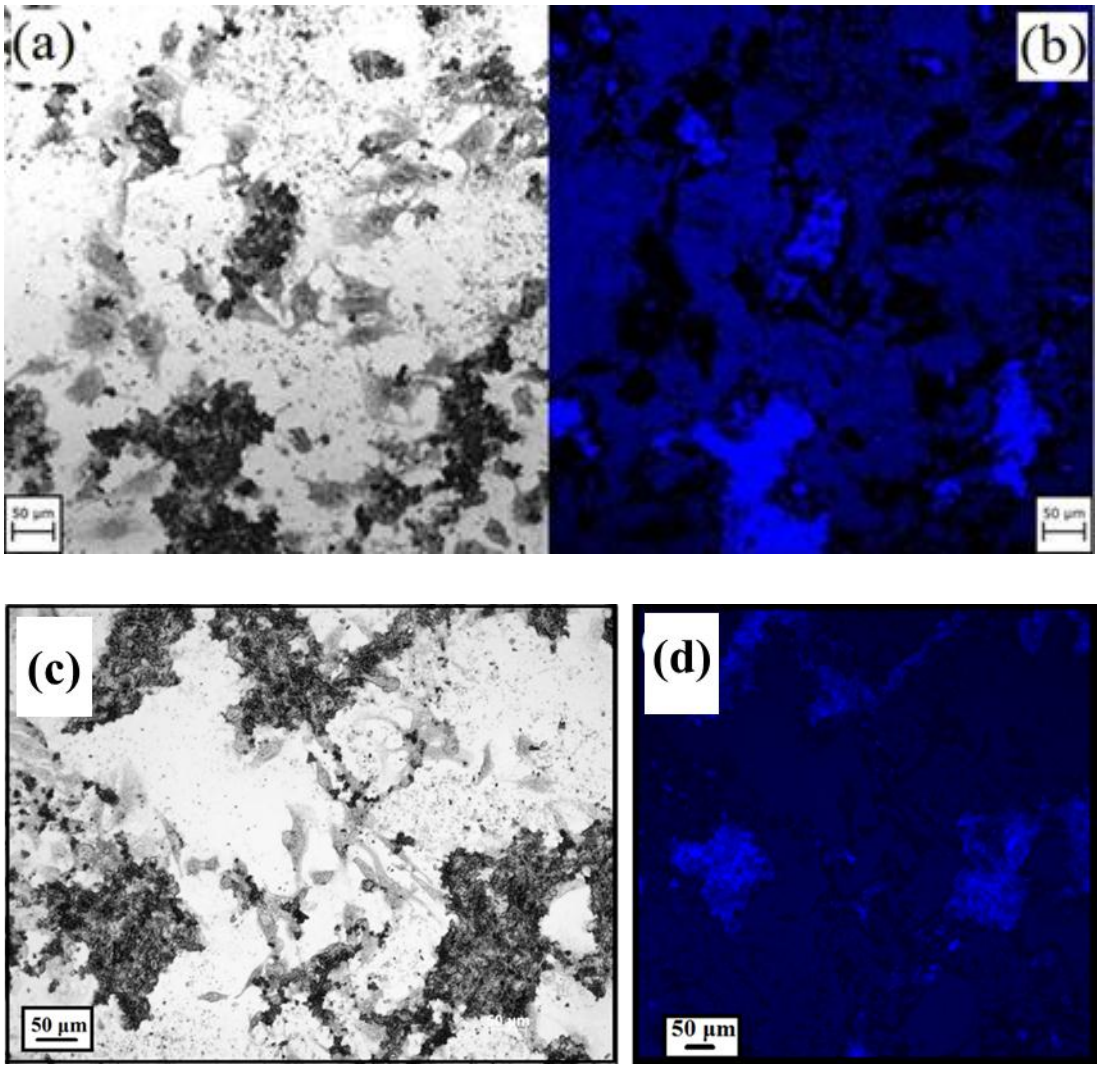

Figure 3.16: Osteosarcoma cells with T-$NiFe_2O_4$ NPs at a concentration of 2 mg/ml cell medium in (a), (c) bright field and (b), (c) LSM with an excitation wavelength of 370 nm.

Figure 3.16 shows human osteosarcoma cells in the presence of culture medium with a NP concentration of 2 mg/ml. From the Figure 3.16.(a) and 3.16.(c), it can be deduced that the cells are alive and in a good condition indicating the non-toxicity of the NPs. Figure 3.16.(b) and 3.16.(d) shows that NPs stick to cells and fluoresce under illumination with light of appropriate wavelength and intensity.

3.4. Conclusion

Through easy surface modification of $NiFe_2O_4$ NPs with Na-tartrate ligands, we have prepared biocompatible multifunctional nanoparticles with intrinsic fluorescence properties covering the whole visible region, ranging from blue, and green, to red. The NPs are found to be efficient in cell imaging using this inherent fluorescent property. Additionally, the T-$NiFe_2O_4$ NPs show good catalytic and photocatalytic activity in the degradation of biologically and environmentally toxic pigments [Bilirubin and Methylene blue] respectively. A thorough experimental and theoretical study has revealed that the LMCT transition from the highest occupied energy level of the tartrate ligand to lowest unoccupied energy levels of Ni^{+2} and d–d transitions centered over Ni^{+2} ions on the NPs' surface play crucial roles in the generation of multicolor fluorescence from the T- $NiFe_2O_4$ NPs. We trust that the development of these multifunctional T-$NiFe_2O_4$ NPs will open new opportunities in the field of diagnostics, such as bio-imaging, therapeutics and drug delivery, as well as in wastewater treatment of contaminants.

Bibliography

1. H. Goesmann, C. Feldmann, *Nanoparticulate Functional Materials*, **Angew. Chem., Int. Ed**., 2010, 49, 1362-1395.

2. M.W. Tibbitt, J.E. Dahlman, R. Langer, *Emerging Frontiers in Drug Delivery*, **J. Am. Chem. Soc.**, 2016, 138, 704-717.

3. M.P. Nikitina, T.A. Zdobnovaa , S.V. Lukasha, O.A. Stremovskiya, S.M. Deyeva, *Protein-assisted self-assembly of multifunctional nanoparticles*, **PNAS**, 2010, 107, 5827–5832.

4. OV Salata, *Applications of nanoparticles in biology and medicine*, **J. Nanobiotechnology**, 2004, 2, 1-6.

5. L.H. Reddy, J.L. Arias, J. Nicolas, P. Couvreur, *Magnetic Nanoparticles: Design and Characterization, Toxicity and Biocompatibility, Pharmaceutical and Biomedical Applications*, **Chem. Rev.**, 2012, 112, 5818-5878.

6. A.K. Gupta, M. Gupta, *Synthesis and surface engineering of iron oxide nanoparticles for biomedical applications*, **Biomaterials**, 2005, 18, 3995-4021.

7. R. Rakshit, M. Pal, A. Chaudhuri, K. Mandal, *Research Update: Facile synthesis of $CoFe_2O_4$ nano-hollow spheres for efficient bilirubin adsorption*, **APL Mat.**, 2015, 3, 110701-110706.

8. M. Colombo, S. Carregal-Romero, M.F. Casula, L. Gutiérrez, M.P. Morales, I.B. Böhm, J.T. Heverhagen, D. Prosperi, W.J. Parak, *Biological applications of magnetic nanoparticles*, **Chem. Soc. Rvw**., 2012, 41, 4306-4334.

9. F. Yang, Y. Li, Z. Chen, Y. Zhang, J. Wu, N. Gu, *Superparamagnetic iron oxide nanoparticle-embedded encapsulated microbubbles as dual contrast agents of magnetic resonance and ultrasound imaging*, **Biomaterials**, 2009, 30, 3882-3890.

10. H.B. Na, I.C. Song, T. Hyeon, *Inorganic Nanoparticles for MRI Contrast Agents*, **Adv. Mater**., 2009, 21, 2133–2148.

11. O. Veiseh, J.W. Gunn, M. Zhang, *Design and fabrication of magnetic nanoparticles for targeted drug delivery and imaging*, **Adv. Drug Deliv. Rev**., 2010, 62, 284-304.

12. M. Liong, J. Lu, M. Kovochich, T. Xia, S.G. Ruehm, A.E. Nel, F. Tamanoi, J.I. Zink, *Multifunctional inorganic nanoparticles for imaging, targeting, and drug delivery*, **ACS Nano**, 2008, 2, 889-896.

13. D.L.J. Thorek, A.K. Chen, J. Czupryna, A. Tsourkas, *Superparamagnetic iron oxide nanoparticle probes for molecular imaging*, **Ann. Biomed. Eng**., 2006, 34, 23-38.

14. C.S.S.R. Kumar, F. Mohammad, *Magnetic nanomaterials for hyperthermia-based therapy and controlled drug delivery*, **Adv. Drug Deliv. Rev**., 2011, 63, 789–808.

15. M. Tamura, F. Yanagawa, S. Sugiura, T. Takagi, K. Sumaru, H. Matsui, T. Kanamori, *Optical cell separation from three-dimensional environment in photodegradable hydrogels for pure culture techniques*, **Sci. Rep**., 2014, 4, 4793-4798.

16. N. Tran, T.J. Webster, *Nanotechnology for bone materials*, **Wiley Interdiscip. Rev. Nanomed. Nanobiotechnol.,** 2009, 1, 336-351.

17. M. Johannsen, U. Gneveckow, L. Eckelt, A. Feussner, N. Waldöfner, R. Scholz , S. Deger, P. Wust, S.A. Loening, A. Jordan, *Clinical hyperthermia of prostate cancer using magnetic nanoparticles: presentation of a new interstitial technique*, **Int. J. Hyperthermia**., 2005, 21, 637-647.

18. Y. Li, H. Tan, X.Y. Yang, B. Goris, J. Verbeeck, S. Bals, P. Colson, R. Cloots, G.V. Tendeloo, B.L. Su, *Well Shaped Mn_3O_4 Nano-octahedra with Anomalous Magnetic Behavior and Enhanced Photodecomposition Properties*, **Small**, 2011, 7, 475-483.

19. P. Zhang, Y. Zhan, B. Cai, C. Hao, J. Wang, C. Liu, Z. Meng, Z. Yin, Q. Chen, *Shape-controlled synthesis of Mn_3O_4 nanocrystals and their catalysis of the degradation of methylene blue*, **Nano. Res**., 2010, 3, 235-243.

20. M.B. Gawande, V.D.B. Bonifacio, R.S. Varma, I.D. Nogueira, N. Bundaleski, C.A.A. Ghumman, O.M.N.D. Teodoro, P.S. Branco, *Magnetically recyclable magnetite–ceria (Nanocat-Fe-Ce) nanocatalyst–applications in multicomponent reactions under benign conditions*, **Green. Chem**., 2013, 15, 1226–1231.

21. M.B. Gawande, A.K. Rathi, I.D. Nogueira, R.S. Varma, P.S. Branco, *Magnetite-supported sulfonic acid: a retrievable nanocatalyst for the Ritter reaction and multicomponent reactions*, **Green. Chem**., 2013, 15, 1895-1899.

22. M.B. Gawande, P.S. Branco, R.S. Varma, *Nano-magnetite (Fe_3O_4) as a support for recyclable catalysts in the development of sustainable methodologies*, **Chem. Soc. Rev.**, 2013, 42, 3371-3393.

23. M. Pal, A.K. Singh, R. Rakshit, K. Mandal, *Surface chemistry modulated introduction of multifunctionality within Co_3O_4 nanocubes*, **RSC Adv**., 2015, 5, 16311-16318.

24. M. Pal, R. Rakshit, K. Mandal, *Facile functionalization of Fe_2O_3 nanoparticles to induce inherent photoluminescence and excellent photocatalytic activity*, **Appl. Phys. Lett.**, 2014, 104, 233110-233114.

25. X. Ren, L. Tong, X. Chen, H. Ding, X. Yang, H. Yang, *Deposition of luminescent $Y_2O_3:Eu^{3+}$ on ferromagnetic mesoporous $CoFe_2O_4@mSiO_2$ nanocomposites*, **Phys. Chem. Chem. Phys**., 2014, 16, 10539-10547.

26. S. Sun, H. Zeng, D.B. Robinson, S. Raoux, P.M. Rice, S.X. Wang, G. Li, *Monodisperse MFe_2O_4 (M = Fe, Co, Mn) Nanoparticles*, **J. Am. Chem. Soc.**, 2004, 126, 273-279.

27. J.E. Huheey, E.A. Keiter, R.L. Keiter, O.K. Medhi, *Inorganic Chemistry: Principles of Structure and Reactivity (Fourth Edition)*, **Pearson Education**: 2006.

28. M. Pal, R. Rakshit, K. Mandal, *Surface Modification of $MnFe_2O_4$ Nanoparticles to Impart Intrinsic Multiple Fluorescence and Novel Photocatalytic Properties*, **ACS Appl. Mater. Interface**., 2014, 6, 4903-4910.

29. A.T.R. Williams, S.A. Winfield, *Relative Fluorescence Quantum Yields Using a Computer-controlled Luminescence Spectrometer*, **Analyst**, 1983, 108, 1067-1071.

30. H.J. Yvon, *A guide to recording fluorescence quantum yields*, **HORIBA Scientific**, 2012.

31. N. Kaneko, M. Kaneko, H. Takahashi, *Infrared and Raman spectra and vibrational assignment of some metal tartrates*, **Spectrochim. Acta Part A**, 1984, 40, 33-42.

32. V. Ramakrishnan, J.M.T. Maroor, *IR and Raman studies of gel grown manganese tartrate*, **Infrared Phys**., 1988, 28, 201-204.

33. R. Rakshit, M. Pal, M. Mandal, K. Mandal, *Charge transfer mediated magnetic response of cobalt ferrite nanoparticles*, **Mater. Lett.**, 2015, 151, 64-67.

34. W. M. A. El Rouby, A. A. Farghali and A. Hamdedein, *Microwave synthesis of pure and doped cerium (IV) oxide (CeO2) nanoparticles for methylene blue degradation*, **Water Sci. Technol.**, 2016, 74, 2325-2336.

35. A. Houas, H. Lachheb, M. Ksibi, E. Elaloui, C. Guillard, J.M. Herrmann, *Photocatalytic degradation pathway of methylene blue in water*, **Appl. Catal., B**, 2001, 31, 145–157.

36. K. R. Kranc, G. J. Pyne, L. Tao, T. D. W. Claridge , D. A. Harris , T. A. D. Cadoux-Hudson, J. J. Turnbull, C. J. Schofield, J. F. Clark, *Oxidative degradation of bilirubin produces vasoactive compounds*, **Eur. J. Biochem**., 2000, 267, 7094-7101.

37. M. Pal, A. Kundu, R. Rakshit, K. Mandal, *Ligand-Induced Evolution of Intrinsic Fluorescence and Catalytic Activity from Cobalt Ferrite Nanoparticles*, ChemPhysChem, 2015, 16, 1627-1634.

38. W.L. Wurster, G.J. Pyne-Geithman, I.R. Peat, J.F. Clark, *Bilirubin oxidation products (BOXes): synthesis, stability and chemical characteristics*, **Acta Neurochir Suppl.**, 2008, 104, 43–50.

Chapter 4

Surface Modification of $CoFe_2O_4$ Nano-Hollowspheres

This chapter demonstrates the improvement of fluorescence and magnetic property upon surface modification strategy of $CoFe_2O_4$ nano-hollowspheres due to the hollow structure and incorporation of Co within the system. Moreover, we have shown excellent photocatalytic property of surface modified $CoFe_2O_4$ nano-hollowspheres.

4. Surface Modification of Cobalt Ferrite ($CoFe_2O_4$) Nano-Hollowspheres for Intrinsic Polychromatic Photoluminescence and Enhanced Photoatalytic Activities

4.1 Preamble

Nanostructures (NSs), compared with bulk materials have distinctive and novel properties and therefore offer great openings for development of new industrial applications. Many nanostructures (NSs) are already in use or have potential to be widely used in a range of applications [1-5]. From last two decades, fabrication of magnetic nanostructures and design them to attain desired morphology has become a subject of great interest. It has been found that materials having building blocks with same configuration but different morphology can have different properties. Throughout last few years, the researchers have developed various synthesizing routes to synthesize different nanostructures (NSs) such as sphere, rod, wire, chain, disc, tiles, etc., and they have found different features for different morphologies. Recently, inorganic hollow nanostructures with defined structure, composition, and tailored properties have attracted substantial attention [6-8].

The magnetic nanomaterials, nano-hollow spheres (NHSs) are found to be very promising because of their high magnetic saturation, large surface area, low density, ability to withstand volume changes due to temperature and pressure and large pore volume, which enable them to be used in wide varieties of applications in the fields of biomedical research [9], energy storage [10], high frequency magnetic devices [11] and chemical sensors [12]. The cavity inside and large surface enhances their capability of capturing and delivering drugs and other materials and their usability in Hydrogen evolution reaction [13], oxidation of organic pollutants [14], super capacitors [15], Li ion battery [16-

18], gas sensing [19-20], anti-bacterial activities [21] and in-vivo cancer treatment [22-23]. Though by definition, the nanomaterials should have dimensions ≤100 nm, in the field of drug delivery comparatively bigger (>100 nm) nanomaterials are desired for loading sufficient amount of drugs. NHSs serve this purpose as they, with size >100 nm, may also behave like nanomaterials because of their shell thickness <100 nm.

Functionalized nanostructures are very promising for applications in catalysis, biolabeling, and bioseparation. Multifunctional nanomaterials with good magnetic and fluorescent properties are in high demand in biomedical applications. There are two methods frequently used for synthesizing magneto-fluorescent nanomaterials, (i) by making nanocomposites with quantum dots (QDs) and (ii) by coating the nanomaterials with fluorescent dyes. Disadvantages like photobleaching properties of fluorescent dyes, chemical instability and toxic effects of the QDs (owing to the presence of heavy metals like Cd^{+2}, Pb^{+2}) [24], their applications are lessened towards the biomedical application. In order to make the nanomaterials biocompatible, surface modifications were done by biomolecules like proteins, DNA, RNA, and polymers, but they failed to induce inherent fluorescence. However we successfully developed biocompatible magnetic nanoparticles with intrinsic fluorescence [25] but their magnetic properties were not up to the mark due to their surface modification and small size. Therefore, in our present work, we prepared of $CoFe_2O_4$ NHS (>100 nm) as a magneto-fluorescent material with better fluorescence and magnetic properties compared to their solid particle counterpart.

Among the all other ferrites, $CoFe_2O_4$ got popularity because of its high saturation magnetization, high coercivity, chemical and physical stability, which give rise to the wide applications in the fields such as biomedical research,

energy storage. We efficaciously generated inherent photoluminescence by modifying the surface of $CoFe_2O_4$ NHSs with Sodium tartrate ligand. Additionally, we tested the photocatalytic capability of the surface modified $CoFe_2O_4$ NHSs in the degradation of water contaminants like methylene blue (MB) and rhodamine b (Rh B). Through the orderly investigations, we found that ligand to metal charge transfer and d-d transitions are responsible for the generation of multicolor photoluminescence which was explained by the ligand field theory (LFT).

4.2. Experiment

4.2.1 Materials Used

Iron chloride hexahydrate [$FeCl_3.6H_2O$], Cobalt chloride hexahydrate [$CoCl_2.6H_2O$], Ethylene Glycol, Urea [$CO(NH_2)_2$], Oleylamine are obtained from Sigma-Aldrich. The dyes, methylene blue (MB) and rhodamine b (Rh B) are also bought from Sigma-Aldrich. Tartaric acid, Ethyl Alcohol [EtOH] and Sodium Hydroxide [NaOH] are purchased from Merck.

4.2.2 Synthesis and Experimental Procedure

We synthesized $CoFe_2O_4$ NHSs by solvothermal method. A solution mixture of Iron (III) chloride hexahydrate, Cobalt (II) chloride hexahydrate, Ethylene Glycol, Urea, Ethanol and Oleylamine was heated in a Teflon lined stainless steel autoclave at 200°C for 20 h in an oven. Then the as-prepared $CoFe_2O_4$ NHSs were washed by ethanol and collected after centrifugation. The removal of the mother solution was done by heating on a hotplate at a temperature of 80°-90°C for 30 min. The Ostwald ripening process has been proposed as a template-free strategy and is used more and more to fabricate inorganic hollow spheres.

The basic principle of the inside-out Ostwald ripening process is that the larger crystals grow from those of smaller size, which have higher solubility than the larger ones. Within a colloidal aggregate, smaller, less crystallized, or less dense crystallites will dissolve into the liquid phase as a nutrient supply for the growth of larger, better crystallized, or denser ones. When the crystals grow in solution, the concentration of growth units varies across the mother solution, due to the size difference of resultant nanocrystals. With the driving force of the minimization of surface energy, metastable nanoparticle aggregates occur first due to the reduction of supersaturation in solution. Once the particles with different sizes are attached to each other, the large particles begin to grow, drawing from smaller ones. Voids gradually form and grow in the cores of large aggregates, and the shell thickness increases owing to the outward diffusion of solutes through the permeable shell.

For the purpose of surface modification of the as-prepared $CoFe_2O_4$ NHSs with tartrate ligands, we cyclomixed the NHSs with a 0.5M Na-tartrate solution (pH~7) at room temperature for 12 h. We obtained a light brown solution of tartrate-functionalized $CoFe_2O_4$ NHSs, and named as T-$CoFe_2O_4$ NHSs.

The X-ray powder diffraction (XRD) of as-prepared $CoFe_2O_4$ NHSs was done using Rikagu miniflex II diffractometer equipped with Cu Kα radiation (at 40 mA and 40 kV) at the scanning rate of 3° per minute in the 2θ range of 20°-70°. A FEI QUANTA FEG 250 field-emission high-resolution scanning electron microscope (FESEM), operated at 5-10 kV was used to study the size, shape, morphology, and size distribution and to record the Energy-dispersive X-ray analysis (EDX) spectrum of the as-prepared and functionalized $CoFe_2O_4$ NHSs. The Ultraviolet-visible (UV/Vis) absorbance spectra of T-$CoFe_2O_4$ NHSs were obtained on a Shimadzu UV-2600 spectrophotometer, using a quartz cuvette of 1 cm path length. To carry out the steady state photoluminescence excitation

and emission study of T-$CoFe_2O_4$ NHSs a Horiba JovinYvon Model Fluorolog fluorometer was used. Fluorescence micrographs of $CoFe_2O_4$ NHSs were captured using a Leica DM1000 LED fluorescence microscope.

FTIR (Fourier transform infrared spectroscopy) measurements were performed using a JASCO FTIR-6300 spectrometer to ensure of the attachment of tartrate molecules to the NHSs' surface. For FTIR study, pellets were made by placing the homogeneous mixture of lyophilized T-$CoFe_2O_4$ NHSs powder samples and KBr (using the ratio 1:4 respectively) under the pelletizer. The background was corrected using a reference KBr pellet. For magnetic measurements of as-prepared $CoFe_2O_4$ NHSs and T-$CoFe_2O_4$ NHSs, a Lake Shore VSM equipped with an electromagnet was used.

Two UV lamps with different wavelength (253 nm and 360 nm) were used in the photocatalytic study. The aqueous solution of T-$CoFe_2O_4$ NHSs (50μL) and 10μM aqueous solution of Methylene Blue (MB) (pH~3) and Rhodamine B (Rh B) (pH~3) were homogenously mixed in a quartz cuvette for 1h in the dark. Then, the cuvette was kept 2 cm away from the UV light source and the absorbance spectra of MB and Rh B in presence of T-$CoFe_2O_4$ NHSs solution were measured from time to time by using UV/Vis spectrophotometer.

4.3. Results and discussion

Figure 4.1.(a) shows the XRD pattern of the as prepared $CoFe_2O_4$ NHSs which confirms that all the peaks perfectly match with the cubic inverse spinel structure of $CoFe_2O_4$ NHSs, as reported in the literature (JCPDS file no. 22–1086). The EDX (energy dispersive X-ray) spectra in the Figure 4.1.(b) confirms the presence of Co, Fe and O in $CoFe_2O_4$ NHSs. Crystallite size of the particles (~ 40 nm) has been calculated taking three peaks from XRD using Scherer formula, $d = (k.\lambda)/(\beta.\cos\theta)$, where d is particle size, k is structural

constant (0.94), λ is working wave length, β is the FWHM of the selected peak in radians, θ is the peak angle in degrees.

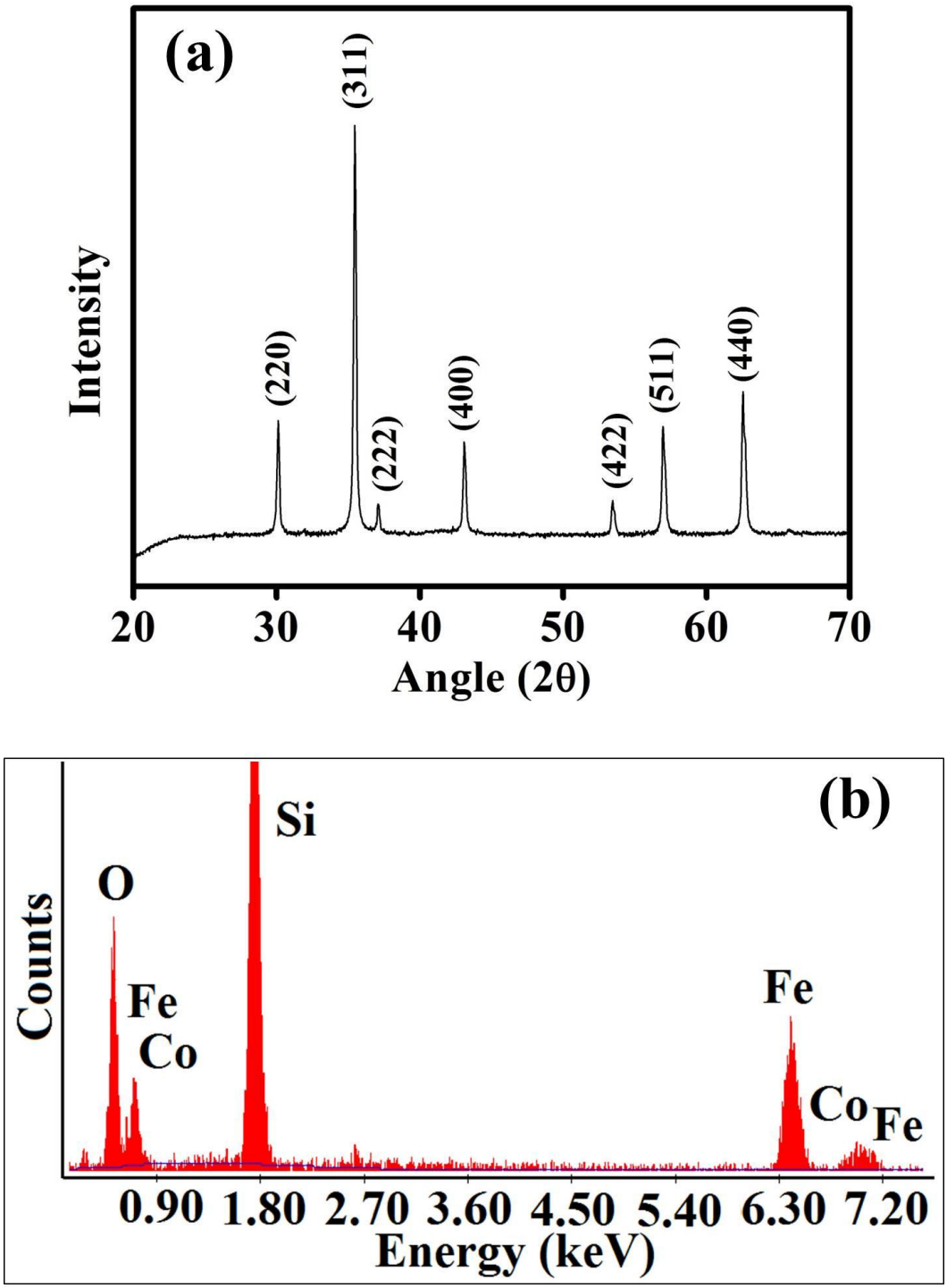

Figure 4.1: (a)XRD of the as-prepared $CoFe_2O_4$ NHSs. (b) EDX spectra of as-prepared $CoFe_2O_4$ NHSs indicating presence of Co, Fe and O.

For understanding morphology and size of the both as-prepared $CoFe_2O_4$ NHSs and T-$CoFe_2O_4$ NHSs, A SEM (Scanning Electron Microscope) study was performed. From Figure 4.2.(a) and (b), it is clearly evident that the as-prepared $CoFe_2O_4$ NHSs have narrow dispersity with an average diameter of 247 nm. Figure 4.2.(c) and (d) show the uniform size distribution of the T-$CoFe_2O_4$ NHSs with an average diameter of 243 nm.

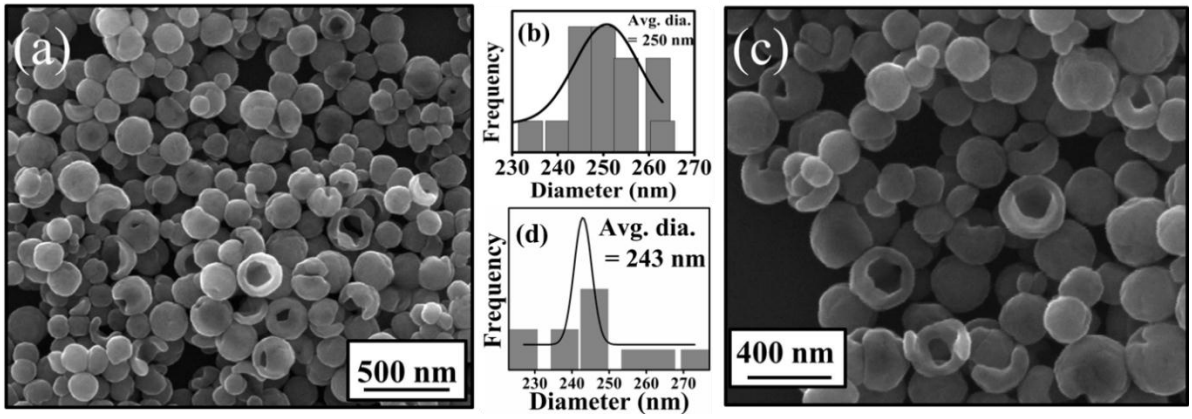

Figure 4.2: (a) SEM image of the as-prepared $CoFe_2O_4$ NHSs. (b) Size distribution graph of as-prepared $CoFe_2O_4$ NHSs. (c) SEM image of the T-$CoFe_2O_4$ NHSs. (d) Size distribution graph of T-$CoFe_2O_4$ NHSs.

In order to solubilize the as-prepared $CoFe_2O_4$ NHSs into aqueous medium, we have functionalized the NHSs with Na-tartrate solution by putting the as-prepared $CoFe_2O_4$ NHSs and 0.5 M tartrate solution together in a Borosil glass vial and placing it on to the top of a vibrator-rotor. By doing so, we also have made the as-prepared $CoFe_2O_4$ NHSs biocompatible. After surface modification, the size of the T-$CoFe_2O_4$ NHSs remains almost unchanged, as shown in Figure 4.2.(c). Then we carried out the absorption analysis of both tartrate and T-$CoFe_2O_4$ NHSs. From Figure 4.3.(a) it is shown that the functionalized $CoFe_2O_4$ NHSs (pH~7) have different absorption property than the only tartrate, indicating a distinct change in the surface electronic structure of the NHSs. In the absorption spectra of the functionalized $CoFe_2O_4$ (Figure

4.3.(a)) the band near 320 nm is clearly visible. In order to see whether fluorescence was present or not, we carried out a preliminary experiment by putting the cuvette filled with T-$CoFe_2O_4$ NHSs under UV light of wavelength 253.7 nm (UV-C), shown in Figure 4.3.(b) and 4.3.(c).

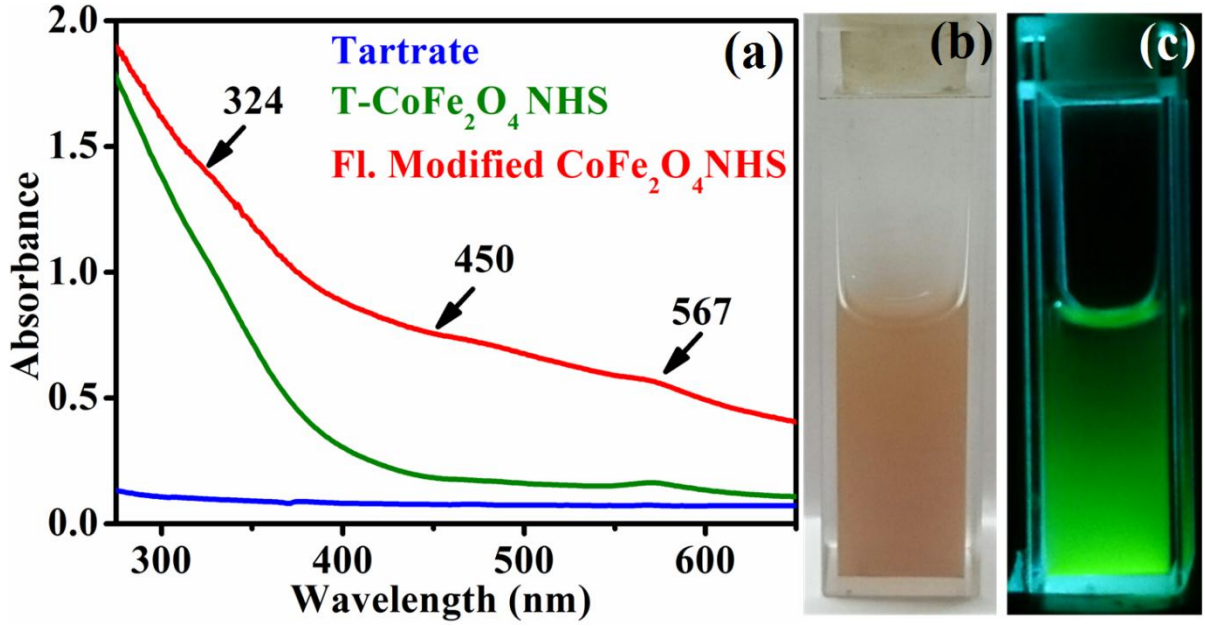

Figure 4.3: (a) Absorption spectra of Na-tartrate,T-$CoFe_2O_4$ NHSs and fluorescence modified $CoFe_2O_4$ NHSs. T-$CoFe_2O_4$ NHSs are under (b) visible and (c) UV light.

After obtaining the information from the absorption spectra, we carried out photoluminescence study of the functionalized $CoFe_2O_4$, and observed fluorescence at λ_{em}= 406 nm while exciting the functionalized solution at λ_{ex}= 324 nm. In order to intensify the photoluminescence, further surface modification was done by heating the functionalized $CoFe_2O_4$ NHSs solution at 70°-80°C for 10 h and at pH~12, which is termed as fluorescence modified (Fl. Mod.) $CoFe_2O_4$ NHSs. Three more photoluminescence peaks were generated with greater intensity as a result of further surface modification, the photoluminescence peaks at λ_{em}= 445 nm, 488 nm and 560 nm were found upon exciting the fl. mod. solution of $CoFe_2O_4$ NHSs at λ_{ex}= 365 nm, 420 nm, 530 nm respectively.

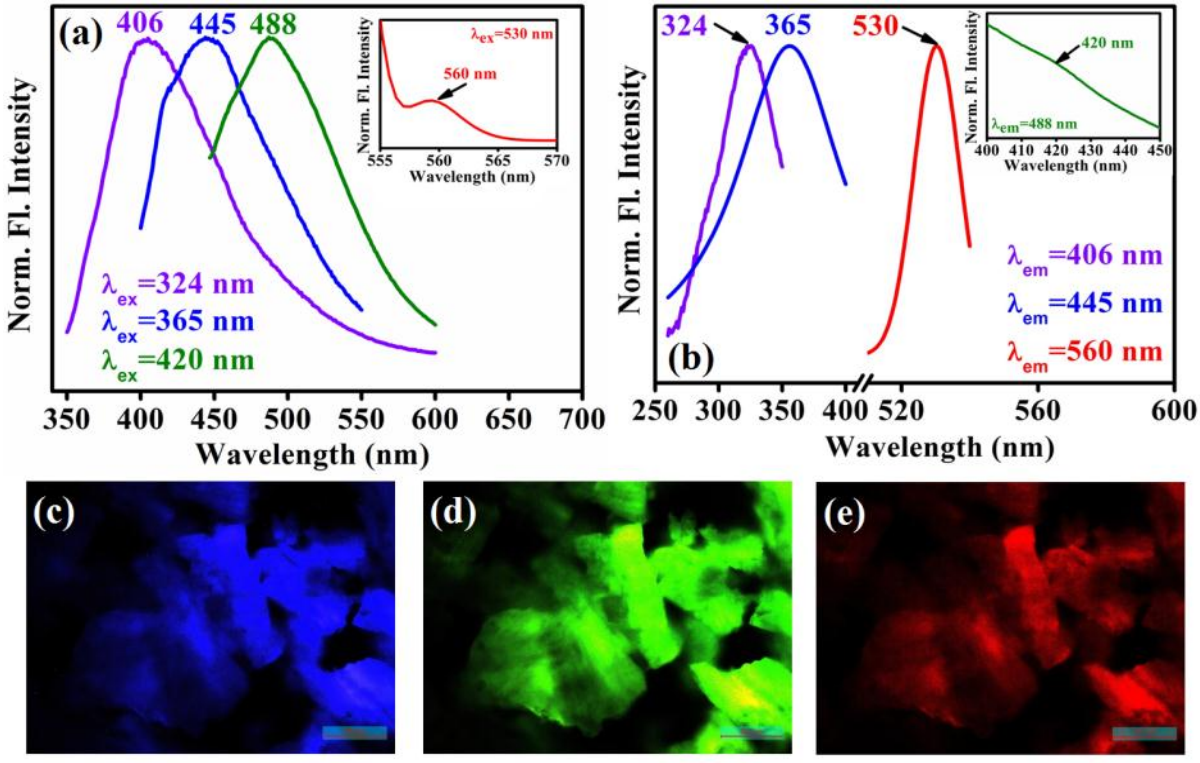

Figure 4.4: (a) Normalized steady-state fluorescence emission spectra obtained from fluorescence-modified T-$CoFe_2O_4$ NHSs after excitation at four different wavelengths, λ_{ex} = 324, 365, 420, and 530 nm.(b)Fluorescence excitation spectra of fluorescence-modified T-$CoFe_2O_4$ NHSs at different emission maxima, that is, λ_{em}= 406, 445, 488 and 560 nm. Fluorescence micrographs of fluorescence-modified T- $CoFe_2O_4$ NHs powder under (c) UV (375 nm), (d) blue (450 nm), and (e) green (515 nm) light irradiation. The scale bars in all images are 200 μm.

With the assistance of Ligand Field theory (LFT), the occurrence of multicolor photoluminescence can be clarified. The photoluminescence peak at λ_{em}= 406 nm for fluorescence modified $CoFe_2O_4$ NHSs, resulting from exciting the solution at λ_{ex}= 324 nm (absorption peak seen in Figure 4.3.(a)), arises from ligand to metal charge transfer (LMCT) involving the highest occupied energy level of tartrate ligands and the lowest unoccupied energy levels of Co^{+2}/Co^{+3} or Fe^{+3} metal ion centers on the NPs' surface. In $CoFe_2O_4$ NHSs Co^{+2} and Fe^{+3} are essentially present but Co^{+3} is more stable in aqueous medium than Co^{+2} [26]. It is most probable that the Co^{+3} may take part in the generation of fluorescence. The other three peaks at 445 nm, 488 nm, 530 nm may be ascribed to the possible d-d transitions of the Co^{+2}/Co^{+3} metal ions. As Fe^{+3} is d^5 system, the d-d transitions are both spin and laporte forbidden, which concludes that Fe^{+3} is not

responsible for the generation of the other three peaks. The three emission bands with maxima at λ_{em}= 445 nm, 488 nm and 560 nm can be described in terms of spectroscopicterm symbols, due to transitions of $^4T_{1g}$ (F)→$^4A_{2g}$ (F),^{4}T1g (F)→$^4T_{1g}$ (P), and $^4T_{1g}$ (F)→ $^4T_{2g}$ (F), respectively, where these energy levels are obtained from the Tanabe Sugano diagram of Co^{+2} [18]. Additional contributions for the emission peaks with maxima at 445 and 488 nm can be interpreted by the d–d transitions ($^1A_{1g}$→$^1T_{2g}$ and $^1A_{1g}$→$^1T_{1g}$, respectively), involving the energy levels of Co^{+3} as obtained from the Tanabe Sugano diagram [27]. The spin allowed transitions that are instrumental for the multicolored photoluminescence, for both Co^{+2} and Co^{+3} are shown in Figure 4.5.(a) and 4.5.(b) respectively. From the transitions the crystal field parameter (*Dq*) and the Racah parameter (*B*) are calculated and found to be 1290 cm^{-1} and 1217 cm^{-1}, which corresponds the octahedral structure of Co^{+2} [28].

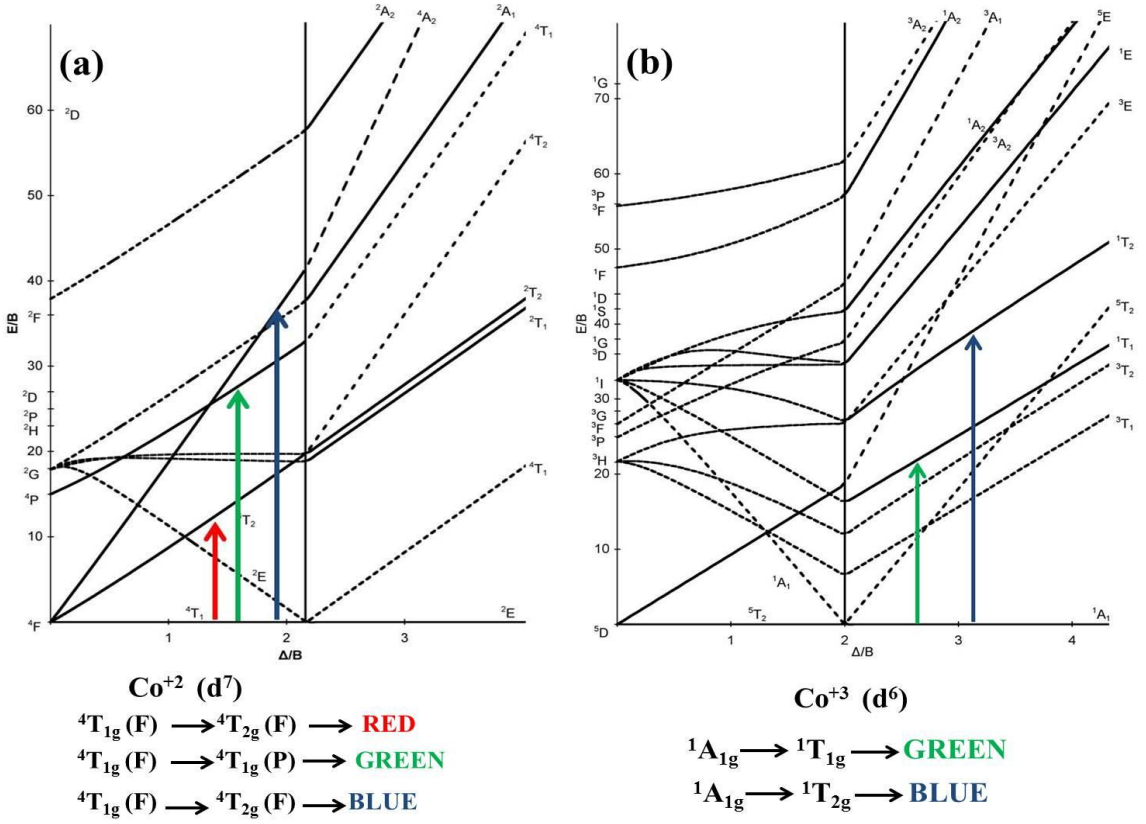

Figure 4.5: (a) The schematic diagram of the spin allowed d-d transitions of Co^{+2} (d^7 system), (b) The schematic diagram of the spin allowed d-d transitions of Co^{+3} (d^6 system), that result in three different colored fluorescence for fluorescence-modified T-$CoFe_2O_4$ NHSs. The transitions are shown using Tanabe Sugano diagram.

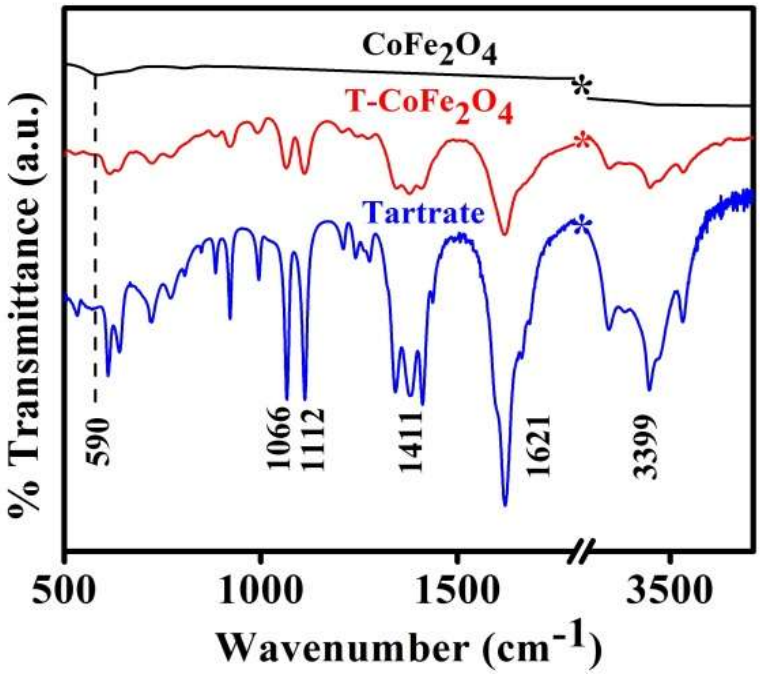

Figure 4.6: FTIR spectra of as-prepared $CoFe_2O_4$ and T-$CoFe_2O_4$ NHs together with Na-tartrate alone.

The FTIR study was carried for $CoFe_2O_4$ NHSs before and after functionalization with tartrate ligand and only tartrate ligand in order to check the attachment of the ligand molecules to the surface of bare $CoFe_2O_4$ NHSs. As depicted in Figure 4.6, the peak arising at 590 cm^{-1} is due to stretching vibration of metal-oxygen bonds in $CoFe_2O_4$ [29]. The peak at 590 cm^{-1} is missing in the case of T-$CoFe_2O_4$ NHSs. Two sharp peaks arising at 1066 and 1112 cm^{-1} in the case of tartrate ligand are due to C–OH stretching modes [30] and two other peaks at 1411 and 1621 cm^{-1} are due to the symmetric and asymmetric stretching of the COO^- [31]. Because of the interactions between the surface of the $CoFe_2O_4$ NHSs and the functional group moieties of the ligand, all the bands are distinctly perturbed along with the band at 3399 cm^{-1} which corresponds the stretching vibrational modes of the O–H group [30]. From this FTIR spectrum it is evident that $–COO^-$ and –OH groups are actively involved in the functionalization.

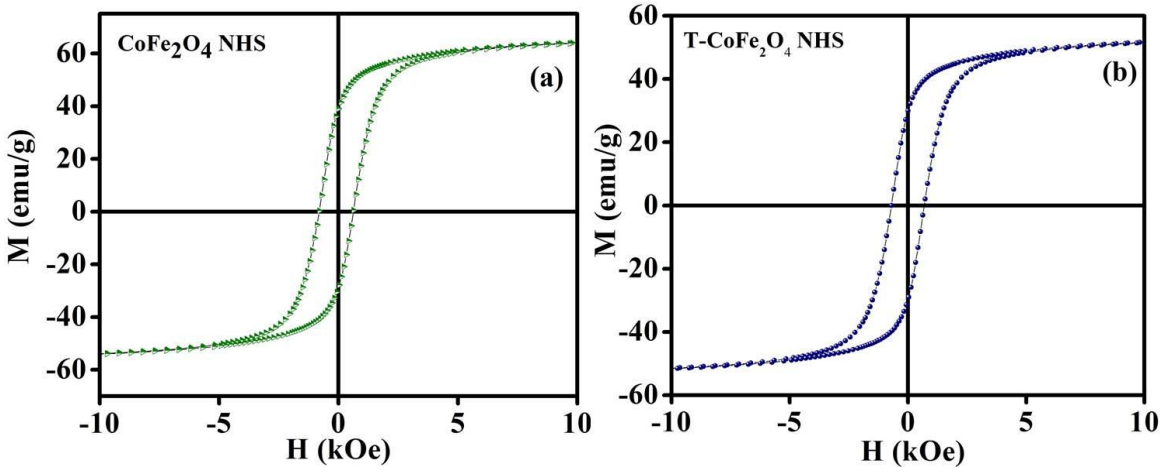

Figure 4.7: (a) Plot of magnetization versus applied magnetic field (M-H) of as-prepared $CoFe_2O_4$ NHSs at 300 K, (b) M-H plot for T-$CoFe_2O_4$ NHSs at 300 K.

Figure 4.7.(a) and 4.7.(b) show the room temperature magnetic behavior of the as-prepared $CoFe_2O_4$ NHSs and T-$CoFe_2O_4$ NHSs. To attain significant magnetization we chose NHSs over NPs. From Figure 4.7.(a) it is found that the saturation magnetization and the coercivity of the bare $CoFe_2O_4$ NHSs are 63.3 emu/g and 0.816 kOe, respectively. From Figure 4.7.(b) the saturation magnetization of functionalized $CoFe_2O_4$ NHSs is found to be 51.5 emu/g, much greater than the saturation magnetization of functionalized $CoFe_2O_4$ NPs which was 0.75 emu/g [32]. The coercivity of functionalized $CoFe_2O_4$ NHSs found to be 0.695 kOe, as depicted in. We have successfully attained significant saturation magnetization in functionalized $CoFe_2O_4$ NHSs, which may be beneficial. Here the coercivity for CFO NHSs and T-CFO NHSs are almost same. The tartrate ligand consists of both σ donor (–OH) and π donor (–COO-) groups which lead to immense LMCT (ligand to metal charge transfer) and spin pairing (i.e. quenching of magnetic moments) of $Co^{+2/+3}$ or Fe^{+3} ions on the surface of T-$CoFe_2O_4$ NHSs, which reduces the net saturation magnetization [33]. Due to both outer and inner spin layer disorder in functionalized $CoFe_2O_4$ NHSs around 250 nm, surface anisotropy increases, that suppresses saturation magnetization compared to same size of functionalized $CoFe_2O_4$ NPs. But for 5

nm NPs, superparamagnetism works and M_S is much lower than that of functionalized $CoFe_2O_4$ NHSs.

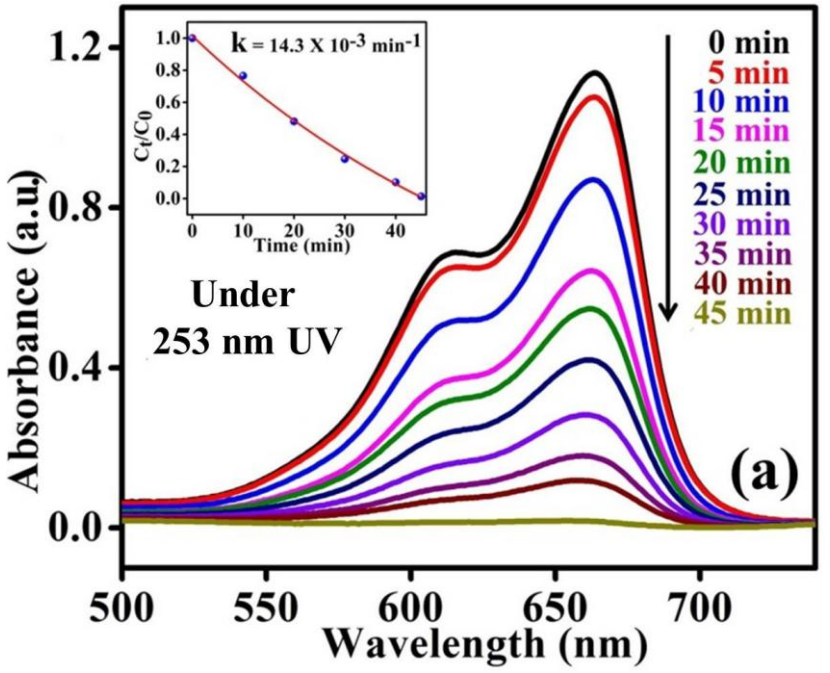

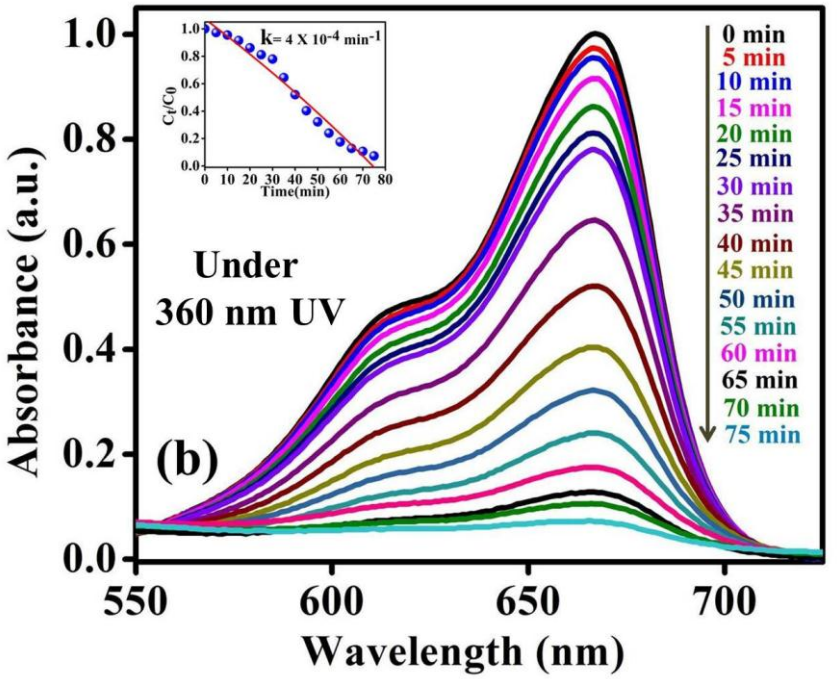

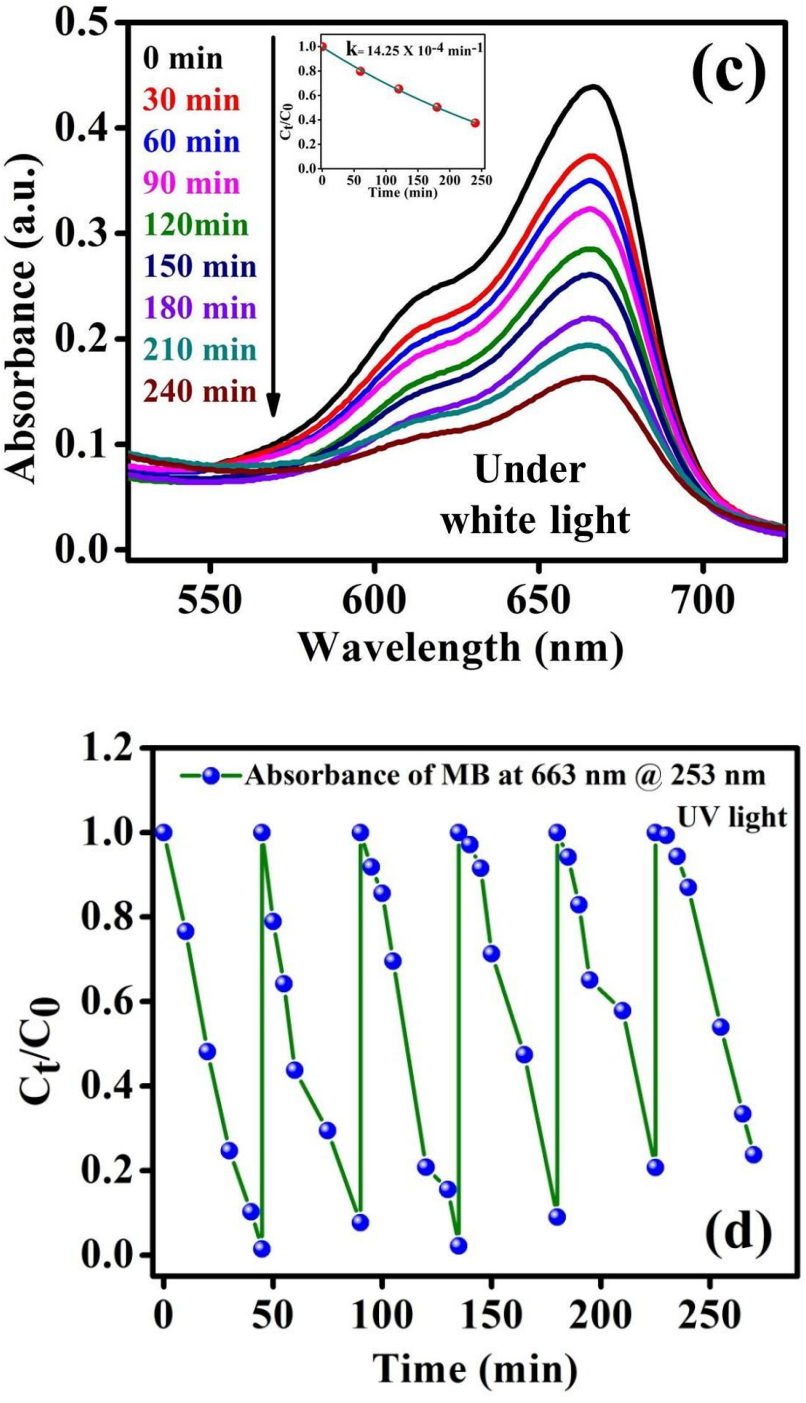

Figure 4.8: (a) The UV/Vis spectral changes of an aqueous solution of MB under 253 nm UV irradiation in presence of T-$CoFe_2O_4$ NHSs NPs with time, (inset of (a) fitted first order reaction rate), (b) The UV/Vis spectral changes of an aqueous solution of MB under 360 nm UV irradiation in presence of T-$CoFe_2O_4$ NHSs NPs with time, (inset of (b) fitted first order reaction rate), (c) The UV/Vis spectral changes of an aqueous solution of MB under visible light in presence of T-$CoFe_2O_4$ NHSs NPs with time, (inset of (c) fitted first order reaction rate) (d) Plots of the relative concentration of Rh B monitored at 663 nm versus time for six consecutive cycles, showing reusability of T-$CoFe_2O_4$ NHSs in the degradation of MB.

Bearing in mind the current advances in the field of nanocatalysis, we examined the broad optical property of the T-$CoFe_2O_4$ NHSs in photocatalytic waste water treatment. The T-$CoFe_2O_4$ NHSs are found to own a good photocatalytic activity towards the water contaminants. Figure 4.8.(a) and 4.8.(b) show the gradual degradation of model water contaminant Methylene Blue (MB) in presence of T-$CoFe_2O_4$ NHSs under two different UV light irradiations. In the inset of the Figure 4.8.(a) the fitted (by fitting with equation $A=A^0e^{-kt}$) first order reaction rate of degradation of MB using the UV irradiation of 253 nm is shown where the rate constant is found to be, $k = 14.3 \times 10^{-3}$ min^{-1}. Figure 4.8.(b) shows the degradation of MB using the less strong UV irradiation of 360 nm, where the rate of the reaction is, $k = 4 \times 10^{-4}$ min^{-1}.

Furthermore, we investigated the photodegradation of MB by T-$CoFe_2O_4$ under visible light, from Figure 4.8.(c) it is shown that the degradation pathway also follows first order kinetics with the rate constant (k) = 14.25×10^{-4} min^{-1}. Figure 4.8.(d) depicts the reusability of the catalyst using UV light, we added same dose of MB (10μl) into the reaction mixture for up to 6 doses, keeping the catalyst concentration unchanged (i.e., without adding further catalyst after 1st cycle). The MB degradation rates of the cycles were monitored by measuring the fall of absorbance at 663 nm with UV-Visible spectroscopy.

We also tried the photocatalytic property towards another water contaminant Rhodamine B (Rh B). Figure 4.9.(a) and 4.9.(b) show the periodical decrease in Rh B concentration at 554 nm determined by UV–Vis spectroscopy versus irradiation time of two different UV light in presence of T-$CoFe_2O_4$ NHSs. We found that the photodegradation of Rh B in presence of T-$CoFe_2O_4$ NHSs at pH ~ 3 takes place exponentially with time following a first-order rate equation (by fitting with equation $A=A^0e^{-kt}$) with a kinetic rate constant $k = 4.6 \times 10^{-2}$ min^{-1}. In Figure 4.9.(b), the degradation of Rh B under 360 nm UV light irradiation is shown, where the rate constant is found to be, $k = 7.7 \times 10^{-3}$ min^{-1}.

Under visible light the photodegradation rate of Rh B by T-$CoFe_2O_4$ NHSs falls,

with the rate constant (k) = 7.2 X 10^{-4} min^{-1}. The photodegradation of Rh B under white light is shown in Figure 4.9.(c). The reusability test was done same way as done for MB using UV light, and found that T-$CoFe_2O_4$ NHSs are worthy up to 5 cycles. Figure 4.9.(d) demonstrates the plots of relative concentration of Rh B versus time, for up to 5 consecutive cycles, indicating the reusability of T-$CoFe_2O_4$ NHSs.

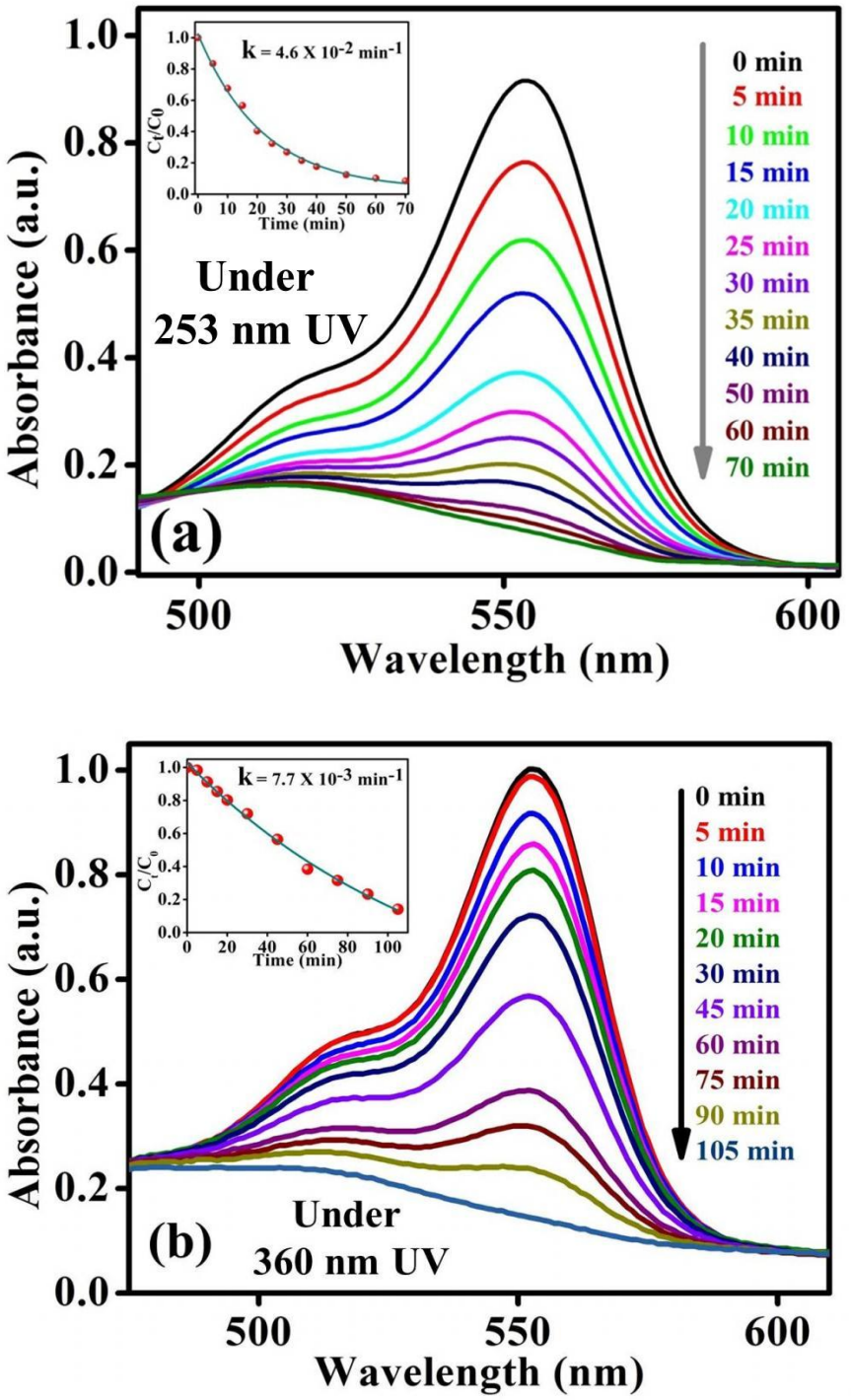

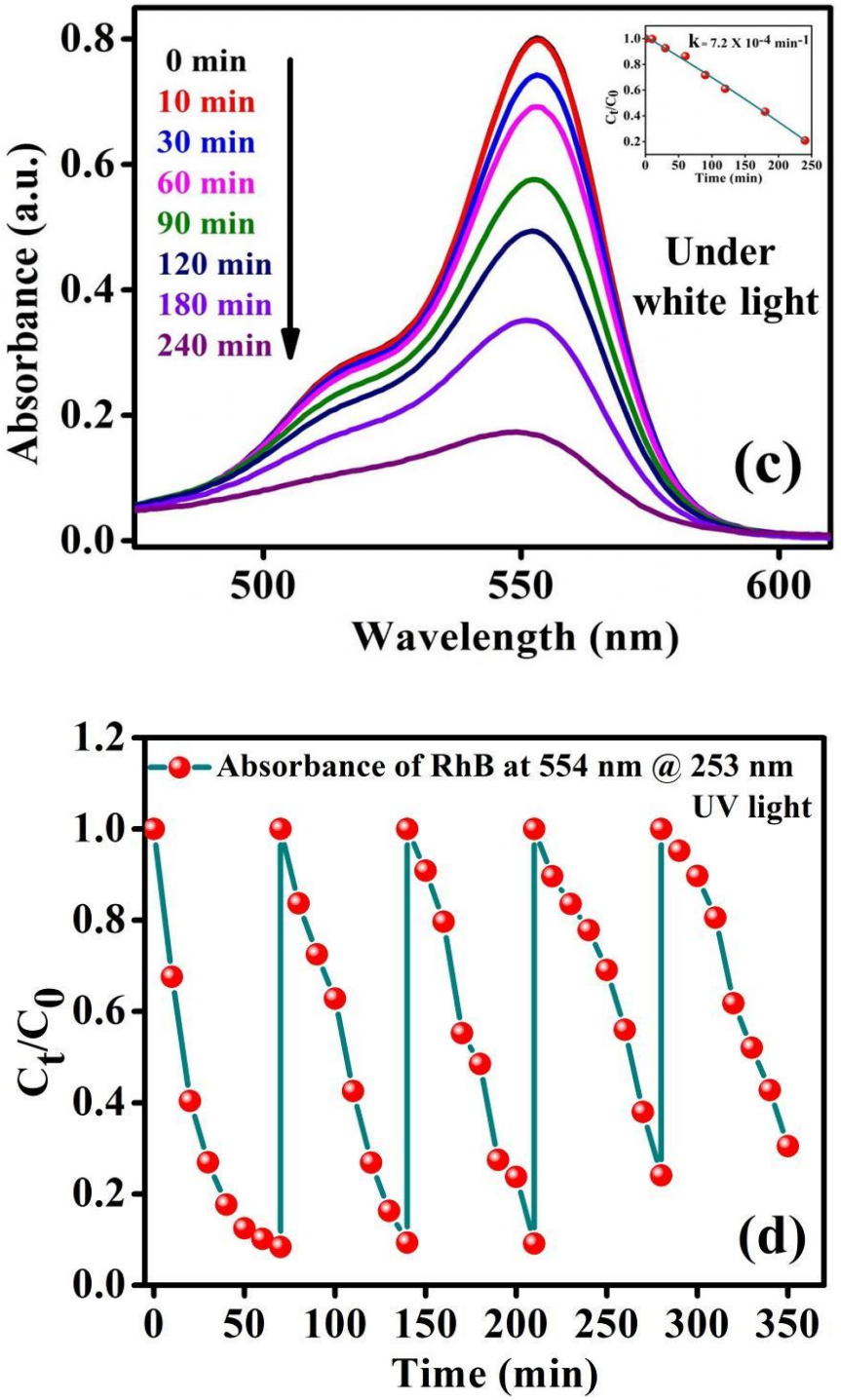

Figure 4.9: (a) The UV/Vis spectral changes of an aqueous solution of Rh B under UV irradiation in presence of T-$CoFe_2O_4$ NHSs NPs with time, (inset of (a) fitted first order reaction rate), (b) The UV/Vis spectral changes of an aqueous solution of Rh B under 360 nm UV irradiation in presence of T-$CoFe_2O_4$ NHSs NPs with time, (inset of (b) fitted first order reaction rate), (c) The UV/Vis spectral changes of an aqueous solution of Rh B under visible light in presence of T-$CoFe_2O_4$ NHSs NPs with time, (inset of (a) fitted first order reaction rate), (c) Plots of the relative concentration of Rh B monitored at 554 nm versus time for five consecutive cycles, showing reusability of T-$CoFe_2O_4$ NHSs in the degradation of Rh B.

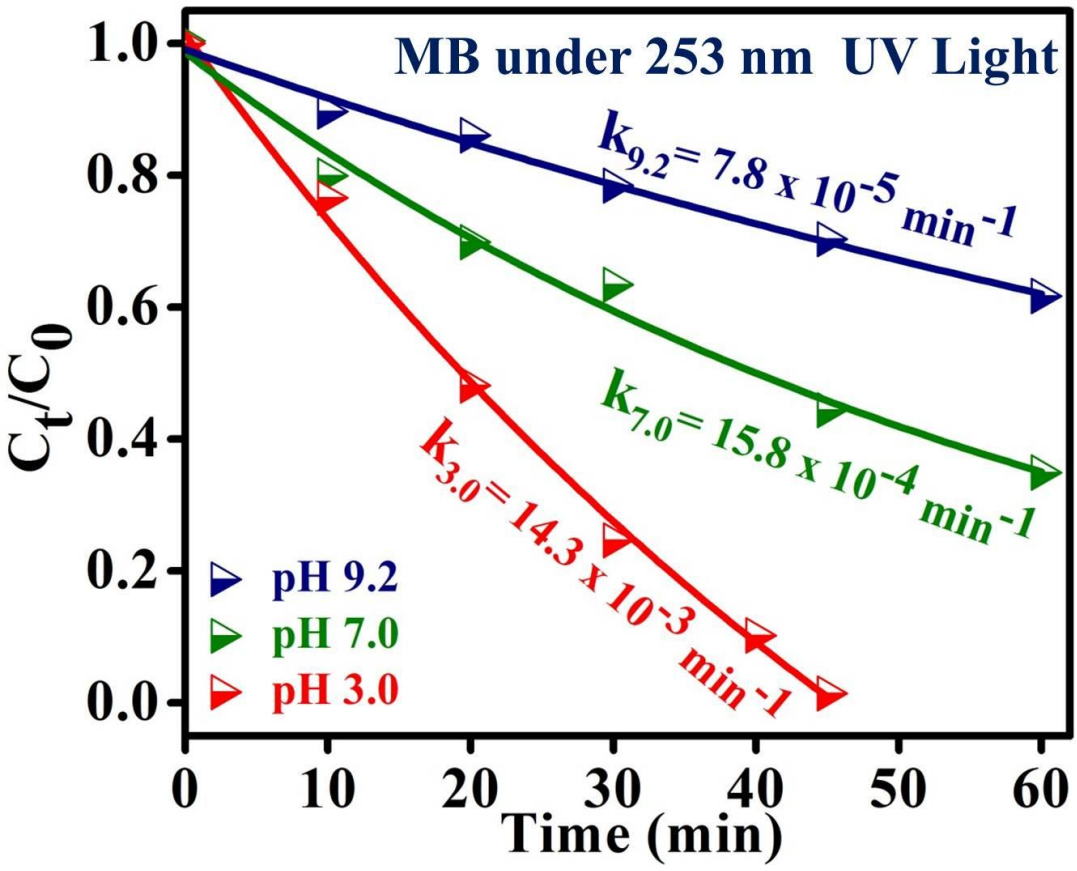

Figure 4.10: The pH dependency of MB degradation under 253 nm UV light irradiation.

To study the effect of pH on the degradation of MB, we carried out the reaction in three different pHs (3.0, 7.0, 9.2) using standard buffer solution. The degradation was studied under the 253 nm UV light irradiation, shown in Figure 9. It is clearly evident that from the Figure 4.10 that with rising pH, the rate of MB degradation falls. The rate constant at pH 9.2 was found to be, $k_{9.2}$ = 7.8 x 10^{-5} min^{-1}, which designates that the reaction in pH 9.2 is 183 times slower than in pH 3.0. The rate constant for pH 7.0, is $k_{7.0}$ = 15.8 x 10^{-4} min^{-1}, that is 9 times slower from the pH 3.0. The T-$CoFe_2O_4$ is found to be worthy as catalyst in the lower pH.

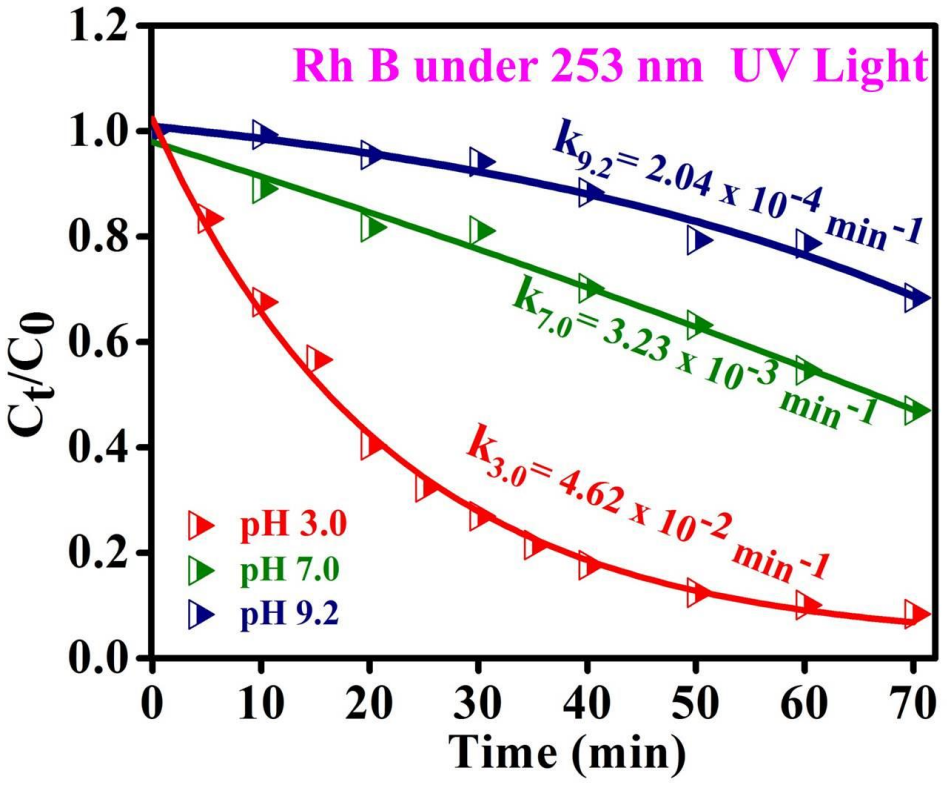

Figure 4.11: The pH dependency of Rh B degradation under 253 nm UV light irradiation.

The same pH dependency experiment was carried out for Rh B also. From the Figure 4.11, we can infer that higher pH slower the rate of degradation of Rh B under 253nm UV light irradiation using T-$CoFe_2O_4$ as a photocatalyst. The rates of Rh B degradation in pH 7.0 and pH 9.2 are found to be $k_{7.0}$ = 3.23 x 10^{-3} min^{-1} and $k_{9.2}$= 2.04 x 10^{-4} min^{-1} respectively. The degradation reaction of Rh B in pH 7.0 is 14 times slower and in pH 9.2 is 226 times slower than the degradation in pH 3.0.

The degradation of Methylene blue (MB) and Rhodamine b (Rh B), by T-$CoFe_2O_4$ under UV light irradiation were found to be dependent of pH. As the pH of the medium increases, the degradation rate of both of the dyes falls significantly. Both the dyes are cationic dye, their degradation occurs through the adsorption of the dyes to the surface of the catalyst. The cationic dye is easily attracted and attached to the surface of the catalyst as the NP's are

functionalized by negatively charged tartrate ions. This attachment helps to degrade the dye faster. At higher pH, the availability of OH^- ions increases, which in results hinders the dye to get attached on the surface. Thus fall of the rate degradation happens.

The mechanism of degradation (shown in Figure 4.12) proceeds through the subsequent steps:

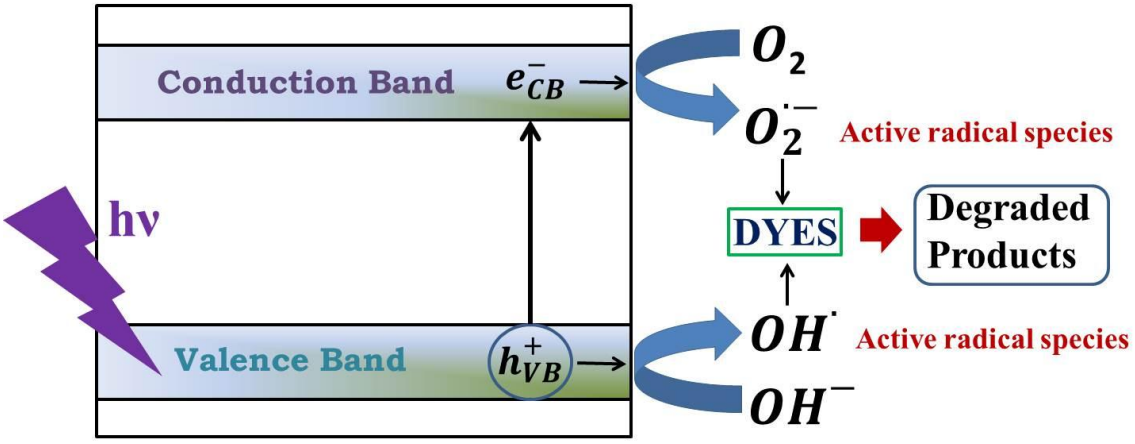

Figure 4.12: Schematic diagram of degradation pathway of MB by T-$NiFe_2O_4$.

1. Absorption of photon by metal oxide

$$\boldsymbol{Metal\ Oxide} + h\upsilon \rightarrow \boldsymbol{e^-_{CB}} + \boldsymbol{h^+_{VB}}$$

2. Oxygen Ionosorption

$$\boldsymbol{O_2} + \boldsymbol{e^-_{CB}} \rightarrow \boldsymbol{O_2^{\cdot -}}$$

3. Neutralization of OH^- groups by photoholes which produces $\boldsymbol{OH^{\cdot}}$ radicals

$$(\boldsymbol{H_2O} \rightarrow \boldsymbol{H^+ + OH^-})\ \boldsymbol{H^+ + OH^- + h^+_{VB}} \rightarrow \boldsymbol{H^+ + OH^{\cdot}}$$

4. Neutralization of $O_2^{\cdot -}$ by protons

$$\boldsymbol{O_2^{\cdot -} + H^+} \rightarrow \boldsymbol{HO_2^{\cdot}}$$

5. Transient hydrogen peroxide formation and dismutation of oxygen

$$2HO_2^{\cdot} \rightarrow H_2O_2 + O_2$$

6. Decomposition of H_2O_2 and second reduction of oxygen

$$H_2O_2 + e^- \rightarrow OH^{\cdot} + OH^-$$

7. Oxidation of the dye via successive attacks by $OH^{\cdot}$ radicals

$$R + OH^{\cdot} \rightarrow \textbf{degradation products}$$

4.4 Conclusion

In conclusion, magneto-fluorescent $CoFe_2O_4$ nano-hollow spheres have been prepared by simple functionalization of their outer surfaces using small organic ligand like tartrate. The developed multifunctional $CoFe_2O_4$ NHSs possess inherent multicolor fluorescence covering a broad visible region ranging from blue, green to red, intrinsic ferromagnetic property. We have found that LMCT and d-d transitions are instrumental behind the photoluminescence of functionalized $CoFe_2O_4$ nano-hollow spheres. As our developed magneto-fluorescent $CoFe_2O_4$ NHSs own biocompatibility and ligand induced intrinsic photoluminescent property, we believe that our material may unfold new prospects in the fields like bioimaging, drug delivery, and other biomedical applications. Moreover, we have shown the admirable photocatalytic property of functionalized $CoFe_2O_4$ NHSs towards degradation of model water contaminants like MB and Rh B, so we hope that our material will be beneficial for the waste water treatment.

Bibliography

1. H.B. Na, I.C. Song, T. Hyeon, *Inorganic Nanoparticles for MRI Contrast Agents,* **Adv. Mater**., 2009, 21, 2133–2148.

2. M.W. Tibbitt, J.E. Dahlman, R. Langer, *Emerging Frontiers in Drug Delivery*, **J. Am. Chem. Soc.**, 2016, 138, 704-717.

3. M. Colombo, S. Carregal-Romero, M.F. Casula, L. Gutiérrez, M.P. Morales, I.B. Böhm, J.T. Heverhagen, D. Prosperi, W.J. Parak, *Biological applications of magnetic nanoparticles*, **Chem. Soc. Rvw**., 2012, 41, 4306-4334.

4. A.K. Gupta, M. Gupta, *Synthesis and surface engineering of iron oxide nanoparticles for biomedical applications*, **Biomaterials**, 2005, 18, 3995-4021.

5. F. Yang, Y. Li, Z. Chen, Y. Zhang, J. Wu, N. Gu, *Superparamagnetic iron oxide nanoparticle-embedded encapsulated microbubbles as dual contrast agents of magnetic resonance and ultrasound imaging*, **Biomaterials**, 2009, 30, 3882-3890.

6. H.M. Chen, R.S. Liu, M.Y. Lo, S.-C. Chang, L.-D. Tsai, Y.-M. Peng, J.-F. Lee, *Hollow Platinum Spheres with Nano-Channels: Synthesis and Enhanced Catalysis for Oxygen Reduction*, **J. Phys. Chem. C**, 2008, 112, 7522-7526.

7. R. Rakshit, M. Pal, A. Chaudhuri, K. Mandal, *Research Update: Facile synthesis of $CoFe_2O_4$ nano-hollow spheres for efficient bilirubin adsorption*, **APL Mat.**, 2015, 3, 110701-110706.

8. Z. Dai, J. Zhang, J. Bao, X. Huanga, X. Mo, *Facile synthesis of high-quality nano-sized CdS hollow spheres and their application in electrogenerated chemiluminescence sensing*, **J. Mater. Chem.**, 2007, 17, 1087-1093.

9. C.Y. Wen, H.Y. Xie, Z.L. Zhang, L.L. Wu, J. Hu, M. Tang, M. Wu, D.W. Pang, *Fluorescent/magnetic micro/nano-spheres based on quantum dots*

and/or magnetic nanoparticles: preparation, properties, and their applications in cancer studies, **Nanoscale,** 2016, 8, 12406-12429.

10. X. Lai, J.E. Halperta, D. Wang, *Recent advances in micro-/nano-structured hollow spheres for energy applications: From simple to complex systems*, **Energy Environ. Sci.,** 2012, 5, 5604-5618.

11. F. Wang, J. Liu, J. Kong, Z.X. Wang, M. Itoh, K.I. Machida, *Facile synthesis of hollowporous cobalt spheres and their enhanced electromagnetic properties*, **J. Mater. Chem.,** 2011, 21, 4314-4320.

12. J.W. Yoon, Y.J. Hong, Y.C. Kang, J.H. Lee, *High performance chemiresistive H2S sensors using Ag-loaded SnO_2 yolk–shell nanostructures*, **RSC Adv.,** 2014, 4, 16067-16074.

13. B. Guo, K. Yu, H. Li, H. Song, Y. Zhang, X. Lei, H. Fu, Y. Tan, Z. Zhu, *Hollow Structured Micro/Nano MoS_2 Spheres for High Electrocatalytic Activity Hydrogen Evolution Reaction*, **ACS Appl. Mater. Interfaces,** 2016, 8, 5517–5525.

14. H. Sun, G. Zhou, S. Liu, H.M.O. Ang, M. Tadé, S. Wang, *Low temperature combustion synthesis of nitrogen-doped graphene for metal-free catalytic oxidation*, **ACS Appl. Mater. Interfaces,** 2012, 4, 6235-6241.

15. Q. Wang, Y. Zhu, J. Xue, X. Zhao, Z. Guo, C. Wang, *General Synthesis of Porous Mixed Metal Oxide Hollow Spheres with Enhanced Supercapacitive Properties*, **ACS Appl. Mater. Interfaces,** 2016, 8, 17226–17232.

16. W.S. Kim, Y Hwa, J.H. Jeun, H.J. Sohn, S.H. Hong, *Synthesis of SnO2 nano hollow spheres and their size effects in lithium ion battery anode application*, **J. Power Sources,** 2013, 225, 108-112.

17. R. Wu, X. Qian, A.W.K. Law, K. Zhou, *Coordination polymer-derived mesoporous Co3O4 hollow nanospheres for high-performance lithium-ions batteries*, **RSC Adv.,** 2016, 6, 50846-50850.

18. C.C. Li, Q.H. Li, L.B. Chen,T.H. Wang, *A facile titanium glycolate precursor route to mesoporous $Au/Li_4Ti_5O_{12}$ spheres for high-rate*

lithium-ion batteries, **ACS Appl. Mater. Interfaces,** 2012, 4, 1233–1238.

19. Z. Li, Q. Zhao, W. Fana, J. Zhan, *Low-toxic and safe nanomaterials by surface-chemical design, carbon nanotubes, fullerenes, metallofullerenes, and graphenes*, **Nanoscale,** 2011, 3, 1646-1652.

20. X. Zou, H. Fan, Y. Tian, M. Zhang, X. Yan, *Microwave-assisted hydrothermal synthesis of Cu/Cu2O hollow spheres with enhanced photocatalytic and gas sensing activities at room temperature*, **Dalton Trans.,** 2015, 44, 7811-7821.

21. S.S. Chen, H. Xu, H.J. Xu, G.J. Yu, X.L. Gong, Q.L. Fang,K.C.F. Leung, S.H. Xuanc, Q.R. Xiong, *A facile ultrasonication assisted method for Fe_3O_4@SiO_2-Ag nanospheres with excellent antibacterial activity*, **Dalton Trans.,** 2015, 44, 9140-9148.

22. J. Chen, W. Zhang, M. Zhang, Z. Guo, H. Wang, M. He, P. Xu, J. Zhou, Z. Liuc, Q. Chen, *Mn(II) mediated degradation of artemisinin based on Fe_3O_4@$MnSiO_3$-FA nanospheres for cancer therapy in vivo*, **Nanoscale,** 2015, 7, 12542-12551.

23. Z.W. Lu, C. Qian, T. Zeng, L. Yin, H. Wang, L. Rao, H. Liua, S. Zeng, *Mesoporous silica coated $Gd_2(CO_3)_3$: Eu hollow nanospheres for simultaneous cell imaging and drug delivery*, **Biomater. Sci.,** 2014, 2, 1404-1411.

24. X. Ren, L. Tong, X. Chen, H. Ding, X. Yang, H. Yang, *Deposition of luminescent Y2O3:Eu^{3+} on ferromagnetic mesoporous $CoFe_2O_4$@$mSiO_2$ nanocomposites*, **Phys. Chem. Chem. Phys.,** 2014, 16, 10539-10547.

25. M. Pal, R. Rakshit, K. Mandal, *Surface Modification of MnFe2O4 Nanoparticles to Impart Intrinsic Multiple Fluorescence and Novel Photocatalytic Properties*, **ACS Appl. Mater. Interfaces,** 2014, 6, 4903-4910.

26. R.N. Collins, A.S. Kinsela, *The aqueous phase speciation and chemistry of cobalt in terrestrial environments*, **Chemosphere,** 2010, 79, 763-771.

27. J.E. Huheey, E.A. Keiter, R.L. Keiter, O.K. Medhi, *Inorganic Chemistry: Principles of Structure and Reactivity*; Fourth ed., **Pearson Education**, New York, 2006.

28. ABP Lever, *The Crystal Field Splitting Parameter Dq: Calculation and Significance*, **Adv. Chem.,** 1967, 29, 430-451.

29. L.A. García Cerda, S.M. Montemayor, *Synthesis of CoFe2O4 nanoparticles embedded in a silica matrix by the citrate precursor technique*, **J. Magn Magn. Mat.,** 2005, 294, e43-e46.

30. N. Kaneko, M. Kaneko, H. Takahashi, *Infrared and Raman spectra and vibrational assignment of some metal tartrates*, **Spectrochim. Acta Part A,** 1984, 40, 33-42.

31. V. Ramakrishnan, J.M.T. Maroor, *IR and Raman studies of gel grown manganese tartrate*. **Infrared Phys.**, 1988, 28, 201-204.

32. M. Pal, A. Kundu, R. Rakshit, K. Mandal, *Ligand-Induced Evolution of Intrinsic Fluorescence and Catalytic Activity from Cobalt Ferrite Nanoparticles*, **ChemPhysChem,** 2015, 1627-1634.

33. R. Rakshit, M. Pal, M. Mandal, K. Mandal, *Charge transfer mediated magnetic response of cobalt ferrite nanoparticles*, **Mater. Lett.,** 2015, 151, 64-67.

Chapter 5

Developing Magneto-fluorescent $CoFe_2O_4$ Nano-Hollowspheres as Nanocarriers

This chapter exhibits the development of inherent photoluminescence, drug loading, excellent catalytic and photocatalytic property upon surface functionalization of $CoFe_2O_4$ nano-hollowspheres by hydrophilic organic ligand.

5. Developing Multifunctional Magneto-fluorescent $CoFe_2O_4$ Nano-Hollowspheres through Simple Surface Functionalization

5.1 Preamble

Magnetic nanostructures (NSs) are widely used in bio-medical applications in the last few decades. Iron-based inorganic nanostructured materials have been synthetized and studied for various applications in bio-medical field, such as imaging, hyperthermia treatments, tissue repair, immunoassay, detoxification of biological fluids, cell separation, drug delivery, etc [1-5]. For these applications, the NSs must have combined properties of high magnetic saturation, biocompatibility and interactive functions at the surface. The surfaces of these particles could be modified through the creation of few atomic layers of organic moieties or inorganic metallic (e.g. gold) or oxide surfaces (e.g. silica or alumina), suitable for further functionalization by the attachment of various bioactive molecules [6-8]. One of the most challenging subject in nanomaterials science and technology is the synthesis of magnetic NSs. Special properties of the NSs required for biomedical applications imply a precise control of particle size, shape, dispersion and conditions that affect these properties. Coating nanomaterials with natural or synthetic polymers or surfactants is a method that provides stability of the colloidal suspensions. Use of surfactants such as: decanoic acid, oleic acid, hexaldehyde or sodium carboxymethylcellulose leads to highly dispersed and high quality NSs with good biocompatibility and smaller particle size [9-11].

In recent years, inorganic hollow nanostructures have attracted great interest because of their unique properties that are substantially different from those of bulk materials, such as low density, large surface area, surface permeability, and special electric, magnetic and catalytic properties. Owing to their special

properties, nano hollow spheres (NHSs) are widely used as artificial cells, catalysts, fillers, and controlled release capsules for drugs and dyes [12-16]. The advantages of using these materials come not only from their improved magnetic properties over nanoparticles, but also from a higher surface, that provides higher sensitivity, better targeting and improvement of the colloidal stability of the NHSs.

Among various ferrites, $CoFe_2O_4$ NHSs extensively studied due to their ability to form an ideal magnetic system toward understanding and tuning magnetic properties at the atomic level through chemical manipulation. $CoFe_2O_4$ has large anisotropy compared to other oxide ferrites [17-18]. Though they are proposed for biomedical application their use in medicine is restricted due to numerous problems such as toxicity due to the remarkable amount of cobalt release in aqueous solutions, aggregation in solution, and poor accessibility of the surface when surfactants are used. This problem can be overcome by surface coating of $CoFe_2O_4$ with a compatible, nontoxic, and hydrophilic material.

5.2. Experiment

5.2.1 Materials Used

Iron chloride hexahydrate [$FeCl_3.6H_2O$], Cobalt chloride hexahydrate [$CoCl_2.6H_2O$], Ethylene Glycol, Urea [$CO(NH_2)_2$], Oleylamine are obtained from Sigma-Aldrich. 4-Nitrophenol and Folic Acid were bought from Loba Chemie., Ethyl Alcohol [EtOH] and Sodium Hydroxide [NaOH] are purchased from Merck.

5.2.2 Synthesis and Experimental Procedure

We synthesized $CoFe_2O_4$ NHSs by solvothermal method. A solution mixture of Iron (III) chloride hexahydrate, Cobalt (II) chloride hexahydrate, Ethylene Glycol, Urea, Ethanol and Oleylamine was heated in a Teflon lined stainless

steel autoclave at 200°C for 20 h in an oven. Then the as-prepared $CoFe_2O_4$ NHSs were washed by ethanol and collected after centrifugation. The removal of the mother solution was done by heating on a hotplate at a temperature of 80°-90°C for 30 min. The Ostwald ripening process has been proposed as a template-free strategy and is used more and more to fabricate inorganic hollow spheres.

The basic principle of the inside-out Ostwald ripening process is that the larger crystals grow from those of smaller size, which have higher solubility than the larger ones. Within a colloidal aggregate, smaller, less crystallized or less dense crystallites will dissolve into the liquid phase as a nutrient supply for the growth of larger, better crystallized or denser ones. When the crystals grow in solution, the concentration of growth units varies across the mother solution, due to the size difference of resultant nanocrystals. With the driving force of the minimization of surface energy, metastable nanoparticle aggregates occur first due to the reduction of supersaturation in solution. Once the particles with different sizes are attached to each other, the large particles begin to grow drawing from smaller ones. Voids gradually form and grow in the cores of large aggregates and the shell thickness increases owing to the outward diffusion of solutes through the permeable shell.

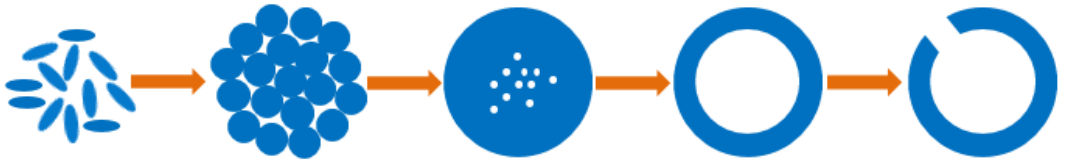

Figure 5.1: Formation mechanism of nano hollow spheres via Ostwald ripening.

For the purpose of surface modification of the as-prepared $CoFe_2O_4$ NHSs with tartrate and folate ligands, we cyclomixed the NHSs with 0.1M Na-tartrate and 0.05M Na-folate solutions (pH~7) at room temperature for 12 h. We obtained tartrate and folate functionalized solutions and named them as TCFO and FCFO

NHSs respectively.

The X-ray powder diffraction (XRD) of as-prepared $CoFe_2O_4$ NHSs was done using Rikagu miniflex II diffractometer equipped with Cu Kα radiation (at 40 mA and 40 kV) at the scanning rate of 3° per minute in the 2θ range of 20°-70°. A FEI QUANTA FEG 250 field-emission high-resolution scanning electron microscope (FESEM), operated at 5-10 kV was used to study the size, shape, morphology, and size distribution and to record the Energy-dispersive X-ray analysis (EDX) spectrum of the as-prepared and functionalized $CoFe_2O_4$ NHSs. Fluorescence micrographs of $CoFe_2O_4$ NHSs were captured using a Olympus BX53 fluorescence microscope.

FTIR (Fourier transform infrared spectroscopy) measurements were performed using a JASCO FTIR-6300 spectrometer to ensure the attachment of the ligands to the NHSs' surface. For FTIR study, pellets were made by placing the homogeneous mixture of lyophilized TCFO and FCFO NHSs powder samples and KBr (using the ratio 1:4 respectively) under the pelletizer. The background was corrected using a reference KBr pellet. For magnetic measurements a Lake Shore VSM equipped with an electromagnet was used.

The Ultraviolet-visible (UV/Vis) absorbance spectra of 4-Nitrophenol (4-NP) were obtained using a quartz cuvette of 1 cm path length on Shimadzu UV-2600 spectrophotometer. UV lamp with wavelength of 360 nm was used in the photocatalytic study. The aqueous solution of FCFO NHSs (50μL) and 50μL aqueous solution of 4-NP (0.01M) were homogenously mixed in a quartz cuvette for 1h in dark. The cuvette was kept 2 cm away from the UV light source and the absorbance spectra of 4-NP in presence of FCFO NHSs solution were measured from time to time by using UV/Vis spectrophotometer. For catalytic purpose 0.02g of powder CFO, 50μL of 4-NP (0.01M) and 20 μL of freshly prepared $NaBH_4$ ($1X10^{-3}$ M) were mixed in a cuvette and degradation of

4-NP was measured periodically using the UV-VIS spectrophotometer.

5.3. Results and discussion

Figure 5.2 shows the XRD pattern of the as prepared $CoFe_2O_4$ NHSs which confirms that all the peaks perfectly match with the cubic inverse spinel structure of $CoFe_2O_4$ NHSs, as reported in the literature (JCPDS file no. 22–1086). The EDX (energy dispersive X-ray) spectra in the inset of Figure 5.2 confirms the presence of Co, Fe and O in $CoFe_2O_4$ NHSs. Crystallite size of the NHSs (d ~ 50 nm) has been calculated from (311) peak of XRD pattern using Scherer formula, $d = (k.\lambda)/(\beta.\cos\theta)$, k is structural constant (0.94), λ is working wave length, β is the FWHM of the selected peak in radians and θ is the peak angle in degrees.

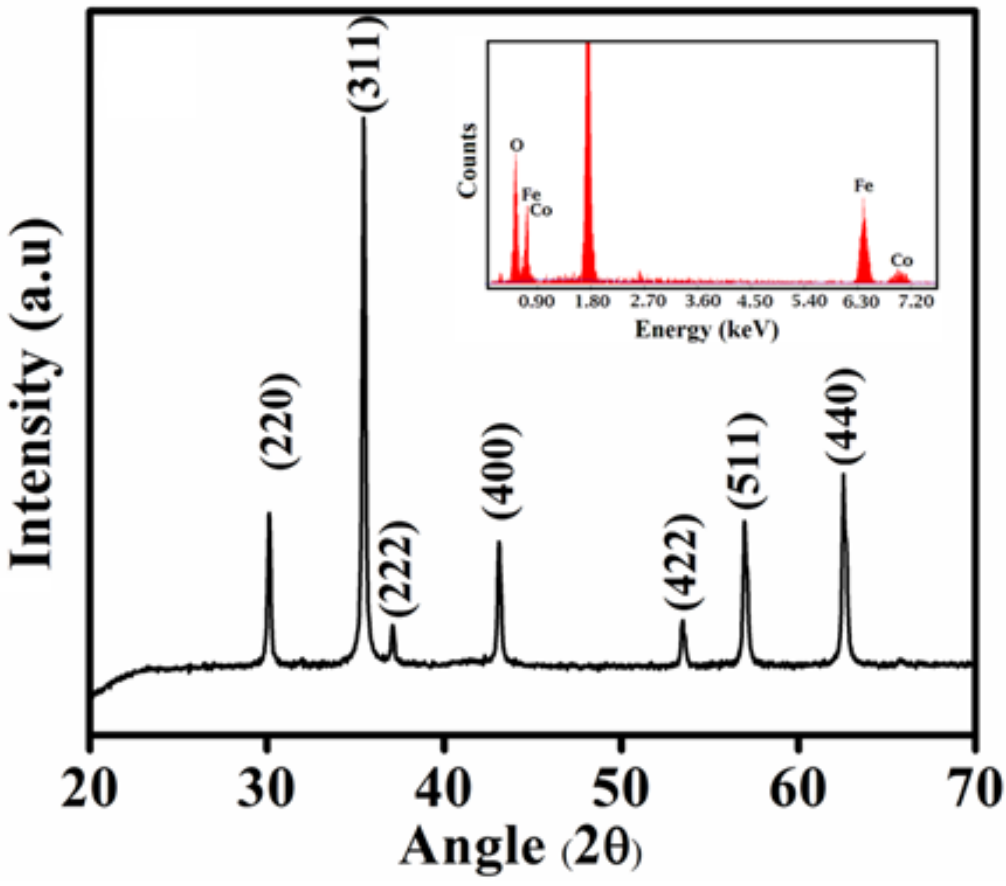

Figure 5.2: XRD pattern of the as-prepared $CoFe_2O_4$ NHSs. The inset shows EDX spectra of

$CoFe_2O_4$ NHSs indicating presence of Co, Fe and O.

For understanding morphology and size of the as-prepared $CoFe_2O_4$ NHSs, TCFO NHSs and FCFO NHSs FESEM (Field Emission Scanning Electron Microscope) and TEM (Transmission Electron Microscope) study were performed. From Figure 5.3.(a) and (b), it is clearly evident that the as-prepared $CoFe_2O_4$ have hollow structure. Figure 5.3.(c) shows narrow dispersity with an average diameter of 200 nm.

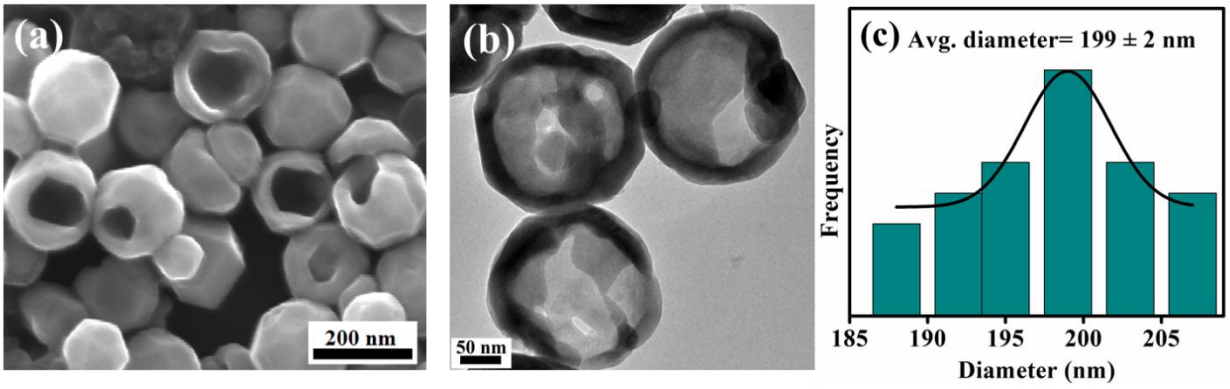

Figure 5.3: (a) FESEM image, (b) TEM image and (c) Size distribution graph of the as-prepared $CoFe_2O_4$ NHSs.

In order to disperse the $CoFe_2O_4$ NHSs into aqueous medium, we have functionalized the NHSs with the two different organic acids, one is Na-tartrate (0.1 M) solution and another is Na-folate (0.05 M) solution, via cyclomixing. By doing so, we also have made the as-prepared $CoFe_2O_4$ NHSs biocompatible. After surface modification, the size of the TCFO and FCFO NHSs remain almost unchanged, as shown in Figure 5.4.(c) and (f).

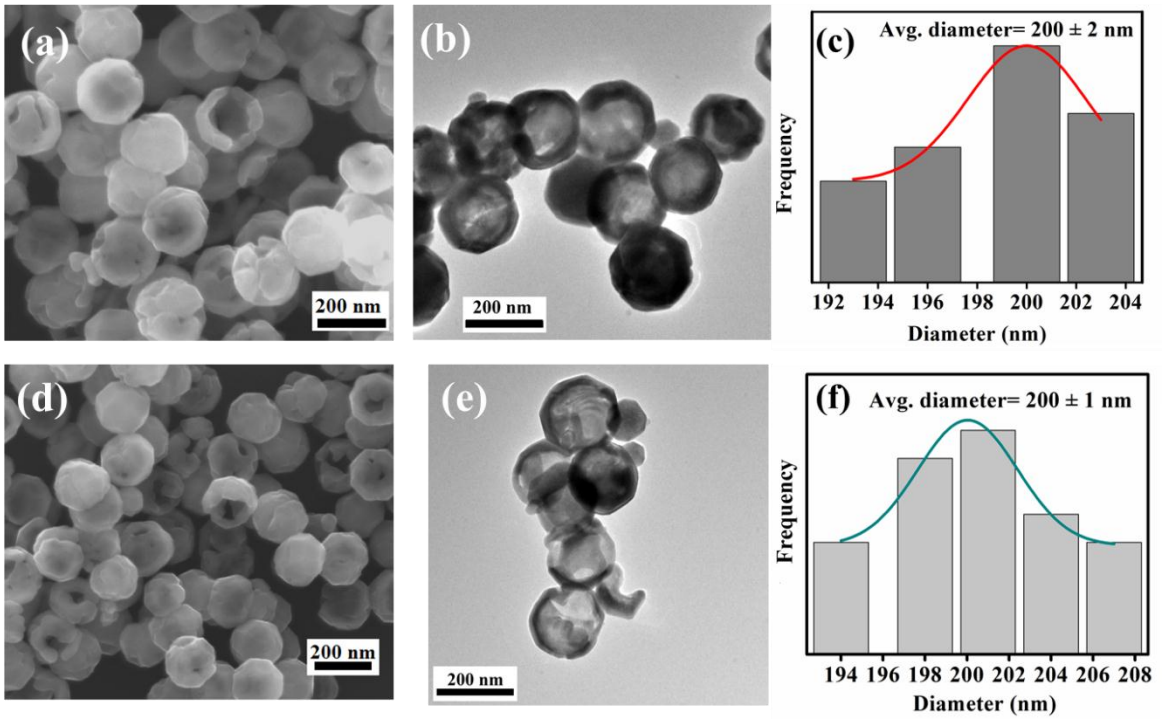

Figure 5.4: (a) FESEM image, (b) TEM image and (c) Size distribution graph of TCFO NHSs and (d) FESEM image, (e) TEM image and (f) size distribution graph of FCFO NHSs respectively.

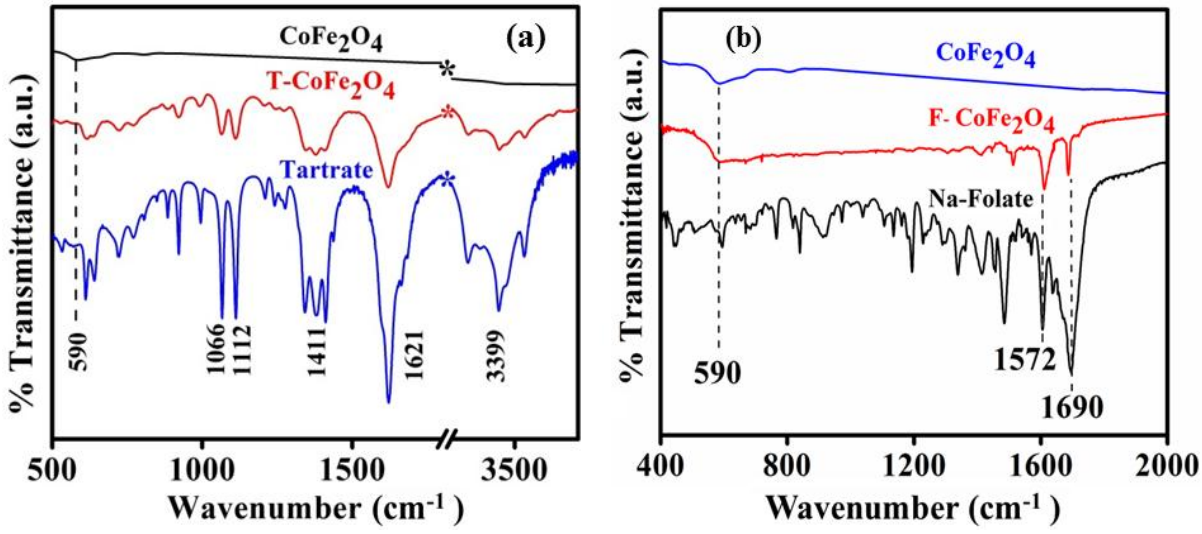

Figure 5.5: FTIR spectra of (a) as-prepared $CoFe_2O_4$, TCFO NHSs, Na-tartrate and (b) as-prepared $CoFe_2O_4$, FCFO NHSs, Na-folate.

The FTIR study was carried for bare and tartrate functionalized $CoFe_2O_4$ NHSs and for only tartrate ligand in order to check the attachment of the ligand molecules to the surface of bare $CoFe_2O_4$ NHSs. As depicted in Figure 5.5.(a), the peak arising at 590 cm^{-1} is due to stretching vibration of metal-oxygen bonds in $CoFe_2O_4$ [19]. The peak at 590 cm^{-1} is missing in the case of TCFO NHSs. Two sharp peaks arising at 1066 and 1112 cm^{-1} in the case of tartrate ligand are due to C–OH stretching modes [20] and two other peaks at 1411 and 1621 cm^{-1} are due to the symmetric and asymmetric stretching of the COO^- [21]. Because of the interactions between the surface of the $CoFe_2O_4$ NHSs and the functional group moieties of the ligand, all the bands are distinctly perturbed along with the band at 3399 cm^{-1} which corresponds the stretching vibrational modes of the O–H group [20]. From this FTIR spectrum it is evident that $–COO^-$ and –OH groups are actively involved in the functionalization. The same study was carried out to check the attachment of the Na-folate ligand molecules to the surface of bare $CoFe_2O_4$ NHSs showing 4 sharp absorption peaks ay 590 cm^{-1}, 1485 cm^{-1}, 1572 cm^{-1} and 1690 cm^{-1} as evident from Figure 5.5.(b) The peak at 1485 cm^{-1} is due to absorption of Phenyl ring and peak at 1572 cm^{-1} is appeared due to N-H bond bending. C=O stretching vibration is responsible for the peak at 1690 cm^{-1} [22].

Drug loading efficiency for the NHSs was checked with the help of UV–Vis absorption spectra taken for the Doxorubicin solution before (initial) and after (final) loading the drug into the particles, shown in Figure 5.6.(a) and (b). The absorption intensity was measured at 486 nm wavelength and observed that about 40% of drug was loaded in case of TCFO and for FCFO it was 60%, which was calculated using the Eq. (5.1) as given below.

$$\text{Loading efficiency} = \frac{A_0 - A_f}{A_0} X\ 100 \qquad (5.1)$$

Where A_0 is the initial absorbance and A_f is the final absorbance of the DOX solution.

DOX release was calculated by following equation:

$$\text{DOX release \%} = \frac{C_t}{A_0 - A_f} \text{ X } 100 \qquad (5.2)$$

Where C_0 is initial concentration of DOX, C_t is concentration of DOX at time t.

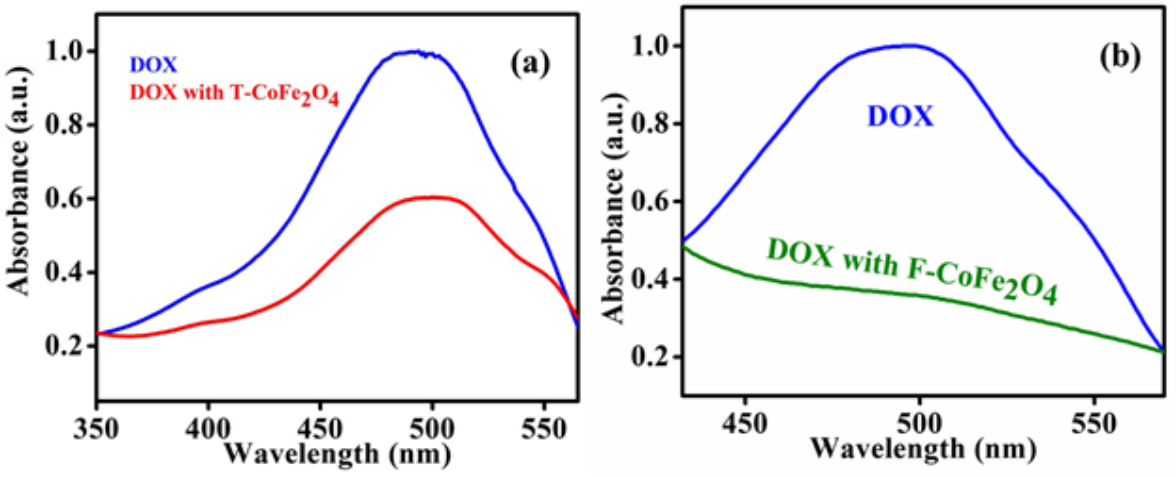

Figure 5.6: Absorption spectra of Doxorubicin solution before and after loading on (a) TCFO and (b) FCFO NHSs.

We implemented another way to load drug molecules onto the surface of NHSs by submerging powder FCFO NHSs in Doxorubicin solution. In this process we have taken 2ml of DOX solution and 0.15g of FCFO NHSs in a cuvette and placed it undisturbed for 24 h on the top of a bar magnet. The drug loading and releasing efficiency were measured in the aforementioned way. Only 50 % of the drug was loaded in this process as shown in Figure 5.7.(b). As the loading efficiency is lower in submerging process we further examined the drug release study for the drug loaded NHSs in the cyclomixing process.

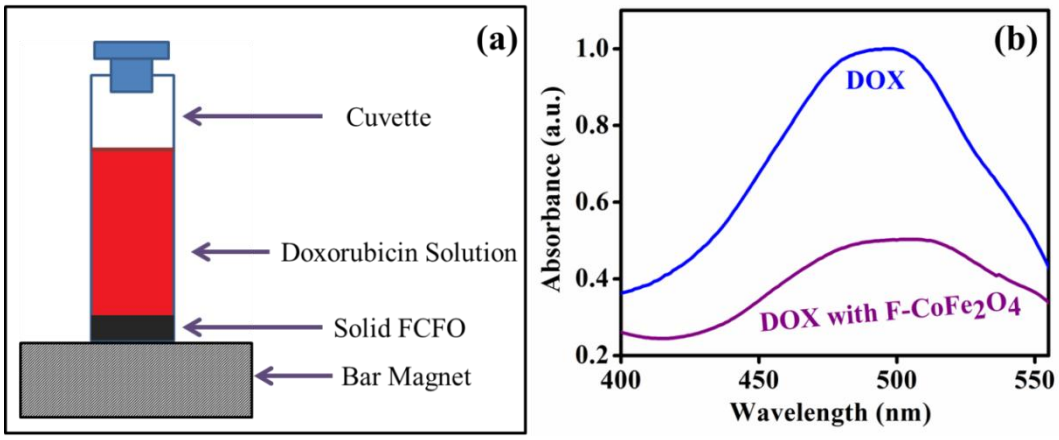

Figure 5.7: (a) Schematic representation of the submerging process and (b) absorption spectra of Doxorubicin solution before and after drug loading.

Figure 5.8 depicts the fluorescence microscopic images of FCFO and DOX loaded FCFO. Figure 5.8.(a)-(c) show the cyan, green and red fluorescence while exciting the FCFO NHSs with UV, blue and green light respectively. The generation of multicolor fluorescence in FCFO NHSs can be explained through the ligand to metal charge transfer and d-d transition, as discussed in the previous chapter [23]. By the same excitation the DOX loaded FCFO NHSs show only red fluorescence shown in Figure 5.8.(d-f). This confirms the attachment of DOX molecule onto the surface of FCFO NHSs.

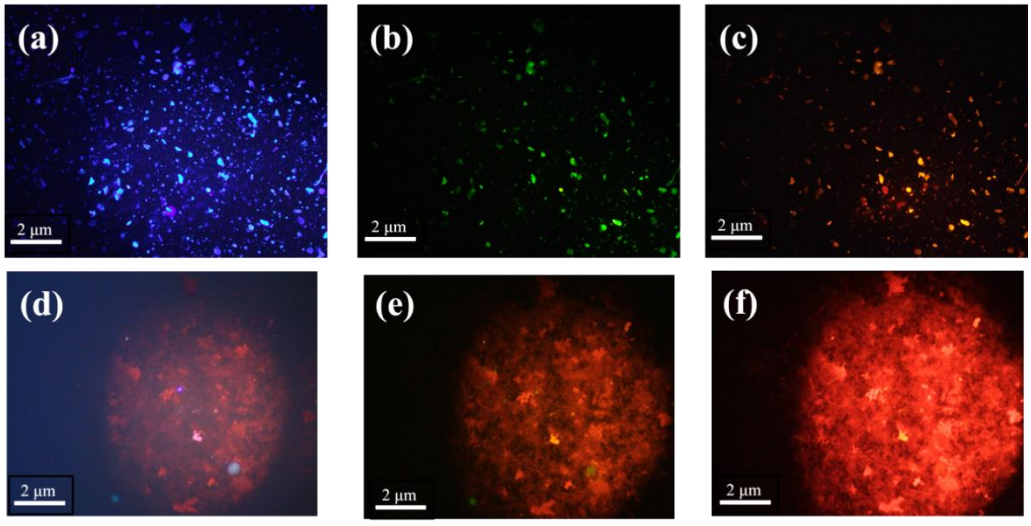

Figure 5.8: Fluorescence micrographs of FCFO NHSs powder under (a) UV (375 nm), (b) blue (450 nm) & (c) green (515 nm) light irradiation and of DOX-FCFO under (d) UV (375nm), (e) blue & (f) green (515 nm). The scale bars in all images are 2 µm.

Further we studied the drug release from drug loaded TCFO and FCFO NHSs at 37°C and pH 7.4. We found TCFO released only 37% of the loaded drug whereas FCFO released 90% of the loaded drug. So we studied drug release in different environment by drug loaded FCFO NHSs only.

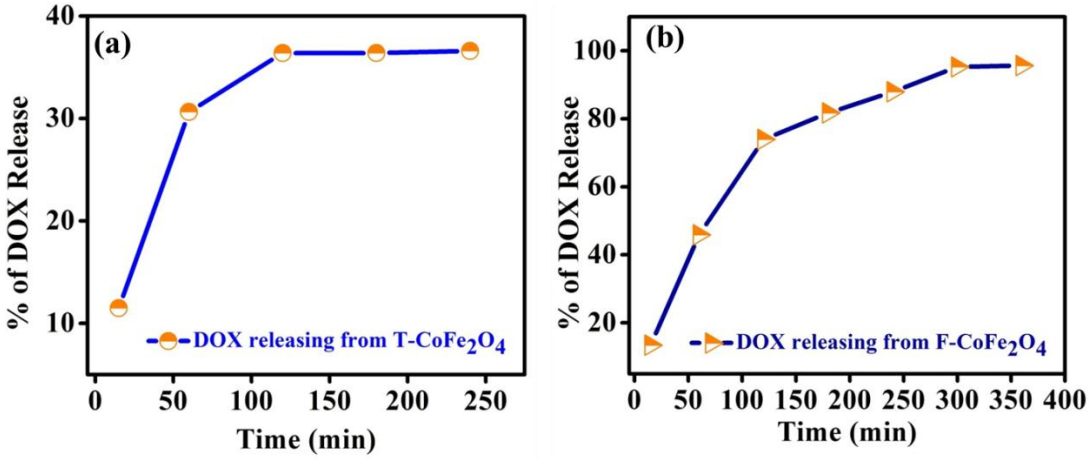

Figure 5.9: Release study of drug from (a) TCFO and (b) FCFO NHSs

After loading the particles with drug, they were undergone for drug release study at two different pHs (i.e. pH 5 and pH 7.4) with respect to time, keeping the temperature constant at 37 °C. 15 mg of this drug (DOX) loaded NHSs were taken in 2 ml of different buffer solutions. The absorption of the released drug was measured at different time interval with the help of UV–Vis spectrometer as shown in Figure 5.10.(a). The drug release rate with time measured at two different temperatures keeping pH at 7.4 were studied and shown in Figure 5.10.(b). The graphs clearly show that the release efficiency is undoubtedly better at lower pH. Figure 5.10.(a) depicts that within 4 h, 99% of the drug was released at pH 5 whereas in pH 7.4, release occurred up to 97% in 5h. This fast release at pH 5 was attributed to the cleavage of hydrogen bond in acidic condition. The attachment of Doxorubicin with folate molecule takes place through hydrogen bonding between the -COOH groups of folate and the $-NH_2$ groups of Doxorubicin [24]. In hydrogen bonding, $-NH_2$ of Doxorubicin forms $-NH_3^+$. In acidic conditions, the H^+ in solution would compete with the hydrogen-bond-forming groups and then weaken the above hydrogen-bonding

interaction. Thus the lower pH triggers the burst release of Doxorubicin. For the temperature dependent release study we observed the FCFO NHSs released 93% of the loaded drug at 44°C in 5 h. At higher temperature drug release rate was increased due to increase of thermal agitation, which in turn detached the drug molecules from the FCFO NHSs surface [25]. Hence, we can conclude that the FCFO magnetic nano-hollowspheres have potentiality to be used in both pH and temperature triggered drug release, where controlled release of drug in a noninvasive way is required.

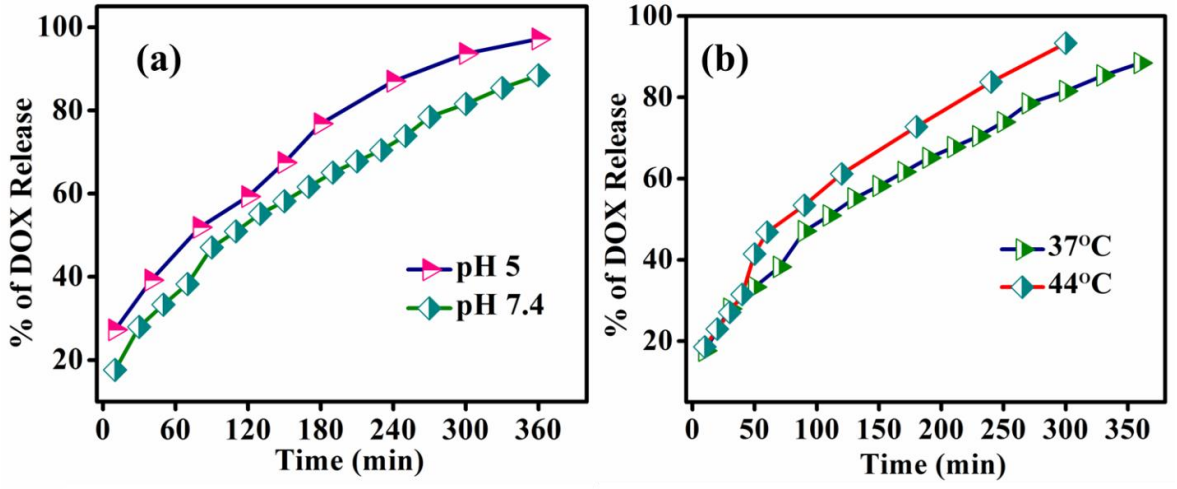

Figure 5.10: Drug release study (a) for different pH and (b) different temperature for drug loaded FCFO NHSs.

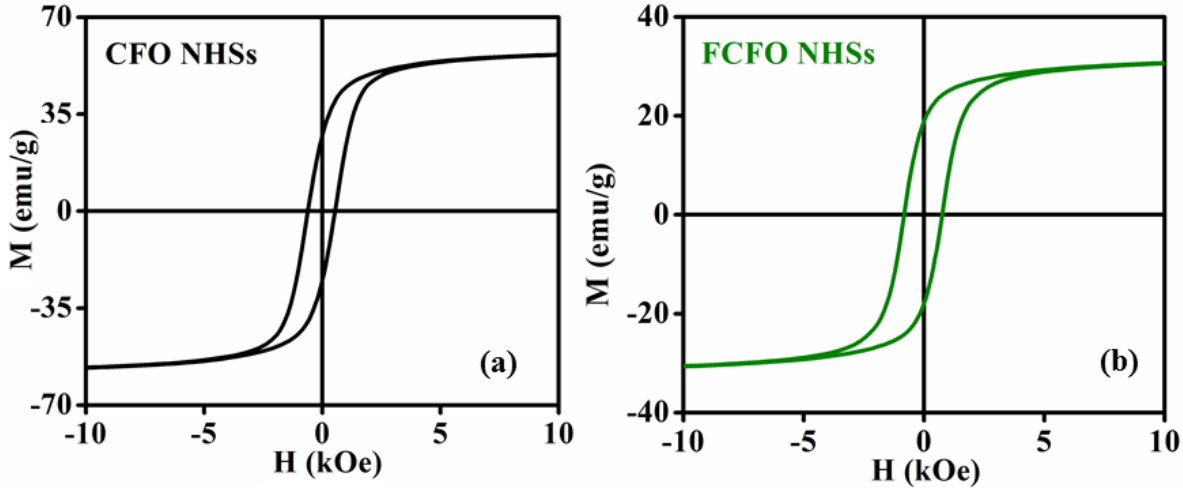

Figure 5.11: Plot of magnetization versus applied magnetic field (M-H) of (a) as-prepared $CoFe_2O_4$ NHSs and (b) FCFO NHSs at 300 K.

Figure 5.11.(a) and (b) show the room temperature magnetic behavior of the as-prepared $CoFe_2O_4$ NHSs and FCFO NHSs. To attain significant magnetization we chose NHSs over NPs. From Figure 5.11.(a) it is found that the saturation magnetization and the coercivity of the bare $CoFe_2O_4$ NHSs are 56.9 emu/g and 64 Oe respectively. From Figure 5.11.(b) the saturation magnetization of functionalized $CoFe_2O_4$ NHSs is found to be 30.9 emu/g. The coercivity of functionalized $CoFe_2O_4$ NHSs found to be 78 Oe, as depicted in Figure 5.11.(b). We have successfully attained significant saturation magnetization in functionalized $CoFe_2O_4$ NHSs, which may be beneficial. Here the coercivity for CFO NHSs and FCFO NHSs are almost same. The folate ligand consists of both σ donor ($–NH_2$) and π donor ($–COO^-$) groups which lead to immense LMCT (ligand to metal charge transfer) and spin pairing (i.e. quenching of magnetic moments) of $Co^{+2/+3}$ or Fe^{+3} ions on the surface of FCFO NHSs, which reduces the net saturation magnetization [23].

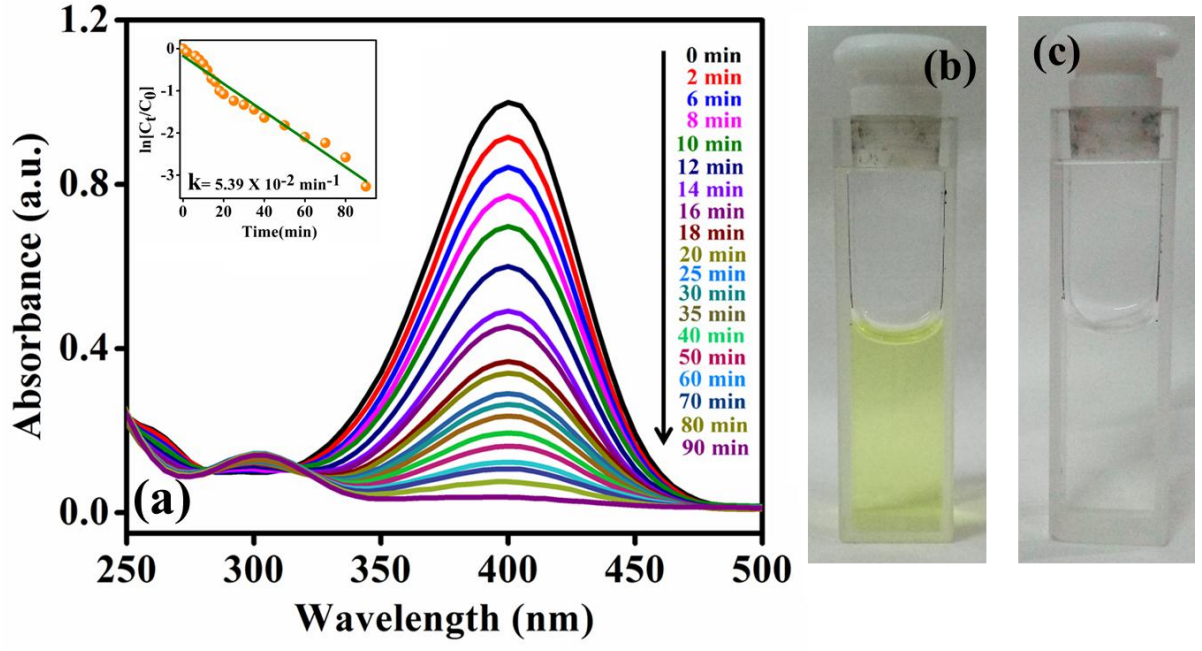

Figure 5.12: (a) The UV/Vis spectral changes of an aqueous solution of 4-NP under 360 nm UV irradiation in presence of FCFO NHSs with time, (inset of (a) fitted first order reaction rate). 4-NP solution (b) before and (c) after the photocatalysis.

Bearing in mind the current advances in the field of nanocatalysis, we examined the photocatalytic property of the FCFO NHSs in photocatalytic degradation of of 4-NP. The FCFO NHSs are found to own a good photocatalytic activity towards the pharmaceutical waste 4-NP. Figure 5.12.(a) show the gradual degradation of model water contaminant 4-NP in presence of FCFO NHSs under UV light irradiation. In the inset of the Figure 5.12.(a) the fitted (by fitting with equation $A=A^0e^{-kt}$) first order reaction rate of degradation of 4-NP using the UV irradiation of 360 nm is shown where the rate constant is found to be, k = 5.39 x 10^{-2} min^{-1}. As we have seen in the previous chapter the functionalized CFO NHSs are able to generate Reactive Oxygen Species (ROS), the hydroxyl radicals generated during the irradiation are responsible for the degradation of 4-NP [26].The organic pollutants got absorbed on surface of the FCFO NHSs and •OH generated due to the irradiation of UV light, immediately oxidize the absorbed pollutants and led to degrading products.

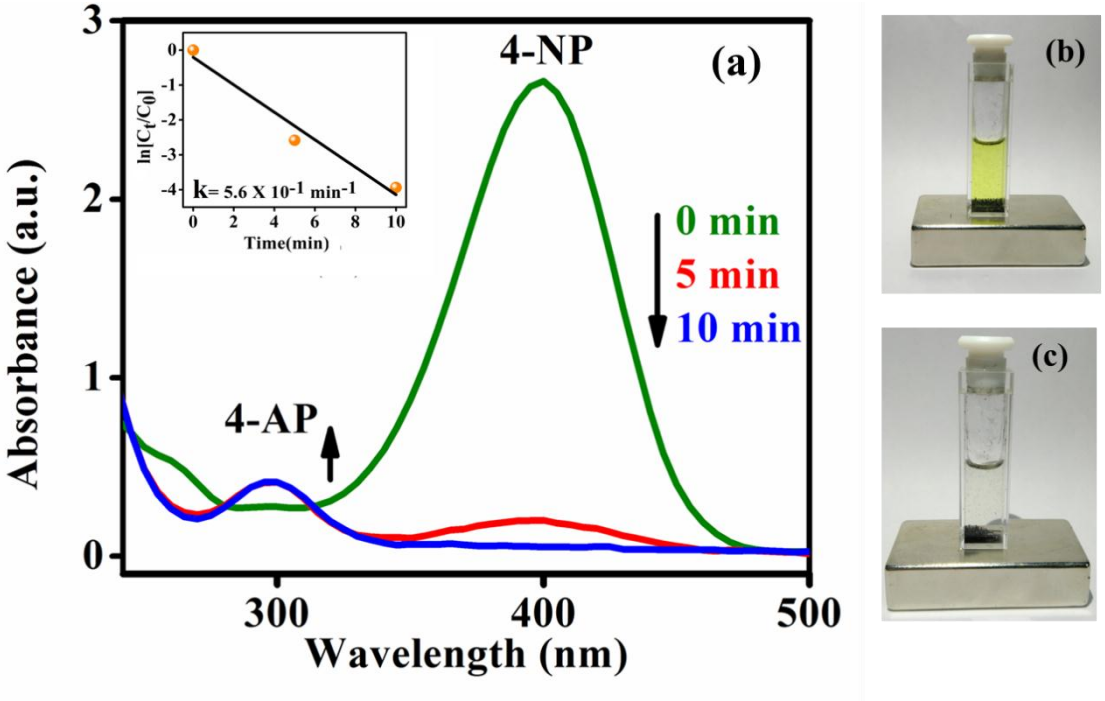

Figure 5.13: (a) The UV/Vis spectral changes of an aqueous solution of 4-NP with $NaBH_4$ solution in presence of CFO NHSs with time, (inset of (a) fitted first order reaction rate). 4-NP solution (b) before and (c) after the catalysis.

Furthermore, we investigated the catalytic property of CFO NHSs under visible light using $NaBH_4$ as reducing agent in transformation of 4-NP. The reduction of 4-nitrophenol (4-NP) to 4-aminophenol (4-AP) is a popularly studied model reaction to evaluate the catalytic activity of metal nanoparticles. In Figure 5.13.(a) it is shown that the transformation of 4-NP to 4-NA occurred in just 10 minutes by $NaBH_4$ in presence of CFO NHSs as catalyst. The reaction follows first order kinetics with the rate constant (k) = 5.6 X 10^{-1} min^{-1}. Though the reduction of 4-NP to 4-AP using aqueous NaBH4 is thermodynamically favourable, the presence of the kinetic barrier due to large potential difference between donor and acceptor molecules decreases the feasibility of this reaction [27-28]. $BH4^-$ ions and 4-nitrophenol co-adsorb on CFO NHSs surface. CFO NHSs relay electrons from donor $BH4^-$ ions to the acceptor 4-nitrophenol to catalyze the reaction.

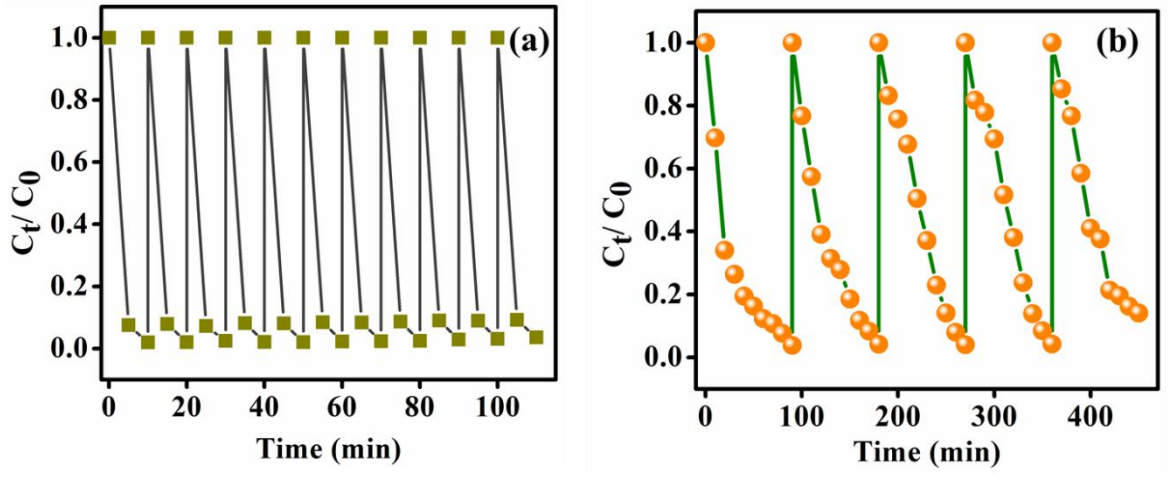

Figure 5.14: Plots of the relative concentration of 4-NP monitored at 400 nm versus time for (a) CFO as catalyst up to 11 consecutive cycles, showing reusability of CFO NHSs in the degradation of 4-NP, (b) FCFO as photocatalyst up to 5 consecutive cycles.

Figure 5.14.(a) depicts the reusability of CFO NHSs as catalyst. We added same dose of 4-NP (50µl) into the reaction mixture up to 11 doses, keeping the catalyst concentration unchanged (i.e., without adding further catalyst after 1st

cycle). The 4-NP degradation rates of the cycles were monitored by measuring the fall of absorbance at 400 nm with UV-Visible spectroscopy. The reusability test was also carried out for FCFO NHSs as photocatalyst and found it worthy up to 5 consecutive cycles, as shown in Figure 5.14.(b).

5.4 Conclusion

Uniform and hollow spherical cobalt ferrite magnetic nanostructures are synthesized by an cost-effective solvothermal method. Through easy surface modification of $CoFe_2O_4$ NHSs with Na-folate and Na-tartrate ligands, we were able to prepare biocompatible multifunctional nano-hollowspheres with intrinsic fluorescence properties covering the whole visible region, ranging from blue, and green, to red. We believe that our material may develop new prospects in the field like bio-imaging. Moreover, the NHSs showed excellent pH and temperature triggered drug release. The loading and pH-dependent releasing of drug occurs due to the hydrogen-bonding interactions between the metal oxide surface attached folate and Doxorubicin. Moreover, we found that the as-prepared and folate functionalized NHSs have efficient catalytic and photocatalytic property respectively towards the transformation of hazardous pharmaceutical waste. In conclusion, this work has demonstrated an efficient multifluorescent anticancer drug delivery system using folate functionalized magnetic nano-hollowspheres.

Bibliography

1. O. Veiseh, J.W. Gunn, M. Zhang, *Design and fabrication of magnetic nanoparticles for targeted drug delivery and imaging*, **Adv. Drug Deliv. Rev**., 2010, 62, 284-304.

2. J. Xie, S. Lee, X. Chen, *Nanoparticle-based Theranostic agents*, **Adv. Drug Deliv. Rev.**, 2010, 62, 1064-1079.

3. C.Y. Wen, H.Y. Xie, Z.L. Zhang, L.L. Wu, J. Hu, M. Tang, M. Wu, D.W. Pang, *Fluorescent/magnetic micro/nano-spheres based on quantum dots and/or magnetic nanoparticles: preparation, properties, and their applications in cancer studies*, **Nanoscale,** 2016, 8, 12406-12429.

4. J. Chen, W. Zhang, M. Zhang, Z. Guo, H. Wang, M. He, P. Xu, J. Zhou, Z. Liuc, Q. Chen, *Mn(II) mediated degradation of artemisinin based on Fe_3O_4@$MnSiO_3$-FA nanospheres for cancer therapy in vivo*, **Nanoscale,** 2015, 7, 12542-12551.

5. S.M. Hoque, C. Srivastava, N. Venkatesha, P.S.A. Kumar, K. Chattopadhyay, *Super paramagnetic behavior and T1, T2 relaxivity of $ZnFe_2O_4$ nanoparticles for magnetic resonance imaging*, **Philos. Mag**., 2013, 93, 1771–1783.

6. M. Chen, S. Yamamuro, D. Farrell, S.A. Majetich, *Gold-coated iron nanoparticles for biomedical applications*, **J. Appl. Phys.**, 2003, 10, 7551-7553.

7. D.K. Yi, S.T. Selvan, S.S. Lee, G.C. Papaefthymiou, D. Kundaliya, J.Y. Ying, *Silica-Coated Nanocomposites of Magnetic Nanoparticles and Quantum Dots*, **J. Am. Chem. Soc.**, 2005, 127, 4990-4991.

8. M. Pal, R. Rakshit, K. Mandal, *Surface Modification of $MnFe_2O_4$ Nanoparticles to Impart Intrinsic Multiple Fluorescence and Novel Photocatalytic Properties*, **ACS Appl. Mater. Interfaces,** 2014, 6, 4903-4910.

9. R.A. Harris, P.M. Shumbula, H. van der Walt, *Analysis of the Interaction of Surfactants Oleic Acid and Oleylamine with Iron Oxide Nanoparticles through Molecular Mechanics Modeling*, **Langmuir**, 2015, 31, 3934−3943.

10. S. Sun, H. Zeng, D.B. Robinson, S. Raoux, P.M. Rice, S.X. Wang, G. Li, *Monodisperse MFe_2O_4 (M = Fe, Co, Mn) Nanoparticles*, **J. Am. Chem. Soc.**, 2004, 126, 273-279.

11. P. Guardia, N. Perez, A. Labarta, X. Batlle, *Controlled Synthesis of Iron Oxide Nanoparticles over a Wide Size Range*, **Langmuir**, 2010, 26, 5843–5847.

12. R. Rakshit, M. Pal, A. Chaudhuri, K. Mandal, *Research Update: Facile synthesis of $CoFe_2O_4$ nano-hollow spheres for efficient bilirubin adsorption*, **APL Mat.**, 2015, 3, 110701-110706.

13. Z. Dai, J. Zhang, J. Bao, X. Huanga, X. Mo, *Facile synthesis of high-quality nano-sized CdS hollow spheres and their application in electrogenerated chemiluminescence sensing*, **J. Mater. Chem.**, 2007, 17, 1087-1093.

14. X. Zou, H. Fan, Y. Tian, M. Zhang, X. Yan, *Microwave-assisted hydrothermal synthesis of Cu/Cu2O hollow spheres with enhanced photocatalytic and gas sensing activities at room temperature*, **Dalton Trans.,** 2015, 44, 7811-7821.

15. S.S. Chen, H. Xu, H.J. Xu, G.J. Yu, X.L. Gong, Q.L. Fang,K.C.F. Leung, S.H. Xuanc, Q.R. Xiong, *A facile ultrasonication assisted method for Fe_3O_4@SiO_2-Ag nanospheres with excellent antibacterial activity*, **Dalton Trans.,** 2015, 44, 9140-9148.

16. P.B. Patil, V.C. Karade, P.P. Waifalkar, P.S. Patil, *Direct functionalization of magnetic hollow spheres with (3-aminopropyl)triethoxysilane (APTES) for targeted drug delivery*, **INTERMAG**, 2017.

17. R.D. Palma, S. Peeters, M.J. Van Bael, H.V. den Rul, K. Bonroy, W. Laureyn, J. Mullens, G. Borghs, G. Maes, *Silane ligand exchange to make hydrophobic superparamagnetic nanoparticles water-dispersible*, **Chem. Mater.**, 2007, 19, 1821-1831.

18. D.H. Kim, D.E. Nikles, D.T. Johnson, C.S. Brazel, *Heat generation of aqueously dispersed $CoFe_2O_4$ nanoparticles as heating agents for magnetically activated drug delivery and hyperthermia*, **J. Magn. Magn. Mater.**, 2008, 320, 2390-2396.

19. L.A. García Cerda, S.M. Montemayor, *Synthesis of CoFe2O4 nanoparticles embedded in a silica matrix by the citrate precursor technique*, **J. Magn Magn. Mat.,** 2005, 294, e43-e46.

20. N. Kaneko, M. Kaneko, H. Takahashi, *Infrared and Raman spectra and vibrational assignment of some metal tartrates*, **Spectrochim. Acta Part A,** 1984, 40, 33-42.

21. V. Ramakrishnan, J.M.T. Maroor, *IR and Raman studies of gel grown manganese tartrate*. **Infrared Phys.**, 1988, 28, 201-204.

22. H.P. Thu, N.H. Nam, B.T. Quang, H.A. Son, N.L. Toan, D.T. Quang, *In vitro and in vivo targeting effect of folate decorated paclitaxel loaded PLA–TPGS nanoparticles*, **Saudi Pharm J**, 2015, 23, 683-688.

23. M. Pal, A. Kundu, R. Rakshit, K. Mandal, , *Ligand-Induced Evolution of Intrinsic Fluorescence and Catalytic Activity from Cobalt Ferrite Nanoparticles*, **ChemPhysChem**, 2015, 16, 1627-1634.

24. X. Yang, X. Zhang, Z. Liu, Y. Ma, Y. Huang, Y. Chen, *High-Efficiency Loading and Controlled Release of Doxorubicin Hydrochloride on Graphene Oxide*, **J. Phys. Chem. C**, 2008, 112, 17554–17558.

25. C. Dey, A. Ghosh, M. Ahir, A. Ghosh, M.M. Goswami, *Improvemnet of anticancer drug release by cobalt ferrite magnetic nanoparticles through combined pH and temperature responsive technique*, **ChemPhysChem**, 2018, 19, 2872-2878.

26. C. Yin, J. Cai, L. Gao, J. Yin and J. Zhou, *Highly efficient degradation of 4-nitrophenol over the catalyst of Mn_2O_3/AC by microwave catalytic oxidation degradation method*, **J. Hazard. Mater.**, 2016, 305,15–20.

27. N. Pradhan, A. Pal, T. Pal, *Silver nanoparticle catalyzed reduction of aromatic nitro compounds*, **Colloids Surf A Physicochem Eng Asp.**, 2002, 196, 247- 257.

28. N. Pradhan, A. Pal, T. Pal, *Catalytic reduction of aromatic nitro compounds by coinage metal nanoparticles*, **Langmuir**, 2001, 17, 1800-1802.

Chapter 6

Adsorption behaviour of $CoFe_2O_4$ nano–hollowspheres

This chapter demonstrates an extraordinary dye adsorption efficiency of $CoFe_2O_4$, which leads to a clean process for textile waste water treatment.

6. Influence of functional group of dye on the adsorption behaviour of $CoFe_2O_4$ nano–hollowspheres

6.1 Preamble

The rapid growth of industry makes people be aware of the need to clean up water effluents. A long term research has been carried out in finding new innovative methods for reducing the environmental pollution caused by water effluents. There are several types of waste materials that do not readily lend themselves to standard methods of water treatment. Dye [1], a stable, recalcitrant, colorant which has been extensively used in textile, paper, leather, and cosmetic industry is one of them since they are very stable to light and oxidizing agents. Dispose of dye effluents into water causes severe problems in nature. It increases the biological and chemical oxygen demands which are very dangerous to aquatic plants and animals. Moreover, it interrupts photosynthesis, degrades soil quality, and affects the growth of plants. Due to carcinogenic and toxic nature of dye, their release into environment poses serious aesthetical, and health problems to human being. Thus, industrial dye effluents need to be effectively treated before being discharged into the environment.

There are a large number of physical methods such as oxidation [2], coagulation and flocculation [3], ultra chemical filtration [4], membrane separation [5], catalysis [6], chemical treatments [7], and adsorption [8] for the removal of dye from its aqueous solution. Among them, adsorption is one of the most investigated techniques for dye removal, mainly due to its simplicity and high level of effectiveness [9]. Various adsorbents including activated carbons [10], zeolites [11], clays [12], and polymers [13] have been used for removing different organic and inorganic dyes from the waste water of textile and dye industries. However, they suffer from low adsorption capacity and separation

inconvenience. In this regards, magnetic metal oxide nanostructures have attracted tremendous attention due to their large specific surface area, magnetism, and chemical stability which facilitate high adsorption, fast magnetic separation after dye adsorption along with excellent recycling capability. Wu et. al. [14] have reported enhanced selective organic dye adsorption of magnetic $CoFe_2O_4$ nanoparticles in terms of different electrostatic interaction between the surface charges of adsorbents and adsorbates. Tan and his research group have demonstrated $CoFe_2O_4$–graphene nanocomposite as a potential candidate for uranium extraction [15]. Recently, researchers are very much interested in developing super adsorbent for very rapid dye sequestration from waste water. For example, Zhou et. al. [16] has reported the adsorption of different organic dyes on carboxylic hyperbranched polyglycerol functionalized iron oxide–silica dendritic magnetic nanoparticles within only 15 min. Chen and co–workers reported polyacrylic acid [17] and carboxymethylated chitosan [18] conjugated Fe_3O_4 magnetic adsorbents for efficient adsorption of basic and acid dyes within 20–30 min respectively. Li et. al.[19] has fabricated magnetic alginate beads with well dispersed polydopamine functionalized $CoFe_2O_4$ nanoparticles which also exhibit excellent dye adsorption performance due to composite effect, large surface area, and porous structure. However, postgrafting of porous nanostructures with different functional groups in order to have high adsorption capability is relatively complicated, cost–effective, and also difficult for recycling. Therefore, development of nanostructures with very high specific surface area is a promising route for fast and worthwhile removal of contaminants from waste water and hollow nanostructures have drawn tremendous attention of the researchers in this regard. Lie et. al. [20] has reported the synthesis of hierarchical NiO–SiO_2 composite hollow microspheres and their excellent adsorption affinity towards congo red in water. The double interfaces and hollow interior of the micro–hollow spheres significantly

enhance the effective surface area for dye adsorption. Moreover, its large pore volume helps to encapsulate toxic material which is impervious for solid particle configuration. The comparative dye adsorption studies between solid and hierarchical porous ZnO microspheres [21] by Lie and his co-workers further confirm that specific surface area, pore size, and pore volume significantly determine the dye adsorption behaviour of adsorbents.

In this article, we have synthesised magnetic $CoFe_2O_4$ nano-hollow spheres (NHSs) of different diameter through one–pot simple template free solvothermal method and highlighted the effect of different functional groups of dye on their adsorption behaviour. For this purpose, we have chosen the dyes named, fluorescein, bromophenol blue, and bromocresol green in which fluorescein contains –COOH and –OH groups whereas bromophenol blue and bromocresol green contain $–SO_3H$ and –OH groups. Moreover, bromophenol blue and bromocresol green, having same functional groups helps to identify the adsorption behaviour of $CoFe_2O_4$ NHSs solely evoked by the steric hindrance offered by the dye molecule. We have demonstrated an elucidative correlation between the nature of dye and the adsorption properties of $CoFe_2O_4$ NHSs in terms of electronic density and complexity of the dye molecule. It is found that the employment of $CoFe_2O_4$ NHSs into the dye solution leads to its complete decolourization within a very few minutes through heterogeneous physisorption, a clean process for textile waste water treatment. Finally, desorption of dyes from the NHS surface has been carried out at higher pH~11 in order to reutilize them as a potent magnetic nanodevice having high dye adsorption efficiency.

6.2. Experimental

6.2.1 Materials Used

For the synthesis of $CoFe_2O_4$ NHSs, the precursor salts, cobalt chloride ($CoCl_2$, $6H_2O$) and ferric chloride ($FeCl_3$, $6H_2O$); the solvents, ethylene glycol and ethanol; the base, urea; and the capping agent, oleylamine are purchased from Sigma–Aldrich. For the investigation of dye adsorption efficiency of $CoFe_2O_4$ NHSs, the dyes fluorescein ($C_{20}H_{12}O_5$), bromophenol blue ($C_{19}H_{10}Br_4O_5S$), and bromocresol green ($C_{21}H_{14}Br_4O_5S$) are obtained from Merck. All laboratory reagents are of analytical grade. Finally, the aqueous solution of dyes of desired concentrations is prepared utilizing double distilled water.

6.2.2 Synthesis and Characterization

We have prepared $CoFe_2O_4$ NHSs by a facile template free solvothermal route in which a mixture solution of $CoCl_2$, $6H_2O$, $FeCl_3$, $6H_2O$, ethylene glycol, ethanol, urea, and oleylamine was heated in a teflon lined stainless steel autoclave at 180 ^{0}C for 12 hours as described in our previous report [22]. The diameter of the $CoFe_2O_4$ NHSs was varied from 100, 160, to 250 nm (NHS–100, NHS–160, and NHS–250) only by reducing the amount of capping agent, oleylamine from 6 to 4 ml while keeping all other parameters same. The key role of oleylamine is to control the growth of $CoFe_2O_4$ nanocrystals where increasing amount of capping agent restricts the crystal growth more. Finally, the as–prepared black precipitation was washed in alcohol and dried at 60 ^{0}C overnight before characterization.

To investigate the phase of as–prepared samples, we have performed X–ray diffraction (XRD) by Rigaku Miniflex II desktop X–ray diffractometer using Cu K_α (λ= 1.5418Å) radiation. The morphology, crystallinity, particle size, and elemental analyses of the nanostructures were carried out using transmission

electron microscope (TEM) with model TECHNAI G^2 TF20, operating at 200 kV. The sample for TEM measurement was prepared by casting a few drops of well dispersed alcohol solution of as–prepared sample on carbon coated Cu grid, followed by drying in open air. The specific surface area and pore size distribution of $CoFe_2O_4$ NHSs of different diameters were measured through N_2 (Nitrogen) adsorption/desorption isotherms using Quantachrome Autosorb 1C by utilizing Brunauere Emmette Teller (BET) and Barrete Joynere Halenda (BJH) methods. The dye adsorption behaviour of $CoFe_2O_4$ NHSs was recorded through Shimadzu model UV–2600 spectrophotometer by using a quartz cuvette of 1 cm path length. Finally, the interaction and the attachment of dye molecules with the adsorbent surface were confirmed through Fourier transformed infra–red (FTIR, JASCO FTIR–6300) and EDX spectroscopic analyses. EDX is performed in field emission scanning electron (FESEM, FEI QUANTA FEG-250), operating at 10 kV. For FTIR measurement, the pellets were prepared after homogeneous mixing of pristine and dye adsorbed $CoFe_2O_4$ NHSs individually with KBr which is used as a reference and the samples for EDX measurement were prepared in a similar manner as TEM except by drop casting well dispersed water solution of dye adsorbed $CoFe_2O_4$ nano-powder on silicon wafer.

6.2.3 Dye adsorption

We have performed the dye adsorption experiments with three kinds of adsorbate, namely (1) Fluorescein, (2) Bromophenol blue, (3) Bromocresol green. Typically, 0.01 g of $CoFe_2O_4$ adsorbent of different diameter was mixed with 4 ml of dye solution at various concentrations ranging from 0.03–0.2 mg ml^{-1} at pH~7. After magnetic stirring at a rate of 120 rpm for 2 min, the mixture solution was centrifuged and a small amount of liquid were taken to be analyzed by UV–visible (UV–Vis) absorption spectroscopy where we monitored the absorbance change at the wavelength of maximum absorbance. The amount of

dye on $CoFe_2O_4$ NHSs was calculated from the following equation:

$$q_t = \frac{(C_0 - C_t)V}{m} \qquad (6.1)$$

where, q_t (mg g^{-1}) is the amount of dye adsorbed at time t, C_0 and C_t (mg ml^{-1}) are the dye concentrations at initial and any time respectively. V (ml) is the volume of dye solution, and V (g) is the mass of the adsorbent. All the experiments were carried out at room temperature.

6.3. Results and discussion

Figure 6.1.(a) shows the XRD patterns for all as–synthesized $CoFe_2O_4$ NHSs of diameter 100, 160, and 250 nm. All the diffraction peaks exactly match with face centred cubic inverse spinel structure (JCPDS card no. 22–1086) of $CoFe_2O_4$. From broadening of the peak (311), the crystallite size of all the samples is calculated using Debye Scherrer's equation and it is found to increase with increasing diameter of the NHSs as mentioned in Table 6.1. Energy–dispersive X–ray (EDX) spectroscopic analysis of $CoFe_2O_4$ NHS–250, as depicted in the inset of Figure 6.1.(a) confirms the presence of carbon (C) and copper (Cu) which are due to carbon coated Cu grid in which well dispersed alcoholic solution of $CoFe_2O_4$ NHSs is drop casted. The presence of C may also be due to the capping agent, oleylamine which is used as a surface stabilizer and growth modifier during the synthesis of $CoFe_2O_4$ NHSs. Finally, the existence of elemental composition of Co, Fe, and O is as a result of $CoFe_2O_4$ phase. Figures 6.1.(b)–(c) indicate the transmission electron micrographs of $CoFe_2O_4$ NHS–100, NHS–160, and NHS–250 where the dark and bright contrasts between the margin and the centre of the particle clearly indicate the hollow interior of as–prepared nanostructures. The average diameter and the shell thickness of the samples were calculated from these TEM images and listed in Table 6.1.

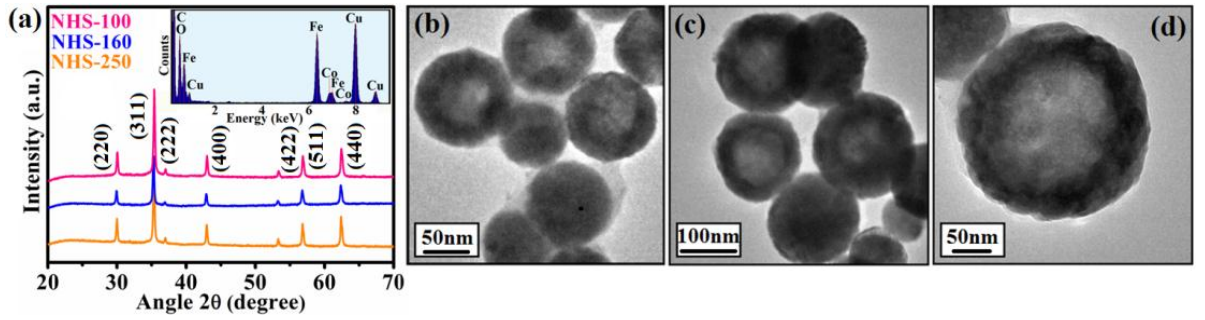

Figure 6.1: (a) XRD patterns of all $CoFe_2O_4$ NHSs of different diameters. Inset shows the EDX spectrum of $CoFe_2O_4$ NHS–250. TEM images of $CoFe_2O_4$ NHS– (b) 100, (c) 160, and (d) 250.

Corresponding to the black rectangular area of $CoFe_2O_4$ NHS–250, as shown in Figure 6.2.(a), we have taken high resolution TEM (HRTEM) image which confirms the high crystallinity of as–prepared sample, as shown in Figure 6.2.(b). The calculated inter–planar distance between the lattice fringes is about 0.251 nm, which corresponds to the distance between (311) planes of $CoFe_2O_4$ crystal lattice. Figure 6.2.(c) shows the selected area electron diffraction (SAED) pattern of the same selected area of NHS–250. Figures 6.2.(d) and 6.2.(e) show the N_2 adsorption–desorption isotherms and BJH plots of all $CoFe_2O_4$ NHSs of different diameters. The isotherms in Figure 6.2.(d) can be categorized as type IV, with a hysteresis loop in the range of 0.3–1.0 p/p_0. The specific surface area and pore volume of $CoFe_2O_4$ NHSs are found to vary from 584–948 $m^2\ g^{-1}$ and 1.05–1.35 $cm^3\ g^{-1}$ respectively whereas the average pore sizes of the NHSs, as observed from BJH plots vary from 2.85–2.98 nm with increasing NHS diameters from 100–250 nm as listed in Table 6.1. These pores facilitate the diffusion which is essential for many applications such as sensing, supercapacitor, immobilization support for enzymes, catalysis, and adsorption studies.

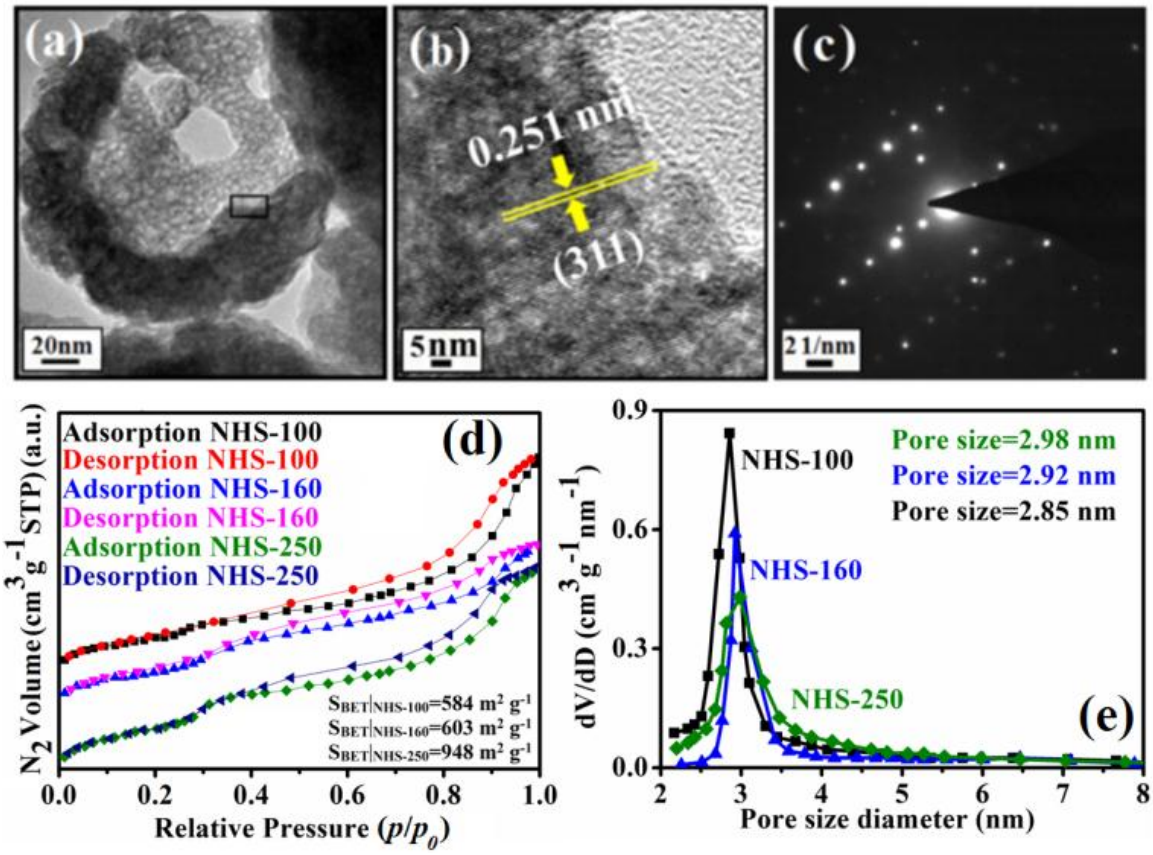

Figure 6.2: (a) TEM image of $CoFe_2O_4$ NHS–250, (b) HRTEM image of the area selected by black rectangle of NHS–250, (c) SAED pattern of that same selected area, (d) N_2 adsorption/desorption isotherms, (e) BJH plot of $CoFe_2O_4$ NHS–100, NHS–160, and NHS–250.

Table 6.1. List of average particle diameter, crystallite size, shell thickness, specific surface area, pore size, and total pore volume of as–synthesized $CoFe_2O_4$ NHSs of different diameters.

Sample Name	Average diameter (nm)	Crystallite size (nm)	Shell thickness (nm)	Surface area ($m^2\ g^{-1}$)	Pore size (nm)	Total Pore volume ($cm^3\ g^{-1}$)
NHS-100	100±4	40.32	18	584	2.85	1.05
NHS-160	160±5	42.57	38	603	2.92	1.18
NHS-250	250±7	44.19	43	948	2.98	1.35

Considering the significant progress in waste water treatment through rational engineering and manipulation of magnetic nanomaterials, we aimed to utilize our developed $CoFe_2O_4$ NHSs in the removal of different dyes such as fluorescein, bromophenol blue, and bromocresol green. The molecular structures of these dyes, as shown in inset of Figures 6.3.(a)–(c) indicate that the dye, fluorescein contains the carboxyl group (–COOH) whereas bromophenol blue and bromocresol green contain the sulfonyl group ($–SO_3H$) in addition to hydroxyl group (–OH). Figures 6.3.(a)–(c) show the comparative adsorption studies of these dyes over time through UV–Vis spectroscopy in presence of $CoFe_2O_4$ NHS–250 at pH~7 with initial dye concentration 0.03 mg ml^{-1}. It is found that $CoFe_2O_4$ NHSs exhibit an unprecedented efficiency in the removal of these dyes. It adsorbs a total 95% of fluorescein, 32% of bromophenol blue, and 15% of bromocresol green dyes within only 2 min and reaches equilibrium in about 4, 6, and 10 min respectively which ensure that the developed magnetic adsorbent is a potential candidate for waste water purification. Figures 6.3.(d)–(f) exhibit the EDX spectroscopic analyses of all dye adsorbed $CoFe_2O_4$ NHSs, indicating the presence of C in case of fluorescein and C, S, and Br for bromophenol blue and bromocresol green dyes in addition to Co, Fe and O of $CoFe_2O_4$ phase. The peak of silicon (Si) is due to the substrate on which dye adsorbed $CoFe_2O_4$ NHSs, dispersed in water through ultra-sonication was drop casted.

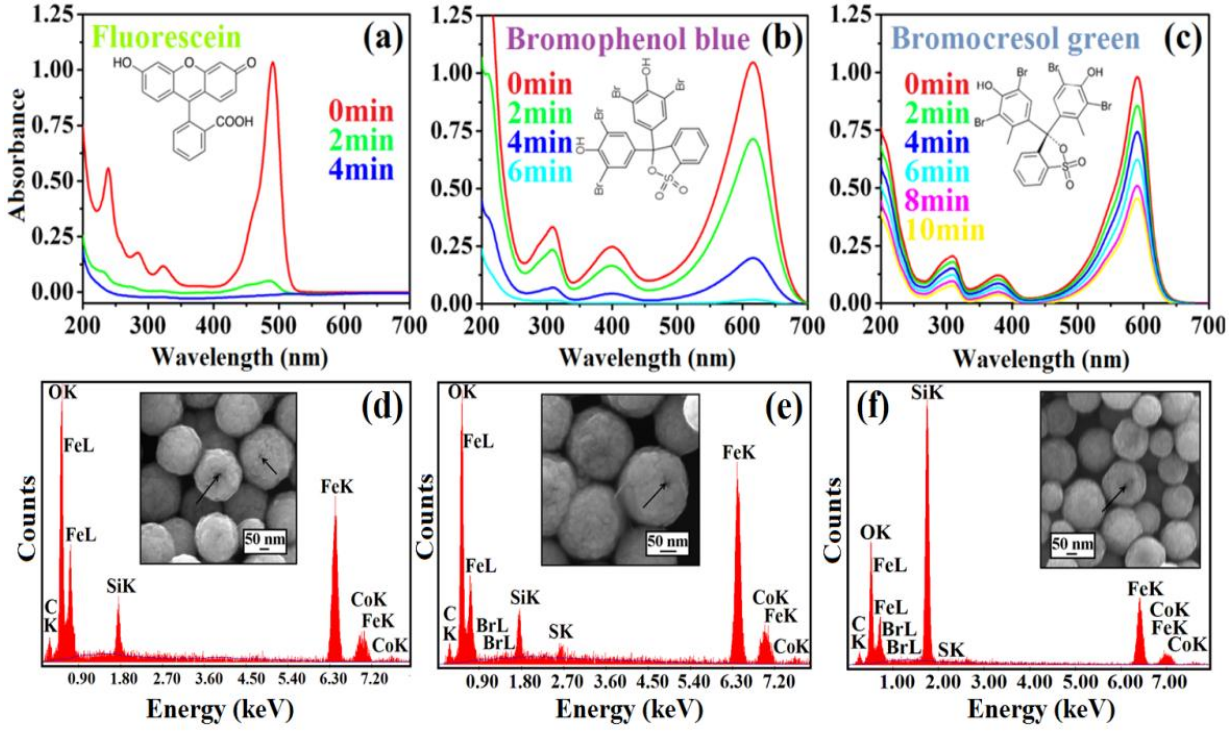

Figure 6.3: UV–vis spectral changes of aqueous solution of (a) fluorescein, (b) bromophenol blue, and (c) bromocresol green with time in presence of $CoFe_2O_4$ NHS–250 at pH~7 respectively. The inset shows the molecular structures of the corresponding dyes.EDX spectrum of the (d) fluorescein, (e) bromophenol blue, and (f) bromocresol green adsorbed $CoFe_2O_4$ NHS–250, indicating the presence of the elemental composition of Co, Fe, and O of $CoFe_2O_4$ in addition the components of dye. Inset shows corresponding FESEM images of dye adsorbed $CoFe_2O_4$ NHS–250 where arrow indicates hollow interior of NHSs.

In order to investigate the origin of excellent adsorption activity of as–prepared $CoFe_2O_4$ NHSs, we have studied the interaction between the adsorbate and the adsorbent molecules through FTIR spectroscopy, as shown in Figure 6.4. The peaks at 584 and 421 cm^{-1} are attributed to the spinel structure of $CoFe_2O_4$ where two modes are due to the motion of oxygen with respect to tetrahedral and octahedral cations in the spinel cell [23]. The complete FTIR spectrum of $CoFe_2O_4$ NHSs indicates that there exist all the characteristic peaks of oleylamine. The low intensity peaks at 3001, 2932, and 2852 cm^{-1} are attributed to the vibration of =C–H group, anti–symmetric and symmetric stretching vibrations of $–CH_2$ group of oleylamine respectively [24]. Moreover,

the shoulder at 1641 cm^{-1} and the peaks at 1514 and 722 cm^{-1} are also the characteristic of C=C and $–NH_2$ groups [25] of oleylamine respectively. Therefore, the excellent dye adsorption of $CoFe_2O_4$ NHSs is derived from the strong electrostatic interaction between the positive surface $–NH_2$ group of adsorbent and the negative functional groups (–OH, $–COO^-$, $–SO_3^-$) of adsorbate which is also visualized from the broadening and shifting of $–NH_2$ peaks of dye adsorbed $CoFe_2O_4$ NHSs. Further, the band around 3000–3600 cm^{-1}, corresponding to the stretching vibrational modes of surface −OH group [26] of $CoFe_2O_4$ NHSs is found to be broadened after dye adsorption. In general, $CoFe_2O_4$ nanomaterials contain surface −OH groups due to atmospheric water that can easily bond with other molecules. Therefore, the broadening of that band for dye adsorbed $CoFe_2O_4$ NHSs indicates the formation of hydrogen bonding between the surfaces –OH groups of adsorbent and the functional –OH groups of adsorbate molecules [27] which leads to outstanding dye adsorption.

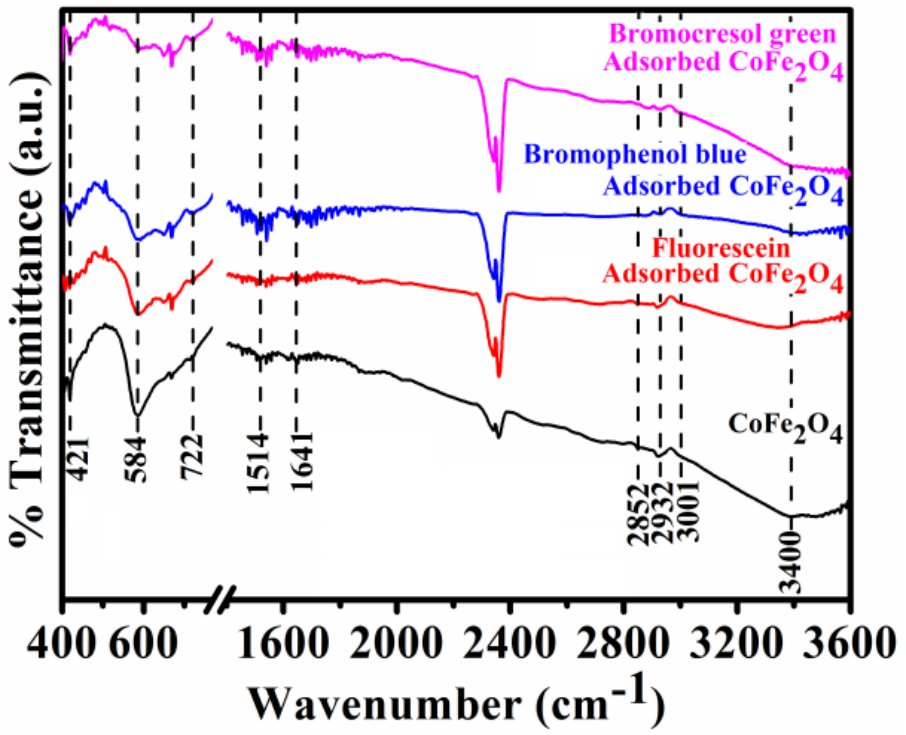

Figure 6.4: Comparative FTIR spectra of as–synthesised $CoFe_2O_4$ NHSs and fluorescein, bromophenol blue, and bromocresol green adsorbed $CoFe_2O_4$ NHSs.

To find the controlling mechanism of adsorption such as mass transfer, physisorption, and chemisorption; we have employed different kinetic models namely, intraparticle diffusion (mass transfer) model, pseudo 1st order (physisorption), and pseudo 2nd order (chemisorption) models to the experimentally obtained UV–Vis spectroscopic data. In case of intraparticle diffusion model of Weber and Morris [28], the rate equation is expressed by Equ. 6.2, where q_t is the amount of dye adsorbed at time t (min), k_i (min$^{-1/2}$) is the intraparticle diffusion rate constant. A straight line of q_t vs. $t^{1/2}$ graph and the positive intercept suggest the applicability of this kinetic model in which adsorption occurs due to mass transfer. The positive intercept is proportional to the extent of boundary layer thickness of dye whereas negative intercept discards the intraparticle diffusion model. For pseudo 1st order model [29], the rate equation of Lagergren is given by Equ. (6.3), where q_{e_1} is the amount of dye adsorbed at equilibrium and k_1 (min^{-1}) is the 1st order adsorption rate constant. Herein, a straight line of $\log(q_{e_1} - q_t)$ vs. t graph suggests the applicability of pseudo 1st order kinetic model where physisorption is the main mechanism for adsorption. Similarly, a straight line of t/q_t vs. t graph corresponding to the pseudo 2nd order rate equation of Langmuir [30] as shown in Equ. 6.4, where k_2 (min^{-1}) is the 2nd order rate constant indicates chemisorption.

$$q_t = k_i t^{1/2} + C \qquad (6.2)$$

$$\log(q_{e_1} - q_t) = log q_{e_1} - \frac{k_1}{2.303} t \qquad (6.3)$$

$$\frac{t}{q_t} = \frac{1}{k_2 q_{e_2}^2} + \frac{1}{q_{e_2}} t \qquad (6.4)$$

The linearized plots of these models for initial dye concentration of 0.07 mg ml^{-1} and 0.01 g of $CoFe_2O_4$ NHS–250 are shown in Figure 6.5.(a) – 6.5.(i). The values of rate constant (k), amount of dye adsorbed on adsorbate at equilibrium

(q_e), and correlation coefficients (R^2) are calculated from these plots and presented in Table 6.2. It is found that the values of R^2 for the intraparticle diffusion and pseudo 1st order models are of the order of 0.99, and the calculated q_e and q_{e_1} values are nearly equal to the experimental values, which suggest that the adsorption process basically follows the intraparticle diffusion and pseudo 1st order models. However, the intercepts (*C*) of intraparticle diffusion model for bromophenol blue and bromocresol green dyes are found to be negative, as listed in Table 6.2 which suggests inapplicability of this model in which mass transfer is the process of adsorption. Hence, the adsorption of fluorescein dye over the NHS surface is determined by both the mass transfer and physisorption processes whereas other dyes follow physisorption only. The FTIR study already confirms that there exists an electrostatic attraction and hydrogen bonding between the adsorbate and the adsorbent which leads to strong physisorption. In addition, meticulous analysis of Table 6.2 indicates that fluorescein dye, having functional group of $–COO^-$ exhibits higher rate of physisorption than the other dyes, containing functional group of $–SO_3^-$ which is also observed from UV–Vis spectroscopic analyses, as shown in Figure 6.3.(a)–(c). It may be due to greater electron density of $–COO^-$ group than $–SO_3^-$ group which strengthens the interaction of dye molecule with the NHS surface and thus accelerates the process of physisorption. In addition, bromophenol blue is found to exhibit higher rate of physisorption than bromocresol green in spite of both having same functional groups (–OH and $–SO_3^-$). It may be due to more sterically hindered configuration of bromocresol green in contrast to bromophenol blue.

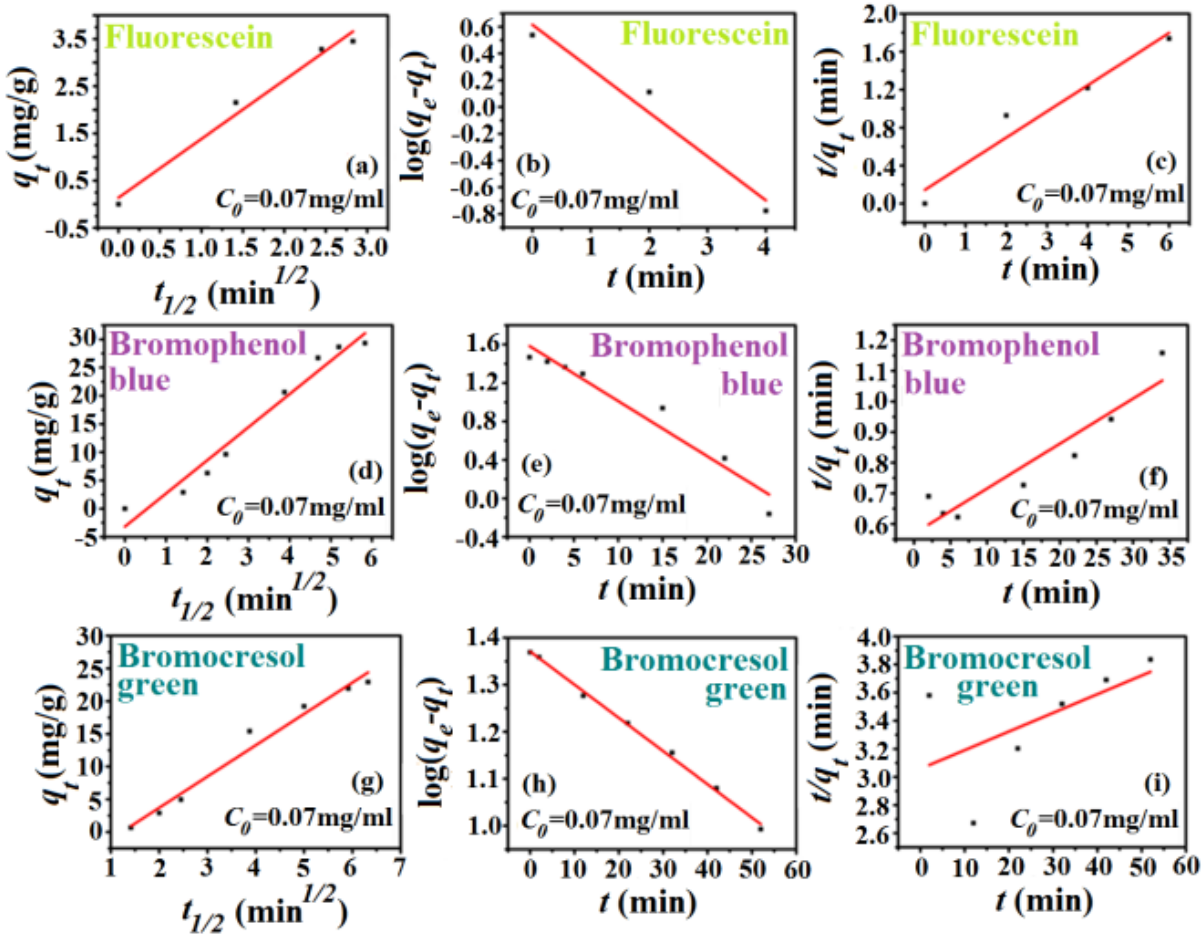

Figure 6.5: Intraparticle diffusion, pseudo 1st order, and pseudo 2nd order kinetic models for fluorescein, bromophenol blue, and bromocresol green adsorption over $CoFe_2O_4$ NHS–250 at room temperature.

Table 6.2. Intraparticle diffusion, pseudo 1st order, and pseudo 2nd order kinetic model parameters for different dye adsorption over $CoFe_2O_4$ NHS–250 at room temperature.

$CoFe_2O_4$ NHS-250 (g)	Name of dye	Dye (mg ml^{-1})	$q_{e,exp}$ (mg g^{-1})	Intraparticle diffusion Model				Pseudo 1st order model			Pseudo 2nd order model		
				q_{e_i} (mg g^{-1})	k_i (mg g^{-1} min$^{-1/2}$)	C	R^2	q_{e_1} (mg g^{-1})	k_1 (min^{-1})	R^2	q_{e_2} (mg g^{-1})	k_2 (g mg^{-1} min^{-1})	R^2
0.01	Fluorescein	0.07	3.45	3.19	1.25	0.14	0.99	4.12	0.76	0.98	3.7	0.52	0.97
	Bromophenol blue		29.3	31.1	5.87	-3.16	0.98	38.3	0.13	0.98	71.4	$3x10^{-4}$	0.94
	Bromocresol green		24.5	23.0	4.78	-5.86	0.99	27.5	0.09	0.99	-134	$3x10^{-5}$	0.17

The linearized plots of pseudo 1st order kinetic model for $CoFe_2O_4$ NHS–250 in presence of bromocresol green with different dye concentration ranging from 0.03 to 0.2 mg ml^{-1} are shown in Figure 6.5.(a) whereas Figure 6.5.(b) indicates the same kinetic model for $CoFe_2O_4$ NHSs of different diameters with a fixed 0.03 mg ml^{-1} bromocresol green concentration. The values of rate constant (k), amount of dye adsorbed on adsorbate at equilibrium (q_e), and correlation coefficients (R^2) are calculated from these plots are presented in Table 6.3 and Table 6.4. Table 6.3 indicates that with variation of initial dye concentration from 0.03 to 0.2 mg/ml, a considerable increase in q_e values occurs and it ranges from 11.49 to 68.22 mg g^{-1} for 0.01 g of $CoFe_2O_4$ NHS–250. It is mainly due to the presence of more adsorbate for a fixed amount of adsorbent. Moreover, the pseudo 1st order rate constants are found to decrease with increasing dye concentration, indicating decrease in driving force with increasing initial dye concentration. The size dependent study as shown in Figures 6.5.(b) reveals that the amount of adsorbate absorbed per unit mass of adsorbent increases with increasing size of the NHSs. Moreover, Table 4 points out that the physisorption rate also increases with increasing size of the NHSs. These increasing adsorption performances are attributed to increasing specific surface area and nano–pore size of $CoFe_2O_4$ NHSs with increasing size.

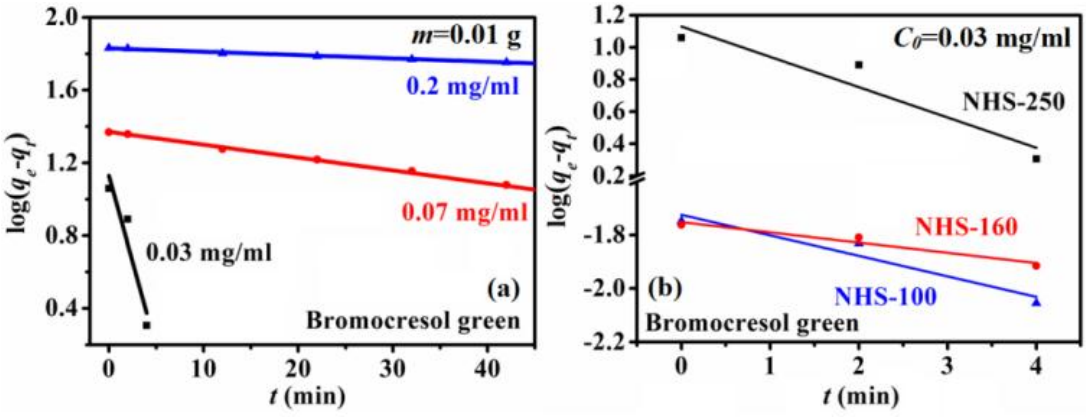

Figure 6.6: Pseudo 1st order adsorption kinetics of bromocresol green dye solution with (a) different initial dye concentration and 0.01 g of $CoFe_2O_4$ NHS–250, (b) fixed initial dye concentration of 0.03 mg ml^{-1} and 0.01 g of $CoFe_2O_4$ NHSs of different diameter.

Table 6.3. Pseudo 1st order kinetic model parameters for different initial bromocresol green concentrations on $CoFe_2O_4$ NHS–250 at room temperature.

Name of adsorbate	Adsorbate (g)	C_0(mg ml^{-1})	$q_{e,exp}$ (mg g^{-1})	Pseudo 1st order model		
				q_{e_1} (mg g^{-1})	k_1 (min^{-1})	R^2
$CoFe_2O_4$ NHS-250	0.01	0.03	11.49	13.48	0.43	0.96
		0.07	24.55	27.48	0.09	0.99
		0.2	68.02	67.59	0.004	0.99

Table 6.4. Adsorption capacity at equilibrium (q_e) of different $CoFe_2O_4$ NHSs for a given amount of adsorbate and bromocresol green concentration in case of pseudo 1st order model.

Size of $CoFe_2O_4$	Adsorbate (g)	C_0 (mg ml^{-1})	$q_{e,exp}$ (mg g^{-1})	Pseudo 1st order model		
				q_{e_1} (mg g^{-1})	k_1 (min^{-1})	R^2
NHS-250	0.01	0.03	12.00	13.48	0.43	0.95
NHS-160			0.018	0.018	0.18	0.98
NHS-100			0.017	0.017	0.08	0.98

The analysis of equilibrium sorption data by fitting them to different isotherm models is another important step for the description of how adsorbate will interact with the adsorbent. Figures 6.7.(a)–(c) show the equilibrium isotherms of bromocresol green adsorption into three different models, named Langmuir [31], Freundlich [32] and Dubinin Radushkevich [33] (D–R) and their corresponding parameters are represented in Table 6.5. The Langmuir equation is valid for monolayer adsorption on a surface of adsorbate with a finite number of identical sites and is expressed as:

$$\frac{C_e}{q_e} = \frac{1}{q_m K_L} + \frac{1}{q_m} C_e \qquad (6.5)$$

where, C_e (mg ml^{-1}) is the initial concentration of adsorbate and q_e (mg g^{-1}) is

the amount of adsorbate adsorbed per unit mass of adsorbent. q_m is the maximum amount of dye per unit mass of adsorbent to form a complete monolayer on the surface at high C_e (mg ml^{-1}) and K_L (ml mg^{-1}) is a constant related to the affinity of binding sites. The Freundlich isotherm based on adsorption on a heterogeneous surface is given by the equation:

$$logq_e = logK_F + \frac{1}{n} logC_e \qquad (6.6)$$

where, K_F (mg g^{-1} (ml $mg^{-1})^{1/n}$) and *n* are Freundlich constants which indicates how favourable is the adsorption process. K_F is the adsorption capacity of the adsorbent which can be defined as the adsorption or distribution coefficient and represents the quantity of dye adsorbed onto $CoFe_2O_4$ NHSs for a unit equilibrium concentration. The slope of 1/*n* ranging between 0 and 1 is a measure of adsorption intensity or surface heterogeneity, becoming more heterogeneous as its value gets closer to zero. D–R isotherm [33] is represented by the following equation:

$$lnq_e = lnQ_0 - K_{DR}\varepsilon^2 \qquad (6.7)$$

where K_{DR} (mol^2 kJ^{-2}) is a constant related to mean adsorption energy and ε is the Polanyi potential. The slope of the plot of lnq_evs. ε^2gives K_{DR}, and the intercept yields the sorption capacity, Q_0 (mg g^{-1}). *T* is the absolute temperature in Kelvin, and *R* is the universal gas constant (8.314 J mol^{-1} K^{-1}). Figure 6.7.(a)–(c) indicates that equilibrium sorption data of bromocresol green on $CoFe_2O_4$ NHS–250 excellently fits to Freundlich adsorption isotherm model with highest correlation co–efficient of 0.99. The 1/*n* value obtained from Freundlich isotherm, as presented in table 6.5 indicates a moderate multilayer adsorption intensity of dye molecule over the heterogeneous surface of $CoFe_2O_4$ NHSs.

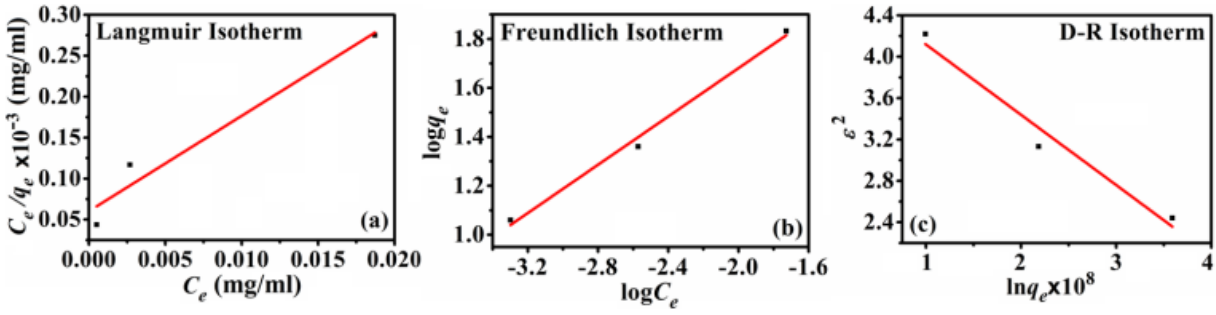

Figure 6.7: (a) Langmuir, (b) Freundlich, (c) D–R isotherm models for bromocresol green adsorption on $CoFe_2O_4$ NHS–250.

Table 6.5. Isotherm model parameters of bromocresol green adsorption on $CoFe_2O_4$ NHS–250.

Name	Langmuir Isotherm			Freundlich Isotherm			D–R Isotherm		
$CoFe_2O_4$ NHS–250	q_m	K_L	R^2	K_F	1/n	R^2	Q_0	K_{DR}	R^2
	85.91	193.35	0.98	464.94	0.49	0.99	121.098	6.791	0.98

The regeneration capability of the adsorbent is very important from the view point of industrial applications. It is found that all the adsorbed dye can be completely desorbed from the surface of $CoFe_2O_4$ NHSs at pH~11 and therefore, these magnetic nanostructures can be used very efficiently for multiple times. Desorption of dyes from the $CoFe_2O_4$ NHSs surface in the pH range of 8–11 is shown in Figure 6.8, indicating that desorption efficiency increases with increasing pH of the solution. At pH~10, the desorption efficiency of fluorescein, bromophenol blue, and bromocresol green is found to vary in the range of 95–98% and at pH of 11, almost 100% desorption is achieved from the $CoFe_2O_4$ NHSs surface for all the dyes. The relative average adsorption efficiency of $CoFe_2O_4$ NHSs for the dyes is found to be ~94%, 81%, 71%, and 65% for second, third, fourth, and fifth cycle respectively, where the average adsorption efficiency of 1st cycle was taken as ~100%. This indicates $CoFe_2O_4$ NHSs are versatile and robust adsorbent with both magnetic property and very high adsorption capacity for dyes containing negative functional

groups (–OH, $–COO^-$, and $–SO_3^-$) with multi–cyclic efficiency.

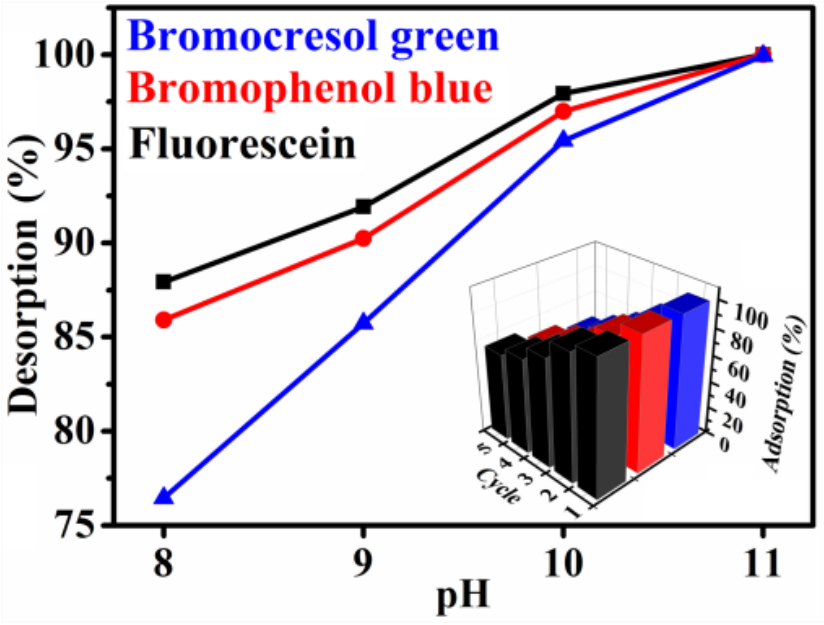

Figure 6.8: Percentage desorption of fluorescein, bromophenol blue, and bromocresol green from $CoFe_2O_4$ NHS–250 at different pH. The inset shows the multi–cyclic percentage adsorption efficiency of the same.

6.4. Conclusion

In summary, we have synthesised $CoFe_2O_4$ NHSs of different diameter through facile solvothermal technique and demonstrated their excellent adsorption activity in the removal of fluorescein, bromocresol green, and bromophenol blue dyes. The nanoscale particle size, hollow porous nature, and the presence of $–NH_2$ and –OH functional groups on the surface of $CoFe_2O_4$ NHSs show favourable adsorption for all these anionic dyes through electrostatic interaction and hydrogen bonding, as confirmed from FTIR analysis. The $CoFe_2O_4$ NHSs are found to exhibit higher rate of adsorption for fluorescein than bromocresol green and bromophenol blue due to difference in strength of electrostatic interaction between the cationic surface functional group of NHSs and anionic functional group of dyes. Moreover, the comparative adsorption rate analysis of bromocresol green and bromophenol blue dyes, both having same functional

group ($–SO_3^-$ and –OH) reveals that steric hindrance offered by the dye molecule plays an important role in adsorbing the dye molecule on $CoFe_2O_4$ surface. The adsorption kinetics and isotherm of $CoFe_2O_4$ NHSs are found to excellently fit to pseudo 1^{st} order kinetics and Freundlich isotherm model respectively, indicating heterogeneous physisorption of dyes over the NHS surface. The process adsorption is also investigated by varying the initial dye concentration and the size of the $CoFe_2O_4$ NHSs which indicates that the amount of dye adsorbed on the surface of $CoFe_2O_4$ NHSs increase with increasing size of the NHSs and initial dye concentration. Moreover, these adsorbed dyes can be completely desorbed from the surface of $CoFe_2O_4$ NHSs at pH ~11 and show significant multi–cyclic adsorption efficiency. We believe that the excellent adsorption efficiency of $CoFe_2O_4$ NHSs in removal of dyes along with multi–cyclic efficiency can be significantly utilized for their potential application in waste water treatment.

Bibliography

1. G. Booth, *Dyes, General Survey*, **Wiley-VCH**, German, 2000.

2. H. Y. Shu, C. R. Huang and M. C. Chang, *Decolorization of mono-azo dyes in wastewater by advanced oxidation process: A case study of acid red 1 and acid yellow 23*, **Chemosphere**, 1994, **29**, 2597-2607.

3. S. A. Parsons and B. Jefferson, *Introduction to Potable Water Treatment Processes*, Blackwell Publishing, Oxford, United Kingdom, 2006.

4. C. Allegre, P. Moulin, M. Maisseu and F. Charbit, *Treatment and reuse of reactive dyeing effluents*, **J. Membr. Sci.**, 2006, **269**, 15-34.

5. A. Gurses, C. Dogar, M.Yalçın, M. Açıkyıldız, R. Bayrak and S. Karaca, *The adsorption kinetics of the cationic dye, methylene blue, onto clay*, **J. Hazard. Mater.**, 2006, **131**, 217-228.

6. R. Jiang, H.-Y. Zhu, J.-B. Li, F.-Q. Fu, J. Yao, S.-T. Jiang, G.-M. Zeng, *Fabrication of novel magnetically separable BiOBr/$CoFe_2O_4$microspheres and its application in the efficient removal of dye from aqueous phase by an environment-friendly and economical approach*, **Appl. Surf. Sci.**, 2016, 364, 604-612.

7. U. Pagga and K. Taeger, *Development of a method for adsorption of dyestuffs on activated sludge*, **Water Res.**, 1994, **28**, 1051-1057.

8. K. Santhy and P. Selvapathy, *Removal of reactive dyes from wastewater by adsorption on coir pith activated carbon Removal of reactive dyes from wastewater by adsorption on coir pith activated carbon*, **Bioresour. Technol.**, 2006, **97**, 1329-1336.

9. R. Han, D. Ding, Y. Xu, W. Zou, Y. Wang, Y. Li and L. Zou, *Use of rice husk for the adsorption of congo red from aqueous solution in column mode.*, **Bioresour. Technol.**, 2008, **99**, 2938-2946.

10. Y. Al-Degs, M. A. M. Khraisheh, S. J. Allen, M. N. Ahmad, *Effect of Carbon Surface Chemistry on the Removal of Reactive Dyes from Textile Effluent*, **Water Res.**, 2000, **34**, 927-935.

11. C. K. Lee, S. S. Liu, L. C. Juang, C. C. Wang, K. S. Lin, M. D. Lyu, *Application of MCM-41 for dyes removal from wastewater*, **J. Hazard. Mater.**, 2007, **147**, 997-1005.

12. A. G. Espantaleón, J. A. Nieto, M. Fernández, A. Marsal, *Use of activated clays in the removal of dyes and surfactants from tannery waste waters*, **Appl. Clay. Sci.**, 2003, 24, 105-110.

13. Y. Yu, Y. Y. Zhuang, Z. H. Wang, M. Q. Qiu, *Adsorption of Water-Soluble Dyes onto Resin NKZ*, **Ind. Eng. Chem. Res.**, 2003, **42**, 6898-6903.

14. X. Wu,, W. Wang, F. Li, S. Khaimanov, N. Tsidaeva, M. Lahoubi, *PEG-assisted hydrothermal synthesis of $CoFe_2O_4$ nanoparticles with enhanced selective adsorption properties for different dyes*, **Appl. Surf. Sci.**, 2016, 389, 1003-1011.

15. L. Tan, Q. Liu, D. Song, X. Jing, J. Liu, R. Li, S. Hu, L. Liu, J. Wang, *Uranium extraction using a magnetic $CoFe_2O_4$–graphene nanocomposite: kinetics and thermodynamics studies*, **New J. Chem.**, 2015, 39, 2832-2838.

16. L. Zhou, C. Gao and W. Xu, *Magnetic dendritic materials for highly efficient adsorption of dyes and drug*s, **ACS Appl. Mater. Interfaces**, 2010, **2**, 1483.

17. M. H. Liao, D. H. Chen, *Preparation and characterization of a novel magnetic nano-adsorbent*, **J. Mater. Chem.**, 2002, 12, 3654.

18. Y. C. Chang, D. H. Chen, *Adsorption kinetics and thermodynamics of acid dyes on a carboxymethylated chitosan-conjugated magnetic nano-adsorbent*, **Macromol. Biosci.**, 2005, **5**, 254-261.

19. X. Li, H. Lu, Y. Zhang, F. He, L. Jing, X. He, *Fabrication of magnetic alginate beads with uniform dispersion of $CoFe_2O_4$ by the*

polydopamine surface functionalization for organic pollutants removal, **Appl. Surf. Sci.**, 2016, **389**, 567-577.

20. C. Lei, X. Zhu, B. Zhu, J. Yu, W. Ho, *Hierarchical NiO-SiO_2 composite hollow microspheres with enhanced adsorption affinity towards Congo red in water*, **J. Colloid Interface Sci.**, 2016, **466**, 238-246.

21. C. Lei, M. Pi, C Jiang, B. Cheng, J. Yu, *Synthesis of hierarchical porous zinc oxide (ZnO) microspheres with highly efficient adsorption of Congo red*, **J. Colloid Interface Sci.**, 2017, **490**, 242-251.

22. R. Rakshit, M. Pal, A. Chaudhuri, M. Mandal and K. Mandal, *Facile synthesis of $CoFe_2O_4$ nano-hollow spheres for efficient bilirubin adsorption*, **Appl. Mater.**, 2015, **3**, 110701-110706.

23. R. D. Waldron, *Infrared Spectra of Ferrites*, **Phys. Rev.**, 1955, **99**, 1727-1735.

24. N. Shukla, C. Liu, P. M. Jones, D. Weller, *FTIR study of surfactant bonding to FePt nanoparticles*, **J. Magn. Magn. Mater.**, 2003, **266**, 178-184.

25. Z. Xu, C. Shen, Y. Hou, H. Gao, S. Sun, *Oleylamine as Both Reducing Agent and Stabilizer in a Facile Synthesis of Magnetite Nanoparticles*, **Chem. Mater.**, 2009, **21**, 1778-1780.

26. N. Kaneko, M. Kaneko, H. Takahashi, *Infrared and Raman spectra and vibrational assignment of some metal tartrates*, **Spectrochim. Acta Part A**, 1984, 40, 33-42.

27. S. Pirillo, M. L. Ferreira and E. H. Rueda, *The effect of pH in the adsorption of Alizarin and Eriochrome Blue Black R onto iron oxides*, **J. Hazard. Mater.**, 2009, **168**, 168-178.

28. W. J. Weber, J. C. Morriss, *Kinetics of Adsorption on Carbon from Solution*, **J. Sanitary Eng. Div. Am. Soc. Civ. Eng.**, 1963, **89**, 31-38.

29. S. Lagergren, *About the theory of so called adsorption of soluble substances*, **Kung Sven. Veten. Hand.**, 1898, 24, 1-39.

30. Y. S. Ho, G. McKay, *Sorption of dye from aqueous solution by peat*, **Chem. Eng. J.**, 1998, **70**, 115-124.

31. I. Langmuir, *The Adsorption Of Gases On Plane Surfaces Of Glass, Mica And Platinum*, **J. Am. Chem. Soc.**, 1918, **40**, 1361-1403.

32. H. M. F. Freundlich, *Over the Adsorption in Solution*, **J. Phys. Chem.**, 1906, **57**, 385-471.

33. M. Jr. Horsfall, A. A. Abia, *Studies on the Influence of Mercaptoacetic Acid (MAA) Modification of Cassava (Manihot sculenta Cranz) Waste Biomass on the Adsorption of Cu^{2+} and Cd^{2+} from Aqueous Solution*, **Al. Spiff, Bull. Korean Chem. Soc.**, 2004, **25**, 969-976.

Chapter 7

Fabricating Multifunctional $ZnFe_2O_4$ nano-hollowspheres

In this chapter we have demonstrated brilliant photoluminescence consequent to surface modification of $ZnFe_2O_4$ nano-hollowspheres by organic ligand. Moreover, their efficiency as nanocarriers of drug has also been exhibited.

7. Folate functionalized $ZnFe_2O_4$ nano-hollowspheres for drug delivery and intrinsic fluorescence

7.1 Preamble

Magnetic nanostructures (NSs) have grown great interest in the bio-medical field because of their controllable size ranging from few nm to 100 nm, which enables them to 'get close' to certain biological entities such as a cell (10–100μm), a protein (5–50 nm), a virus (20–450 nm), or a gene (2 nm wide and 10–100 nm long). They can be coated with biological molecules to make them interact with or bind to a biological entity, thus providing a controllable means of 'tagging' or addressing it. Moreover, the magnetic nanostructures can be controlled by an external magnetic field, which opens up many applications involving the transport of magnetic nanostructures, or of magnetically tagged biological entities. Thus the magnetic NSs can deliver a package, such as an anticancer drug, or radionuclide atoms, to a targeted region of the body, such as a tumor [1-8]. Magnetic nanostructure-based targeting can decrease or eradicate the side effects of conventional chemotherapy by reducing the systemic distribution of drugs and lower the doses of the cytotoxic compounds [9-11].

It has been accepted that targeted delivery is very necessary for anticancer drug delivery system, as most of the commonly used anticancer drugs have serious side effects due to unspecific action on healthy cells. Moreover, targeted delivery would enhance the therapeutic efficacy. Magnetic targeting could enable drug delivery systems to reach the targeted organs or tissues quickly, but it could not effectively enhance cell uptake of drug delivery systems by cancer cells. It has been believed that cellular targeting by utilizing antibodies or specific ligands to selectively bind to the cell surface to enhance the efficiency of cell uptake of drug delivery systems, which could significantly enhance the therapeutic efficacy. Folic acid, a small-molecule vitamin, is essential for the

human body. It is an important coenzyme in DNA synthesis and serves as a co-factor in the synthesis of several enzyme systems. Folic acid (FA), which is a water-soluble form of vitamin B, targets tumors. This is because FA has a high affinity for folate receptors (FRs), which are overexpressed in various types of human tumors but generally are absent in most normal tissues. FA has several advantages over macromolecules as a tumor-targeting ligand: (1) easy availability; (2) low cost; (3) applicability over a wide range of tumors, such as laryngeal, ovarian, endometrial, colorectal, breast, lung, renal-cell, and neuroendocrine carcinomas, (4) ease of cytosolic delivery when combined with magnetic NPs (5) potential for repeated administration, because of its small size, as compared to other targeting ligands. Due to this reasons, FA is most commonly used in targeted drug delivery purposes nowadays [12-16].

Zinc ferrite nanoparticles received a great deal of attention in nanomedicine due to the lesser toxicity of Zn^{+2} and its permissible RDI (Reference Daily Intake) doses 15 mg/day, which is much higher than any other biocompatible material [17]. Complexation between metal ions and ligands is an acid–base reaction that is driven primarily by electrostatic interactions. The binding of ligands depends on the nature of the atom donor, e.g., oxygen, nitrogen and sulfur, many of the ligands obey the Irving–Williams series, which forecasts that the association binding constants for the divalent transition metals are in the following order: $Mn^{+2}<Fe^{+2}<$ $Co^{+2}<Ni^{+2}<Cu^{+}2<Zn^{+2}$ [18]. The higher the association constant, the higher complexation occurs. The ferrites have molecular formula of AB_2O_4, where *A* is the tetrahedral voids and *B* is the octahedral sites. Here, A^{+2} is the divalent metal ions and B^{+3} are the trivalent ions of Fe. The Zn^{+2} ions have ionic radius of 74 Å and thus they occupy the tetrahedral (*A*) sites in the spinel structure which results in a normal spinel [19]. We have synthesized $ZnFe_2O_4$ Nano-hollowspheres (NHSs) and made them biocompatible with Sodium folate ligand, which in turn generated inherent

multiple fluorescences. Additionally, the NHSs were tested as nano-carriers for pH responsive drug delivery using low concentration of Doxorubuicin and found to be worthy.

7.2. Experimental

7.2.1 Materials Used

Iron chloride hexahydrate [$FeCl_3.6H_2O$], Zinc chloride [$ZnCl_2$], Ethylene Glycol, Urea [$CO(NH_2)_2$], Oleylamine and Doxorubicin hydrochloride are obtained from Sigma-Aldrich. Ethyl Alcohol [EtOH] and Sodium Hydroxide [NaOH] are purchased from Merck. Folic Acid is bought from Loba Chemie.

7.2.2 Synthesis and Characterization

$ZnFe_2O_4$ (ZFO) NHSs were synthesized using solvothermal method. A solution mixture of Iron (III) chloride hexahydrate, Zinc (II) chloride, Ethylene Glycol, Urea, Ethanol and Oleylamine was heated in Teflon lined stainless steel autoclave at 180°C for 18 h in an oven. Then the as-prepared $ZnFe_2O_4$ NHSs were washed by ethanol and collected after centrifugation. Further, the as-prepared $ZnFe_2O_4$ NHSs were dried by heating on a hotplate at a temperature of 80°-90°C for 10 min.

In order to modify surface of the as-prepared $ZnFe_2O_4$ NHSs with folate ligands we cyclomixed the NHSs with 0.05M Na-folate solution (pH~7) at room temperature for 12 h. We obtained a light yellowish solution of folate-functionalized $ZnFe_2O_4$ NHSs, and named as FZFO NHSs.

The X-ray powder diffraction (XRD) of as-prepared $ZnFe_2O_4$ NHSs was done using Rikagu miniflex II diffractometer equipped with Cu Kα radiation (at 40 mA and 40 kV) at the scanning rate of 3° per minute in the 2θ range of 20°-70°. A FEI Technai G2 TF-20 field-emission high-resolution transmission electron

microscope (TEM) and A FEI QUANTA FEG 250 field-emission high-resolution scanning electron microscope (FESEM), were used to study the size, shape, morphology, and size distribution and to record the Energy-dispersive X-ray analysis (EDX) spectrum of the as-prepared and functionalized $ZnFe_2O_4$ NHSs. The Ultraviolet-visible (UV/Vis) absorbance spectra of FZFO NHSs were obtained using a quartz cuvette of 1 cm path length on Shimadzu UV-2600 spectrophotometer. To carry out the steady state photoluminescence excitation and emission study of FZFO NHSs a Horiba Jovin Yvon Model Fluorolog fluorometer was used. Fluorescence micrographs of FZFO NHSs were captured using Olympus BX53 fluorescence microscope.

FTIR (Fourier transform infrared spectroscopy) measurements were performed using a JASCO FTIR-6300 spectrometer to ensure of the attachment of folate molecules to the NHSs' surface. For FTIR study, pellets were made after homogeneous mixing of lyophilized FZFO NHSs powder samples with KBr. The background was corrected using a reference KBr pellet. For magnetic measurements of as-prepared $ZnFe_2O_4$ NHSs and FZFO NHSs, a Lake Shore VSM equipped with an electromagnet was used.

7.2.3 Loading of Drug molecule

In order to study the drug loading Doxorubicin on to the surface of FZFO NHSs, we prepared Doxorubicin solution of 5 X 10^{-3} M using D.I water (pH 7). For loading of the drug, the Doxorubicin solution was cyclomixed with Na-folate functionalized $ZnFe_2O_4$ for 1 hour at 25°C. Further the drug loaded NHSs were magnetically separated and dried. The drug loading percentage was measured using UV/Vis Spectrometer.

7.3 Results and Discussion

The XRD pattern shown in Figure 7.1 confirms that all the peaks perfectly

match with the normal spinel structure of $ZnFe_2O_4$ NHSs, as reported in the literature (JCPDS file no. 89-1010). The EDX (energy dispersive X-ray) spectra in the inset of Figure 1 confirms the presence of Zn, Fe and O in $ZnFe_2O_4$ NHSs.

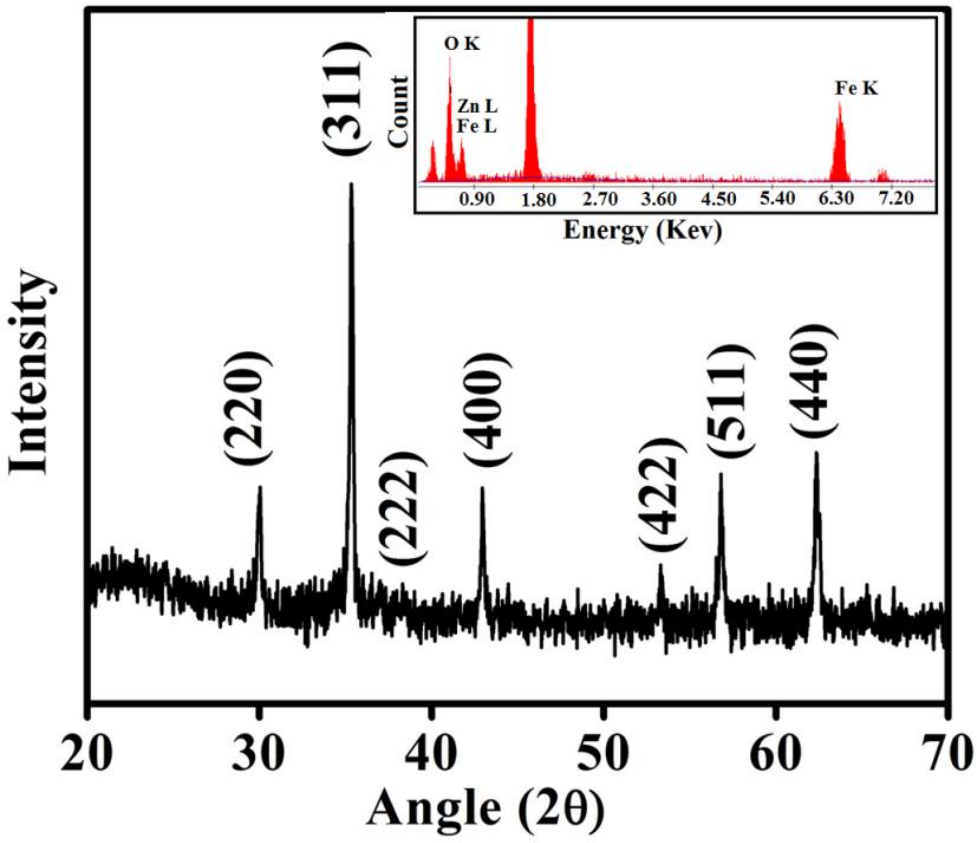

Figure 7.1: XRD of the as-prepared $ZnFe_2O_4$ NHSs. Inset shows the EDX spectra of as-prepared $ZnFe_2O_4$ NHSs indicating presence of Zn, Fe and O.

For understanding morphology and size of the both as-prepared $ZnFe_2O_4$ NHSs and FZFO NHSs, TEM (transmission Electron Microscope) and SEM (Scanning Electron Microscope) studies were done. From Figure 7.2.(a) and (b), it is clearly evident that the as-prepared ZFO NHSs have hollow structure and Figure 7.2.(c) confirms the narrow dispersity with an average diameter of 200 nm. Figure 7.2.(d) shows SAED pattern of the as-prepared ZFO NHS.

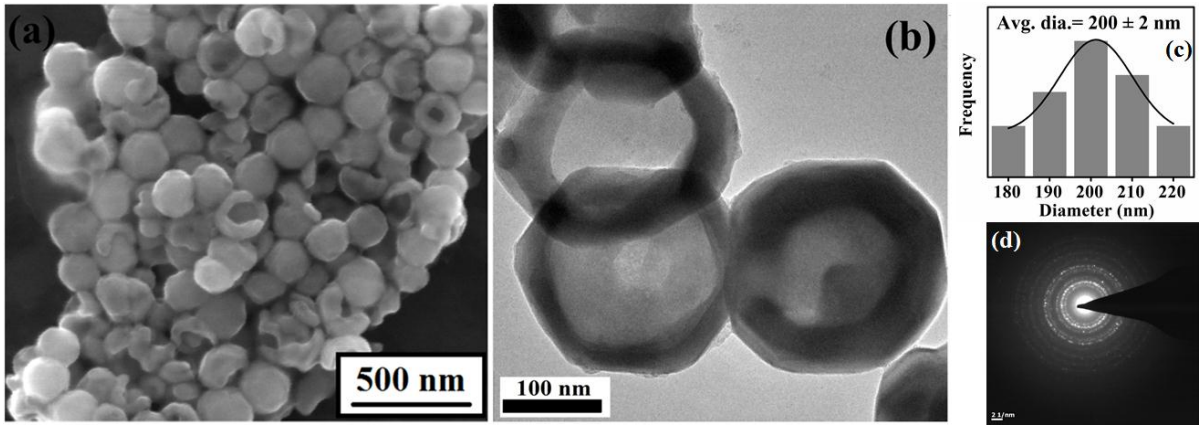

Figure 7.2: (a) SEM and (b) TEM image of the as-prepared $ZnFe_2O_4$ NHSs. (c) Size distribution graph of as-prepared $ZnFe_2O_4$ NHSs. (d) SAED pattern of as-prepared $ZnFe_2O_4$ NHSs indicates high crystallinity.

In order to solubilize the as-prepared ZFO NHSs into aqueous medium, we have functionalized the NHSs with Na-folate solution. As the result of functionalizing, we also have made the as-prepared ZFO NHSs biocompatible. After surface modification, the size of the FZFO NHSs remains almost unchanged, that is evident from Figure 7.3.(a).

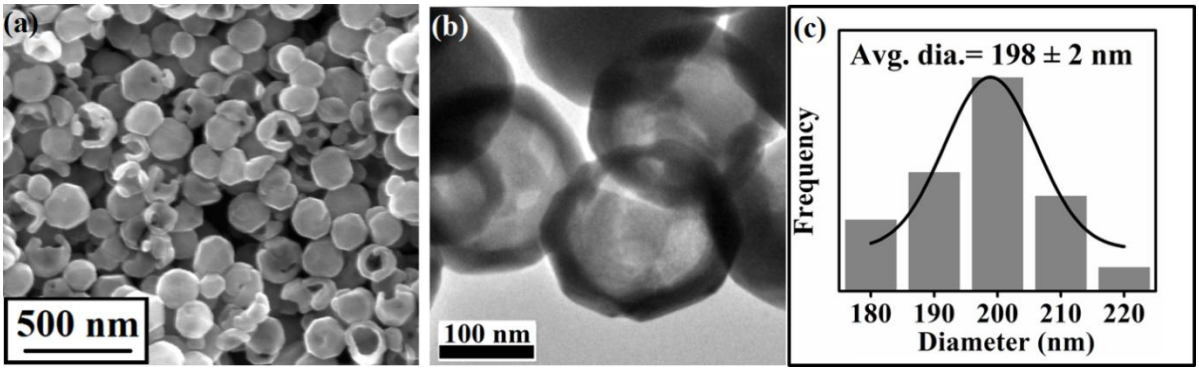

Figure 7.3: (a) SEM and (b) TEM image of the folate functionalized $ZnFe_2O_4$ NHSs. (c) Size distribution graph of folate functionalized $ZnFe_2O_4$ NHSs.

Further we carried out the absorption study on folate functionalized ZFO (FZFO) NHSs and from Figure 7.4.(a), it was found that the functionalized ZFO

NHSs (pH~7) have different absorption property than the only tartrate, indicating a distinct change in the surface electronic structure of the NHSs. In the absorption spectra of the functionalized ZFO (Figure 7.4.(a)) the bands around 300 and 360 nm is clearly visible along with the 280 nm band which is characteristic absorption band for folate. In order to examine the photoluminescence property, we carried out a pilot experiment by placing the cuvette filled with FZFO NHSs under UV light of wavelength 253.7 nm (UV-C), shown in Figure 7.4.(b). The FZFO NHSs showed a bright cyan color under UV light irradiation. In order to intensify the photoluminescence, further surface modification was done by increasing the pH of the FZFO NHSs to10 and again carried out the absorption study. After the second surface modification, the bands at 305 and 363 nm become distinct along with the band at 256 nm, shown in Figure 7.4.(a).

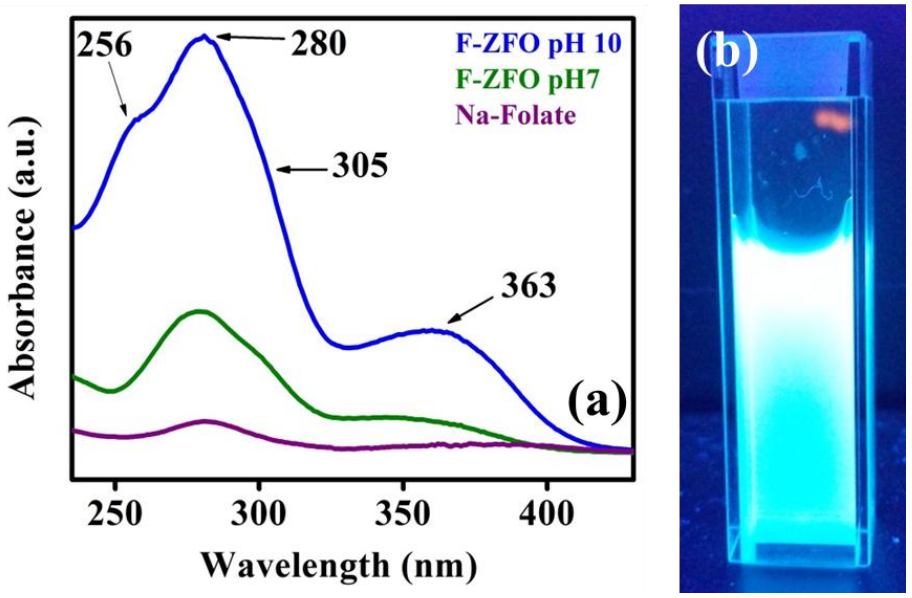

Figure 7.4: (a) Absorption spectra of Na-folate, FZFO NHSs at pH 7 and 10. (b) FZFO NHSs (pH 7) are under UV light.

After acquiring the information from the absorption spectra, we carried out photoluminescence study of the FZFO, and observed fluorescence at λ_{em}= 358 nm while exciting the functionalized solution at λ_{ex}= 258 nm. Three more

photoluminescence peaks were generated with greater intensity as a result of further surface modification, the photoluminescence peaks at λ_{em}= 417 nm, 475 nm and 620 nm were found upon exciting the fl. mod. solution of ZFO NHSs at λ_{ex}= 310 nm, 393 nm, 508 nm respectively. With the assistance of Ligand Field theory (LFT), the occurrence of multicolor photoluminescence can be clarified. The photoluminescence peak at λ_{em}= 358 nm for fluorescence modified ZFO NHSs, resulting from exciting the solution at λ_{ex}= 258 nm (absorption peak seen in Figure 7.5), arises from ligand to metal charge transfer (LMCT) involving the highest occupied energy level of tartrate ligands and the lowest unoccupied energy levels of Fe^{+3} metal ion centers on the NPs' surface.

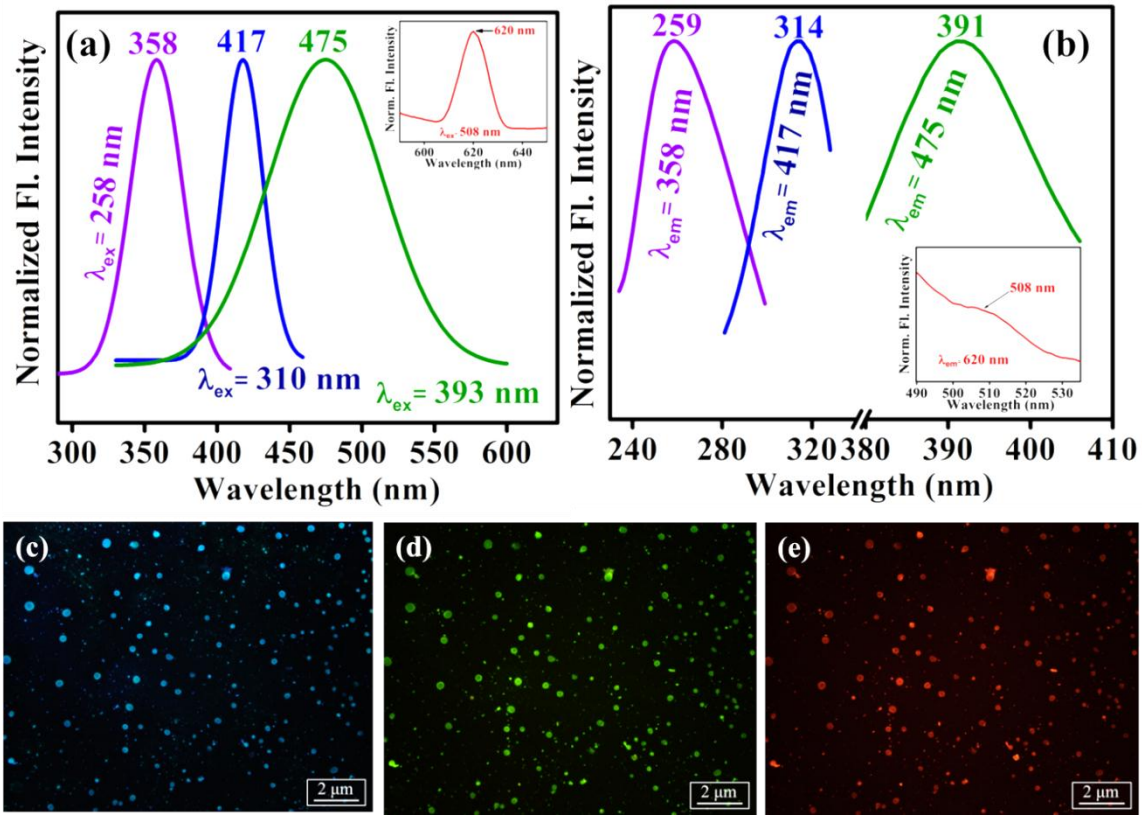

Figure 7.5: (a) Normalized steady-state fluorescence emission spectra obtained from FZFO (pH 10) NHSs after excitation at four different wavelengths, λ_{ex} = 258, 310, 393, and 508 nm. (b)Fluorescence excitation spectra of FZFO (pH 10) NHSs at different emission maxima, that is, λ_{em}= 358, 417, 475 and 620 nm. Fluorescence micrographs of FZFO (pH 10) NHs powder under (c) UV, (d) blue, and (e) green light irradiation. The scale bars in all images are 2 μm.

It is most probable that the Fe^{+3} may take part in the generation of fluorescence. The other three peaks at 417 nm, 475 nm, 620 nm may be ascribed to the possible d-d transitions of the Fe^{+3} metal ions. As Fe^{+3} is d^5 system, the d-d transitions are both spin and laporte forbidden, however, they can have considerable strengths due to the relaxation of selection rules by lattice distortion and spin-orbit coupling as discussed in other Fe^{+3} (d^5) materials [20-21]. The three emission bands with maxima at λ_{em}= 445 nm, 488 nm and 560 nm can be described in terms of spectroscopic term symbols, due to transitions from $^6A_{1g}$ to $^4T_{1g}$, $^4T_{2g}$ and $^4A_{1g}$ transitions involving d-d orbitals of Fe^{+3} ions, respectively, due to the crystal field splitting.

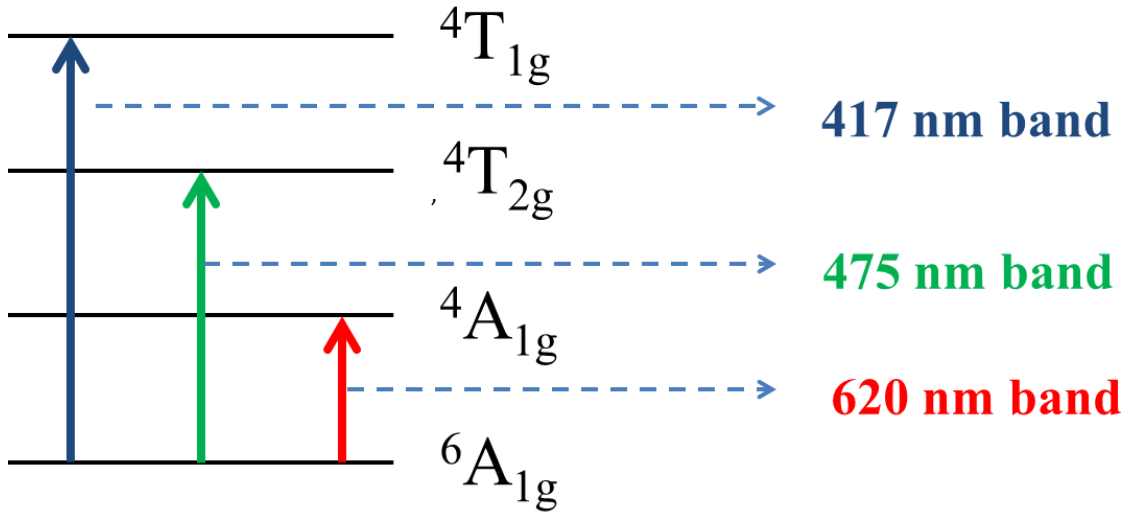

Figure 7.6: The schematic diagram of the spin allowed d-d transitions of Fe^{+3} (d^5 system), that result in three different colored fluorescence for FZFO (pH 10) NHSs. The transitions are shown using Tanabe Sugano diagram.

In order to see the effect of higher pH and to establish the data we have found on further surface modification, we carried out the photoluminescence study at three different pH scales. The folate ion has σ donor (NH_2 group) and π donor (COO^- group). With increasing basicity, both donor groups get deprotonated and the deprotonated σ donor groups interacts with the metal much more

efficiently in basic medium than in neutral medium. The increased interaction causes more splitting in the d orbitals. In case of acidic and neutral medium, the donor groups get protonated which in turn hinders the folate molecules to attach on the metal surface. Thus, as the pH of the solution increases the interaction of the metal and the ligands increases which in turn results in the higher intensity fluorescence bands. The intensification of the bands at 358 nm and 417 nm with increasing pH, can easily be seen from the Figure 7.7.(a) and (b).

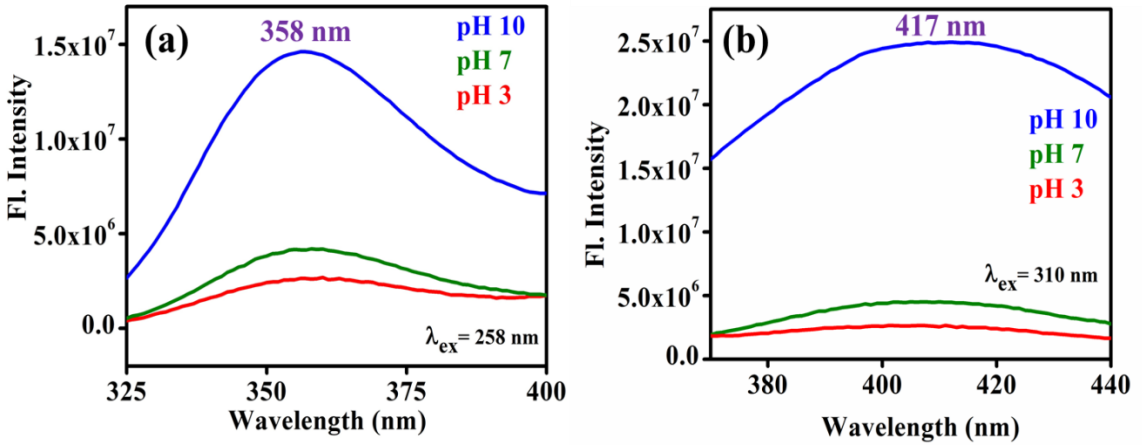

Figure 7.7: Normalized steady-state intensity comparison spectra of (a) 358 nm and (b) 417 nm band of FZFO NHSs at 3 different pH scales.

The FTIR study was carried out for ZFO NHSs before and after functionalization with folate ligand and for Folic acid, in order to inquire about the attachment of the ligand molecules to the surface of bare ZFO NHSs. As depicted in Figure 7.8, the peak arising at 420 cm^{-1} and 574 cm^{-1} are attributed to stretching vibration of metal-oxygen bonds in $ZnFe_2O_4$ due to Zn^{2+} and Fe^{3+} ions respectively [22]. The peaks at 420 cm^{-1} and 574 cm^{-1} are not distinguishable in the case of FZFO NHSs. The sharp peak arising at 1485 cm^{-1} is the characteristic band for phenyl and PT ring. Two other peaks at 1411 and 1621 cm^{-1} are due to the symmetric and asymmetric stretching of the COO^-. The peak at 1690 cm^{-1} is attributed to stretching vibration of C=O, whereas at 1450 cm^{-1} peak is due to folate amide bond [23]. Because of the interactions between

the surface of the $ZnFe_2O_4$ NHSs and the functional group moieties of the ligand, all the bands are clearly perturbed.

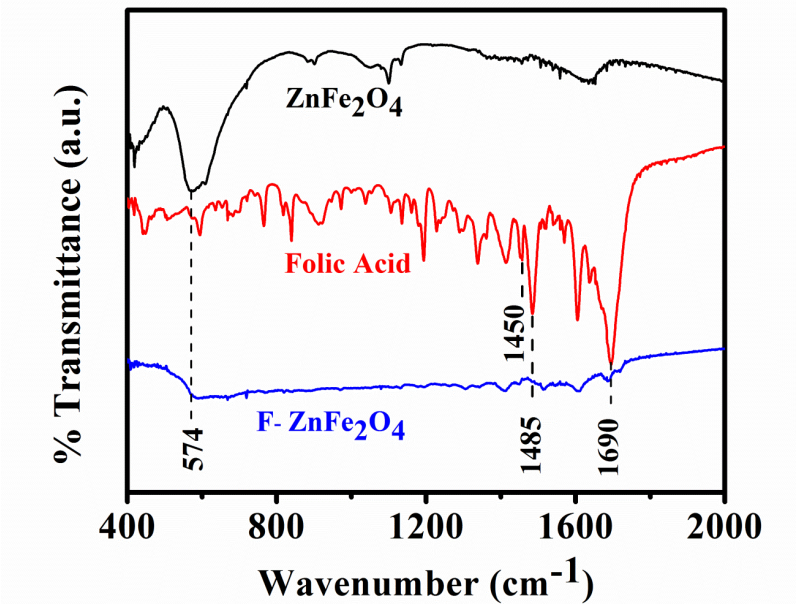

Figure 7.8: FTIR spectra of as-prepared ZFO and FZFO NHSs together with Na-folate.

Drug loading efficiency for the particles was checked with the help of UV–vis absorption spectra taken for the Doxorubicin solution before (initial) and after (final) loading the drug into the particles, shown in Figure 7.9. The absorption intensity was measured at 486 nm wavelength and it was observed that about 78% of drug was loaded, which was calculated using the Eq. (7.1) as given below.

$$\text{Loading efficiency} = \frac{A_0 - A_f}{A_0} X\ 100 \qquad (7.1)$$

Where A_0 is the initial absorbance of the DOX solution, and A_f is the final absorbance of the DOX solution. DOX release was calculated by following equation (7.2):

$$\text{DOX release \%} = \frac{C_t}{A_0 - A_f} \text{ X } 100 \qquad (7.2)$$

where C_t is concentration of DOX at time t.

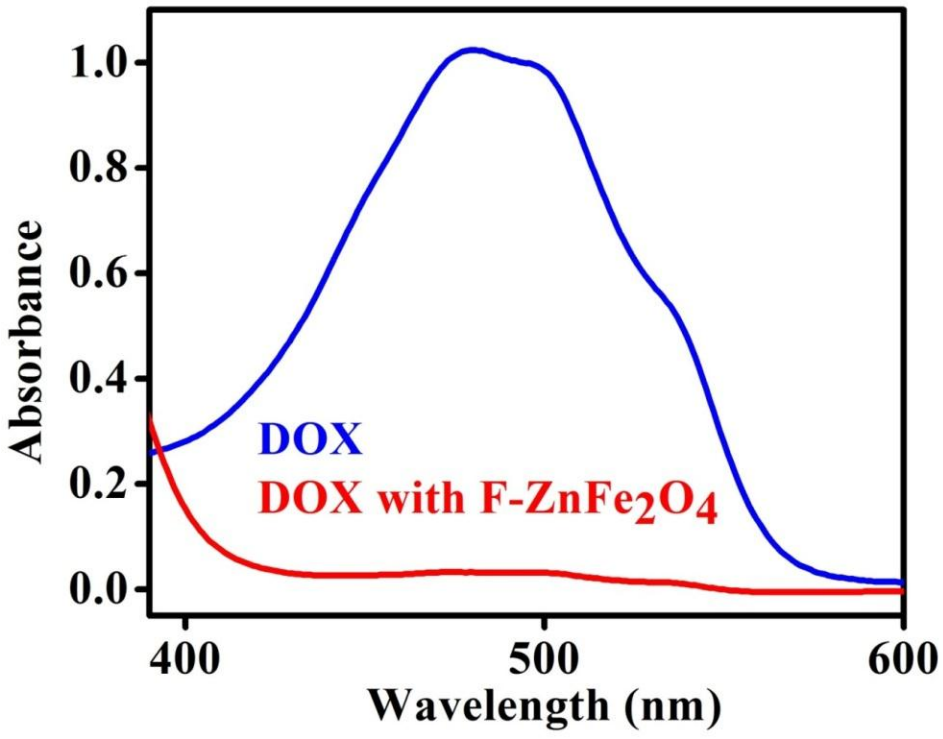

Figure 7.9: UV–visible spectra of initial drug solution and finally after drug loading by the FZFO NHSs.

After loading the particles with drug, they were undergone for drug release study at two different pHs (i.e. pH 5 and pH 7.4) with respect to time. 12 mg of this drug (DOX) loaded particles were taken in 2 ml of different buffer solutions and these experiments were carried out at 37 °C. The drug release intensity was measured at different interval of time with the help of UV–Vis spectrometer. The representative graphs on relative drug release rate with time measured at two different temperatures are shown in Figure 7.10. The graphs clearly show that the release efficiency is undoubtedly better at lower pH. Figure 7.10 depicts that within 4 h, 99% of the drug was released at pH 5 whereas in pH 7.4, release occurred up to 95% in 5h. This fast release at pH 5 was attributed to the cleavage of hydrogen bond in acidic condition. The attachment of Doxorubicin with folate molecule takes place through hydrogen bonding between the -COOH groups of folate and the $-NH_2$ groups of Doxorubicin. In hydrogen

bonding, $-NH_2$ of Doxorubicin forms $-NH_3^+$. In acidic conditions, the H^+ in solution would compete with the hydrogen-bond-forming groups and then weaken the above hydrogen-bonding interaction. Thus the lower pH triggers the release of Doxorubicin. Hence, we can conclude that the ZFO magnetic nano-hollowspheres have potentiality to be used in pH triggered drug release, where controlled release of drug in a noninvasive way is required.

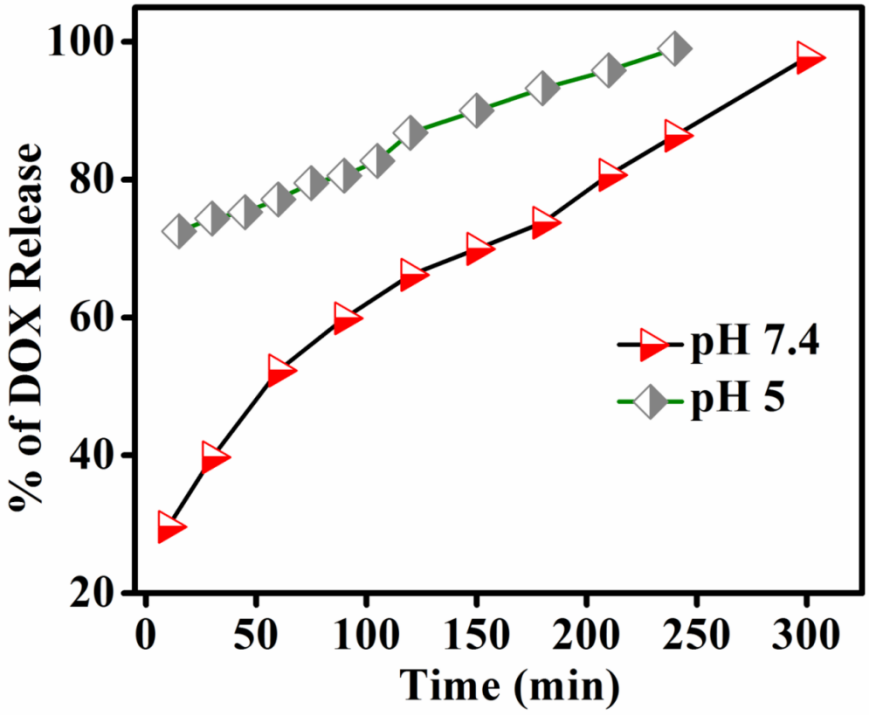

Figure 7.10: Time dependent drug release graphs of DOX loaded FZFO NHSs in two different pHs.

The room temperature magnetic behavior of the Doxorubicin loaded FZFO NHSs along with the as-prepared and functionalized ZFO NHSs were studied using VSM. Figure 7.11 depicts the field dependent magnetization (M-H loops) of the three afore mentioned samples due to the application of 14 kOe field. From Figure 7.11.(a), 7.11.(b) and 7.11.(c), it is found that the saturation magnetization is gradually decreased from as prepared ZFO NHS to Doxorubicin loaded FZFO NHSs. Due to the extensive charge transition from

folate to the d orbitals of Fe^{+3}, the saturation magnetization of the FZFO NHSs falls to 39.9 emu/g from 47.8 emu/g. Further the diamagnetic capping of the drug molecules, saturation magnetization further drops to 10.15 emu/g for Doxorubuicin loaded FZFO NHSs. The coercivity of the FZFO and Doxorubicin loaded FZFO NHSs got increased due to the diamagnetic layer on the magnetic ZFO NHSs [24].

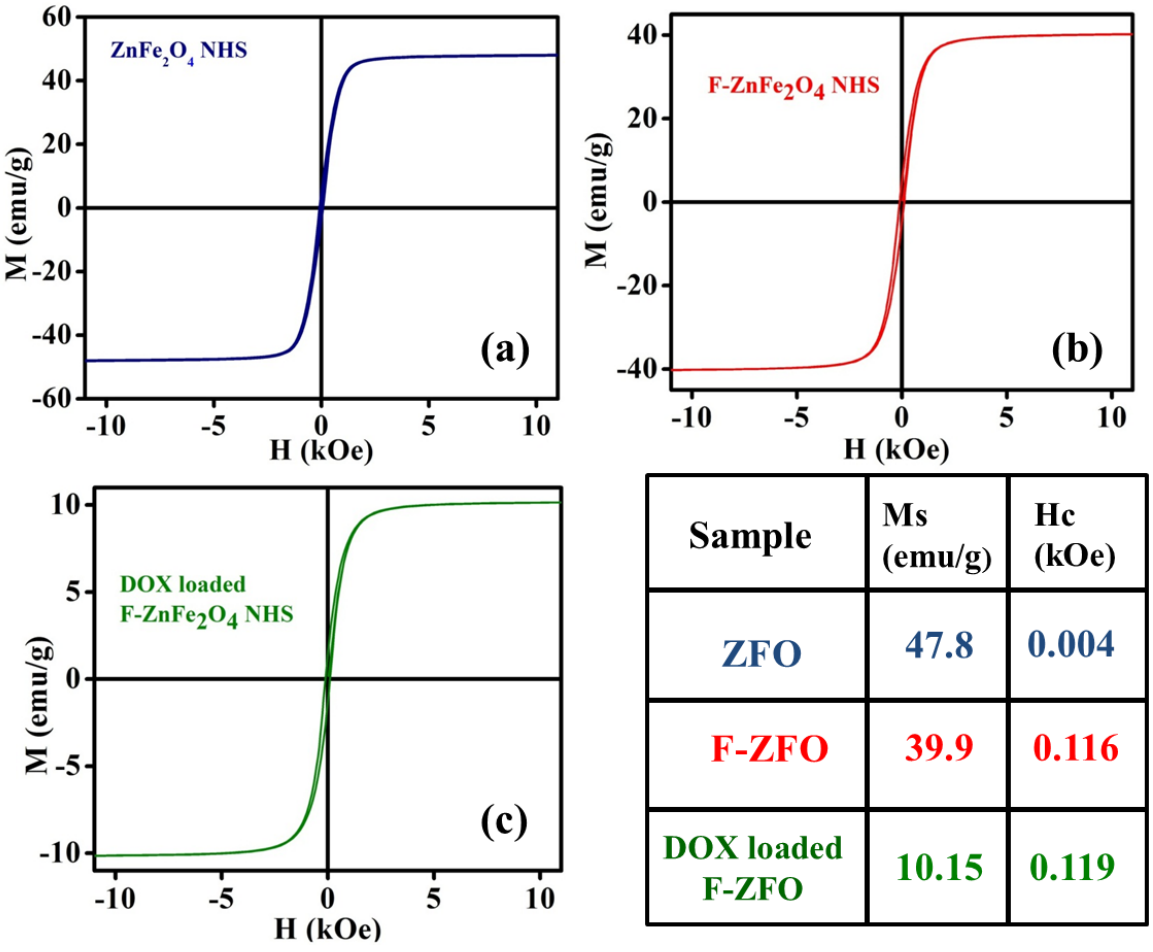

Sample	Ms (emu/g)	Hc (kOe)
ZFO	47.8	0.004
F-ZFO	39.9	0.116
DOX loaded F-ZFO	10.15	0.119

Figure 7.11: (a) Plot of magnetization versus applied magnetic field (M-H) of as-prepared $ZnFe_2O_4$ NHSs at 300 K. M-H plot for (b) FZFO and (c) Doxorubicin loaded FZFO NHSs at 300 K.

7.4 Conclusion

In conclusion, by easy surface modification of $ZnFe_2O_4$ NHSs with Na-folate ligands, we have prepared biocompatible multifunctional nano-hollowspheres with intrinsic fluorescence properties covering the whole visible region, ranging from blue, and green to red. We believe that our material may develop new prospects in the field like bioimaging. Moreover, the NHSs showed excellent pH triggered drug release. The loading and pH-dependent releasing of drug occurs due to the hydrogen-bonding interactions between the metal oxide surface attached folate and Doxorubicin. In conclusion, this work has demonstrated an efficient multifluorescent anticancer drug delivery system using folate functionalized magnetic nano-hollowspheres.

Bibliography

1. S.C. McBain, H.H.P. Yiu, J. Dobson, *Magnetic nanoparticles for gene and drug delivery*, **Int J. Nanomedicine**, 2008, 3, 169–180.

2. M. Arruebo, R.Fernández-Pacheco, M.R. Ibarra, J. Santamaría, *Magnetic nanoparticles for drug delivery*, **Nano Today**, 2007, 2, 22-32.

3. X. Mou, Z. Ali, S. Li, H. Nongyue, *Applications of Magnetic Nanoparticles in Targeted Drug Delivery System*, **J. Nanosci. Nanotechnol**., 2015, 15, 54-62.

4. S. Kayal, R.V. Ramanujan, *Doxorubicin loaded PVA coated iron oxide nanoparticles for targeted drug delivery*, **Mater. Sci. Eng. C**., 2010, 30, 484-490.

5. C. Sun, J.S.H. Lee, M. Zhang, *Magnetic nanoparticles in MR imaging and drug delivery*, **Adv. Drug Deliv. Rev**, 2008, 60, 1252-1265.

6. Y.H. Xu, Ji.Bai J.-P.Wang, *High-magnetic-moment multifunctional nanoparticles for nanomedicine applications*, **J. Magn. Magn. Mater**., 2007, 311, 131-134.

7. B. Zhang, Q.Li, P. Yin, Y. Rui, Y. Qiu, Y. Wang, D. Shi, *Ultrasound-Triggered BSA/SPION Hybrid Nanoclusters for Liver-Specific Magnetic Resonance Imaging*, **ACS Appl. Mater. Interfaces**, 2012, 4, 6479–6486.

8. K. Zhu, Z. Deng, G. Liu, J. Hu, S. Liu, *Photoregulated Cross-Linking of Superparamagnetic Iron Oxide Nanoparticle (SPION) Loaded Hybrid Nanovectors with Synergistic Drug Release and Magnetic Resonance (MR) Imaging Enhancement***, Macromolecules**, 2017, 50, 1113–1125.

9. A. Saha, P.S. Devi, *Surface Functionalized Multifunctional Gd2O3–Fluorescein Composite Nanorods for Redox Responsive Drug Delivery and Imaging Applications*, **ACS Appl. Nano Mater.**, 2018, 1, 2898–2911.

10. A.K. Gupta, A.S.G. Curtis, *Surface modified superparamagnetic nanoparticles for drug delivery: Interaction studies with human fibroblasts in culture*, **J. Mater. Sci. Mater. Med**., 2004, 15, 493–496.

11. A.K. Gupta, S. Wells, *Surface-modified superparamagnetic nanoparticles for drug delivery: preparation, characterization, and cytotoxicity studies*, **IEEE Trans Nanobioscience,** 2004, 3, 66-73.

12. J.A. Vassie, J.M. Whitelock, M.S. Lord, *Targeted Delivery and Redox Activity of Folic Acid-Functionalized Nanoceria in Tumor Cells*, **Mol. Pharmaceutics**, 2018, 15, 994−1004.

13. M.de Sousa, L.A.V. de Luna, L.C. Fonseca, S. Giorgio, O.L. Alves, *Folic Acid-Functionalized Graphene Oxide Nanocarrier: Synthetic Approaches, Charectarization, Drug Delivery Study, and Antitumor Screening*, **ACS Appl. Nano Mater.**, 2018, 1, 2, 922-932.

14. X. Chen, Z. Shi, R. Tong, S. Ding, X. Wang, J. Wu, Q. Lei, W. Fang, *Derivative of Epigallocatechin-3-gallatea Encapsulated in ZIF-8 with Polyethylene Glycol−Folic Acid Modification for Target and pH-Responsive Drug Release in Anticancer Research*, **ACS Biomater. Sci. Eng.**, 2018, 4, 4183−4192.

15. R. Bhanumathi, M. Manivannan, R. Thangaraj, S. Kannan, *Drug-Carrying Capacity and Anticancer Effect of the Folic Acid- and Berberine-Loaded Silver Nanomaterial To Regulate the AKT-ERK Pathway in Breast Cancer*, **ACS Omega**, 2018, 3, 8317−8328.

16. Y. Wang, X. Chen, D. He, Y. Zhou, L. Qin, *Surface-Modified Nanoerythrocyte Loading DOX for Targeted Liver Cancer Chemotherapy*, **Mol. Pharmaceutics**, 2018, 15, 5728−5740.

17. S.M. Hoque, C. Srivastava, N. Venkatesha, P.S.A. Kumar, K. Chattopadhyay, Super paramagnetic behavior and T1, T2 relaxivity of $ZnFe_2O_4$ nanoparticles for magnetic resonance imaging, **Philos. Mag.**, 2013, 93, 1771–1783.

18. D. Burshtain, D. Mandler, *The effect of surface attachment on ligand binding: studying the association of Mg^{2+}, Ca^{2+} and Sr^{2+} by 1-thioglycerol and 1,4-dithiothreitol monolayers*, **Phys. Chem. Chem. Phys.**, 2006, 8, 158–164.

19. V.G. Harris, N.C. Koon, C.M. Williams, Q. Zhang, M. Abe, Z.P. Kirkland, *Cation Disrtibution in NiZn-Ferrite films via extended X-Ray absorption fine Structure*, Appl. Phys. Lett., 1996, 68, 2082-2084.

20. X. S. Su, T. V. Brinzari, S. Lee, Y.H. Chu, L.W. Martin, S. McGill, R. C. Rai, R. Ramesh, V. Gopalan, S. W. Chewong, J. L. Musfeldt, *Optical Properties and magnetochorism in multiferroic* $BiFeO_3$, **Phys. Rev. B**, 2009, 134425-134427.

21. O. N. Noksha and S.V. Grum-Grzhimailo, *Studies of the Optical Spectra of Crystals with Iron Group Ions at Room and Low Temperatures*, (Nauka, Moscow), 1972.

22. R.R. Shahraki, M. Ebrahimi, S.A. Seyyed Ebrahimi, S.M. Masoudpanah, *Structural characterization and magnetic properties of superparamagnetic zinc ferrite nanoparticles synthesized by the coprecipitation method*, **J. Magn. Magn. Mater.,** 2012**,** 324, 3762–3765.

23. H.P. Thu, N.H. Nam, B.T. Quang, H.A. Son, N.L. Toan, D.T. Quang, *In vitro and in vivo targeting effect of folate decorated paclitaxel loaded PLA–TPGS nanoparticles*, **Saudi Pharm J**, 2015, 23, 683-688.

24. R. Rakshit, M. Pal, M. Mandal, K. Mandal, *Charge transfer mediated magnetic response of cobalt ferrite nanoparticles*, **Mater. Lett.,** 2015, 151, 64-67.

Chapter 8

Conclusion and Future Scope

This chapter concludes the whole work and gives an idea of imminent possibilities in diverse fields.

8.1. Epilogue

In this thesis, we have primarily focused our work on the synthesis of transition metal oxide ($NiFe_2O_4$, $CoFe_2O_4$, and $ZnFe_2O_4$) based magnetic nanostructures (nanoparticles (NPs) and nano hollow spheres (NHSs) by two different chemical synthesis procedure (Reflux-condensation and Solvothermal Method) followed by functionalization in order to tune their optical properties. Very promisingly, the surface functionalized NSs are found to exhibit excellent optical properties. The nano-hollowstructures (NHSs) exhibit higher coercivity in comparison to its solid configuration of same diameter.

We have used the organic ligands such as tartaric acid and folic acid in order to functionalize the surface of NSs. We have found that surface modified NSs showed brilliant multicolor photoluminescence, ranging from UV to visible scale, which in turn can be beneficial for targeted cell imaging. The multicolor fluorescence can also be used in bio-marking for cancer cells. The ligand to metal charge transfer and the d-d transition of the metal electrons, are responsible the polychromatic fluorescence. We have applied the tartrate functionalized NSs in Osteosarcoma cell line and found that the NSs got absorbed in the cells and showed brilliant blue coloration with UV light irradiation.

To resolve the challenges of environmental pollution due to mismanagement of pharmaceutical waste, industrial dye waste need to be effectually treated before being discharged into the environment. Due to large specific surface area, chemical stability, excellent magnetic property, facile separation and low cost of synthesis, ferrite NSs have attracted incredible attention in this regards. We have studied the catalytic and photocatalytic property of functionalized and as-prepared NSs on different environmentally and biologically hazardous materials such as MB, RhB, 4-NP, BR respectively. Thorough studies have revealed that

the UV irradiation on the surface of NSs generate electron hole pair, which in consequence generates Reactive Oxygen Species (ROS) and the ROS are instrumental behind the degradation of the harmful chemical entities. In case of catalytic studies, the as-prepared NSs surface acts as a mediator to transfer the electron from acceptor to donor, which facilitates the reaction.

Further, we have studied the NHSs as the nano-carriers of the anticancer drugs. We have found that NHSs are efficient in loading the anti-cancer drug Doxorubicin in room temperature, while the release study was carried out in different situations. Usually the cancer cells have lower pH than the normal cells and we found that the NHSs show excellent drug release ability in lower pH due to the breakage of H-bonding between the surface attached folate group and Doxorubicin. In the higher temperature release, the thermal agitation helps to release the Doxorubicin from surface of folate functionalized NHSs.

8.2. Future Scope

The advanced inherent multicolor fluorescent magnetic nanostructures can simultaneously be used in imaging, MRI, and targeted drug delivery. We are planning in vitro experiments for dual imagining of MRI and fluorescence along with vigorous toxicological study of NSs on different cell lines. Moreover, the folate functionalized magnetic nanostructures can be used as nano-carriers in targeted drug delivery and also in bio-marker for cancer cells.

The excellent catalytic property of the both as-prepared and functionalized NSs towards the noxious chemical entities can be extended to variety of environmentally harmful dyes.